Development of a High Power Density Combustion System for a Silicon Micro Gas Turbine Engine

by

Amitav Mehra

B.S., Engineering and Applied Science, California Institute of Technology, (June 1995)
S.M., Aeronautics and Astronautics, Massachusetts Institute of Technology, (June 1997)

Submitted to the Department of Aeronautics and Astronautics
in partial fulfillment of the requirements for the degree of

Doctor of Philosophy
at the
Massachusetts Institute of Technology

February 2000

Author ____________________
Department of Aeronautics and Astronautics
January 26, 2000

Certified by ____________________
Professor Ian A. Waitz
Associate Professor of Aeronautics and Astronautics, Committee Chairman

Certified by ____________________
Professor Alan H. Epstein
R. C. Maclaurin Professor of Aeronautics and Astronautics

Certified by ____________________
Professor Jack L. Kerrebrock
Professor of Aeronautics and Astronautics, Emeritus

Accepted by ____________________
Professor Nesbitt W. Hagood
Associate Professor of Aeronautics and Astronautics
Chairman, Department Graduate Committee

Development of a High Power Density Combustion System for a Silicon Micro Gas Turbine Engine

by

Amitav Mehra

Submitted to the Department of Aeronautics and Astronautics
on January 26, 2000,
in partial fulfillment of the requirements for the degree of Doctor of Philosophy

Abstract

As part of an effort to develop a microfabricated gas turbine engine capable of providing 10-50 Watts of electrical power in a package less than one cubic centimeter in volume, this thesis presents the design, fabrication, packaging and testing of the first combustion system for a silicon micro heat engine. The design and operation of a microcombustor is fundamentally limited by the chemical reaction times of the fuel, by silicon material and fabrication constraints, and by the inherently non-adiabatic nature of the operating space. This differs from the design of a modern macrocombustion system that is typically driven by emissions, stability, durability and pattern factor requirements. The combustor developed herein is shown to operate at a power density level that is at least an order of magnitude higher than that of any other power-MEMS device (2000 MW/m^3), and establishes the viability of using high power density, silicon-based combustion systems for heat engine applications at the micro-scale.

This thesis presents the development of two specific devices - the first device is a 3-wafer level microcombustor that established the viability of non-premixed hydrogen-air combustion in a volume as small as 0.066 cm^3, and within the structural constraints of silicon; the second device is known as the engine "static-structure", and integrated the 3-stack microcombustor with the other non-rotating components of the engine. Fabricated by aligned fusion bonding of 6 silicon wafers, the static structure measures 2.1 cm × 2.1 cm × 0.38 cm, and was largely fabricated by deep reactive ion etching through a total thickness of 3,800 μm. Packaged with a set of fuel plenums, pressure ports, fuel injectors, igniters, fluidic interconnects, and compressor and turbine static airfoils, this structure is the first demonstration of the complete hot flow path of a multi-level microengine. The 0.195 cm^3 combustion chamber has been tested for several tens of hours and is shown to sustain stable hydrogen combustion with exit gas temperatures above 1600K and combustor efficiencies as high as 95%. The structure also serves as the first experimental demonstration of hydrocarbon microcombustion with power density levels of 500 MW/m^3 and 140 MW/m^3 for ethylene-air and propane-air combustion, respectively.

In addition to the development of the two combustion devices, this thesis also presents simple analytical models to identify and explain the primary drivers of combustion phenomena at the micro-scale. The chemical efficiency of the combustor is shown to have a strong correlation with the Damkohler number in the chamber, and asymptotes to unity for sufficiently large values of Da. The maximum power density of the combustor is also shown to be primarily limited by the structural and fabrication constraints of the material.

Overall, this thesis synthesizes experimental and computational results to propose a simple design methodology for microcombustion devices, and to present design recommendations for future microcombustor development. Combined with parallel efforts to develop thin-film igniters and temperature sensors for the engine, it serves as the first experimental demonstration of the design, fabrication, packaging and operation of a silicon-based combustion system for power generation applications at the micro-scale.

Thesis Supervisor: Professor Ian A. Waitz
Title: Associate Professor of Aeronautics and Astronautics

Acknowledgments

I would like to thank Professor Ian Waitz for his valuable guidance and direction throughout the course of this research. I also wish to express my sincere gratitude to Professor Alan Epstein for his guidance, and for being a great teacher and mentor; to Professor Jack Kerrebrock for his invaluable advisory role; to Professor Stephen Senturia for his insightful suggestions during the igniter study, and to Dr. Choon Tan for his encouragement throughout my Masters and Ph.D. research.

Along with all the other members of the MIT microengine team, I wish to express special thanks to Dr. Arturo Ayón for his help with the fabrication process, to Dr. Xin Zhang for spending painfully long hours in front of the STS during the fabrication of the last two builds of the static structure, and to Professor Mark Spearing, Dr. Stuart Jacobson, Dr. Eugene Huang, Jin-Wook Lee, Dr. Chris Cadou, Chris Spadaccini, Steve Lukachko, Todd Harrison and Sumita Pennathur for their help along the different design and analyses stages of the combustion devices.

I would also like to express my gratitude to Mr. Gregory Simpson at Thunderline-Z for his personal dedication and creativity in coming up with packaging solutions for my combustor...Thanks Greg - without you I'd probably still be messing around with epoxy!!!

I am also grateful to Viktor Dubrowski for machining countless little "widgets" for me, and to Bill Ames and Jimmy Letendre for facilitating my experimentation efforts. Thanks to Diana Park as well for converting all my mask sets into pretty 3-D schematics, and for all the additional help with the figures.

In addition to the above people who have helped me with my research efforts, I am especially thankful to all those who have helped make my stay here at the GTL a pleasant one....Lori - thanks for being a great friend and taking care of all of us grad. students; Luc, Zolti, Adam, Rory, and Erik - thanks guys, couldn't have done it without your help and friendship!!

Finally, I'd like to thank my family - my brother and sister-in-law for their encouragement; my grandparents, who gave me more love than I could ever hope for; and my mom and dad, to whom I will always owe every bit of my success and happiness.

This work was sponsored by the United States Army Research Office, Drs. R. Paur and T. Doligalski, technical managers, and by DARPA, Drs. R. Nowak, D. Fields and S. Wilson, program managers. Their support is gratefully acknowledged.

Also, special thanks to Miss Jodi-Ann Patterson for inspiration during the last stages of this research.

Contents

List of Figures

List of Tables

Nomenclature

Roman

Bi	Biot number
d	Diameter (m)
E	Young's modulus of elasticity (N/m^2)
h	Convective heat transfer coefficient (W/m^2K), Specific enthalpy (J/kg)
k	Thermal conductivity (W/mK)
L	Characteristic length scale (m)
M	Mach number
Nu	Nusselt number
U	Velocity (m/sec)
V	Volume (m^3)
P	Pressure (Pa)
Re	Reynolds number
T	Temperature (K)
X	Mole fraction

Greek

α	Linear coefficient of thermal expansion ($/^\circ C$)
ϵ	Radiative emissivity
η	Efficiency
γ	Gas constant
ν	Kinematic viscosity (m^2/sec)
ϕ	Equivalence ratio
π	Static-to-static pressure ratio
Π	Total-to-total pressure ratio

ρ	Density (kg/m^3)
σ	Stefan-Boltzmann constant(W/m^2K^4)

Subscripts

a	Air
c	Combustor
f	Fuel
j	Fuel jet

Full quantities

Cp	Specific heat at constant pressure (J/kgK)
Da_h	Homogeneous Damkohler number
h_f	Fuel heating value (J/kgK)
$\dot{m}$	Mass flow rate (g/sec)
$\eta_{thermal}$	Thermal efficiency
η_{chem}	Chemical efficiency
η_c	Overall combustor efficiency
P_t	Total pressure (Pa)
$\dot{Q}$	Heat loss (W)
σ_f	Fracture stress (N/m^2)
S_L	Laminar flame speed (m/sec)
T_t	Total temperature (K)
$\tau_{reaction}$	Characteristic chemical reaction time (sec)
τ_{res}	Residence time (sec)
u'	Root mean square of the fluctuating velocity(m/sec)

Acronyms

CFD	Computational Fluid Dynamics
CVD	Chemical Vapor Deposition
DRIE	Deep Reactive Ion Etching

IR	Infra-red
MEMS	Micro Electro Mechanical Systems
PSR	Perfectly Stirred Reactor
SCCM	Standard Cubic Centimeters per Minute
SEM	Scanning Electron Microscope/Micrograph
TCR	Temperature Coefficient of Resistance
TMDE	Time Multiplexed Deep Etching
TEOS	Tetra-ethyl-ortho-silicate
UAV	Unmanned Air Vehicle

Chapter 1

Introduction

1.1 Background

Recent advances in silicon fabrication techniques have led to the realization of micromachined combustion systems for applications in chemical process development [14] & [64], energy transfer in heat exchangers and evaporators [46] & [113], and micro-scale power generation [36].

In particular, Epstein *et al.* have described the possible use of micro heat engines for portable power generation and micro air vehicle propulsion [37]. Based on a Brayton gas turbine cycle, such a microengine could be part of a new generation of centimeter-scale power-MEMS fabricated from silicon-based materials using semiconductor chip manufacturing techniques. It would contain all the main functional components of a conventional large-scale gas turbine engine, yet be about *one millionth* of its volume. Given the benefits of the cube-square law and the higher strength-to-density of silicon[1], the power density of this microengine could even be made to exceed that of a conventional large-scale engine [38], thereby allowing it to provide over 10 times the power density of the best batteries available today. Microengines could also become the enabling technology for numerous other applications such as boundary layer control, micro air vehicle propulsion, microrefrigeration, micro rocket engines, and air samplers for chemical and biological sensors.

As part of a current MIT program to develop such technologies, efforts are underway to produce a micro gas turbine generator using microfabrication techniques for silicon-based materials. Although this microengine would contain all the same functional components of a conventional gas turbine engine, it is not a scaled-down version of a large-scale engine. In fact, since the design of the components will change with scale, the realization of such an engine will require the simultaneous development of low Reynolds number turbomachinery, stable high-efficiency microcombustors, high-load air bearings, high power microelectronic generators, and silicon and silicon carbide microfabrication techniques.

---

[1] Cube-square law: Since the power output of an engine scales with mass flow, and hence the area, and the weight scales with volume, the power density of a device linearly increases as its size is reduced (component efficiencies being equal).

This thesis addresses the scientific and engineering issues that are specific to the design, development and system integration of the combustor for such an engine. It is the first demonstration of the ability to design, fabricate and operate a fully-packaged microcombustion system within the structural constraints of silicon, and to use it to explore the possibility of hydrogen and hydrocarbon combustion at the micro-scale. The thesis also seeks to empirically define the feasible operating space of the device, identify the unique functional requirements and constraints of the system, and to present design guidelines and recommendations for the future development of microcombustion systems.

1.2 The MIT Microengine

The primary motivation for the work presented in this thesis is the development of a micro gas turbine engine capable of providing 10-50 Watts of electrical power in a package less than 1 cm^3 in volume while consuming approximately 7 grams of jet fuel per hour. This will be a high power density device that is primarily intended for, but not limited to, power generation in portable electronic devices.

In addition to the core micro gas turbine generator, efforts are also underway to develop a flight-ready microturbojet. This is intended as a propulsion unit for a 6" wingspan unmanned micro air vehicle (μ-UAV). Details for this application can be found in Ref. [35].

1.2.1 Baseline Design

The preliminary design and feasibility study for a micro gas turbine engine has been completed by Epstein *et al.* [31], and Groshenry [44]. The baseline device is shown in Figure 1-1, and is fueled by hydrogen, weighs 1 gram, and has a mass flow rate of 0.18 gm/sec. It is expected to produce 0.2 N of thrust or 10-20 Watts of electrical power. Future versions that are presented in subsequent sections of this thesis have higher mass flows, and may operate on a recuperated hydrocarbon cycle with a potential power output of up to a 100 Watts.

The detailed design and functioning of this device is described in Ref. [38]. This single-spool turbojet employs a single-stage 4:1 pressure ratio centrifugal compressor and a radial inflow turbine that are connected by a shaft and separated by an annular combustion chamber. The overall dimensions of the device are approximately 1 cm in diameter and 3 mm in height. Air enters the device axially through the inlet hole and makes a right angle turn into the impeller. Fuel is injected downstream of the compressor through a circumferentially distributed array of fuel injector holes and mixes with the air in the vaneless space downstream of the impeller. The fuel air mixture then enters the combustion chamber through a set of axial inlet ports, reacts in the annular combustion chamber, and finally exhausts through the turbine. For power generation applications, an electrostatic induction generator is incorporated on the top face of the compressor shroud; for turbojet applications, the hot turbine exhaust can directly be used for propulsion.

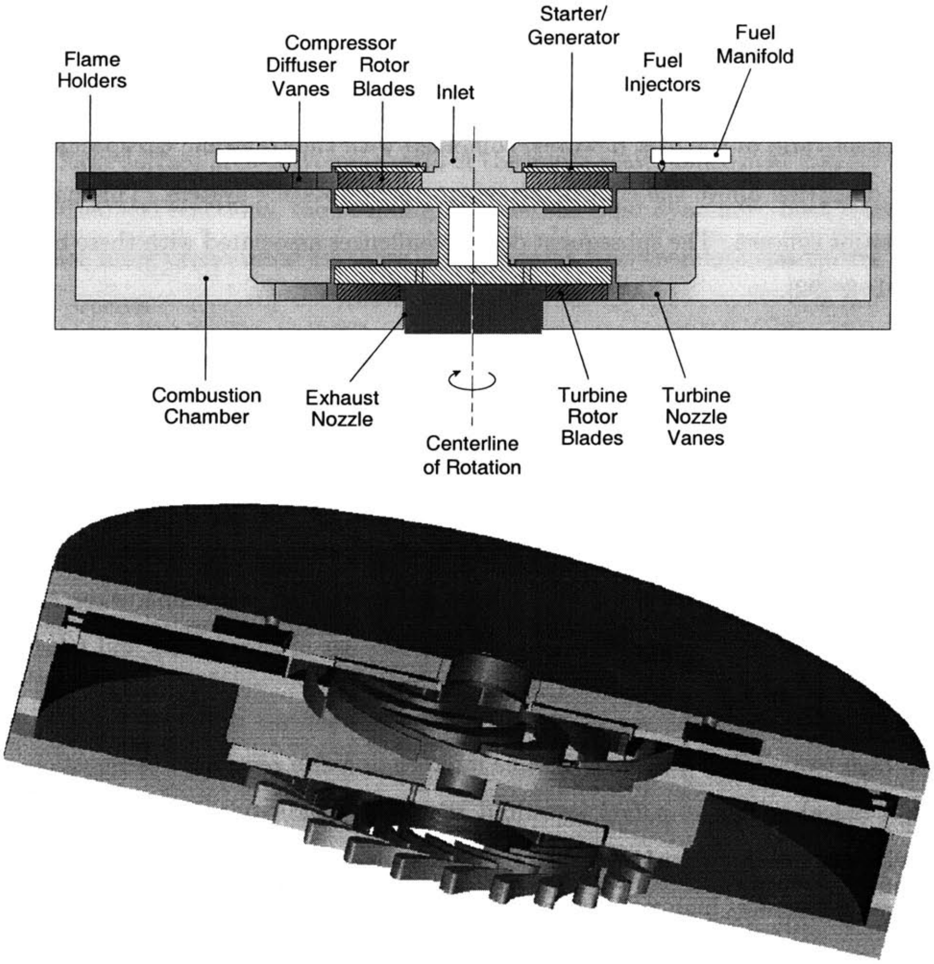

Figure 1-1: Baseline design for the MIT micro gas turbine engine [32]. (Picture courtesy: Diana Park)

1.2.2 Component Requirements and Technologies

The ability to achieve the high power density of a micro gas turbine engine relies on the satisfactory design and performance of each of the functional components. However, operation and integration within the system constraints at the micro-scale pose new challenges to the areas of fluid dynamics, combustion, material science, electrical engineering, heat transfer, and rotordynamics. These challenges are elucidated below for some of the main functional components:

1. *Low Reynolds number, high-speed turbomachinery*: Since the pressure ratio of a compressor depends on the tip speed of the rotor, the microcompressor must spin at high peripheral speeds (400-600 m/sec) in order to achieve a pressure ratio of 3-4 from a single-stage centrifugal impeller. This results in components that are highly stressed due to centrifugal loading (~100's MPa). Combined with the inability to diffuse the flow at low Reynolds numbers, and high viscous losses at the micro-scale, these factors pose a significant challenge for the design of efficient, transonic, low Reynolds number microturbomachinery components [54], [79] & [80].

2. *Low friction bearings*: Even though previously reported rotating-MEMS devices have relied on dry-friction bearings [27], operation at a design tip-speed of several hundred meters per second mandates a gas film lubrication system to support the microengine rotor against fluid and electrical forces. The low aspect-ratio of the disk however, combined with the transonic tip speeds of the rotor, result in bearing operation above the critical frequency of the rotating system. This makes stability of the journal a major concern. The subsequent design challenges associated with these bearings are detailed in Refs. [91] & [92].

3. *Efficient electrical machinery*: The microengine requires an electromechanical energy conversion subsystem to convert between the mechanical energy of the rotor and the electrical energy of the load. The baseline microengine employs an electric induction motor/generator as the energy converter. However, unlike typical MEMS micromotors that have operated at $\sim 10^{-8}$ Watts [11], [83] & [109], the microengine electrical machinery needs to operate at power levels that are several orders of magnitude higher than that. Consequently, the high temperature and high speed operation, combined with high viscous drag in the small rotor-stator gap, poses a new set of engineering and fabrication challenges. These are detailed in Ref. [87].

4. *Efficient, high temperature combustors*: The microengine also requires a combustion chamber to convert the chemical energy of a fuel into fluid thermal and kinetic energy. Since power output and thermal efficiency of a gas turbine cycle monotonically increase with turbine inlet temperature [60], the microengine requires high peak cycle temperatures to realize a high power density (1200-1800K). It is therefore necessary to develop viable combustion strategies that satisfy power output requirements within the structural and fabrication constraints of silicon.

This thesis shall specifically focus on the development and demonstration of these combustion strategies. Before presenting them however, it is instructive to elucidate the key design considerations that differentiate the microcombustor from its large-scale counterparts.

1.3 Microcombustor Design Considerations

The design and operation of a microcombustor is differentiated from that of a traditional gas turbine combustor by the following considerations:

1. *Micro-scale effects:* The ability to transfer the chemical energy of a fuel into a fluid at high mass flow rates and in small volumes makes the power density of a microcombustor particularly appealing for portable power generation and micropropulsion applications. The realization of a high power density however, requires effective completion of the combustion process within a small volume, and is therefore limited by the chemical reaction time constraints of the fuel. Unlike large-scale combustors that approximate "fast equilibrium chemistry", and are governed by stability, durability, performance and

emissions considerations, the operation of a microcombustor therefore tends to be more fundamentally limited by the chemical reaction rates of the fuel.

This chemical kinetics constraint is further exacerbated by the enhanced heat transfer effects that result from a large surface area-to-volume ratio at the micro-scale. Since heat loss can have a significant effect on the chemical reactions, the coupling between the fluid dynamics, heat transfer and chemical kinetics is much more pronounced for these small systems, and therefore constitutes a critical element of the design process.

Finally, since single-stage microfabricated turbomachinery is currently limited to providing pressure ratios of approximately 4:1 [54] & [80], microcombustors need to be integrated into low pressure ratio cycles. The gas temperature and pressure at the inlet of the microcombustor is therefore much lower than that in a large-scale combustor that is fed by a multi-stage axial compressor with a pressure ratio as high as 40:1.

2. *Materials and fabrication limitations:* Materials such as silicon, silicon carbide and silicon nitride have provided superior mechanical and thermal properties for micro and macrodevices [78] & [88]. Not only can these materials survive uncooled operation at temperatures as high as 1750K [111] & [112], they can also be used to fabricate millimeter-sized parts with 1-2 micron clearances to provide a dimension-to-tolerance ratio that is competitive with large-scale turbomachinery components [57].

   To date however, most of this micromachining technology has only been refined for silicon. Since silicon begins to exhibit creep problems at temperatures in excess of 900K [19], care must be taken to ensure that the high-stress components do not exceed these temperatures.

   Silicon micromachined parts are also limited to planar two-dimensional shapes. Since the depths and aspect ratios of the structures are limited by state-of-the-art etching tools [6], these geometries are somewhat rudimentary when compared to their larger counterparts.

   Therefore, whereas on the one hand, the use of microfabrication techniques for silicon could provide high tolerances and possibly alleviate the need for combustor wall cooling due to the better material properties of ceramics at the micro-scale, their use also greatly limits the geometrical flexibility available to the designer of a microcombustor.

3. *Multi-disciplinary systems approach:* In a complex system such as a gas turbine engine, the performance of one component must be weighed against the constraints on another. The design of a microengine also involves compromises between conflicting engineering requirements. For example, while increasing engine pressure ratio and wheel speed can improve combustor performance, it also results in complex turbomachinery geometries, higher rotor stresses and bearing instability.

   Since the microengine is a developing system wherein many of the component constraints and requirements are still being defined, the interplay between the mechanical, aerodynamic and electrical components is even more pronounced in this case. The design of the engine combustor will therefore mandate careful trade offs between power output requirements, cycle parameters, material limitations, physical dimensions and manufacturing processes, and will require a multi-disciplinary approach to understand the chemical kinetics, fluids, heat transfer and materials fabrication aspects of the problem.

These considerations only briefly outline some of the design issues facing microcombustors. A more detailed discussion of the uniqueness of the design and operating space for microcombustors shall be presented in Chapters two and six.

1.4 Review of Previous Research

This section reviews previous microcombustion research in order to place this work in the context of what has been done before.

1.4.1 MIT Microengine Combustor Research

Combustion phenomena at the geometrical scales of the microengine were first investigated by Tzeng and Waitz, who used a simple flame tube apparatus to map the flammability boundaries of hydrogen, and to establish the conditions under which a stable flame can be sustained inside a small diameter tube [33] & [114]. They demonstrated the feasibility of burning a low equivalence ratio hydrogen-air mixture and showed that a flame could be established in a millimeter-scale tube provided the heat transfer was low enough to sustain a stable flame holding zone. The results from the flame tube experiments were also used to validate a three-dimensional reacting flow solver [18], to develop strategies for employing thermocouples in miniature environments, to develop numerical schemes for data reduction, and to assess the reliability of the thermocouples depending on their type and conditions of use [114].

Using the experience from the flame tube experiments, Waitz *et al.* also proceeded to demonstrate premixed hydrogen-air combustion in a 0.13 cm^3 macrofabricated steel combustor whose geometrical layout was compatible with the baseline engine configuration shown in Figure 1-1 [34], [114] & [115]. These results laid the foundation for the development of microcombustor strategies for the MIT microengine, and established the viability of burning a hydrogen fuel at these length scales.

1.4.2 Silicon Power-MEMS

In addition to the MIT research, other applications of micro-scale combustion have primarily involved evaporators, heat exchangers, and channel flow reactors for temperature controlled chemical reactions. These devices have either been fabricated from metals using conventional machining or casting techniques, or never specifically been used for power generation. As such, the combustors presented in this thesis are the *first demonstration of the design, fabrication and use of a silicon-based microcombustion system for continuous power generation at the micro-scale.*

Since this microcombustion system is primarily targeted for portable power and air vehicle propulsion applications wherein the power density of the energy conversion unit is a primary figure of merit, it is useful to compare its power density with that of other MEMS devices. These numbers are summarized as follows:

Chemical Reactors: Microfabricated silicon reactors have previously been identified as an economical means of improving chemical process development [14], [64] & [65]. Although such reactors are not specifically intended for power generation, the exothermic partial oxidation reactions employed in these processes can generate substantial energy. Particularly, T-shaped reactors reported by Jensen *et al.* [56], and Srinivasan *et al.* [106] & [107], feature a 18 mm × 1.3 mm × 0.55 mm reaction zone that can be used to study the catalytic partial oxidation of ammonia. Typical experiments have produced approximately 0.25 Watts of power from the heat of reaction, resulting in a power density of the order of 20 MW/m^3.

Electrostatic and Magnetic Motors: Since micromotors use electrical or magnetic fields to generate torque, they can also be categorized as silicon power-MEMS. Typical electrical motors are reported to generate 100 μWatts, the power density being approximately 1.7 MW/m^3 [110], [82] & [83]. Magnetic micromotors fabricated by Ahn and Allen [2] & [3], have a power output of 60 μWatts and a power density of 200 MW/m^3. (It should be noted that these numbers are based on the field density of the air gap only; since the dimensions of the device are much larger, the *device* power density per unit volume will be lower.)

Solar Cells and Microbatteries: Miniaturized solar cells and lithium microbatteries have also been proposed as integrated power sources for MEMS applications. Solar cell arrays generate approximately 400 μWatts over a 1 cm^2, 3 μm high volume, the estimated power density being ~1 MW/m^3 [63]. Rechargeable solid-state lithium microbatteries are reported to produce 40 μWatts using a 1 cm^2, 1 μm electrolyte, resulting in a power density of 0.4 MW/m^3 [12].

Microchannel Reactors/Heat Exchangers: In addition to microfabricated silicon power-MEMS, conventionally fabricated devices have also been used to generate power at similar scales. In particular, metallic channel flow reactors employing controlled H_2-O_2 reactions have been used as heat exchangers and evaporators [16], [46] & [113]. Using a platinum catalyzed reaction of H_2 and O_2, Hagendorf *et al.* [46], have reported a maximum heat generation of 150 Watts in a 1 cm^3 volume, and a power density of 150 MW/m^3.

The MIT Microcombustor: As stated before, the key ability to transfer the chemical energy of a fuel into the fluid at high mass flow rates and in small volumes makes the power density of a microcombustor particularly appealing. For a baseline engine combustor volume of 0.066 cm^3 and an engine mass flow rate of 0.045 gm/sec at 1 atm., the power generated by the complete combustion of hydrogen at stoichiometric conditions is 156 Watts [81]. The resulting power density of the device is in excess of 2300 MW/m^3 - this is an order of magnitude higher than that of any other existing MEMS device.

1.4.3 Macrocombustion Systems

To place this power density in the context of large-scale power generation, the microcombustor is compared to two macrocombustion systems:

JT9D Aircraft Engine: At a fuel flow rate of 2 kg/sec, the JT9D aircraft engine produces approximately 85 MW of power in its 0.1 m^3 combustion chamber [77]. This corresponds to a power density of 850 MW/m^3. (Note: The JT9D was developed 30 years ago; the power density of a modern aircraft engine combustor is approximately twice as high.)

The Space Shuttle Main Engine (SSME): At a hydrogen fuel flow rate of 75 kg/sec [48], the space shuttle main engine produces approximately 9000 MW of power. Using a combustion chamber volume of approximately 0.13 m^3 [108], the power density of the SSME is *70,000* MW/m^3.

Device	**Power density (MW/m^3)**
Micro-lithium batteries [12]	0.4
Micro solar cells [63]	1
Micro-electric motors [83]	1.7
Microreactors (silicon) [107]	20
Micro channel reactors (metal) [46]	150
Micro-magnetic motors [3]	200
JT9D combustor [77]	850
Silicon microcombustor	2300
Space shuttle main engine [48] &[108]	70000

Table 1.1: A comparison of the power density levels achieved by various devices.

The power densities of the devices mentioned above are summarized in Table 1.1. While this is not an exhaustive review of all the silicon power-MEMS or macro power generation devices in the literature, it tabulates the power levels that have been achieved to date, and serves to place this research in the perspective of what has been done before[2].

1.5 Development Approach

This section describes the approach that was adopted for the development of a microcombustion system for the MIT microengine.

The development process is illustrated in Figure 1-2, and is explained as follows:

---

[2] Arrays of "digital propulsion" micro-thrusters have also been demonstrated to produce up to 100 Watts of impulse power in a 0.6 mm^3 volume [66]. This corresponds to an instantaneous power density of 170,000 MW/m^3. However, these thrusters are a one-shot device that that can only be used to deliver a *single* impulse of thrust. Since they are incapable of providing a continuous source of power, they have not been included in the context of the devices mentioned earlier.

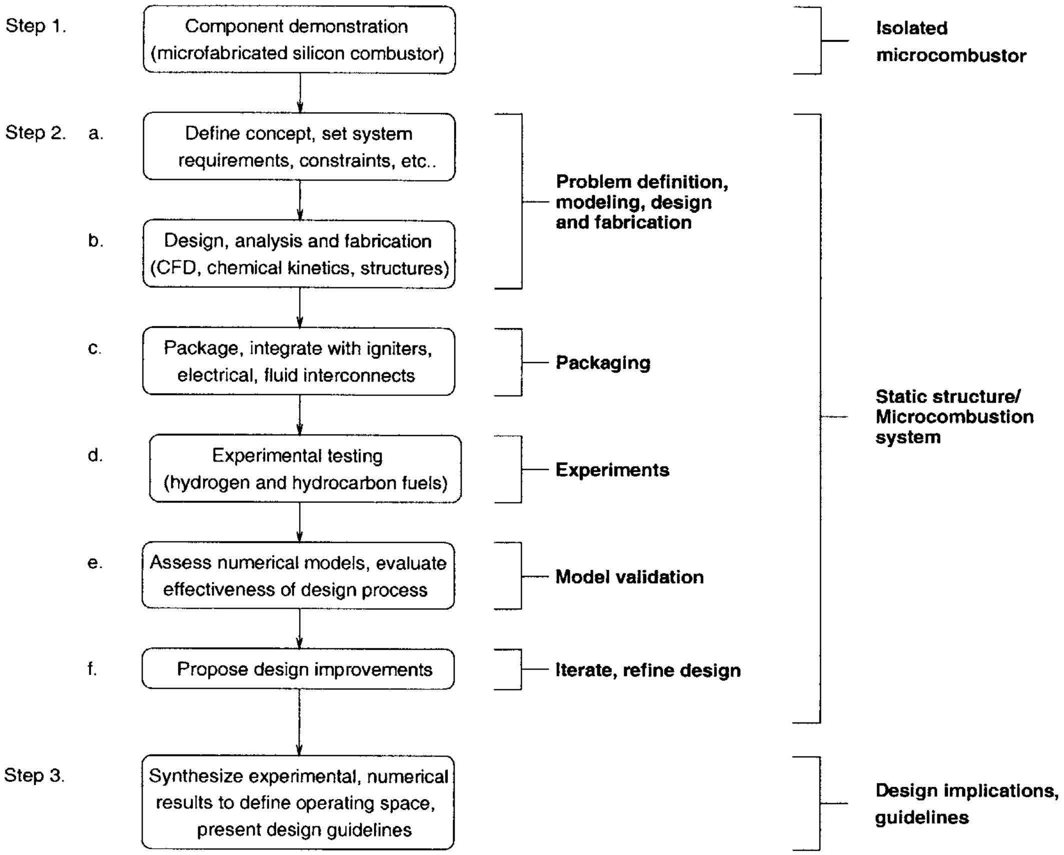

Figure 1-2: A flowchart illustrating the approach adopted for the development of the combustion system for the microengine.

1. The first step involved the demonstration of an isolated hydrogen combustor that was microfabricated from silicon, and established the viability of high temperature combustion in small volumes and within the structural constraints of silicon.

2. Having demonstrated the isolated component, the second step involved integrating the microcombustor with the other non-rotating components of the engine. This resulting device was called the "engine static-structure", and was developed via the following steps:

   (a) Based on the system requirements and constraints of the engine, and by using a combination of chemical kinetics, CFD and structural models, a geometry was designed, analyzed and fabricated.

   (b) The structure was subsequently packaged with supporting technologies such as *in situ* igniters and fluidic interconnects to develop a complete *microcombustion system.* A parallel development effort to design, fabricate and test on-chip thin-film igniters and temperature sensors was also undertaken.

   (c) The geometry was experimentally tested using hydrogen and hydrocarbon fuels to characterize its performance and to define the operating space of the device.

    (d) To complete the design loop, the experimental results were then compared with the numerical analyses to validate the models.
    (e) Finally, the results were fed back into the design process to propose future device improvements.
3. The experimental and numerical results were also synthesized to empirically identify the key drivers of combustion phenomena at the micro-scale, and to propose design guidelines for future microcombustor development.

1.6 Contributions of the Research

The specific contributions of this thesis are intended to be along the lines of the design process outlined in Figure 1-2, and are as follows:

1. Development of a fabrication and packaging methodology for the combustion system of a microengine.
2. Experimental identification of the operating space of the microengine combustor:
    (a) Identification of flashback, blow out and structural boundaries.
    (b) Demonstration of a recirculation jacket design to allow high efficiency combustion with low overall heat loss.
    (c) Evaluation of different fuel injection schemes, device pressure loss, etc.
3. Development of analytical models for:
    (a) Identification of the thermally and chemically limited regimes of operation.
    (b) Reduction of the experimental data to show Damkohler number limitations.
4. Presentation of design guidelines for future devices:
    (a) Need for multiple recirculation zones in order to facilitate uniform and rapid ignition of the incoming reactants.
    (b) Need for minimizing the effect of heat loss.
    (c) Consideration of operating line issues.
    (d) Benefits of high pressure operation.

1.7 Organization of the Thesis

This chapter introduces the concept of a high power density microcombustor, identifies the top-level considerations that distinguish it from other combustion and power-MEMS devices, and summarizes the key objectives and contributions of this thesis.

Chapter two sets the design space for the combustor of the microengine by identifying the unique functional requirements, constraints and performance criteria for the device. It also discusses the primary challenges facing its design, and presents the overall design philosophy and strategy that was adopted in the face of these constraints.

Chapter three presents the first step of the hydrogen combustor development process by describing the design, fabrication and testing of a microfabricated silicon combustor. The primary purpose of this device was to evaluate the viability of using silicon for the construction of the microengine. Combined with the results of a materials and oxidation study, this chapter sets the foundation for an all-silicon microengine.

Chapter four presents the integration of the hydrogen combustor with the remaining non-rotating components of the engine. It begins by describing the design of the static structure, then presents its fabrication and packaging, and finally discusses the tests that were carried out to map the operating space for hydrogen and hydrocarbon combustion.

Chapter five describes the parallel development of on-chip igniters and temperature sensors. It presents a concept demonstration of the dual-use of thin-film polysilicon resistive elements as igniters and temperature sensors by describing their design, fabrication and test results, and then discusses overall implications for their use in the microengine combustor.

Chapter six aims to synthesize the experimental and numerical results to provide an insight to combustion physics at the micro-scale. It begins with a comparison of the experimental findings with the numerical results to assess the effectiveness of the design methodology. It then examines the key scientific issues to identify the primary drivers that differentiate microcombustion systems from their large-scale counterparts, and finally presents design recommendations for the future development of such a system.

Chapter seven presents the conclusions of this thesis along with recommendations for future work.

Chapter 2

Microcombustor Design Issues

2.1 Introduction

This chapter presents the key issues that dictate the design and operation of a combustor at the micro-scale. It is intended to achieve the following goals:

1. To identify the primary functional requirements and constraints for a microengine combustor,
2. To present the primary design challenges and link them with limitations on power density, and
3. To describe the overall design philosophy and approach that was adopted to develop a suitable combustion strategy for microengines.

2.2 Functional Requirements

2.2.1 General Combustion Systems

The primary requirement of any combustion system is to convert the chemical energy of a fuel into fluid thermal and kinetic energy with high efficiency. The combustor must do so within the overall constraints of the cycle, and must integrate with other components inside the engine.

As stated by Mellor [84], the requirements of a typical large-scale combustion system are:

- *Operability:* Ground start, altitude relight, and stable operation in the entire flight envelope and during transients.
- *Performance:* Typical combustion efficiencies in excess of 99.9% at cruise and 95% at idle conditions, a pressure drop of 4-6%, and desired exit temperature distributions.
- *Configuration:* Low weight, short length, manufacturability and maintainability.

- *Durability:* Structural integrity and cyclic life.
- *Emissions:* Low NO_X, unburned hydrocarbons, carbon monoxide and smoke.

2.2.2 Microengine Combustor

The microengine combustor is also subject to a similar set of system constraints, however, the requirements for the first development microcombustors presented in this thesis are not as stringent as those for a state-of-the-art combustor in the mature gas turbine industry. These may be stated as follows:

1. The microcombustor must provide a turbine inlet temperature of 1600K within a volume that is small enough to fit inside a centimeter-scale engine,
2. It must maintain its structural integrity within the material constraints of silicon and be manufacturable using existing micromachining techniques for silicon-based materials,
3. It must have a low pressure loss across the chamber ($\pi_c \geq 0.95$),
4. It must have an overall thermal efficiency in excess of 90%[1], and
5. It must be stably operable over the full range of start-up to full-power conditions.

The operating parameters, requirements and constraints for the baseline microcombustor configuration are summarized in Table 2.1, and compared with those for a conventional large-scale combustor.
(Note: Although $\dot{m}_{micro}/\dot{m}_{large}=1.6\times10^{-6}$, vol_{micro}/vol_{large} is approximately three times smaller, and equals 0.6×10^{-6}. The microcombustor therefore passes three times more mass flow per unit volume. Furthermore, since the inlet pressure is only 4 atm., the volumetric flow rate per unit volume, i.e. $1/\tau_{res}$ for the microengine is approximately fifteen times larger than that for a conventional large-scale combustor.)

2.3 Primary Design Challenges

Given these requirements, the primary design challenges for a microcombustor may be classified as:

2.3.1 Residence Time Constraints for a High Power Density Device

As shown in Table 2.1, the high power density of a microcombustor directly results from a higher mass flow per unit volume. Since chemical reaction times do not however scale with mass flow rates or combustor volume, the realization of this high power density is contingent upon completing the combustion process within a *shorter* through-flow time.

---

[1] Since one can always increase the power output of the cycle by adding more fuel, the 90% efficiency requirement is not a "hard" requirement for closing the thermodynamic cycle of the microengine. A low combustor efficiency will however impact the specific fuel consumption and overall thermal efficiency of the engine.

	Conventional Combustor	**Microcombustor**
Length	0.44 m	0.001 m
Volume	0.1 m^3	6.6×10^{-8} m^3
Cross-sectional area	0.2 m^2	6×10^{-5} m^2
Inlet total pressure	21 atm.	4 atm.
Inlet total temperature	800K	500K
Mass flow	110 Kg/sec	1.8×10^{-4} Kg/sec
Residence time	$\sim$ 7 msec	$\sim$ 0.5 msec
Efficiency	$> 99\%$	$> 90\%$
Combustor pressure ratio	> 0.95	> 0.95
Exit temperature	1600K	1600K
Space heating rate	850 MW/m^3atm	2300 MW/m^3atm

Table 2.1: A comparison of the operating parameters and requirements for a microengine combustor with those for a conventional JT9D combustor [77]. (Note: Residence times are calculated using inlet pressure and an average flow temperature of 1000K.)

This residence time constraint can be quantified in terms of a homogeneous Damkohler number that depicts the ratio of the residence time to the characteristic chemical reaction time:

$$Da_h = \frac{\text{residence time}}{\text{reaction time}} = \frac{\tau_{res}}{\tau_{reaction}} \tag{2.1}$$

In order to ensure a Damkohler number greater than unity, the designer of a microcombustor can therefore either a.) increase the flow residence time, or b.) decrease the chemical reaction time.

Limitations on Increasing Flow Residence Time: The combustor residence time is given by

$$\tau_{res} = \frac{\text{Volume}}{\text{Volumetric flow rate}} = \frac{V}{\dot{m}/\rho} \tag{2.2}$$

and can either be increased by a.) increasing the size of the chamber, b.) by reducing the mass flow rate, or c.) by increasing the operating pressure.

Since the current design of the microfabricated compressor is limited to a pressure ratio of approximately 4:1 [54] & [80], the maximum operating pressure of the device can be assumed to be constant. Furthermore, since high power density requirements mandate high mass flow rates through small chamber volumes, the mass flow rate per unit volume cannot be reduced without compromising the device power density - hence, the basic trade-off between power density and flow residence time:

$$\text{Power density} \propto \frac{\dot{m}}{V} \propto \frac{1}{Da_h}\frac{\rho}{\tau_{reaction}} \tag{2.3}$$

Assuming a desired Damkohler number of unity and a given operating pressure, *reducing the chemical reaction time of the fuel is therefore the only means of ensuring complete combustion without compromising the high power density of the device.*

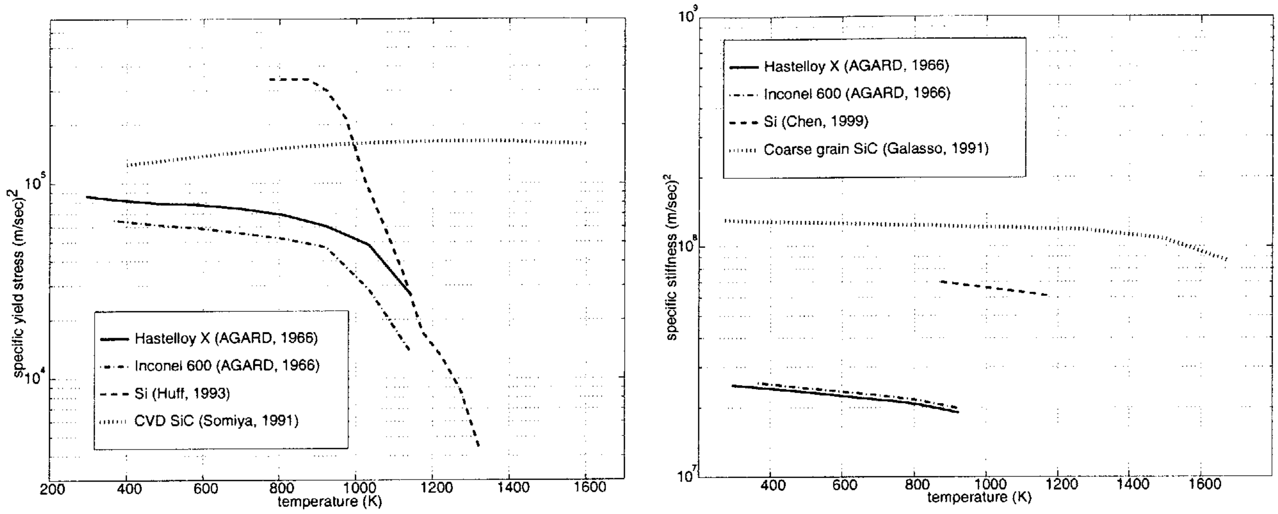

(a) Specific yield stress (σ_f/ρ). (Since the burst speed of a rotating disk is proportional to the specific strength of the material, a microfabricated silicon or silicon carbide rotor can operate at higher speeds due to the low density and high fracture strength of the ceramic.)

(b) Specific stiffness (E/ρ). (Due to their high modulus of elasticity, ceramics have high specific stiffness. This reduces the deformation of stressed structures, allowing a rotor to operate at speeds higher than those permissible by conventional metals.)

Figure 2-1: Specific strength and stiffness for different materials. (Source: Refs. [1], [19], [42], [53] & [104].) (Note: $\rho_{Hastelloy}$=8000 Kg/m^3, $\rho_{Inconel}$=8200 Kg/m^3, ρ_{Si}=2330 Kg/m^3 and ρ_{SiC}=3200 Kg/m^3.)

Limitations on Reducing the Chemical Reaction Times: Since the chemical reaction rates of a fuel are a strong function of the temperature and pressure inside the combustion chamber, they are primarily limited by the structural and material constraints of the device. This introduces the next challenge facing the design of microcombustion systems - pressure and temperature limitations due to structural constraints.

2.3.2 Materials and Fabrication Constraints

Although the high strength-to-weight of silicon is critically enabling for the operation of a highly stressed microengine rotor, creep considerations limit the maximum operating temperatures inside the structure. Figures 2-1 and 2-2 plot the specific stress, stiffness, yield stress and thermal susceptibility of silicon, silicon carbide and two different superalloys, and show that even though the high specific fracture strength of silicon makes it a superior choice for the rotating components of the microengine, the yield strength of silicon drops off rapidly beyond 900K. The resulting transition from a brittle to a plastic material, and subsequent creep failure at temperatures above 900K [19], therefore limit the maximum wall temperature of a stressed component in the hot section of the engine to below 900K.

Given a desired turbine inlet temperature of 1600K, this creep limit has the following implications on microcombustor design and operation:

1. Either the walls of the hot section must be cooled to allow operation within the structural limits of silicon, or

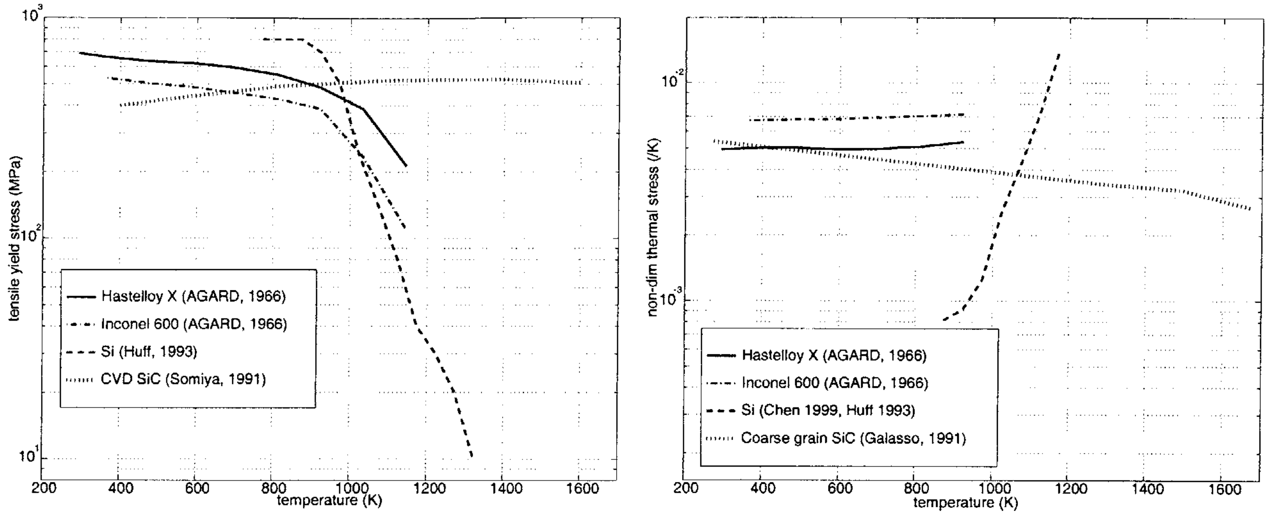

(a) A comparison of the ultimate tensile yield stress (σ_f) for silicon, silicon carbide, Hastelloy X and Inconel 600. (Note the superior strength of silicon carbide at high temperatures.)

(b) A comparison of the non-dimensional thermal stress per unit degree ($\alpha E/\sigma_f$) for silicon, silicon carbide, Hastelloy X and Inconel 600. The low expansion coefficient and high strength of silicon and silicon carbide make them more suitable as structural materials for a combustor.

Figure 2-2: Yield stress and the thermal stress per unit degree. (Source: Refs. [1], [19], [42], [53], [94] & [104].) (Note: For the purpose of these plots, $\alpha_{Hastelloy}$=17×10^{-6}/°C [1], $\alpha_{Inconel}$=17×10^{-6}/°C [1], α_{Si}=4.0×10^{-6}/°C [94], and α_{SiC}=4.8×10^{-6}/°C [94].)

2. Higher temperature materials such as silicon carbide must be employed.

Furthermore, since this material constraint limits the maximum operating temperature and pressure inside the chamber, (and hence the chemical reaction rates), *it is the key factor limiting the achievement of higher power densities in the microcombustor*[2].

2.3.3 Heat Transfer Constraints

The chemical kinetic constraint is further exacerbated by enhanced heat transfer effects at the micro-scale. Since the surface area-to-volume ratio of a device approximately scales as $\frac{1}{length}$, the surface area-to-volume ratio of a microcombustor is higher than that of a conventional large-scale combustor (500 m^{-1} vs. 3-5 m^{-1}, [115]). Consequently, the fractional heat transfer out of the chamber can be expected to be considerably larger, making non-adiabatic operation intrinsic to the design of microcombustion systems. This introduces the following challenges:

1. Heat transfer out of the combustor will reduce the gas temperature in the combustion chamber. Since the corresponding reduction in chemical reaction rates can greatly exacerbate the residence time

---

[2] In practice, improved cooling schemes may allow the walls to operate several hundred degrees lower than combustion gas temperatures, however, these may require complex geometries and fabrication trade-offs. Cooling the combustor will also reduce the enthalpy content of the fluid - unless the heat loss is re-cycled back into flow path, it may have a severe impact on the thermal efficiency of the engine.

required for completing combustion, the coupling between the heat transfer, chemical kinetics, and fluid mechanics is much more pronounced for a *reaction-time limited* microcombustor, and is therefore a critical element of the design process.

2. Heat transfer losses out of the device also reduce the amount of fuel energy that is available for extracting useful work in the turbine. Thus, unlike large-scale combustors that are able to transfer the fuel energy into the gas flow with efficiencies in excess of 99.9%, the efficiency of a microcombustor can be expected to be lower.

In addition to the enhanced surface heat transfer effects, the high thermal conductivity of silicon and small length scales in the device result in a Biot number as low as 0.01 - this implies that most of the device will be nearly isothermal[3]. While this is advantageous from a thermal stress perspective, it complicates the thermal isolation of the outer walls of the device. In fact, if the chamber walls do indeed operate at temperatures as high as those mandated by the combustion constraints, packaging of the device can pose a severe challenge.

2.3.4 Other Challenges

The design of a micro-scale combustor is also faced with the following additional challenges:

1. Due to the reduced length-scale of the device, the Reynolds number of the microcombustor is ~200 compared to ~3 million for a large-scale combustor[4]. This has two effects - first, the viscous losses are higher, and second, the flow is laminar. This laminar nature of flow limits the rates of the momentum, heat and mass transfer inside the combustor, thereby hindering effective mixing between the cold reactants and hot products.

2. The laminar nature of the flow also places the microcombustor in a different regime for computational simulations. While the ability to directly model laminar flows and simpler combustor geometries reduces the complexity of the numerical analysis, the close coupling between the heat transfer, fluid dynamics, chemical kinetics, and structural aspects mandates conjugate heat transfer and reacting flow CFD solutions. The complexity of turbulence models is therefore traded-off against that of a coupled heat transfer and reacting flow calculation.

3. Operating at the micro-scale also poses the practical challenge of instrumenting experimental test rigs with conventional diagnostics. In the absence of on-chip *in situ* transducers that are microfabricated as part of the device, the designer is therefore limited by the quantity and accuracy of the data that can be collected from the experimental rigs.

---

[3] $Bi = \frac{hL}{k}$; assuming a baseline heat transfer coefficient of 150 W/m^{2}K, a characteristic length scale of 1 cm, and a silicon room temperature thermal conductivity of 125 W/mK, Bi=0.008.

[4] Reynolds numbers are based on the inlet conditions listed in Table 2.1; Damkohler showed that the onset of fine-scale turbulence in Bunsen burner flames was experienced at Re ~2,300 [24] & [25].

2.4 Combustor Design Philosophy and Approach

Microengine Combustion Strategy: Faced with the residence time and material constraints discussed thus far, the operation of a microengine mandates a combustion strategy that ensures timely completion of the chemical reactions within a small volume, and within the material constraints of silicon. Waitz *et al.* [115], propose a lean-burn premixed gaseous hydrogen combustor for the first demonstration microengines, trading the fabrication and design complexity of a hydrocarbon combustor for the simplicity of a homogeneous, single-zone combustor. This approach has the following advantages:

1. Unlike hydrocarbon fuels that have a lean flammability limit at $\phi \sim 0.5$, hydrogen can sustain stable homogeneous combustion at equivalence ratios as low as 0.3. Since the flame temperature under these lean conditions may be low enough to permit stable homogeneous combustion within the structural constraints of silicon, it may obviate the need for wall cooling or a dual-zone combustor geometry.
2. The reaction rates for hydrogen are an order of magnitude higher than those for hydrocarbon fuels [115]. Since fuel reaction rates are the primary determinant of the minimum combustor volume for a given mass flow rate and combustor operating pressure, a hydrogen-fueled combustor can be much smaller than an equivalent hydrocarbon combustor.
3. Finally, by premixing the fuel upstream of the combustor, one can further increase the residence time that is available for fuel-air mixing.

It should be noted that the use of hydrogen should be considered as the first step towards the realization of a demonstration microengine. Although hydrogen serves as an ideal fuel for the microengine, its low energy density and storage constraints make it less desirable for micro air propulsion applications. This thesis shall therefore also explore the use of hydrocarbon fuels at the micro-scale.

Approach: This thesis shall adopt the following experimental approach towards the development of a combustion system for the microengine:

1. A component demonstration of a hydrogen-air combustor shall first be used to establish the viability of stable micro-scale combustion within the fabrication and material constraints of silicon.
2. The hydrogen combustor shall then be integrated with the rest of the non-rotating engine components to develop a *hydrogen combustion system* for the microengine.
3. The device will finally be used to evaluate the combustion stability boundaries for hydrogen and hydrocarbon fuels, and to make design recommendations for future microcombustors.

The first component demonstration of a hydrogen microcombustor is described in Chapter three, its integration with the rest of the engine is described in Chapter four, parallel efforts to develop thin-film igniters and temperature sensors is described in Chapter five, recommendations and design implications for the future development of microcombustors are presented in Chapter six.

2.5 Chapter Summary

This chapter described the primary challenges and constraints facing the design of a microengine combustor.

It presented the overall functional requirements for a microcombustor and contrasted its design and operation with that of conventional large-scale combustors. It also described the overall combustion strategy that was chosen given the unique requirements and constraints of a microengine, and then briefly outlined the approach adopted to accomplish this goal.

Chapter 3

Development of the Engine Combustor

3.1 Introduction

This chapter presents the development of a hydrogen combustor for the MIT microengine. Using the lean-premixed hydrogen combustion strategy described in Chapter two, this chapter presents the design, fabrication and experimental test results for a first-of-its-kind high power density silicon microcombustor. Combined with the results of a materials and oxidation study, the satisfactory performance of this microcombustor lays the foundation for using silicon microfabricated devices for power generation in a new and emerging class of high power density micro heat engines.

3.2 Goals of the Silicon Microcombustor

The silicon microcombustor described herein was developed with the following objectives:

1. It would be a fabrication demonstration of the ability to make a silicon combustor using high aspect ratio etching and aligned wafer bonding,

2. It would be used to evaluate the structural integrity of the material to establish the viability of using silicon for micro heat engine applications, and

3. It would be the first demonstration of *non-premixed* hydrogen-air combustion in a chamber as small as 0.066 cm^3 in volume. The resulting space heating rates would not only be sufficient to close a micro gas turbine cycle; they would be at least an order of magnitude higher than that of any other power-MEMS device.

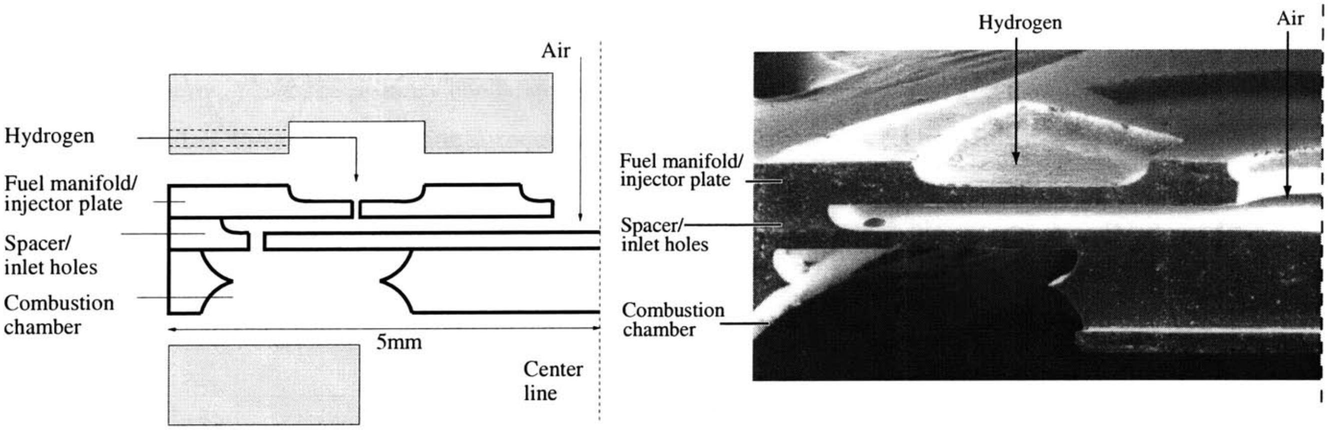

Figure 3-1: Schematic and SEM cross-section of half of the axisymmetric combustor, showing the fuel manifold, injectors and air flow path.

3.3 Design of the Silicon Microcombustor

The design of the microengine is based on the ability to etch deep fluid channels in individual silicon wafers and stack them up to achieve a three-dimensional structure. Since current microfabrication technology is limited to the fabrication of planar two-dimensional shapes, this wafer bonded approach is the most effective way to achieve a closed structure with internal fluid paths and a freely spinning compressor-turbine spool.

In keeping with this paradigm, the microcombustor was designed to consist of three fusion bonded silicon wafers. The geometry of this 3-stack was similar to the steel combustor used by Waitz *et al.* [115], however it was designed to include fuel plenums and fuel injector holes. It was also intended to be compatible with the baseline engine configuration shown in Figure 1-1. A Scanning Electron Micrograph (SEM) of the fabricated device is shown in Figure 3-1, alongside a schematic representation of the structure.

Similar to the baseline engine configuration described in Section 1.2.1, air enters the device axially from the top, makes a right angle turn, and flows outwards through a duct where the compressor would nominally be housed. Hydrogen is injected downstream of the compressor through the fuel injectors and mixes with the air before entering the combustor through axial inlet ports. The mixture then burns in an annular shaped chamber and finally exits through a circular exhaust. (In an engine application, the flow would also pass through a turbine for power extraction prior to being exhausted.)

The detailed design aspects of this device are presented in subsequent sections.

Overall Size and Geometry: The overall geometry and arrangement of the device was set by preliminary design and feasibility studies for the microengine [38] & [115]. The outer dimension of the annular combustion chamber was dictated by the overall size of the microengine, and was set at 10 mm. The inner diameter was constrained by the size of the compressor and turbine rotor, and was set at 5 mm.

The axial length of the combustor was dictated by the following considerations:

1. In order to minimize the total number of wafer bonds in the device, it was desired that the combustion

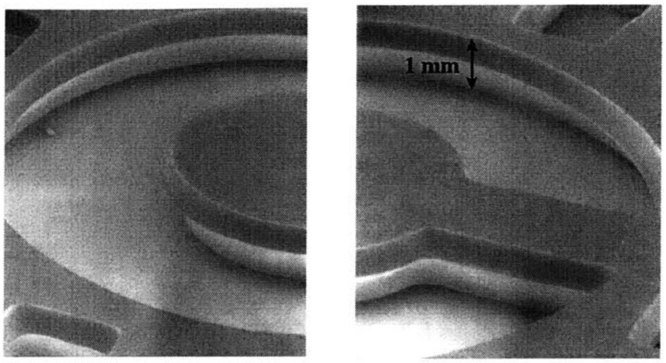

Figure 3-2: An SEM of the annular combustion chamber.

Outer diameter (mm)	10
Inner diameter (mm)	5
Axial length (mm)	1
Chamber volume (mm^3)	66
Air mass flow rate $\dot{m}_a$ (gm/sec)	0.045
Fuel mass flow rate $\dot{m}_f$ (gm/sec)	1.3×10^{-3}
Flow residence time (sec)	5.2×10^{-4}
Space heating rate (MW/m^3)	2300

Table 3.1: Operating parameters for stoichiometric hydrogen combustion in the microcombustor at atmospheric conditions. (Note: The residence time is based on an average flow temperature of 1000K.)

chamber be fabricated from a single silicon wafer. Since 1200 μm was expected to be the maximum wafer thickness available, it was set as an upper bound for the axial length of the combustor.

2. CFD solutions for the 0.13 cm^3 macrofabricated combustor used by Waitz *et al.* showed that it might be possible to cut down the volume of the combustor by a factor of two without compromising the combustion efficiency of the device [34]. A pressure scaling of the design mass flow to maintain the same residence time in the combustor showed that a combustor axial length of 1 mm would be sufficient to allow complete combustion at atmospheric conditions. The axial length of the combustor was therefore set at this value; the resulting chamber volume was 0.066 cm^3. (This was approximately half the volume of the macrofabricated combustor that was previously used by Waitz *et al.* to demonstrate hydrogen-air combustion at the micro-scale [115].)

An SEM of the resulting combustion chamber is shown in Figure 3-2 (this is the bottom wafer in the 3-stack); the key operating parameters for the device are summarized in Table 3.1.

Design of the Fuel Injectors: Since the small volume of the microengine imposes constraints on the time available for fuel-air mixing, the fuel injectors were located immediately downstream of where the compressor blades would nominally be located in the engine. This design was dictated by the system requirement for maximizing the time available for fuel-air mixing, while maintaining the inertness of the

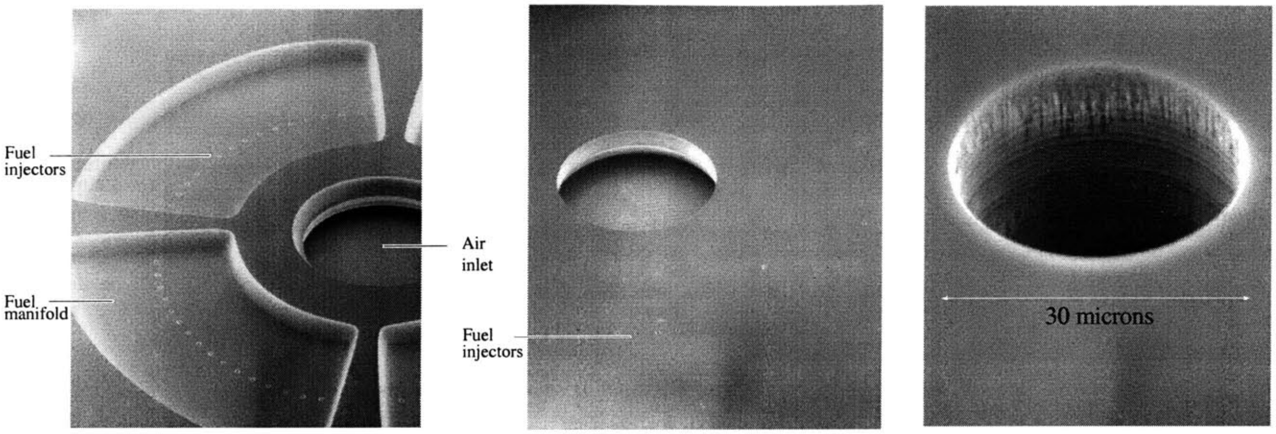

(a) Top view of wafer one.

(b) Bottom view of wafer one.

(c) Close-up SEM of a 200 μm deep, 30 μm diameter fuel injector hole.

Figure 3-3: An SEM of the first wafer in the 3-stack microcombustor, showing the ring of 76 30 μm diameter fuel injector holes.

compressor bleed air used to support the journal and axial thrust bearings in the engine.

In order to evaluate the effectiveness of this scheme, the 3-stack microcombustor was designed with an integral fuel plenum and fuel injector holes. Previously designed by Gauba using semi-empirical models for normal jet injection and mixing [41] & [101], the injectors were located at approximately 50 injector hole diameters upstream of the combustor inlet ports. The design was optimized by varying the size and number of injector holes to satisfy lateral penetration and spreading requirements for the fuel jets, and to ensure complete fuel-air mixing in the compressor exit flow duct. The final device consisted of total of 76 injector holes with a diameter of 30 μm, equally spaced at a radius of 3 mm.

SEM's of the fabricated fuel plenum and injector holes are shown in Figure 3-3.

Design of the Combustor Inlet Ports: The design of the combustor inlet ports was chosen to be the same as that used by Waitz *et al.* [115], and was completed with the intent of providing the slowest flow velocity into the combustion chamber while eliminating the upstream propagation of the flame into the compressor exit flow path. The separated flow regions between the ports were also intended to act as recirculation zones to stabilize the flame. The final device consisted of a total of 24, 340 μm diameter combustor inlet ports, located at a radius of 4.5 mm.

An SEM of this geometry is shown in Figure 3-4.

3.4 Fabrication of the Silicon Microcombustor

Fabrication of the microcombustor was enabled by the ability to selectively "mask" a planar 2-D geometry and etch the exposed silicon surface with a plasma. The individual wafers were then aligned and fusion

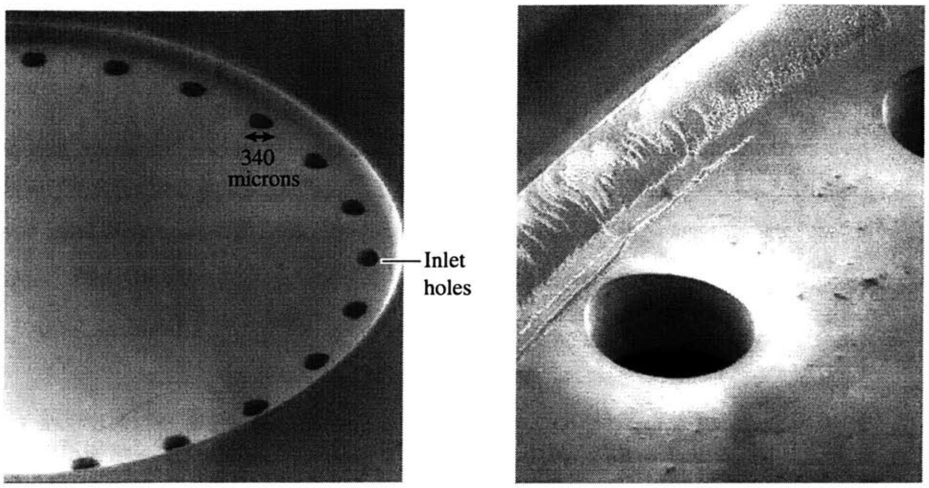

Figure 3-4: An SEM of the second wafer in the 3-stack microcombustor, showing the 24, 340 μm combustor inlet ports at r=4.5 mm.

bonded to obtain a closed structure with requisite fluid channels.

Using silicon microfabrication techniques has two key advantages:

1. Combined with the superior material properties of single crystal silicon, the micron-level tolerances routinely achieved by silicon micromachining techniques are critical for the fabrication of the highly stressed and tight-clearance geometries of a micro gas turbine engine.
2. Similar to the process for manufacturing integrated circuit chips, multiple dies can be repeated on a single wafer. Each process therefore yields a batch of individual devices, making the production of each unit more economical. Microfabrication methods like these are also suitable for mass production; these may eventually make the commercial production of microengines as repeatable and reliable as the current manufacture of microprocessors and memory chips.

In the integrated-circuit manufacturing industry, the template used to define the geometry is called a "mask". The masking material is usually a photo-sensitive polymer called photoresist; the process of "patterning" and developing the photoresist is called photolithography.

A schematic illustration of a photolithography and subsequent etching step is shown in Figure 3-5.

The fabrication of the 3-stack microcombustor required a total of six masks. One of these masks contained global wafer-level alignment marks. A combination of four dry isotropic and two dry anisotropic etches were used to define the various components. The overall fabrication process is illustrated in Figure 3-6, and is described as follows:

1. First, the top side of each of the wafers was coated with photoresist and patterned with the appropriate fuel manifold, spacer plate and combustion chamber geometry.
2. Then, the 200 μm deep fuel manifold and spacer plate, and half of the 1000 μm deep combustion

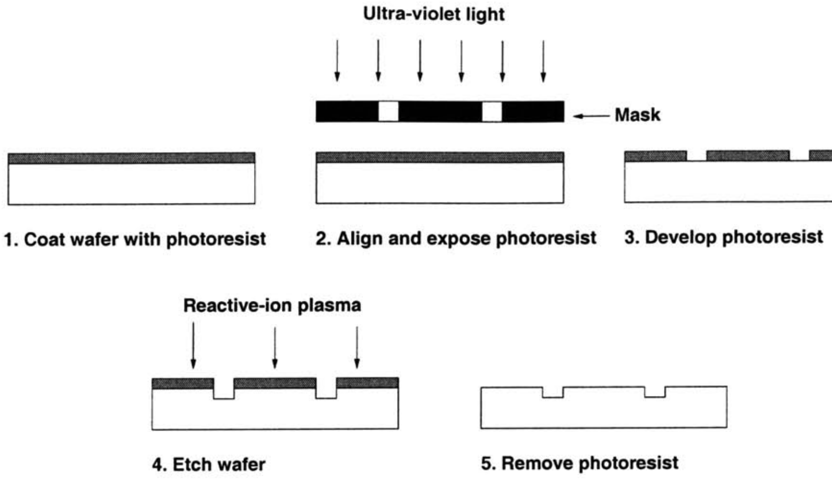

Figure 3-5: A schematic illustration of the process of photolithography and wafer etching.

chamber were isotropically dry etched. (Since none of these features required parallel side walls, isotropic etching was used to minimize process time[1].)

3. After completing the top side etches, the bottom side of the wafers were coated with resist and infra-red alignment was used to pattern the corresponding fuel injectors, combustor inlet ports and combustion chamber geometry on the bottom side of each wafer. The 200 μm deep fuel injectors and combustor inlet ports were then anisotropically dry etched. (The combustion chamber was isotropically etched from both sides to limit the lateral run-out in the side walls of the combustor.)

4. The three wafers were then aligned fusion-bonded; the resulting 1.8 mm thick stack was subsequently die-sawed to obtain thirteen 1.5 cm × 1.5 cm dies from the 100 mm wafer.

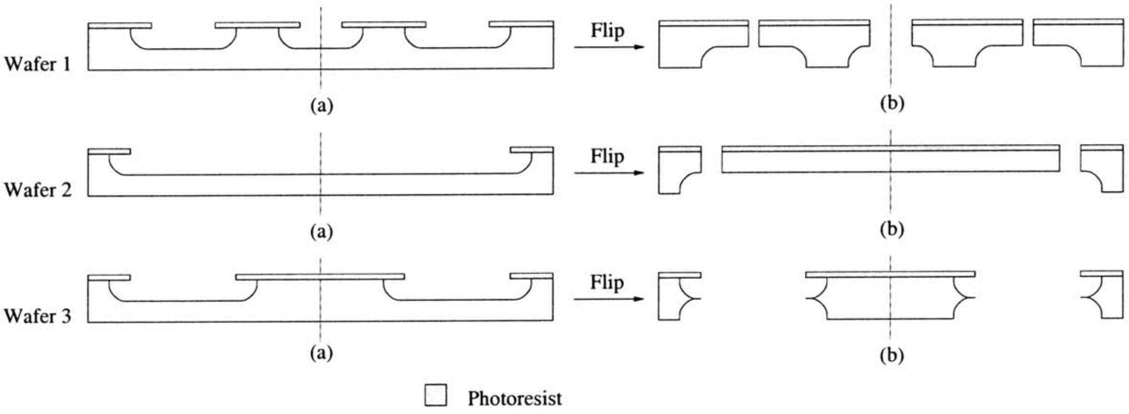

Figure 3-6: An illustration of the fabrication process for the 3-stack microcombustor.

The major fabrication steps are explained in more detailed in the following sections.

---

[1] Compared to etch rates of approximately 3 μm/min for anisotropic etching, rates of up to 7 μm/min could be achieved using isotropic etches.

3.4.1 Photolithography

For all of the deep etches, the wafers were patterned using coating techniques similar to those reported in Ref. [85]. Following a dehydration bake in an HMDS (hexamethyldisilazane) oven, approximately 10 μm of thick positive photoresist (Hoechst, AZ-4620) was spun cast on the wafer surface. The resist was pre-baked for one half hour in a 90°C convection oven and then exposed using a contact mask aligner with a ultra-violet light source. After developing in AZ 440 MIF, the photolithography was completed with a half hour post-bake in a 120°C ambient.

3.4.2 Deep Reactive Ion Etching

Following the evolution of Bosch's patented technique for time-multiplexed deep etching (TMDE) [97], DRIE combined with silicon fusion bonding are becoming enabling technologies for MEMS devices [61] & [50]. The use of DRIE to etch high aspect ratio structures for complex fluid paths is also instrumental to the fabrication of the microcombustor test rig.

As stated before, the microcombustor was fabricated using four isotropic and two anisotropic dry etches. The isotropic etches employed straight SF_6 chemistry. The anisotropic etches used a time-multiplexed inductively coupled plasma of SF_6 as the etchant and C_4F_8 as the side wall passivating polymer. The performance of the etcher was also previously optimized over a wide parameter space in order to enable the fabrication of high tolerance and high aspect ratio structures such as the 30 μm diameter, 200 μm deep fuel injector holes shown in Figure 3-3 [7].

(Note: It should be reiterated that although these silicon micromachining techniques are critical for the fabrication of a micro gas turbine engine, they are limited to rudimentary 3-D shapes. Consequently, the design of many of the engine components is dictated by microfabrication limitations - this trade-off is a classic illustration of the conflicting engineering requirements encountered during the design and fabrication of the MIT microcombustor and engine generator.)

3.4.3 Aligned Wafer Bonding

After individual processing, each of the wafers was put through a standard RCA clean [59] and aligned fusion-bonded. The bonding was completed in two steps - the second and third wafers were bonded first; the stack was then annealed, RCA cleaned and finally bonded to the first wafer. Consistent with results reported in Ref. [100], a one hour post-bond anneal in an inert ambient at 1100°C was found to significantly improve the bond quality.

Figure 3-7 shows infra-red images of the two and three-wafer stacks. Although the three-wafer stack shows large fringes that indicate poor bonding quality along the edge of the wafers, the wafer bonding process yielded thirteen out of a possible sixteen, fully-bonded microdevices. The experimental testing of these devices shall be presented in the following section.

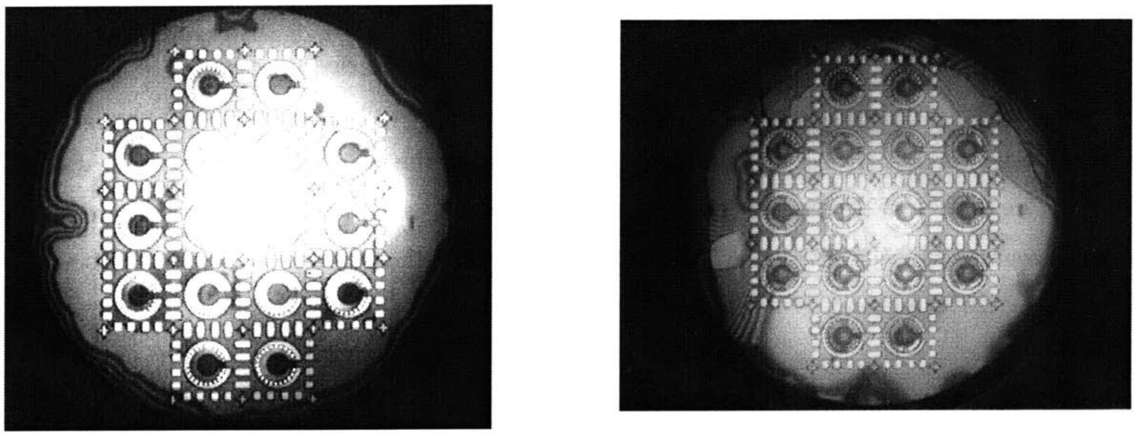

(a) Singly-bonded wafers 2 and 3.

(b) Doubly-bonded wafers 1, 2 and 3.

Figure 3-7: An infra-red image of the 3-stack, double-bonded wafers, indicating a high quality bond over most of the wafer. The fringes on the edges indicate poor bond quality in these regions.

(Note: The results shown in Figure 3-7 represent one of the earlier attempts at multiple wafer bonds. Since then, the wafer bonding protocol has been changed. The wafers are now bonded in vacuum; the tooling has also been modified so that it contacts the wafers at only three points. These changes have recently resulted in nearly 100% yields at diesaw for devices with similar levels of multiple wafer-bonding [68].)

3.5 Experimental Testing

3.5.1 Experimental Apparatus

Hydrogen-air combustion tests were carried out in the 3-stack by clamping the structure between a set of invar plates chosen to match the thermal expansion coefficient of silicon. These plates housed the fluidic connections for hydrogen and air, and also carried the inlet and exit gas temperature thermocouples. The apparatus was designed so that the experiment could be run in premixed and non-premixed modes - for the latter case, the hydrogen was separately introduced into the fuel plenum and allowed to mix with the air downstream of the fuel injectors.

During all tests, the mixture was ignited via an externally heated platinum wire that was temporarily inserted into the combustion chamber through the exhaust port.

Figure 3-8 shows an exploded 3-D schematic of this experimental test rig.

3.5.2 Experimental Diagnostics

Gas temperature measurements were made through 250 μm type K thermocouples. Because of large temperature gradients along the length of the wire, an error analysis for the thermal conductivity, radiative

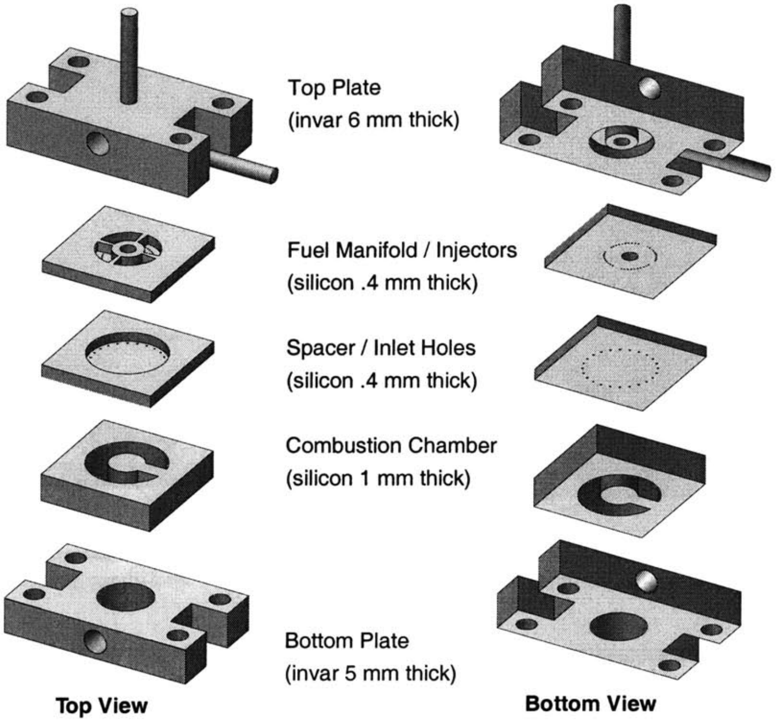

Figure 3-8: An exploded schematic of the microcombustor test rig. (Note: Wafer thicknesses are exaggerated for illustrative effect).

emissivity and calibration drifts [114], predicted absolute uncertainties up to ±130K in the exit gas temperature measurements[2].

Type K 250 μm sheath thermocouples were also inserted into the top and bottom invar plates to serve as proxies to silicon wall temperature measurements. In the absence of diagnostics to directly measure the silicon wall temperatures, the invar plate temperatures were considered to be an acceptable substitute based on a heat transfer analysis that predicted the entire structure to be isothermal within 100K [19].

Since the sheath thermocouples were inserted through long thin channels in the invar to reduce the heat transfer losses along the length of the wire, the uncertainty in wall temperature measurements was much lower (±12K).

3.5.3 Hydrogen Test Results

Exit Gas Temperature Measurements

Atmospheric test results were obtained for premixed and non-premixed hydrogen-air combustion over most of the flammability range. Since the engine was designed for a mass flow of 0.18 gm/sec at a compressor pressure ratio of four, the combustor mass flow was scaled-down to 0.045 gm/sec to maintain the same flow residence time under atmospheric test conditions.

---

[2] See Appendix A. for uncertainty analysis.

The corrected gas temperature measurements at the exit of the combustor are plotted in Figure 3-9 (a). These indicate the satisfactory attainment of temperatures as high as 1800K. As expected, the peak exit temperatures are also seen to occur slightly beyond stoichiometric conditions.

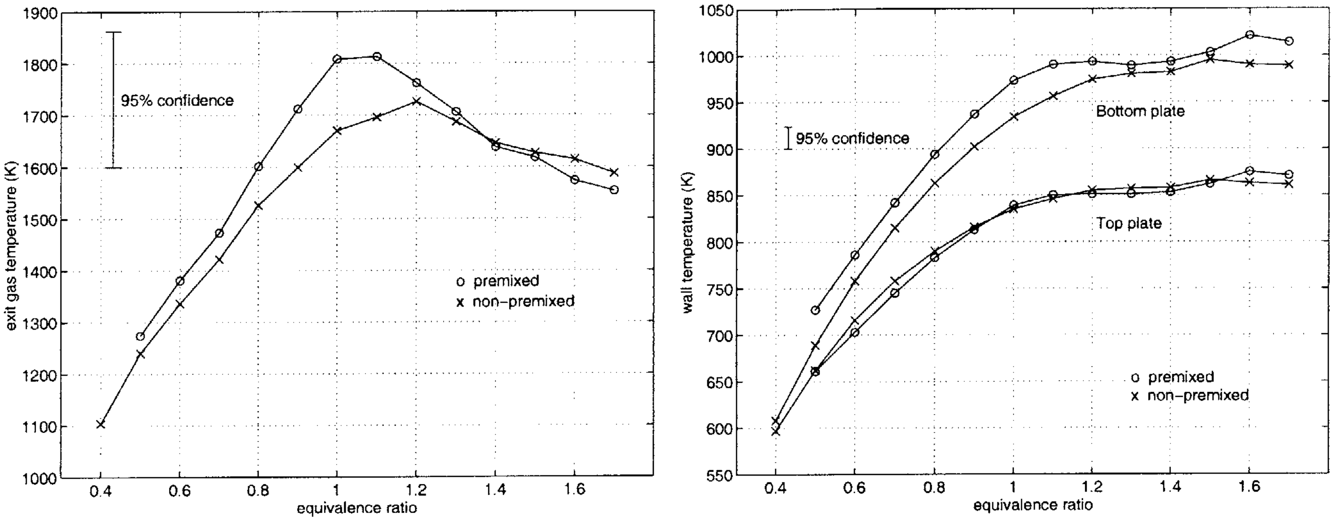

(a) Exit temperatures.

(b) Wall temperatures.

Figure 3-9: Experimental exit and wall temperature measurements in the 3-stack microcombustor.

The results also show higher exit temperatures for the premixed case. While this difference is within the error bars, the systematic deviation is considered to be physical, and is indicative of incomplete fuel-air mixing upstream of the combustion chamber. This was partly attributed to a wafer misalignment during bonding that resulted in a reduction of the mixing length on one side of the combustion chamber.

The premixed and non-premixed exit temperatures are also seen to converge at high equivalence ratios. This can be explained by the fact that in a fuel-rich regime, the energy release of the combustion process may be limited by oxygen depletion, not by fuel-air mixing.

Mechanical Integrity of the Device

At stoichiometric operating conditions, the power released by the complete combustion of the fuel is 156 Watts. This corresponds to a power density of 2360 MW/m^3. (Figure 3-10 (a) shows the operating device as a qualitative illustration of the heat being generated in this centimeter-scale microcombustor[3].)

At these high temperatures and space heating rates, the survivability of the silicon cannot be taken for granted. As shown in Figure 3-10 (b) however, an examination of the device after fifteen hours of operation showed no visible damage. The survival of the silicon can be explained by examining the wall temperatures of the top and bottom invar plates shown in Figure 3-9 (b). (As explained before, the isothermal nature of

---

[3] As shown later, the energy is transferred into the fluid with an overall efficiency of approximately 65%. The power density based on the power transferred to the exit fluid stream is therefore approximately 1500 MW/m^3.

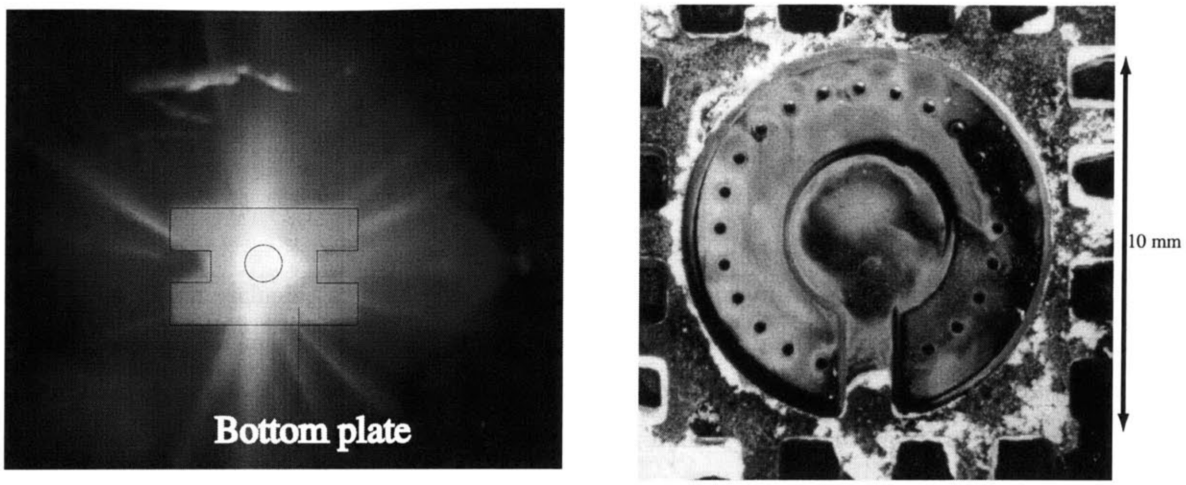

(a) A picture of the glowing 3-stack microcombustor at stoichiometric operating conditions.

(b) 3-stack microcombustor after 15 hours of testing at T_{exit} ~1600K.

Figure 3-10: Post-combustion examination of the microcombustor after high temperature operation. (The white regions show the ceramic adhesive that was used for sealing.)

the device allows these temperatures to be representative of the silicon wall temperatures to within 100K.) The results show that even though the gas temperatures in the device were as high as 1800K, the walls operated at relatively cooler temperatures in the range of 600K-1000K. This low temperature operation of the walls was attributed to the heat loss through the top and bottom invar plates which cooled the silicon to well below its melting point, thereby allowing it to survive for several hours without any visible degradation.

Calculation of the Combustor Efficiency

Although the ambient heat transfer was critical to the survival of the silicon at high combustion temperatures, it severely impacted combustor efficiency. Defined as:

$$\eta_c = \frac{(\dot{m}_a + \dot{m}_f)h_2 - \dot{m}_a h_1}{\dot{m}_f h_f} \tag{3.1}$$

where station (1) refers to the inlet and station (2) refers to the combustor exit, the overall combustor efficiency may be written as a product of two sub-efficiencies - a *chemical efficiency* that accounts for incomplete combustion, and a *"thermal" efficiency* that accounts for heat loss from the device, i.e.,

$$\eta_c = \eta_{chem} \times \eta_{thermal} \tag{3.2}$$

$$\frac{(\dot{m}_a + \dot{m}_f)h_2 - \dot{m}_a h_1}{\dot{m}_f h_f} = \frac{[(\dot{m}_a + \dot{m}_f)h_2 - \dot{m}_a h_1] + \dot{Q}_{loss}}{\dot{m}_f h_f} \times \frac{(\dot{m}_a + \dot{m}_f)h_2 - \dot{m}_a h_1}{[(\dot{m}_a + \dot{m}_f)h_2 - \dot{m}_a h_1] + \dot{Q}_{loss}} \tag{3.3}$$

$$\eta_{chem} = \frac{[(\dot{m}_a + \dot{m}_f)h_2 - \dot{m}_a h_1] + \dot{Q}_{loss}}{\dot{m}_f h_f} = \frac{\text{total enthalpy released}}{\text{maximum enthalpy release possible}} \tag{3.4}$$

$$\eta_{thermal} = \frac{(\dot{m}_a + \dot{m}_f)h_2 - \dot{m}_a h_1}{[(\dot{m}_a + \dot{m}_f)h_2 - \dot{m}_a h_1] + \dot{Q}_{loss}} = \frac{\text{enthalpy rise of fluid}}{\text{total enthalpy released}} \tag{3.5}$$

Note: For $\dot{Q}_{loss}$=0, $\eta_{thermal}$=1, and η_c=η_{chem}.

Although the exit temperature measurements can only be used to calculate an overall combustor efficiency, a simple heat transfer model based on the wall temperature measurements may be used to estimate the *thermal efficiency* of the combustor to subsequently estimate a *chemical efficiency* for the chamber.

Figure 3-11 (a) plots the overall combustor efficiency as calculated from the exit temperature measurements using Eq. 3.1; Figure 3-11 (b) shows a schematic illustration of a control volume that may used to estimate the heat loss through the experimental rig shown in Figure 3-8.

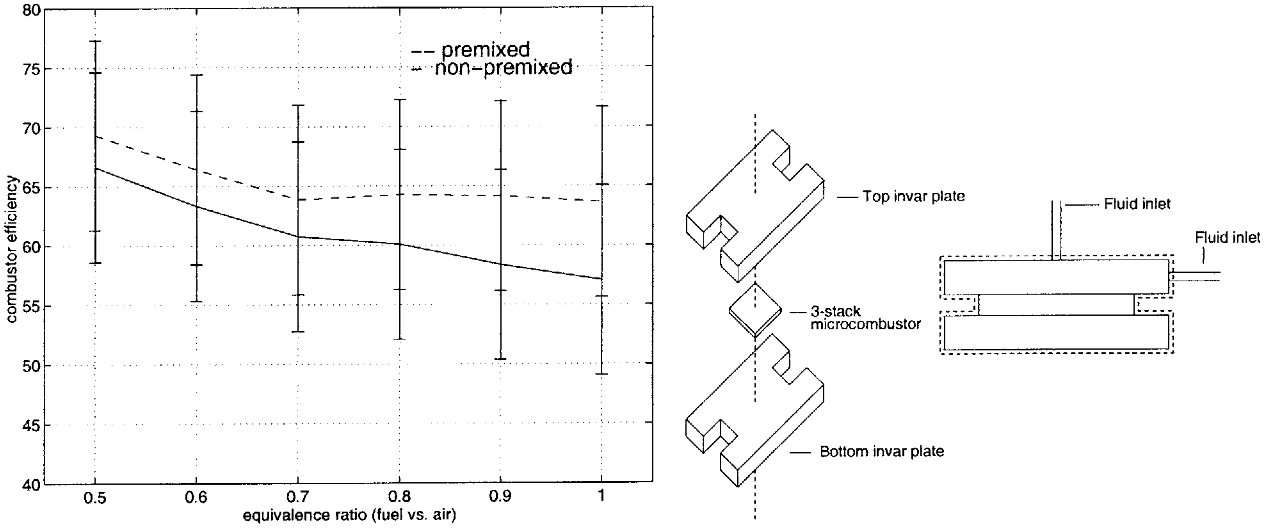

(a) Exit temperature-based efficiency calculation using Eq. 3.1.

(b) Schematic illustration of the control volume used to estimate the heat transfer losses through different surfaces of the 3-stack test rig.

Figure 3-11: Calculation of the combustor efficiency for the 3-stack microcombustor.

Heat Transfer Model for the 3-Stack Microcombustor: The results in Figure 3-11 (a) show premixed efficiency in the 65%-75% range, however, since CFD solutions had predicted close to complete combustion, it was hypothesized that most of this inefficiency resulted from heat loss out of the combustor and supporting invar plates. Consequently, a simple 1-D heat transfer model was used to quantify the conductive, convective and radiative losses out of the device:

1. *Conductive losses:* out of the experimental rig occurred along the two fuel and air tubes. These

comprised of a stainless steel tube that connected to a copper tube, and then ultimately to a *Swagelok* connection; their dimensions and thermal properties are listed below:

$$L_{steel} = 1\ cm, \quad d_{inner} = 1.2\ mm, \quad d_{outer} = 3.1\ mm, \quad k = 20\ W/mK;$$

$$L_{copper} = 20\ cm, \quad d_{inner} = 3.2\ mm, \quad d_{outer} = 6.3\ mm, \quad k = 360\ W/mK;$$

Neglecting the convective heat transfer along the length of the tubes, the conductive heat transfer is given by the 1-D conduction equation:

$$q_{cond} = \frac{\Delta T}{R_{thermal}}; \qquad R_{thermal} = \frac{L_{SS}}{k_{SS}A_{SS}} + \frac{L_{Cu}}{k_{Cu}A_{Cu}} \tag{3.6}$$

where ΔT is the temperature difference along the length of the tube.

Using Eq. 3.6, the magnitude of conductive heat loss out of the rig is plotted as a function of the equivalence ratio in Figure 3-12 (a).

2. *Convective losses:* The magnitude of the convective heat transfer through the control volume surfaces is given by:

$$\dot{q}_{conv} = hA(T_{wall} - T_{ambient}) \tag{3.7}$$

Laminar heat transfer coefficients for these surfaces were assumed as given by Holman [49]:

$$\text{Horizontal heated plate facing upward:} \qquad h = 1.32(\frac{\Delta T}{L})^{1/4} \tag{3.8}$$

$$\text{Horizontal heated plate facing downward:} \qquad h = 0.59(\frac{\Delta T}{L})^{1/4} \tag{3.9}$$

$$\text{Vertical heated plate:} \qquad h = 1.42(\frac{\Delta T}{L})^{1/4} \tag{3.10}$$

Using these, the magnitude of the convective heat transfer out of the control volume is also plotted in Figure 3-12 (a).

3. *Radiative losses:* through the control volume surfaces are given by:

$$q_{rad} = \epsilon\sigma A(T^4_{wall} - T^4_{ambient}) \tag{3.11}$$

Using ϵ=0.3 for a dark-gray oxidized surface [49], the radiative heat loss through the control volume is shown in Figure 3-12 (a).

The results in Figure 3-12 support the hypothesis that the chemical combustion efficiency in the microcombustor is close to unity, and that low overall combustor efficiency stems from high heat loss to the ambient, not from incomplete combustion.

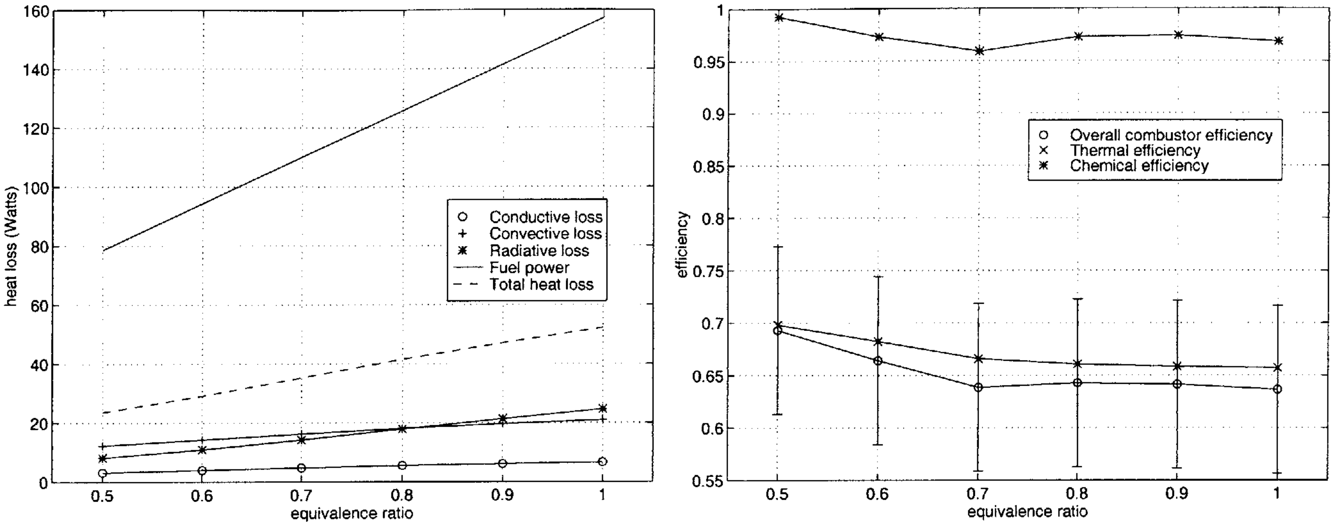

(a) An estimate of the conductive, convective and radiative losses through the 3-stack microcombustor.

(b) Estimates of the thermal and chemical efficiency of the 3-stack microcombustor.

Figure 3-12: Results of the 1-D heat transfer model, and estimates of the chemical efficiency in the 3-stack microcombustor.

The results also illustrate the trade-off between combustor efficiency and durability - although combustor heat loss reduces the device efficiency, it is necessary for the structural integrity of the silicon. In theory, one could reduce combustor heat loss in order to improve the efficiency, however, this may increase the wall temperatures and begin to push against the material constraints of silicon. This poses a trade-off between a combustor that is efficient, and one that is more durable.

Resolving this trade-off to design a combustor that is efficient, yet structurally viable, was one of the key objectives of the future design refinements, and is presented in Chapter four of this thesis.

3.5.4 Hydrocarbon Test Results

Although a hydrogen-fueled combustor is the first step towards a working silicon microengine, energy density and storage requirements ultimately dictate the use of hydrocarbon fuels. Consequently, in addition to the hydrogen tests, gaseous propane-air experiments were also conducted to evaluate the feasibility of burning a hydrocarbon fuel inside the 3-stack microcombustor.

Preliminary chemical kinetics considerations described in Chapter two showed that there was little or no feasible operating space for hydrocarbon microcombustion within the structural constraints of a silicon engine. The following factors could however facilitate homogeneous hydrocarbon combustion inside the 3-stack microcombustor:

1. Since the heat loss out of the microcombustor was large, the combustor walls were found to operate at several hundred degrees lower than the combustion gas temperatures. This suggested that in the

absence of a highly stressed rotating component to limit the maximum combustor exit temperature, the heat loss (i.e., combustor wall cooling), might naturally permit stable hydrocarbon combustion above the lean flammability limit, and within the material constraints of silicon.

2. Additionally, in the absence of a turbine rotor, the residence time constraint could also be relaxed by increasing the volume of the combustion chamber.

Using this approach, it was possible to operate in a small window in the design space and sustain stable propane combustion within a 0.2 cm^3 volume chamber. (This volume was three times the baseline volume of the 3-stack microcombustor, and was obtained by bonding additional level-3 wafers at the die-level.)

During the initial tests however, instead of stabilizing inside the chamber, the flame blew downstream and stabilized along the outer edge of the exhaust hole. Excessive heat loss that quenched the reactions at the walls was identified as a possible cause for this behavior. The combustor was subsequently heated with a flame to reduce the heat loss; this allowed the flame to move back upstream and operate stably inside the chamber until the walls cooled back down. Figure 3-13 shows the stable hydrocarbon flame with and shortly after the application of the external heat source. (Note: The fuel power density for this device was estimated to be approximately 670 MW/m^3.)

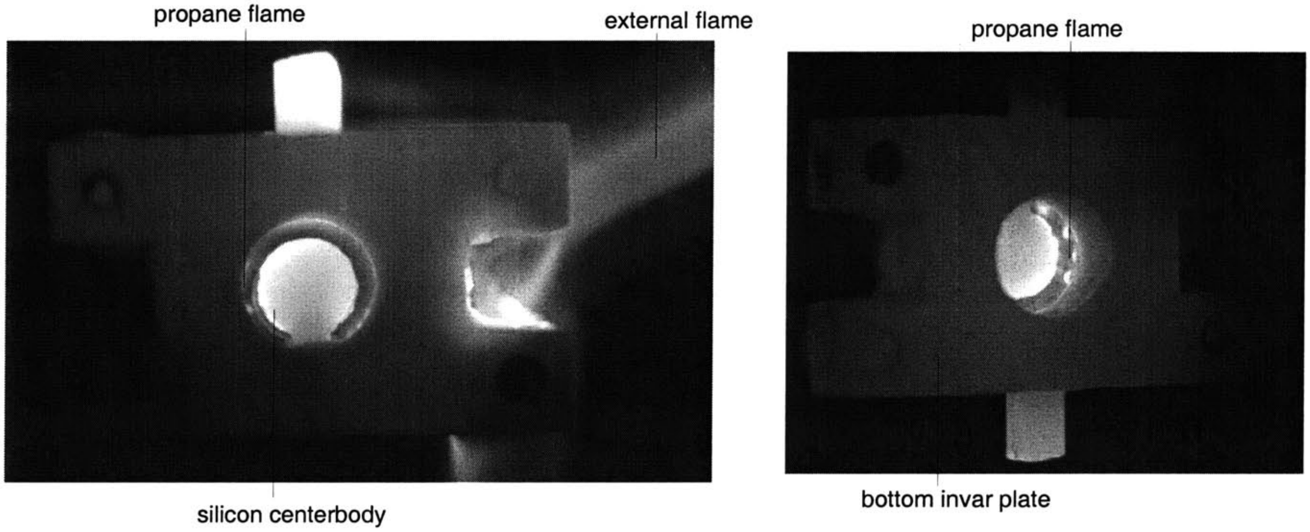

Figure 3-13: Demonstration of a propane flame inside a 0.2 cm^3 silicon microcombustor stabilized by external heating. The exhaust hole is 7 mm in size. (Picture by: Felice Frankel)

It should be noted that these hydrocarbon tests were only intended to be a proof-of-concept demonstration of the ability to burn hydrocarbons at the micro-scale. They illustrated the fact that the combustion requirements for high temperature walls may be in direct conflict with the structural constraints for silicon, and re-emphasized the controlling influence of heat loss out of the device.

Additional hydrocarbon tests with propane and ethylene will be presented in Chapter four.

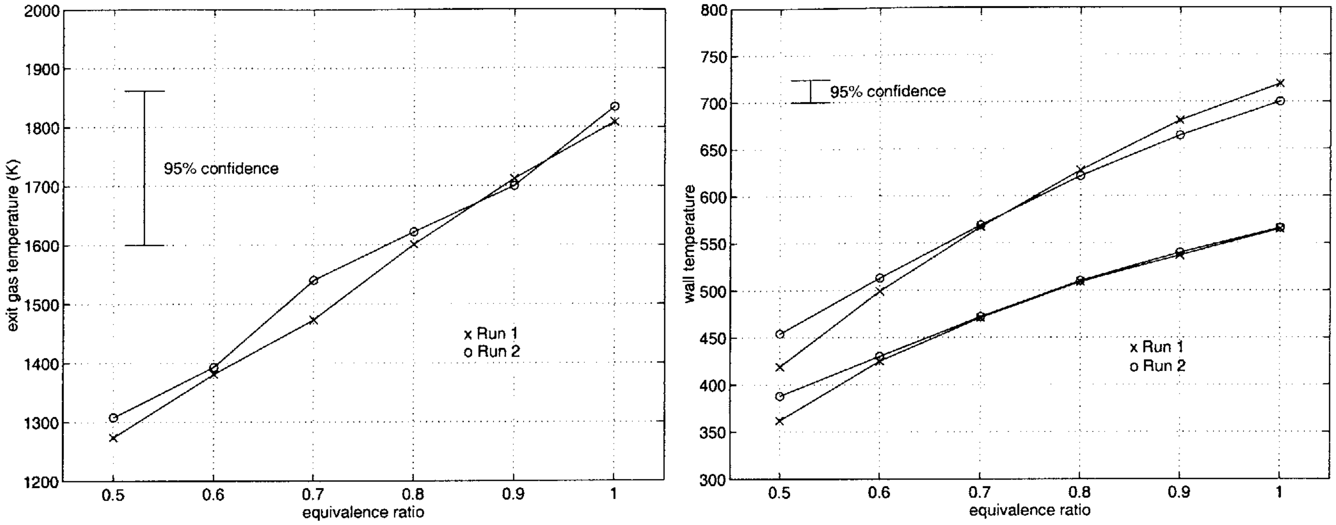

Figure 3-14: A comparison of the exit and wall temperature measurements on the 3-stack microcombustor showing repeatability of the test results.

3.5.5 Repeatability of the Results

To establish the repeatability of the temperature measurements, the hydrogen-air experiments were repeated for different die, and for multiple runs. Figure 3-14 shows the wall and exit temperature measurements for two of these runs, and show that the experimental results are within the expected uncertainty.

3.6 Materials and Oxidation Testing

As shown in Figure 3-10 (b), post-combustion examination of the silicon microcombustor indicated oxidation patterns around the combustor inlet ports. A materials study was consequently undertaken to quantify the effects of oxidation in a combustion environment.

3.6.1 Atmospheric-Pressure Oxidation Tests

As part of the first set of experiments, a silicon combustor plate consisting of "finger-like" structures with sizes between 20 μm × 500 μm × 450 μm and 1600 μm × 2000 μm × 450 μm was fabricated and tested inside the combustor. This plate is shown in Figure 3-15, and was fabricated by anisotropically etching through a single 450 μm wafer. A schematic of the combustor setup used to test this structure is also shown in Figure 3-15. (Note: This is the same setup used by Waitz, Gauba and Tzeng [115].)

The structure was exposed to a combustion environment for over eight hours at atmospheric pressure and flow temperatures in excess of 2000K. Depending on the size and aspect ratio of the fingers, and hence the temperature at which they equilibrated, the fingers grew between 1 μm and 7 μm of oxide. This corresponds to an oxidation rate between 0.1-0.9 μm/hour.

Most of the fingers grew amorphous oxide that was less that a couple of microns thick (Figure 3-16 shows

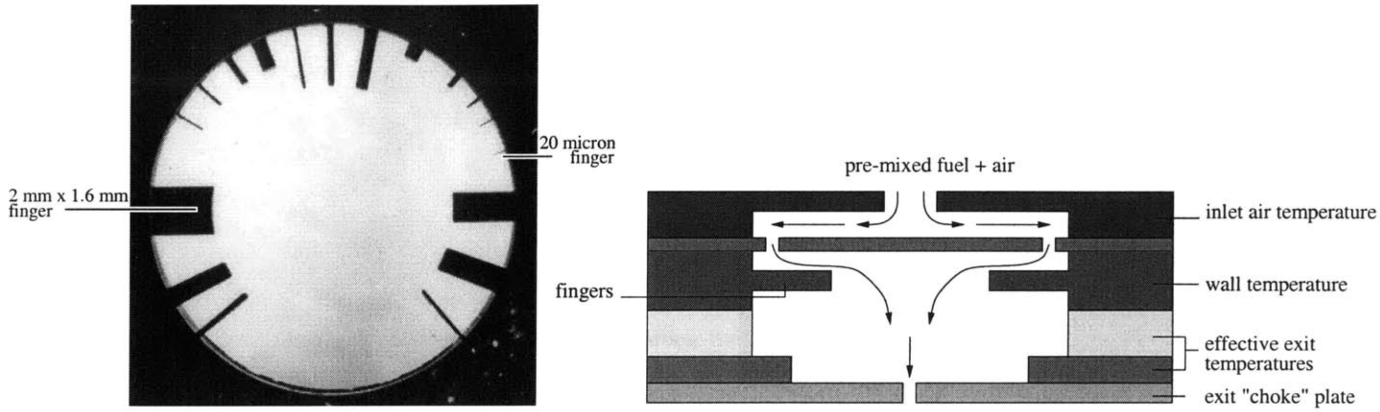

(a) Silicon combustor plate with "finger-like" structures.

(b) A schematic illustration of the combustor geometry used to test the oxidation fingers.

Figure 3-15: Setup for the combustion oxidation tests.

the patterns on a representative finger). The thinnest of the fingers however, grew flakes of crystalline oxide. This is also shown in Figure 3-16. The exact cause of this crystalline growth needs further examination.

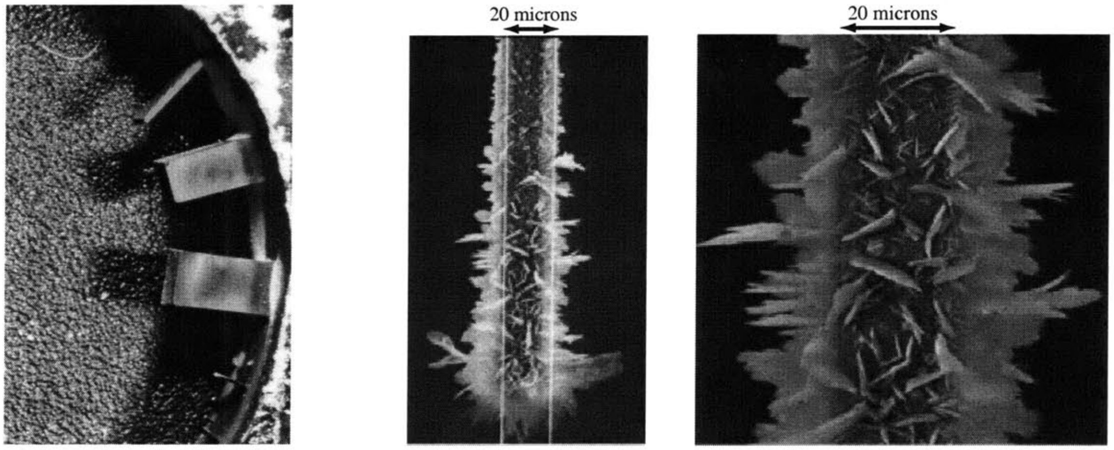

(a) Amorphous oxidation on a 800 μm and 1000 μm finger.

(b) Crystalline oxide growth on the 20 μm wide finger.

Figure 3-16: Oxidation results for the "fingered-combustor" geometry.

Overall, the oxide thickness was found to be of the same order of magnitude as that predicted by the Deal-Grove passive oxidation model [26]. This suggests the absence of "active-oxidation" of silicon in the presence of a moist and corrosive combustion environment; conventional thermal oxidation models may therefore be used to predict oxidation behavior inside the device. (To aid in the design of future devices, Appendix B tabulates the oxidation rate constants and plots the oxide thickness as a function of temperature.)

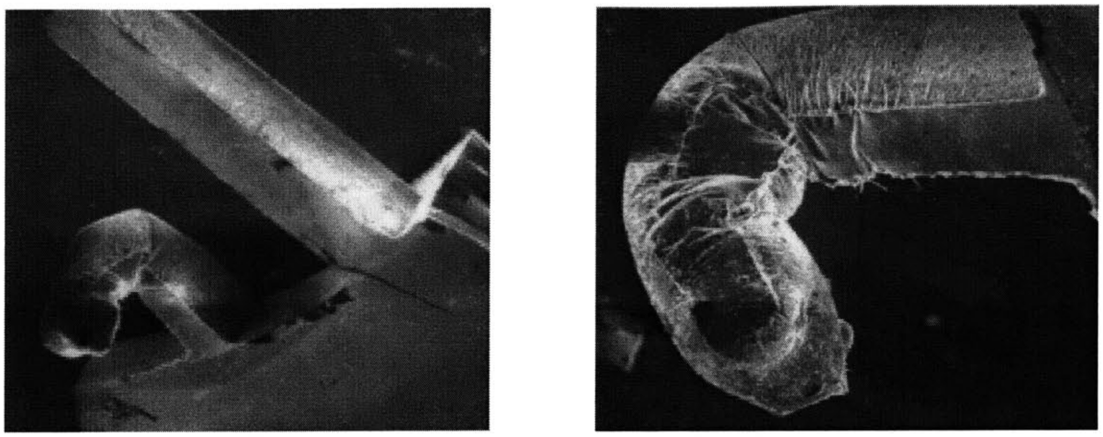

Figure 3-17: SEM of a 200 μm × 450 μm × 2000 μm structure after combustion, showing creep limited performance of silicon.

3.6.2 High Pressure Oxidation Tests

Following atmospheric testing, the fingered-combustor plate was also tested at higher pressures and temperatures to try to identify the dominant failure mechanisms inside the combustor. As shown in Figure 3-17, testing at fluid temperatures in excess of 2200K, and at operating pressures of approximately 3 atm., several of the fingers were found to creep.

The location of the point where the different fingers began to bend correlated well with a two-dimensional heat transfer model for the temperature distribution along the length of the fingers (see Appendix B.). The model predicted higher temperature at the tip and along the length of the longer and thinner fingers, consequently, these were expected to exhibit the maximum damage and fail closer to their root. This trend is illustrated in Figure 3-18, and was borne out in the following observations:

1. Out of the two 100 μm wide fingers, the 2000 μm long finger melted while the 1000 μm long finger showed relatively less damage.
2. Among the 2000 μm long fingers, the 100 μm wide finger melted, the 200 μm wide finger bent near the root, and the 400 μm wide finger remained intact.
3. Among the 1000 μm long fingers, the 50 μm wide finger bent closer to its root than the 100 μm wide finger; the 250 μm wide finger showed no damage.

The model was therefore found to qualitatively agree with the experimental observations; the creep failure of the fingers was attributed to the brittle-to-plastic transition of silicon occurring at approximately 900K [19].

3.6.3 Turbine Vane Oxidation Tests

Finally, as the last part of the oxidation study, tests were conducted to identify the effects of the high Mach number, high pressure, and high heat transfer environment of a turbine. Although atmospheric-pressure

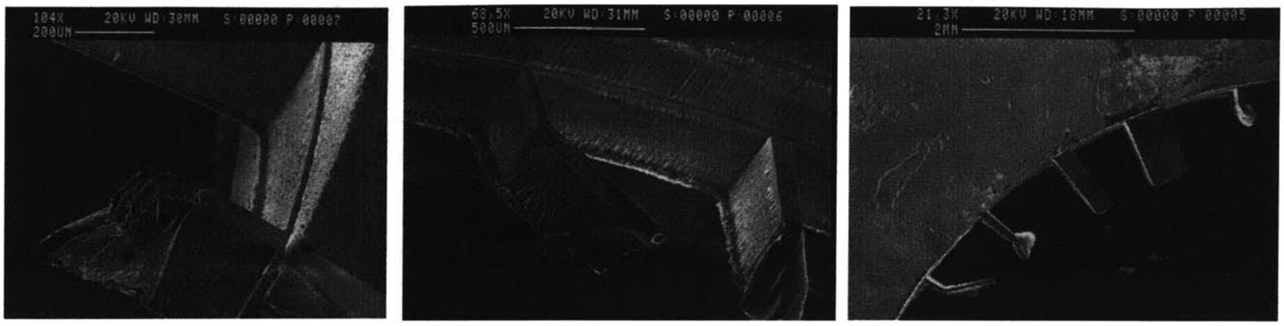

Figure 3-18: SEM's of the fingered-combustor showing the different sized fingers that melted and failed due to creep.

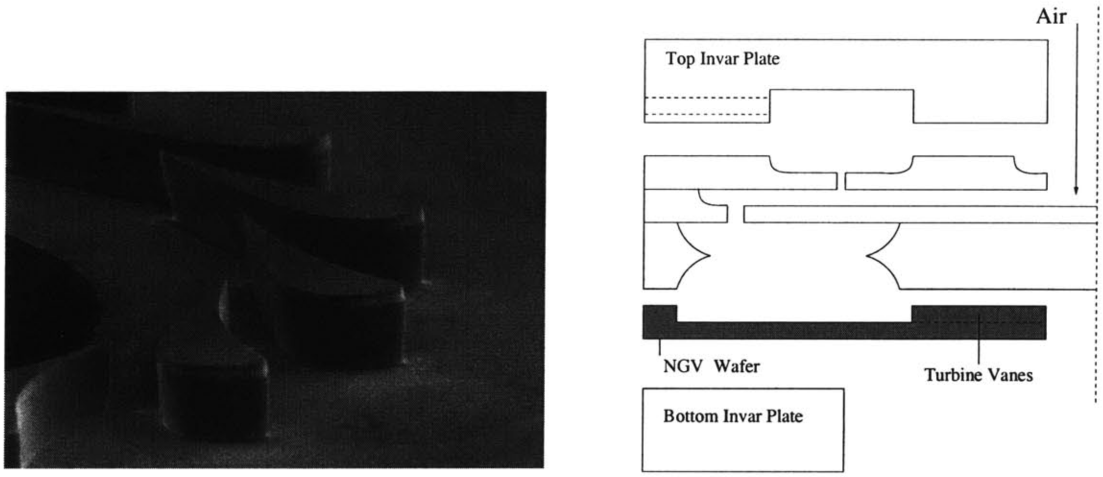

(a) An SEM of the turbine vanes.

(b) A schematic illustration of the placement of the turbine vanes in the microcombustor test rig.

Figure 3-19: Setup used to test the behavior of the turbine vanes upon exposure to combustor exhaust gases.

combustion tests had shown that oxidation would not be a limiting factor in the operation of a silicon microcombustor, effects in the turbine environment of a microengine were unknown. In the absence of being able to assess the effects on a spinning rotor, a set of 150 μm high turbine vanes (static nozzle guide vanes - NGV's) was exposed to the combustor exhaust to examine the effects of oxidation in a potentially erosive, high temperature and pressure, supersonic flow environment. An SEM of the turbine vanes used for this test is shown in Figure 3-19, along with a schematic illustration of the placement of the vane pack inside the microcombustor. The resulting 4-stack microcombustor rig is also shown in Figure 3-20.

The vanes were exposed to combustion exhaust gases at 1800K and 2.5 atm., and at a mass flow rate of 0.1 gm/sec. Figure 3-21 shows before and after pictures of one of the turbine stator vanes following five hours of testing. While "pitting" and erosion is visible on the blade surface, the vanes maintained their overall structural integrity, there being no more than a 2% change in throat area, and hence mass flow. These results demonstrate the survivability of a static vane structure in a high pressure, temperature, and

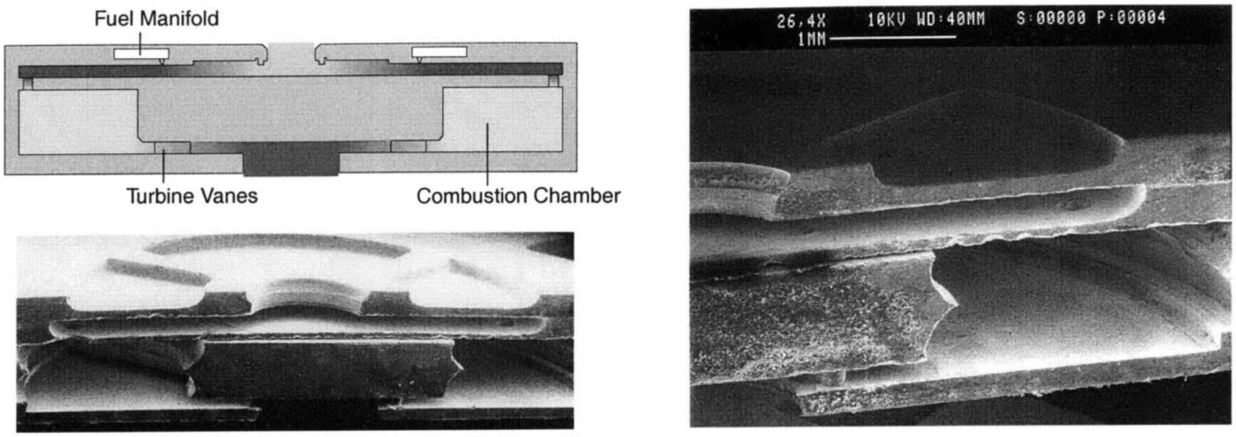

Figure 3-20: SEM cross-section of the 4-wafer microcombustor and turbine NGV stack alongside a schematic of the baseline engine structure.

high Mach number flow environment, and are suggestive of the ability to build a combustor and engine static structure out of silicon.

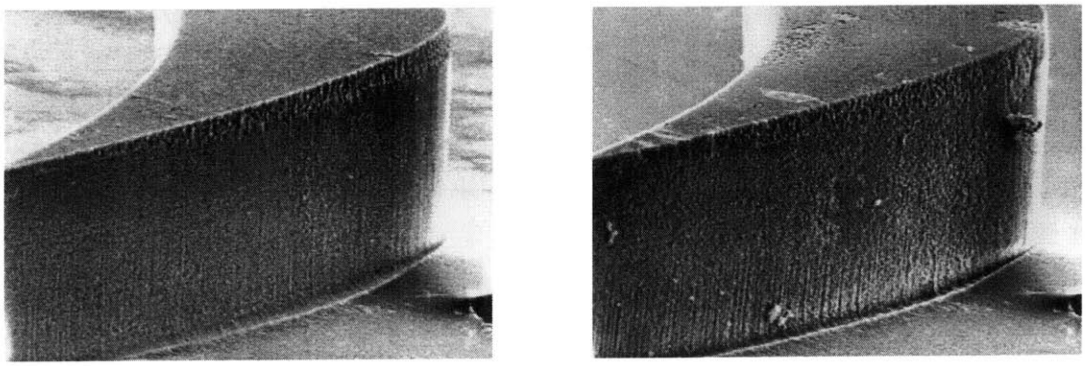

(a) Before

(b) After

Figure 3-21: Before and after pictures of a turbine vane following a five hour exposure to combustion exhaust gases at 1800K, and Mach number$\sim$1. Although the blades exhibit minor erosion and "pitting", they maintain their structural integrity.

3.7 Overall Implications and Chapter Summary

This chapter described the development of the first silicon microcombustor to be fabricated using deep reactive ion etching and aligned wafer bonding techniques. Complete with a fuel manifold and set of fuel injector holes, the 0.066 cm^3 combustion chamber was shown to sustain stable premixed and non-premixed hydrogen air combustion with exit gas temperatures as high as 1800K. The resulting space heating rate was also demonstrated to be an order of magnitude higher than that of any other power-MEMS device.

Compared to large-scale devices however, the combustor was found to be plagued by poor thermal efficiency. Ambient heat loss, although enabling to the structural integrity of the silicon, was identified to be the major source of inefficiency. Future devices were therefore intended to reduce combustor heat loss without compromising the structural integrity of the material, and are described in the following chapter.

The device was also used to demonstrate the feasibility of burning hydrocarbons at the micro-scale. Careful control of the thermal boundary conditions to allow stable combustion within the structural constraints of the material was identified to be the key challenge facing the use of hydrocarbon fuels.

Overall, after fifteen hours of hydrogen-air testing at elevated temperatures, the combustor maintained its structural integrity and showed no visible degradation. Combined with the results of an oxidation study that showed acceptable oxidation rates and minimal damage to the stator vanes in a hot turbine environment, the experiments demonstrated the satisfactory performance of a micromachined silicon combustor for a micro gas turbine engine application. They also established the viability of using silicon for the hot static section of the device, and laid the foundation of building an all-silicon engine.

Following this successful demonstration of a hydrogen microcombustor for the engine, the next step involved the integration of the combustor with the other components of the engine. This is described in the next chapter.

Chapter 4

Development of the Engine Static Structure

This chapter presents the detailed design, fabrication and operation of a hydrogen microcombustor in an engine-like configuration. Known as the engine "static-structure", the device described in this chapter comprises all the non-rotating components of the MIT microengine. Fully-packaged, and complete with a set of fuel plenums, pressure ports, fuel injectors, igniters, and compressor and turbine static airfoils, this static structure integrates the 3-stack microcombustor with the other non-rotating components of the engine, and is the first demonstration of the complete hot flow path of a multi-level microengine.

The chapter describes the objectives of this device, then presents its detailed design, then describes the fabrication and packaging process, and finally concludes by presenting the experimental test results.

4.1 Goals of the Engine Static Structure

The engine static-structure was specifically developed with the following objectives:

1. Designed to be compatible with the overall fabrication sequence for a complete engine, the static structure would be the first fabrication demonstration of the ability to deep etch, wafer bond and diesaw six wafers to obtain a multi-level microengine structure.
2. It would be used to evaluate the performance of a hydrogen combustor in an "engine-configuration", and to evaluate the structural capabilities of silicon in engine-like geometries.
3. It would be used for the experimental identification of the combustion stability boundaries for hydrogen and hydrocarbon fuels in the current design of the microengine, and provide additional understanding of the key drivers of microcombustion phenomena in the device.

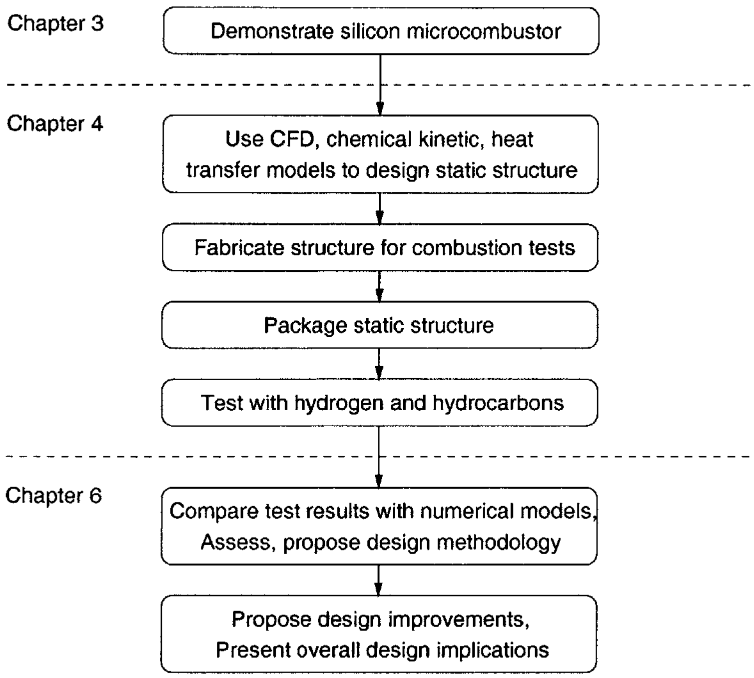

Figure 4-1: A flowchart illustrating the development plan for the static structure.

4. It would provide experimental data to validate numerical models in order to assess the effectiveness of the design methodology.

5. Finally, it would be the first fully-packaged microcombustion system for the MIT microengine, incorporating *in situ* igniters and mechanical fluidic interconnects.

4.2 Development Plan

The development plan for the engine static structure is shown in Figure 4-1 as a subset of the overall development process illustrated in Figure 1-2.

The first step of the development process involved the use of CFD, chemical kinetics, and heat transfer models to design a suitable geometry that fulfilled the engine requirements within the structural and fabrication constraints of the system (described in Section 4.3). After a suitable geometry was designed, the device was fabricated, packaged and tested (described in Sections 4.4, 4.5 and 4.6). The experimental data was then compared with the numerical results to close the design loop, and to present overall design implications for future versions of the microengine combustor (presented in Chapter six).

4.3 Design of the Engine Static Structure

The design of the static structure required a multi-disciplinary approach to account for the fluid dynamic, chemical kinetic, fabrication, and structural aspects of the engine, and is described as follows:

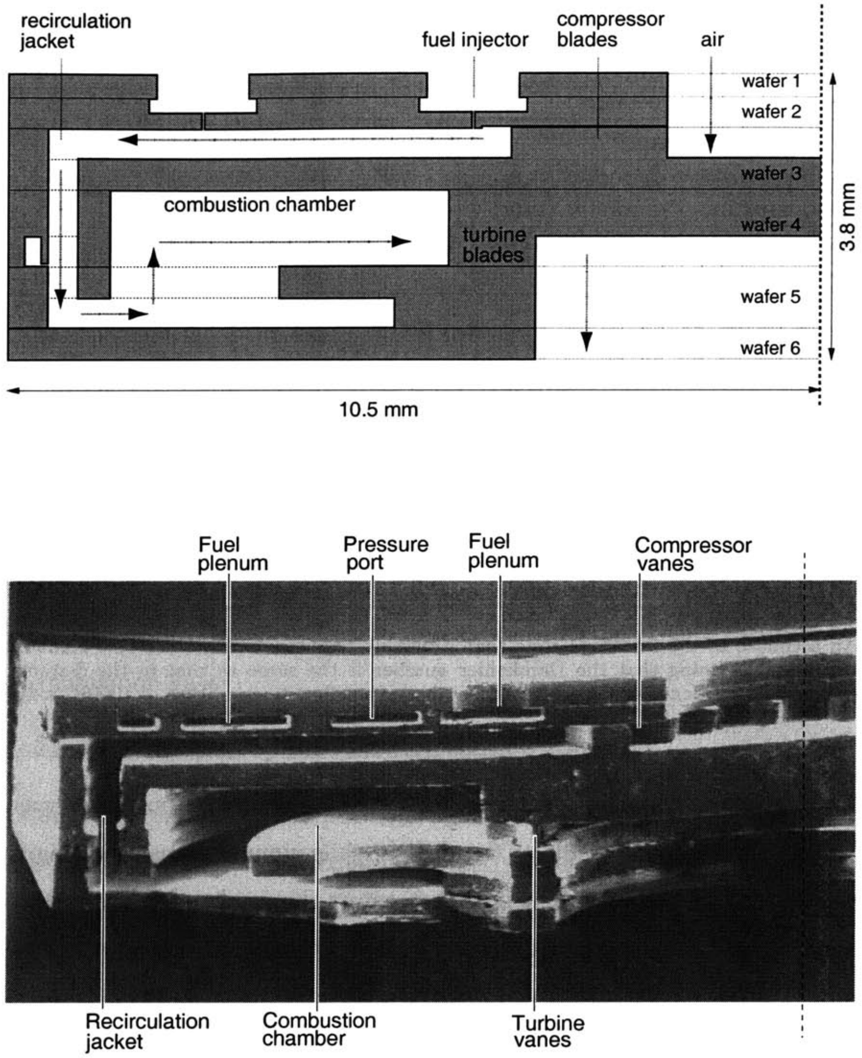

Figure 4-2: Schematic and SEM cross-section of half of the axisymmetric 6-wafer static structure. (Note: The dies on the wafer had two types of combustor inlet holes - one type had slots as shown in Figure 4-16, the other had an annular opening as shown above.)

4.3.1 Overall Configuration

A schematic of the overall geometry of the static structure is shown in Figure 4-2 alongside an SEM of the fabricated device. The device comprises six wafers that are aligned and stacked on top of each other in order to achieve a closed structure.

As highlighted in Figure 4-2, air enters the device axially and makes a right angle turn into the compressor. In the absence of a rotating impeller, stationary compressor vanes are used to provide the requisite swirl into the combustor[1]. Fuel is injected axially through multiple fuel injector holes[2], and mixes with the

---

[1] During the initial design of the device, the effect of swirl on combustor performance was unknown. In oder to closely mimic the flow at the exit of the engine impeller, stationary compressor vanes were therefore designed in order to produce 80° of swirl.

[2] Multiple fuel injectors were designed to evaluate the trade-off between duct burning and fuel-air mixing, and are described in more detail in Section 4.3.2.

	3-stack microcombustor	Static structure
Air mass flow rate (gm/sec)	0.18	0.36
Operating pressure (atm.)	4	3
Overall die size (mm)	15 × 15 × 1.8	21 × 21 × 3.8
Combustor outer diameter (mm)	10	18.4
Combustor inner diameter (mm)	5	9.6
Combustor axial length (mm)	1	1
Combustor volume (mm^3)	66	190

Table 4.1: A comparison of the operating parameters for the 3-stack microcombustor and engine static structure.

	Microcombustor		Static structure	
	Hydrogen	HC	Hydrogen	HC
Mass flow (gm/sec)	0.045	0.045	0.13	0.13
Volume (mm^3)	66	198	191	572
Residence time (msec)	0.5	1.5	0.5	1.5

Table 4.2: An estimate of the residence time that would be required to sustain stable combustion in the static structure assuming that the Damkohler number is the same as that in the 3-stack microcombustor. (Note: The residence times are based on an average flow temperature of 1000K, and P=1 atm.)

air as it flows through a combustor recirculation jacket. This recirculation jacket was designed with the dual purpose of insulating the outer walls of the device while simultaneously cooling the hot walls of the chamber with compressor discharge air. The flow then enters the combustion chamber axially, burns in the annular-shaped volume, and finally exhausts through NGV's that are designed to choke the flow.

Sizing the Combustion Chamber: Since the development of the 3-stack microcombustor, the size of the microengine had subsequently grown to increase the power output from the device. The static structure was therefore sized for this new engine configuration; Table 4.1 lists the operating parameters for the new device, and compares it with those for the 3-stack microcombustor.

Based on the design mass flow rate and operating pressure of the larger engine, the chamber was re-scaled to maintain the same flow residence time as that in the already demonstrated 3-stack microcombustor. The maximum die size was also limited to 2.1 cm to accommodate at least ten dies on a 4" wafer.

Table 4.2 compares the residence time in the static structure with that in the 3-stack microcombustor, and suggests that re-scaling the 3-stack microcombustor to ensure stable hydrogen combustion at the higher mass flow rate of the static structure would require a combustor volume of 190 mm^3. The outer diameter of the combustion chamber was therefore increased to 18.4 mm; the axial length of the combustor was still maintained at 1 mm in keeping with the maximum desirable etching thickness for a single wafer[3].

---

[3] Since the static structure was only intended to be a test article to explore the use of hydrocarbon fuels at the micro-scale, the combustion chamber was sized for design-point hydrogen combustion only.

Design of the Recirculation Jacket

Although the overall configuration of the static structure was similar to that of the 3-stack microcombustor, it included a combustor recirculation jacket. By allowing the compressor discharge air to flow over the walls of the combustion chamber, this recirculation jacket was designed for the following purposes:

1. Previous experimental testing of the 3-wafer microcombustor showed that although ambient heat loss reduced combustor efficiency to approximately 70%, it was instrumental to the survival of the silicon at high temperatures (Section 3.5.3). In an effort to improve combustor efficiency within the structural constraints of silicon, the recirculation jacket therefore:
   (a) Recycled the lost energy of the combustion chamber to preheat the incoming reactants, while
   (b) Using compressor discharge air for cooling the hot chamber walls to allow the silicon to survive at high temperatures necessary for stable combustion.
2. The recirculation jacket also alleviated packaging concerns by insulating the outer walls of the device from the hot combustion gases.

The width of this jacket was dictated by the following considerations:

- Given the system requirement for 400 μm high blades, cold-flow CFD solutions showed that the flow did not diffuse to fill the entire recirculation jacket, instead, it propagated as a 400 μm wide jet regardless of the width of the recirculation jacket (Figure 4-3). Consequently, to minimize the lateral dimension of the device, 400 μm was considered to be an upper bound on the width of the recirculation jacket.

- Reducing the width of the channel below 400 μm was found to "constrict" the flow and increase the velocity of the reactants entering the combustor. Since this would reduce the effective flow residence time inside the chamber, it was considered undesirable.

The recirculation jacket width was therefore set at a constant value of 400 μm.

In order to support the interior chamber, eight 100 μm wide bridges were used to connect it with the outer walls of the device. These bridges were intended to minimize the thermal connection between the combustion chamber and the outer walls.

Pictures of such a bridge in the fabricated device are shown in Figure 4-4.

4.3.2 Design of the Fuel Injectors

The static structure was designed with fuel injectors at three different locations to evaluate the trade-off between mixing effectiveness and duct-burning. If the fuel is injected too close to the combustion chamber, there might not be enough mixing length; if it is injected too far upstream, the mixture might burn in the recirculation jacket and compromise the insulation of the outer walls.

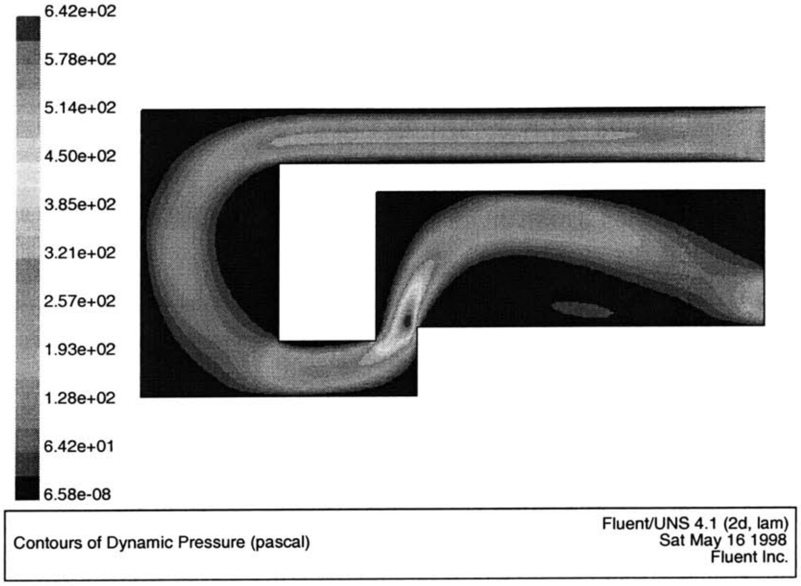

Figure 4-3: Cold-flow solution for a 800 μm recirculation jacket showing that the flow propagates as a 400 μm wide jet even if the width of the jacket is larger than that. (Picture courtesy: S. Pennathur)

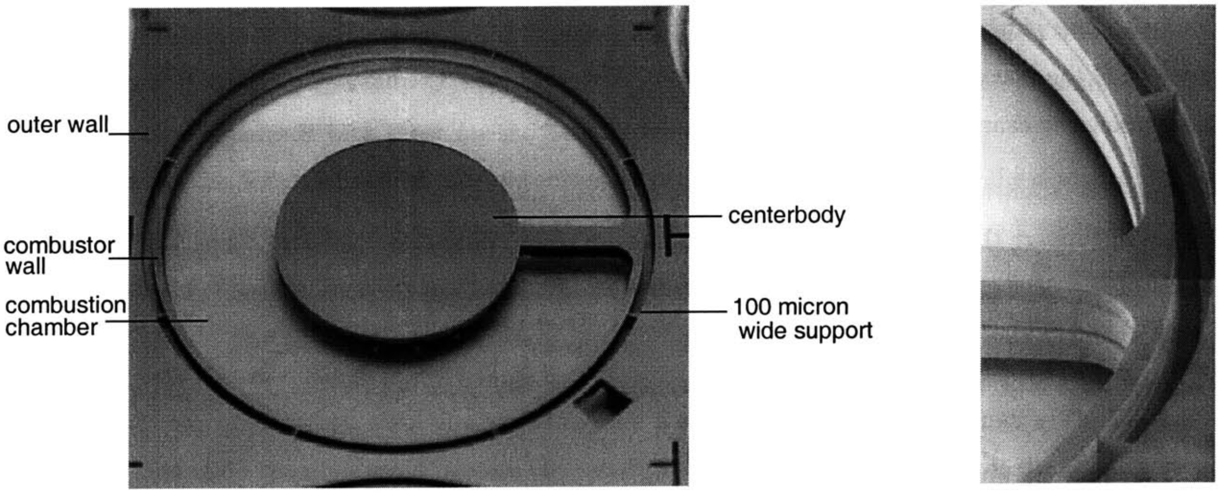

Figure 4-4: An SEM and an optical image of the eight 100 μm bridges that connected the combustion chamber to the outer walls of the static structure.

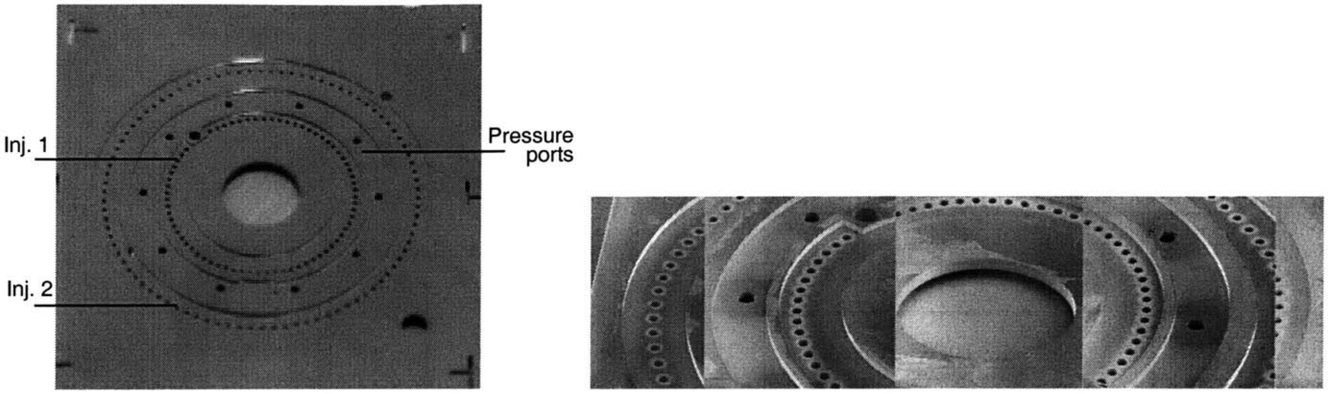

Figure 4-5: Images of the fuel plenums and axial fuel injector holes in the static structure.

To identify an acceptable location for injection in the microengine, the static structure was therefore designed with three sets of fuel injectors:

- 2 sets of axial injectors were located downstream of the compressor vanes at diameters of 9.6 mm and 16 mm, respectively. These comprised of a set of round holes that were arranged in a circular pattern, and were similar to the fuel injectors described in Section 3.3 for the 3-stack microcombustor.
  Figure 4-5 shows pictures of these two sets of axial injectors.
- A set of radial injectors were also designed to be located at the base of the recirculation jacket. As shown in Figure 4-6, these rectangular slots connected an outer fuel plenum to the recirculation jacket and introduced fuel immediately upstream of the inlet to the combustor.
  Images of these injectors are shown in Figure 4-7.

The size and spacing of the axial fuel injectors was determined by using semi-empirical models for jet penetration and lateral spreading. By varying the diameter and spacing of the injector holes, half of the dies were optimized for hydrogen injection, the other half were optimized for propane injection. The primary goal of this design was to optimize the penetration and lateral spreading of the fuel jets so as to minimize the streamwise length needed for complete fuel-air mixing upstream of the combustion chamber.

Assuming transverse injection into a cross-flow (Figure 4-8), and inputs for the mass flow rate, temperature, pressure, velocity and physical properties of the fuel and air at each injection location, a model was subsequently developed to optimize 1.) The size of the fuel injectors (d_j), and 2.) The number (or inter-hole spacing) of the injectors.

Using empirical correlations suggested by Margason [76], the centerline of a transverse jet was given by:

$$\frac{y}{d_j} = \sqrt[3]{4\frac{x}{d_j}\frac{1}{j^2}}; \qquad j = \sqrt{\frac{\rho_\infty U_\infty^2}{\rho_j U_j^2}} \tag{4.1}$$

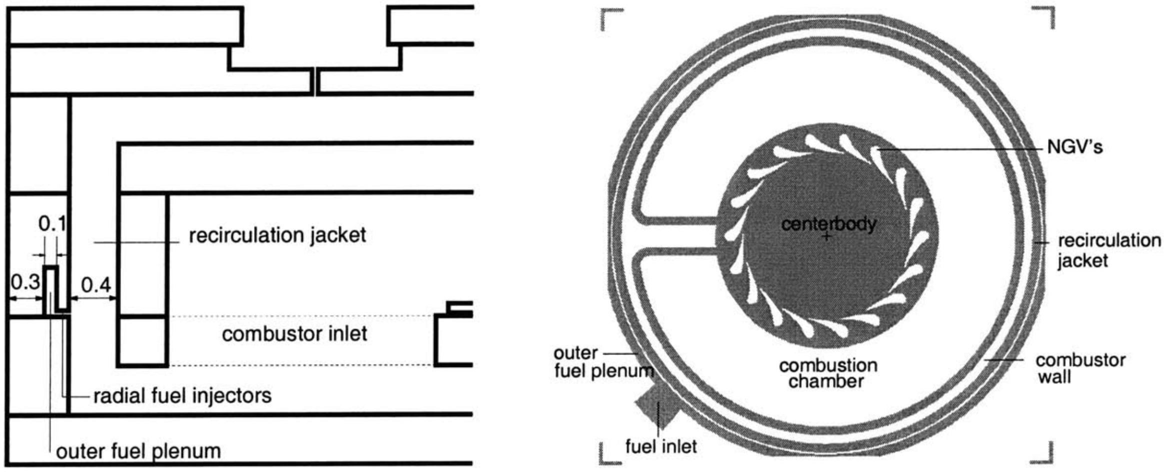

(a) Schematic illustration of the radial fuel injectors.

(b) Mask configuration of the outer fuel plenum, recirculation jacket and chamber.

Figure 4-6: Illustrations of the radial fuel injectors that connected the outer fuel plenum to the recirculation jacket in the static structure (all dimensions in *mm*).

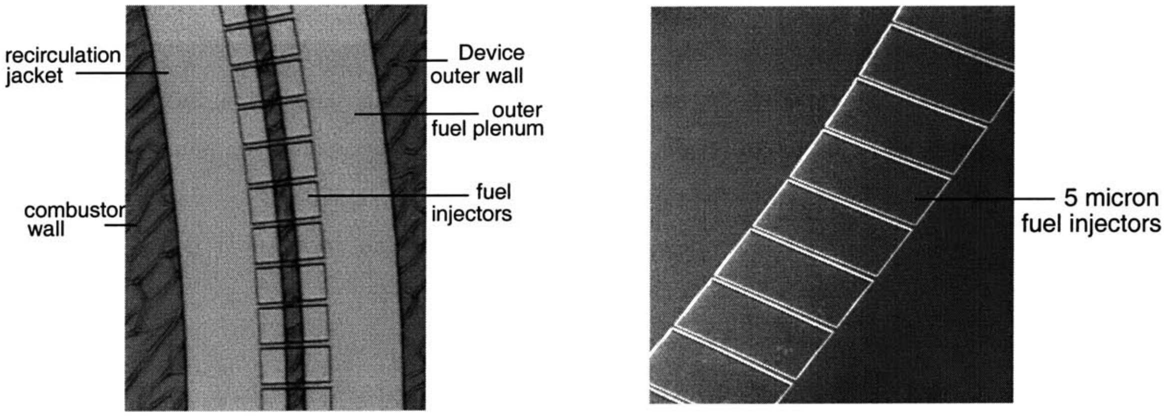

(a) Patterned optical image of the fuel injectors connecting the outer fuel plenum to the recirculation jacket. (Note: The dark regions are photoresist.)

(b) An SEM of the fuel injectors after shallow etching.

Figure 4-7: Images of the radial fuel injectors in the fabricated static structure.

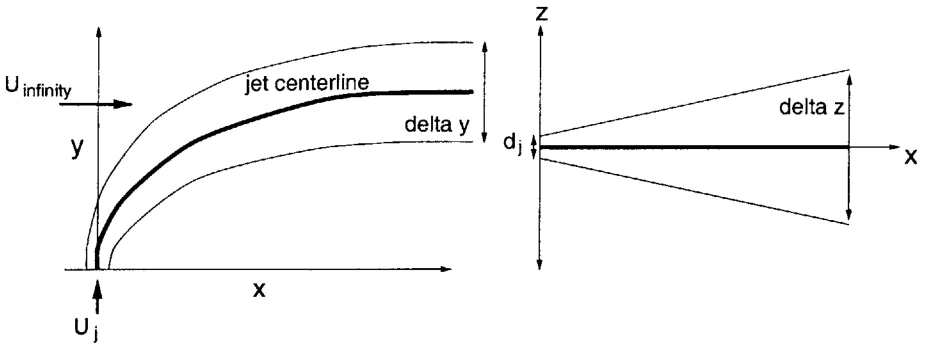

Figure 4-8: A schematic illustration of transverse fuel injection into a cross-flow, indicating all the relevant parameters.

As suggested by Schetz [101], the lateral spreading of the jet along the y and z axes was given by:

$$\frac{\delta y}{d_j} = 0.92\frac{U_j}{U_\infty}(\frac{x}{d_j[U_j/U_\infty]})^{.4}; \qquad \frac{\delta z}{d_j} = 1.25\frac{U_j}{U_\infty}(\frac{x}{d_j[U_j/U_\infty]})^{.4} \tag{4.2}$$

Using these relations, and by specifying the fuel and air operating parameters, the size and spacing of the the two axial injectors was optimized by minimizing the streamwise distance over which:

1. The jet penetrated halfway into the 400 μm high passage,
2. The circumferential spreading of the jet exceeded the sum of the diameter and inter-hole spacing of the injectors, and
3. The axial spreading of the jet exceeded the height of the passage.

The optimization was conducted for hydrogen as well as propane injection. A mathematical formulation of the optimization is presented below:

$$Minimize: \qquad x_{min} = \frac{d_j j^2}{4}[\frac{h}{2d_j}]^3 \qquad \text{by changing: } d_j,\ n,\ \text{subject to the constraints:}$$

1. n=integer (i.e. there are an integral number of holes)
2. $2\pi r/n > d_j$ (i.e. the inter-hole spacing is greater than the hole diameter)
3. $\delta z|_{x_{min}} > 2\pi r/n$ (i.e. the circumferential spreading of the jet is greater than the center-to-center distance between the holes)
4. $\delta y|_{x_{min}} > h$ (i.e. the axial spread of the jet exceeds the height of the passage)

The final size and number of the injectors as obtained from the optimization is listed in Table 4.3.

Using a similar optimization for the radial fuel injectors showed that the injector height required for optimal mixing exceeded the maximum depth permissible by shallow etching technology. Consequently, the

	Hydrogen		Propane	
	Dia. (μm)	Num.	Dia. (μm)	Num.
Inj. 1 (axial at r = 4.8 mm)	224	72	140	60
Inj. 2 (axial at r = 8.0 mm)	210	90	120	90
Inj. 3 (radial at r = 10 mm)	5 × 160	360	5 × 160	360

Table 4.3: Dimensions of the fuel injectors in the static structure.

size of the radial fuel injectors was primarily dictated by fabrication constraints, and was set at 5 μm. The circumferential spacing between the injectors was dictated by the minimum photolithography linewidth, and was also set at 5 μm.

4.3.3 Design of the Flame Holders

Recirculation zones in a combustor are critical for flame stability because they serve as reservoirs for the hot products and ignite the reactants flowing into the combustor.

Since residence time constraints limited the possibility of burning hydrocarbon fuels in the 190 mm^3 combustion chamber, a combination of CFD and chemical kinetic models were used to tailor the flow recirculation zones inside the chamber. The objective of this exercise was to maximize the stability of the recirculation zones in order to sustain a stable flame over the widest range of mass flows and heat loss conditions.

The resulting analyses yielded two inlet configurations for the combustor (details of these models are presented in Appendix C.):

1. The first of these configurations consisted of 60 slots that were 2.2 mm long and were located at an inner and outer diameter of 14 mm and 18.4 mm, respectively. These were intended to allow stable flame holding in the separation zones between the slots.

2. The second of these configurations consisted of a single annular opening that was 1.2 mm wide. This was intended to set up a large recirculation zone of the type depicted in Figure 4-3, and was sized using a perfectly stirred reactor (PSR) model to establish the stability of the recirculation zone. Details of this analysis are also presented in Appendix C.

SEM's of both these configurations in the fabricated device are shown in Figure 4-9.

4.3.4 Turbomachinery Stator Blade Design

The static structure contained two sets of stationary turbomachinery blades that were designed using a 2-D airfoil design code called MISES [29] & [121]. The code used interacting boundary layer theory (IBLT) to couple an inviscid Euler core with analytical solutions for the boundary layer region, and was also previously utilized to design other turbomachinery components for the engine [54].

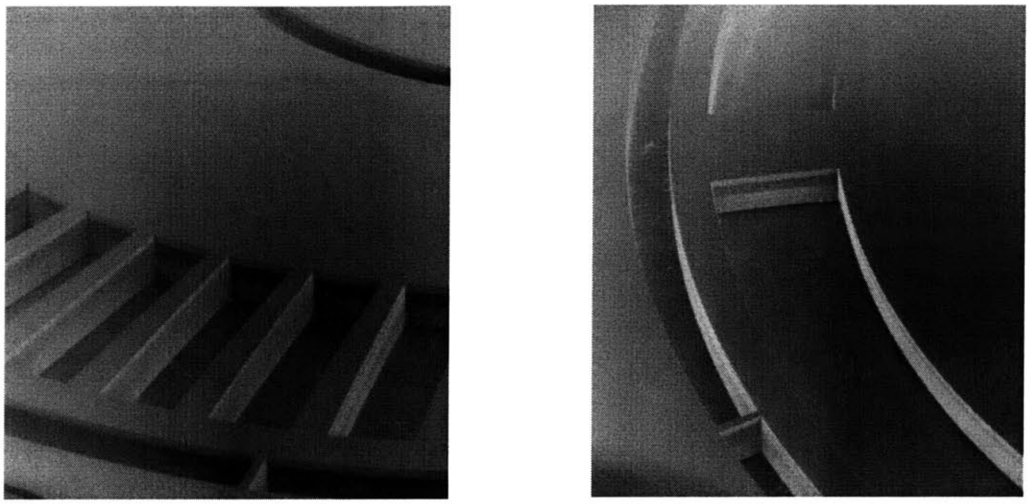

(a) Slotted inlet.

(b) Annular inlet.

Figure 4-9: SEM's of the two combustor inlet configurations. (Note: The 100 μm wide supporting bridges can also be seen in the images. The slots are 2.2 mm long; the annulus is 1.2 mm wide.)

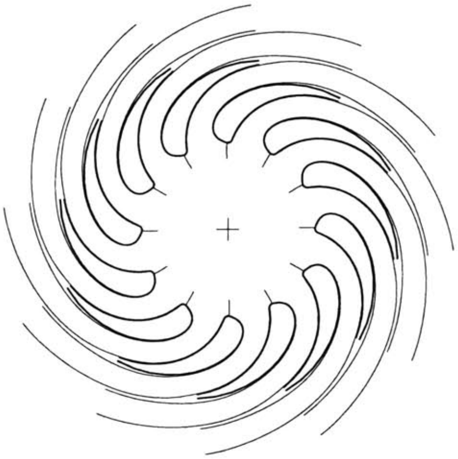

Blade height (microns)	400
Inlet radius (mm)	2
Outer radius (mm)	4
Number of blades	12
Inlet pressure (atm)	3.0
Inlet Mach number	.065
Mass flow (gm/sec)	.36
Total pressure ratio	.99
Exit flow angle	74.9°
Reynolds number	9220

Figure 4-10: 2-D design and operating parameters for the stationary compressor vanes in the static structure. The edges of the boundary layer are also shown alongside the blade surfaces.

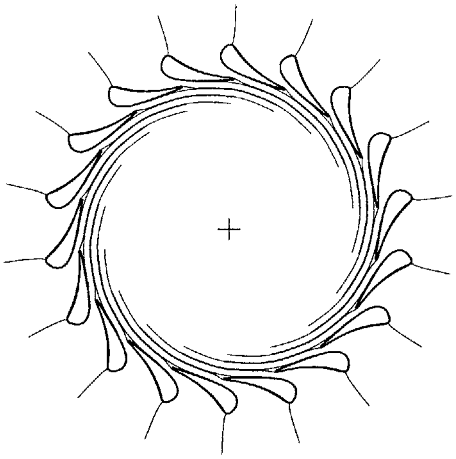

Blade height (microns)	400
Inlet radius (mm)	4.8
Outer radius (mm)	3.7
Number of blades	18

Inlet pressure (atm)	2.7
Inlet Mach number	.054
Mass flow (gm/sec)	.36
Total pressure ratio	.88
Reynolds number	1695

Figure 4-11: 2-D design and operating parameters for the stationary turbine vanes in the static structure.

Using this code, stationary compressor vanes were designed to pre-swirl the flow into the combustor, and also mimic the impeller surface area available for heat transfer to the fluid in the recirculation jacket. Static turbine vanes were also designed to choke the flow and allow elevated pressure testing at the design mass flow of the microengine.

The 2-D blade shape and operating parameters are presented in Figures 4-10 and 4-11; pictures of the compressor and turbine blades in the fabricated device are shown in Figure 4-12.

4.3.5 Structural and Thermal Design

Given an overall geometry that satisfied combustion requirements for the engine, a structural/heat transfer analysis was carried out in conjunction with MIT Lincoln Laboratory in order to size the critical dimensions in the device. This analysis was primarily intended to ensure that the thermal stresses in the device would not exceed the structural constraints of silicon at elevated temperatures. Details of the structural modeling are presented in Appendix D; the final dimensions of the critical features are shown in Figure 4-13.

4.3.6 Diagnostics

The static structure was designed to incorporate the following diagnostics:

Pressure ports: In order to measure the combustor pressure drop, the static structure included two pressure ports upstream and downstream of the combustor.

The upstream pressure port connected to a plenum between the two fuel manifolds and was located at a radius of 6 mm. The flow Mach number at this location was expected to be less that 0.25, hence, the static pressure was expected to be within 5% of the upstream total pressure.

The downstream pressure port connected directly to the combustion chamber and was intended to measure the static pressure upstream of the NGV's. The Mach number in this region was expected to be

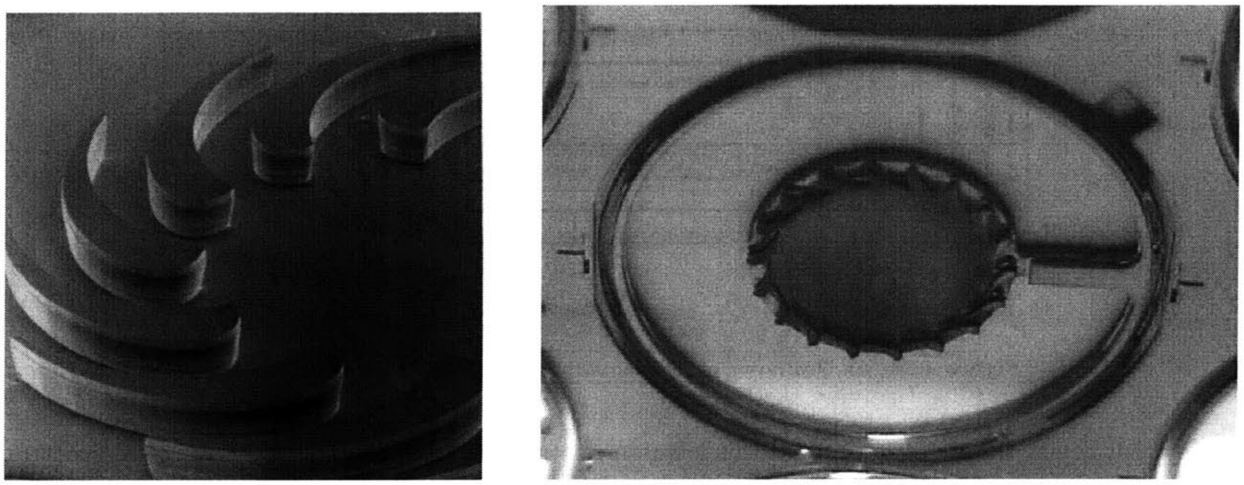

(a) SEM of the 400 μm high compressor vanes.

(b) Optical image of the 400 μm high NGV's in the static structure.

Figure 4-12: Pictures of the stationary turbomachinery blades in the static structure.

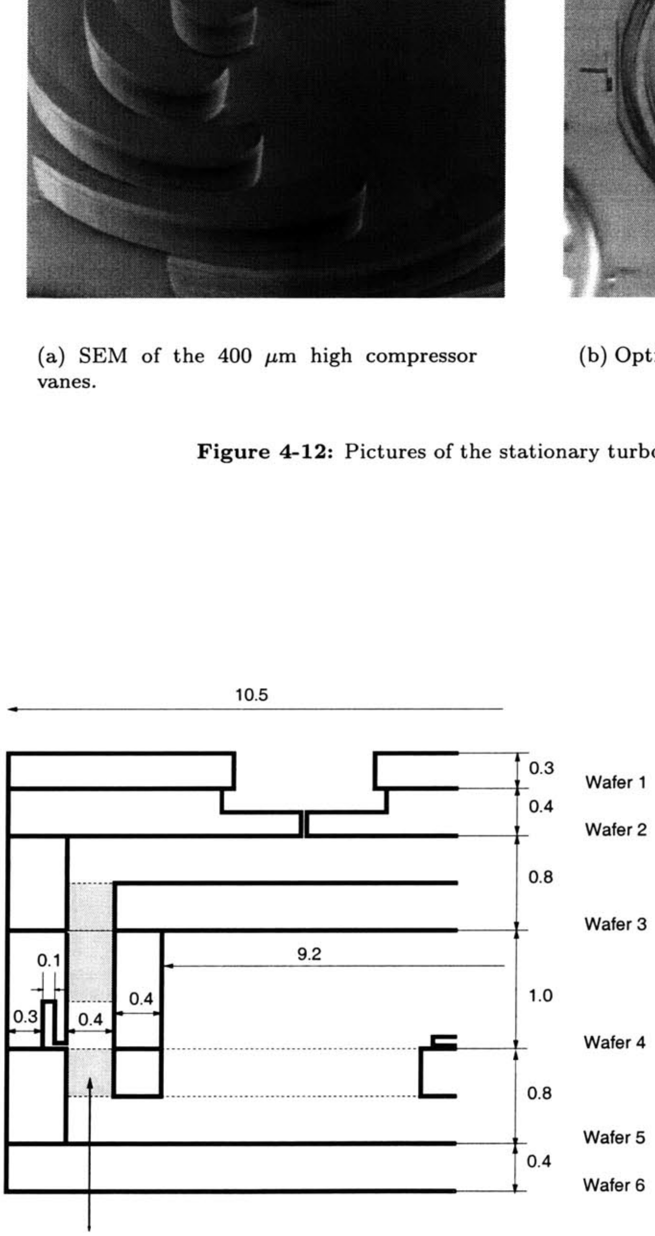

8 bridges, 100 microns thick
Note: All dimensions in mm

Number of supporting bridges	8
Width of supporting bridges	100 μm
Combustor wall thickness	400 μm
Outer fuel plenum wall thickness	100 μm
Inter-die spacing	600 μm

Figure 4-13: Wafer thicknesses and critical dimensions in the static structure.

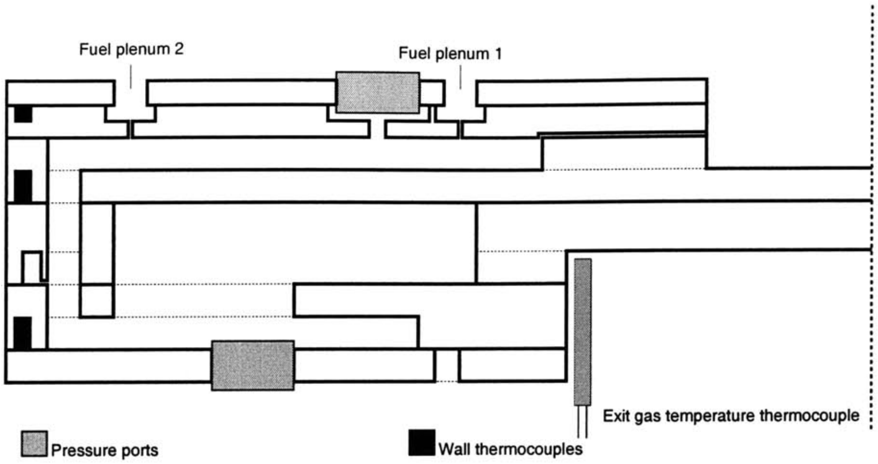

Figure 4-14: An illustration of the placement of diagnostics in the static structure.

below 0.1, hence, the static pressure at this location was expected to be within 1% of the total pressure.

External wall temperature sensors: The static structure included three 250 μm × 7000 μm channels that were etched into the outer walls of wafers 2, 3 & 5 for 10 *mil* sheath thermocouples. The high aspect ratio of these channels was intended to minimize the heat transfer along the length of the thermocouple wire in order to maximize the accuracy of the wall temperature reading.

Gas temperature sensors: In addition to the wall temperature sensors, a 10 *mil* thermocouple was also placed downstream of the NGV's to measure the gas temperature at the exit of the combustor.

The location of each of these diagnostics is shown in Figure 4-14.

4.3.7 Igniter Design

The static structure had provisions for external igniter ports that could be used to insert a resistively heated wire to into the combustion chamber. The packaging of these igniters shall be described in Section 4.5.

Parallel attempts to develop and demonstrate thin film microfabricated "on-chip" igniters were also made. A discussion of this development effort shall be deferred until Chapter five.

4.4 Fabrication of the Engine Static Structure

Fabrication of the static structure required a total of 10 deep anisotropic etches and 2 shallow etches.

The 13-mask process is illustrated in Figure 4-15, and is detailed as follows:

Wafer 1: required a single 400 μm deep dry anisotropic etch to define the inlet holes to the three fuel plenums, the pressure plenum, and the compressor.

Wafer 2: was first 5 μm shallow-etched from the bottom to define the tip clearance for the compressor. (Even though there were no rotating blades in the static structure, this clearance was required to maintain the thermal insulation between the chamber and the outer walls of the device.) Following the shallow etch,

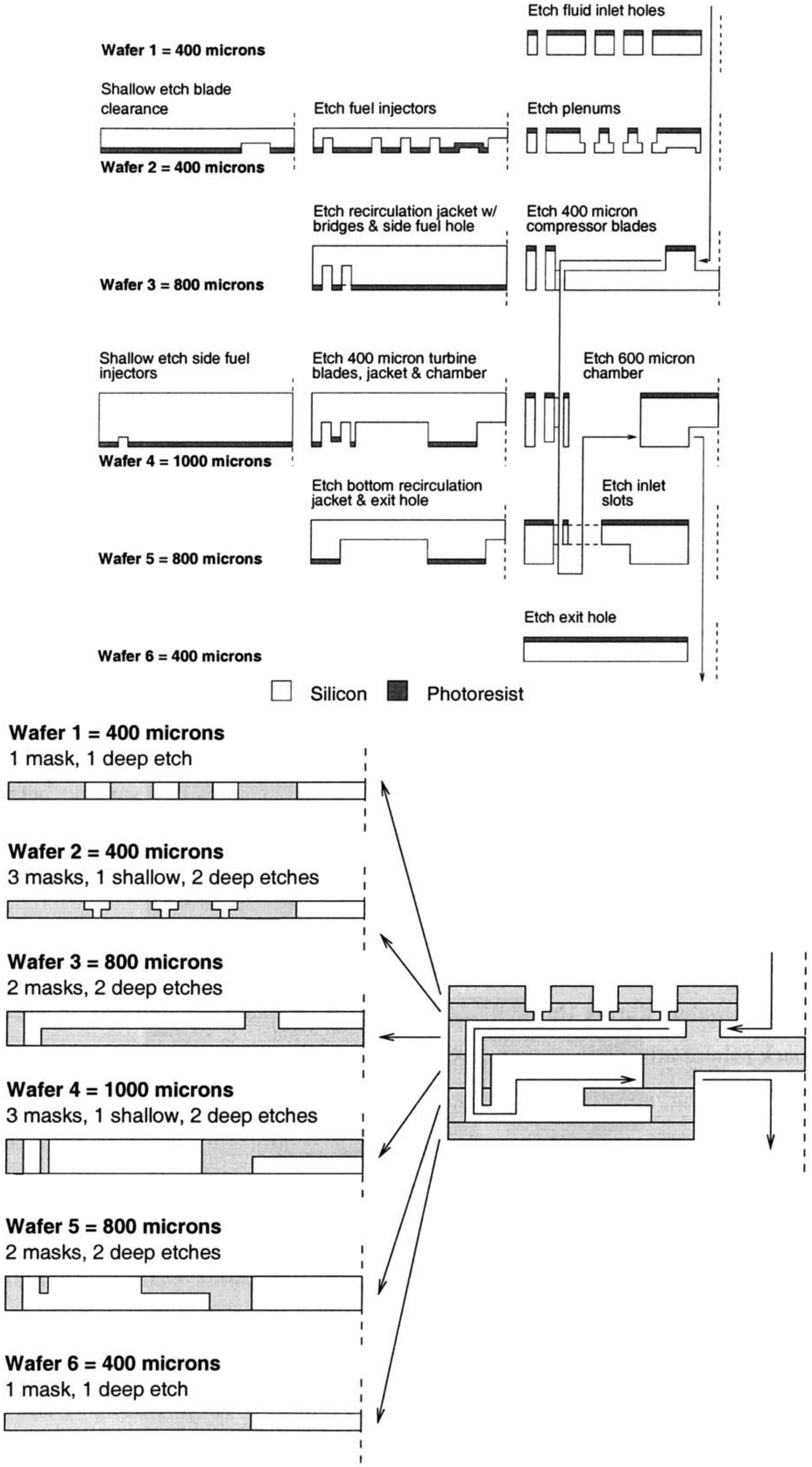

Figure 4-15: An illustration of the fabrication process for the 6-wafer static structure. (Note: The cross-sections are not to scale.)

the wafer was flipped and 200 μm deep fuel and pressure plenums were anisotropically dry etched from the top. Finally, 200 μm deep fuel injector holes were anisotropically dry etched from the bottom.

Wafer 3: comprised the compressor blades and involved two 400 μm deep anisotropic etches. The 400 μm compressor blades were first etched from the top side, the wafer was flipped, the 400 μm recirculation jacket was then etched from the bottom.

Wafer 4: comprised the 1000 μm deep combustion chamber and the turbine NGV's. First, 5 μm deep fuel injectors and 400 μm deep NGV blades were etched from the bottom. The wafer was flipped and the remaining 600 μm of the combustion chamber was then etched from the top.

Wafer 5: contained the combustor inlet holes, and like wafer 3, also involved two 400 μm deep anisotropic etches. The combustor inlet slots were first etched from the top side of the wafer. The remaining 400 μm recirculation jacket was then etched from the bottom.

Wafer 6: required a single 400 μm etch for the exit hole, the igniter ports, and the aft pressure port.

For each of the etches, the photolithography and DRIE steps were similar to those described in Sections 3.4.1 & 3.4.2 for the 3-wafer microcombustor.

Figure 4-16 shows SEM's of each of the wafers prior to bonding, along with a schematic illustration of the air flow path; Figure 4-17 shows an optical image of the device along different axial planes.

Wafer Bonding: Following completion of the individual wafer processing, all six wafers were aligned-fusion bonded to obtain a multi-level microengine structure.

Given the complexity of bonding six patterned wafers with thicknesses varying between 400 μm and 1000 μm, and a total stack thickness of 3800 μm, this step posed a significant challenge. In fact, as shown in Figure 4-18, the first two builds of the static structure suffered from poor bonding yield and did not produce any dies that sealed upon pressurization.

This poor bonding was attributed to surface contamination resulting from fluorocarbon deposits on the bottom surface of the wafers during through-wafer DRIE. Subsequently, sacrificial oxide coatings were used to protect the back side of all wafers during through-wafer etches. The bonding protocol was also improved to minimize wafer handling, and to allow multiple wafer bonding of all six wafers in a single step.

As a result of these measures, bonding yield on the next build improved to 50%. In this case, poor bonding along half the wafer was attributed to a photoresist residue that contaminated one of the bonding surfaces during a piranah wet-strip.

Subsequently, in the final build, all wafers were carefully inspected and accordingly re-built to ensure that all the surfaces were pristine prior to bonding. As shown in Figure 4-18 (d), this attempt resulted in perfect bonding between all six wafers and produced 100% yield at diesaw.

An SEM cross-section of a bonded device is shown in Figure 4-19. The packaging and experimental test results for the static structure are presented in the following sections.

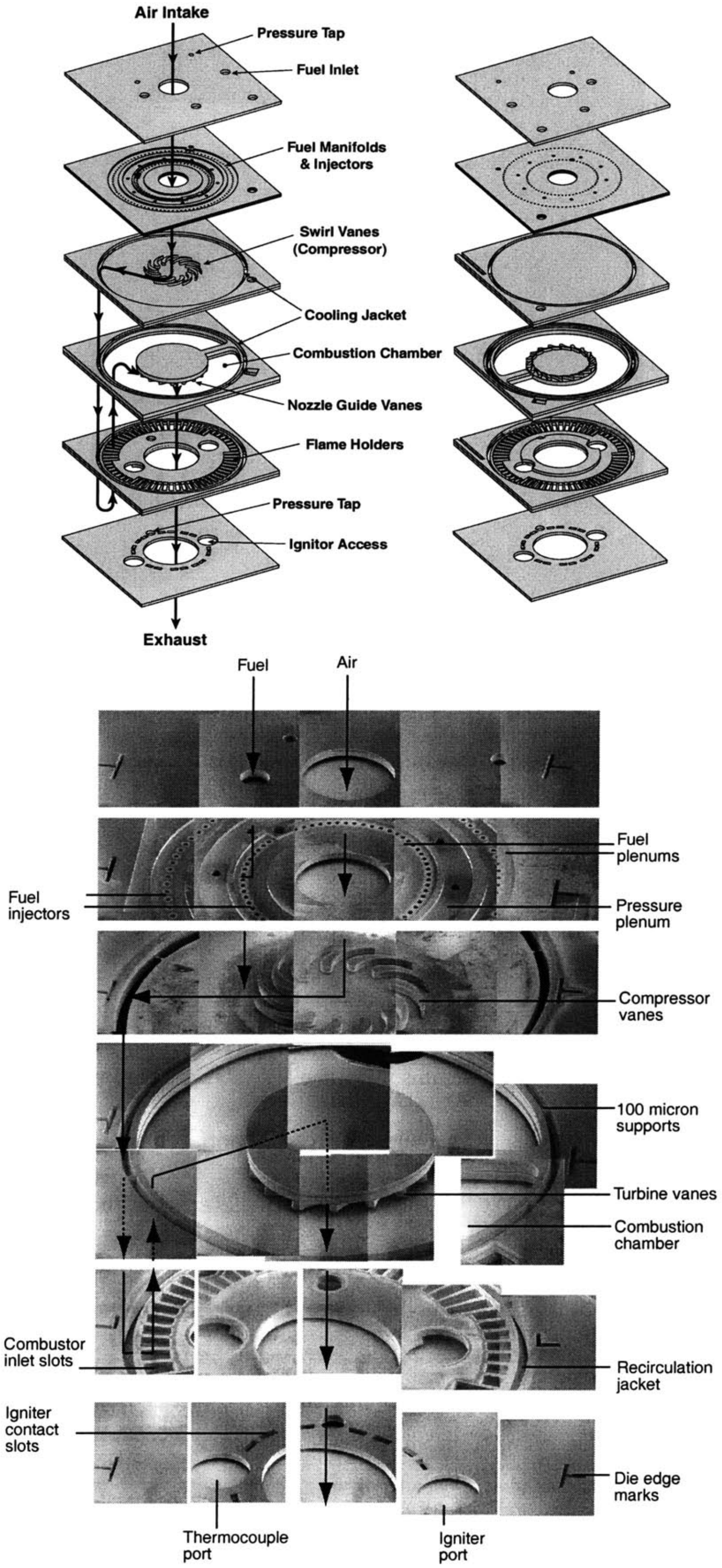

Figure 4-16: SEM's of the static structure prior to bonding, along with a schematic of the flow path. (Picture courtesy: Diana Park)

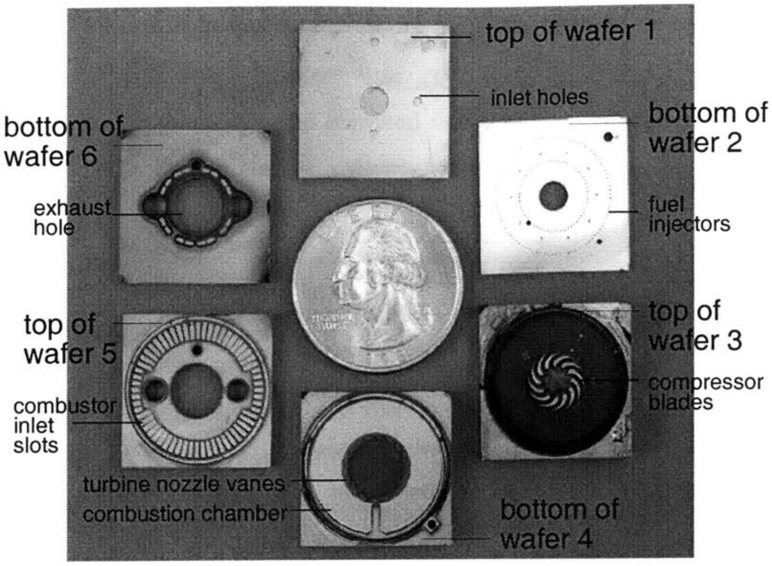

Figure 4-17: Optical image of the static structure along different axial planes. (Picture courtesy: MIT Lincoln Laboratory)

4.5 Packaging

Following the satisfactory fabrication of the static structure, and prior to experimental testing, significant effort was spent in packaging the device in a suitable experimental test rig. The static structure required:

1. *Frontside fluidic connections:* There were five inlet holes on the frontside - one for the main inlet air, three for each of the fuel injection plenums, and one for the upstream pressure plenum.
2. *Backside fluidic connections:* There was one aft pressure port connection.
3. *Electrical interconnects:* There were two sets of backside igniters that required electrical interconnects.

The requirement for pressure-sealed electrical and mechanical interconnects was complicated by the high temperature operating environment of the device. Combined with the brittle nature of silicon, and the inability to directly connect a macro fitting onto the fragile die, hermetic, high temperature interconnects to silicon therefore constituted a significant design challenge.

4.5.1 Fluidic Interconnects

The first versions of the test rig utilized a high temperature ceramic adhesive to seal custom-machined invar ferrules into silicon. Ceramic tubes were then used to connect the ferrules to a metal block with macro

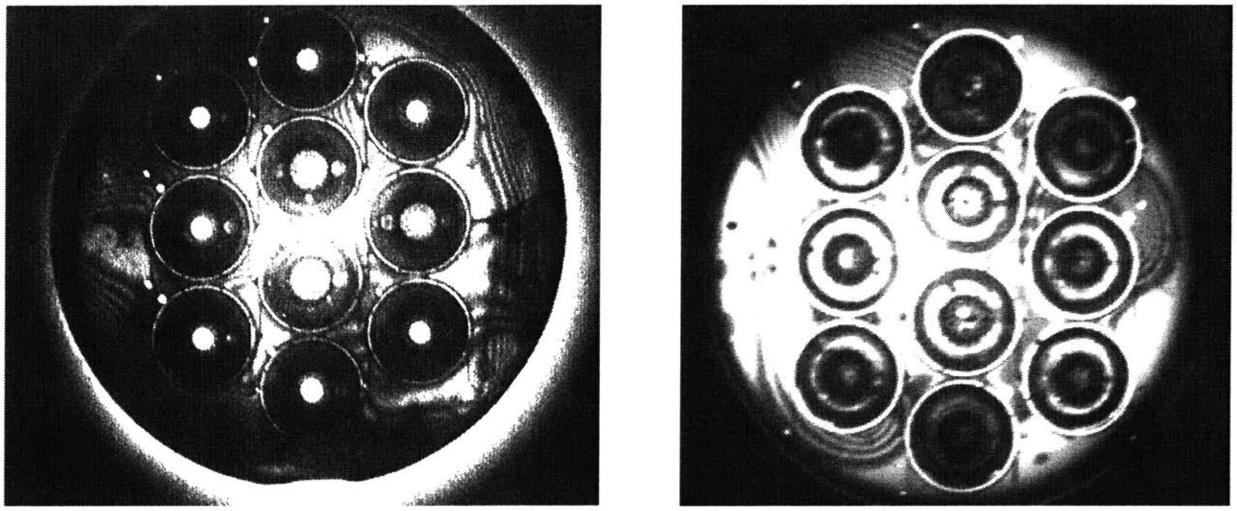

(a) Build 1 (fluorocarbon contamination).

(b) Build 2 (fluorocarbon contamination).

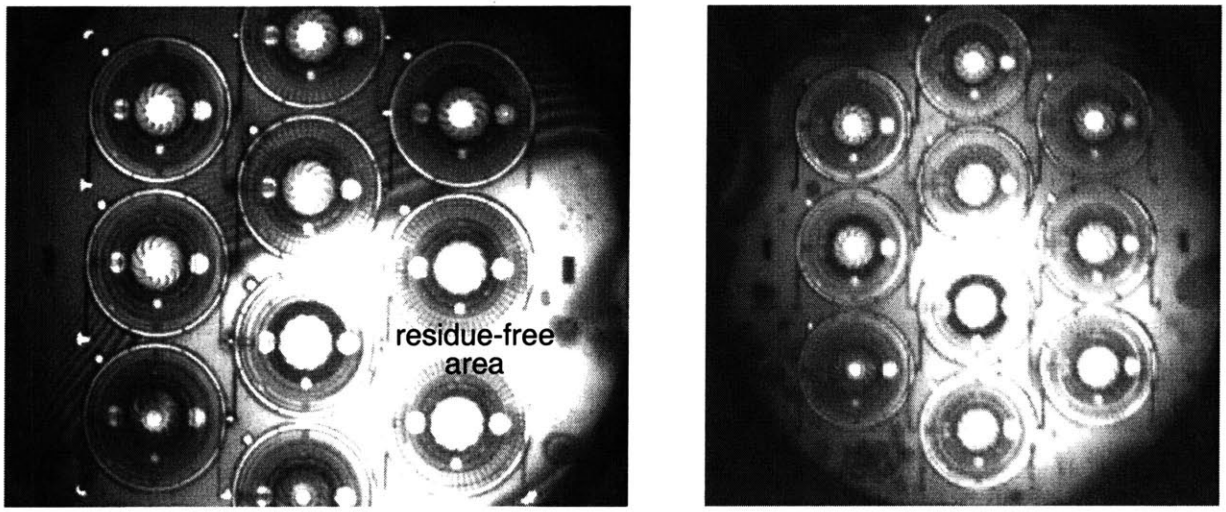

(c) Build 3 (piranah residue contamination).

(d) Build 4 (100% device yield).

Figure 4-18: Infra-red images of the bonded 6-wafer static structure.

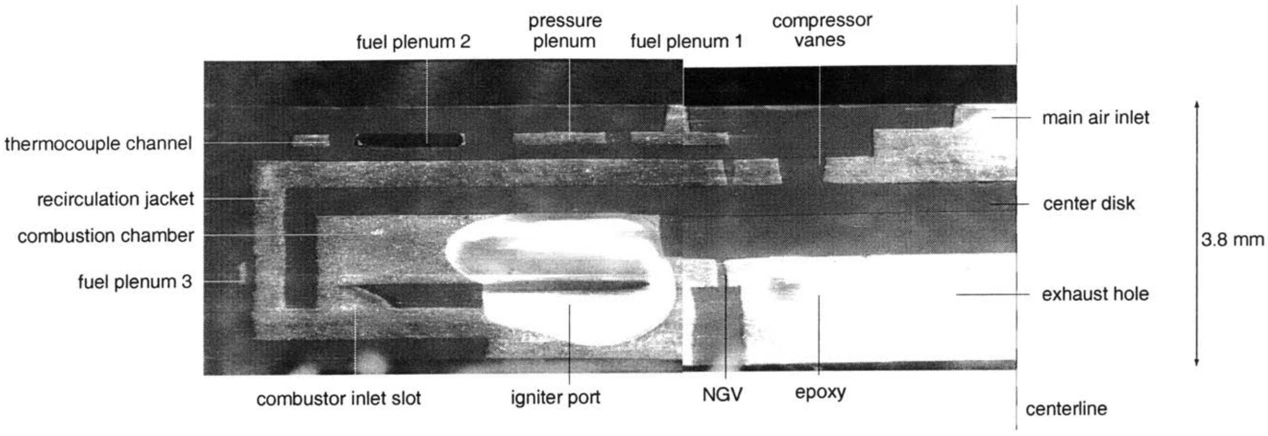

Figure 4-19: SEM cross-section of the fully-bonded static structure. (Note: For the purpose of this picture, the die was first potted in epoxy and then cross-sectioned. The cavities inside are therefore partially filled with epoxy.)

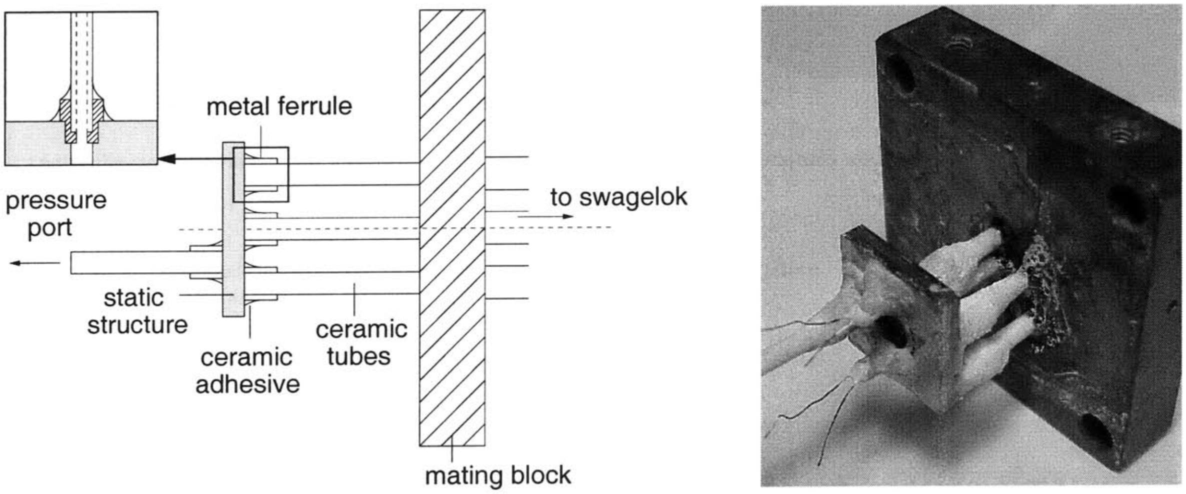

Figure 4-20: Images of the ceramic epoxy setups that were used for the initial testing of the static structure. The epoxy was found to unsuitable for pressure-sealing the combustor.

Swagelok connections. Figure 4-20 shows an illustration of these connections.

Preliminary flow testing of the device however showed that even though the ceramic adhesive survived at high temperatures, it was too porous to pressure-seal the combustor. Repeated attempts with a variety of different adhesives yielded similar results.

This methodology was therefore abandoned in favor of a glass bead interconnect scheme being developed by London, Harrison and Spearing [71], for similar applications in micro rocket engines. As illustrated in Figure 4-21, this glass bead interconnect was made by heating an annular-shaped glass-preform in a 1300K furnace in order to directly bond a kovar tube to the silicon surface.

Using this scheme, the first development device was intended to demonstrate multiple fluidic connections to the frontside only; the backside pressure and igniter ports were sealed-off with solid glass preforms. Figure 4-22 shows pictures of this device along with pictures of the invar mating block used to house the

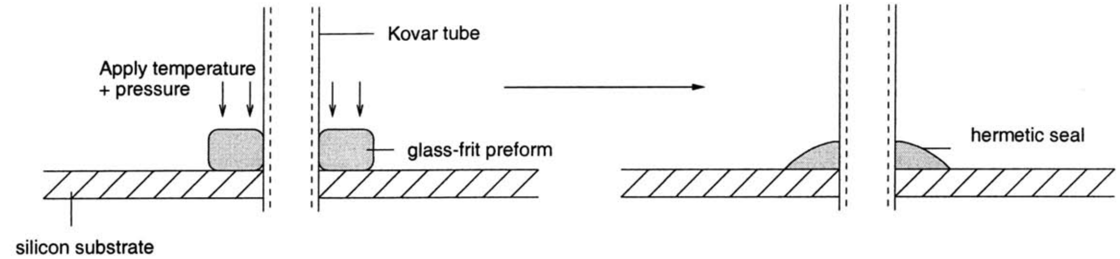

Figure 4-21: An illustration of the process used to make the glass bead interconnects to the static structure.

macro fluidic connections. High temperature epoxy was still used to attach the other end of the kovar tubes to the invar block; a copper heat shield was used to protect the epoxy from high temperature exposure.

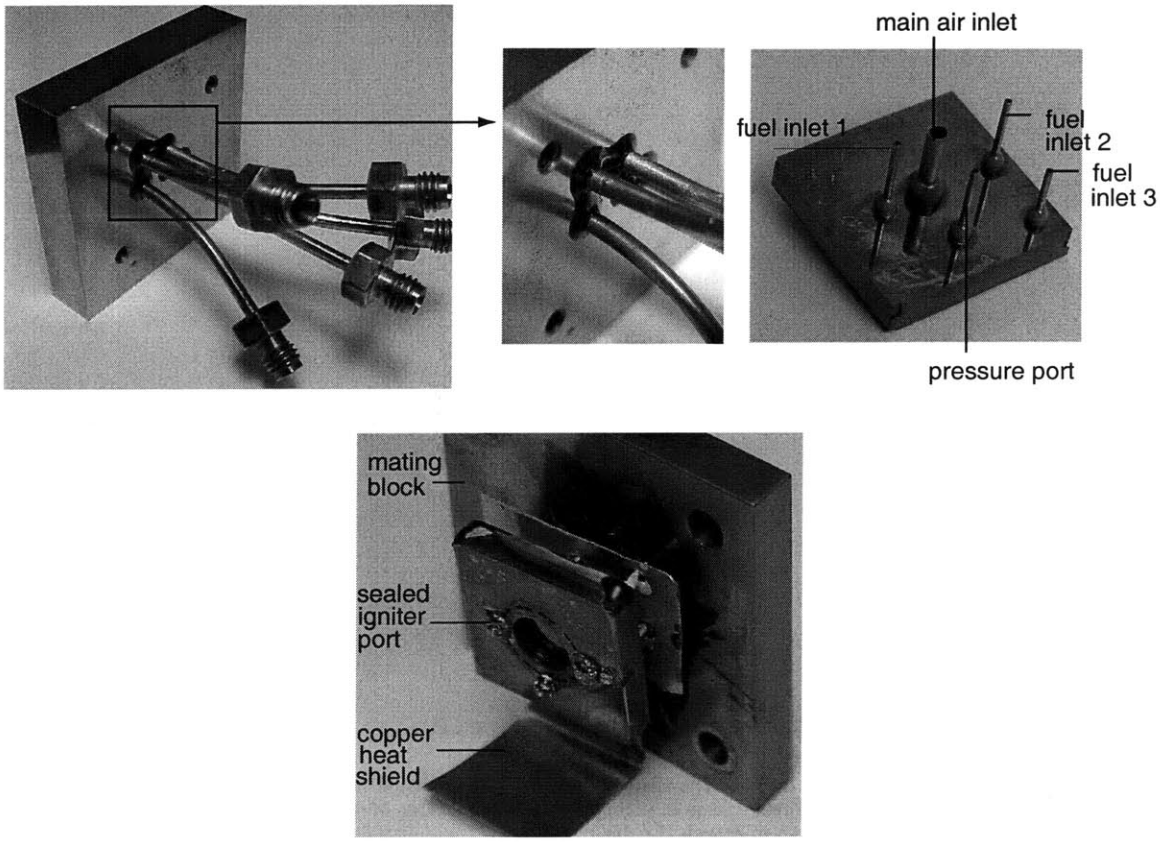

Figure 4-22: Images of the static structure test rig that incorporated the glass bead mechanical interconnects. (Note: High temperature epoxy was still used to connect the device to the mating block.)

Preliminary high temperature testing of this device at exit gas temperatures in excess of 1600K and outer wall temperatures of 800K showed no visible damage to the glass bead interconnects after several hours of operation[4]. Although this rig could not be pressurized because one of the interconnects fractured during assembly, it established the viability of using this interconnect scheme at high temperatures, and

---

[4] In the absence of igniters, the device was ignited by lighting the exhaust downstream of the NGV's. Sufficient reduction of the mass flow rate allowed the flame to travel upstream and stabilize inside the combustion chamber.

alleviated prior concerns about thermal mismatch of the silicon and glass at high temperatures.

The second development device was consequently packaged to build upon this success and demonstrate simultaneous backside interconnects. The copper heat shield was additionally replaced with a self-aligning carbon fixture; the kovar tubes were also directly brazed into the invar mating block. Figure 4-23 shows pictures of this device before and after assembly. (Note: The backside igniter ports were still sealed-off in this version with solid glass preforms.)

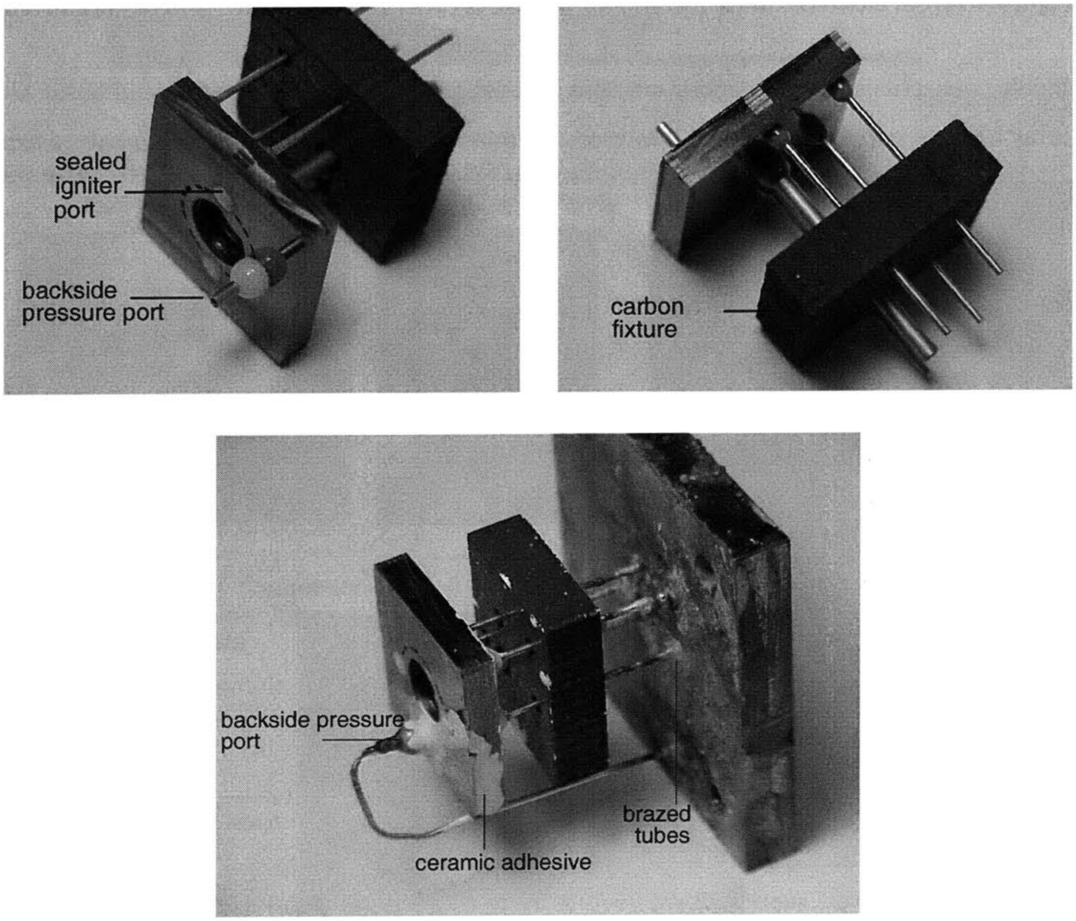

Figure 4-23: Images of the first build of the static structure with backside interconnects (Note: The brazing was done in-house, and resulted in cracking of the bottom edge of the die. High temperature epoxy was consequently used to re-attach the die.)

Unfortunately, excess heating of the glass beads during a brazing operation to the invar block resulted in a fracture of the silicon. This prevented the rig from being pressurized. For the next device, the in-house brazing operation with a micro-torch was therefore replaced by a one-step oven braze outsourced to the same vendor making the glass bead interconnects. Figure 4-24 shows a picture of one such device that was completely packaged by an external vendor, displaying working fluidic interconnects to the front and backside of the static structure and brazed connections to a mating invar block. The device was successfully pressurized and established the viability of using this packaging scheme for making fluidic interconnects to the microfabricated silicon structure. Detailed test results are presented in Section 4.6.

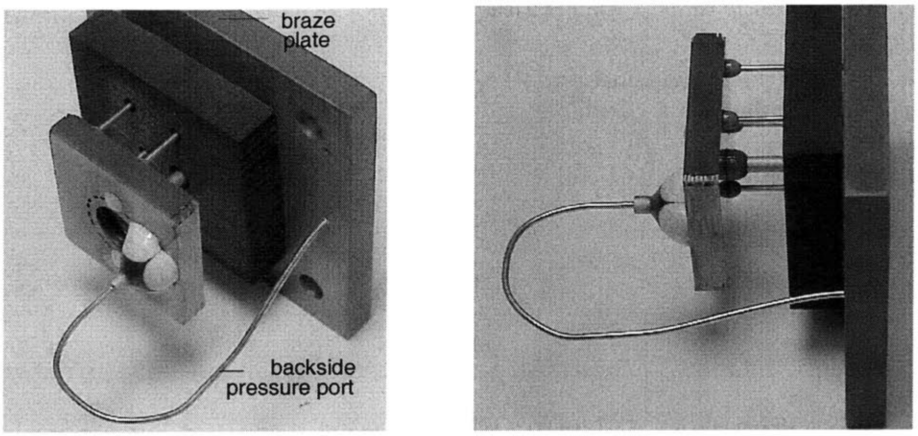

(a) Packaged static structure with one-step glass bead and brazed interconnects.

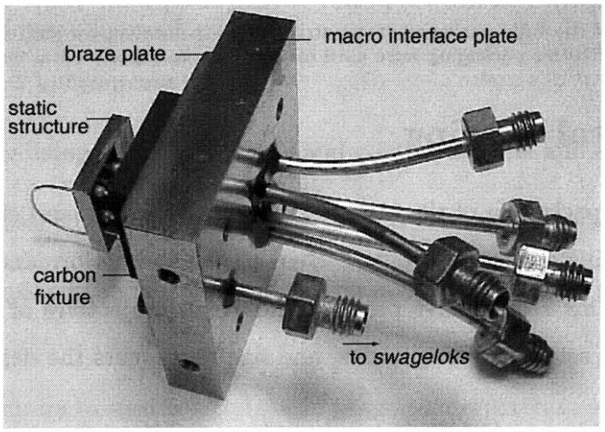

(b) Fully assembled test rig used the tests presented in Section 4.6.

Figure 4-24: Pictures of the third development device that was outsourced for one-step glass bead and brazed interconnects. This was the first device to be successfully pressurized.

4.5.2 Electrical Interconnects - Integrated Igniters

The last step in the packaging of the static structure involved the placement of integrated igniters inside the chamber. Using custom glass-to-metal feedthroughs to pot kovar wires in glass and pressure-seal them through the backside of the static structure, two types of igniters were initially considered for this purpose:

1. A resistively heated kovar wire such as that used in the 3-stack microcombustor, and
2. A feedthrough-type spark-igniter of the kind shown in Figure 4-25 (a).

Figure 4-25 (b) shows a picture of a fully-packaged static structure with fluidic interconnects and a backside igniter. The performance of these igniters will be evaluated in Section 4.6.4.

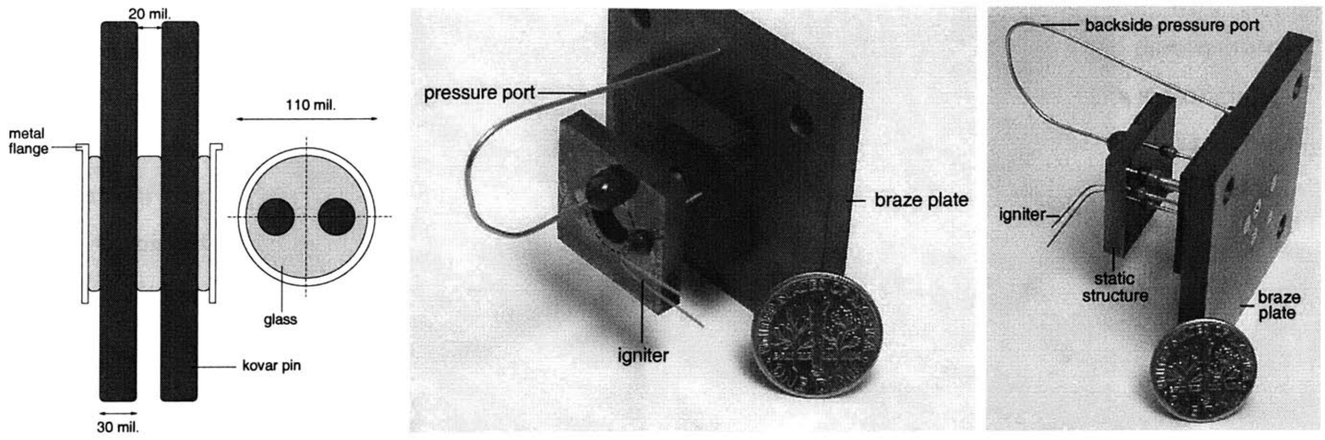

(a) A schematic illustration of the "spark-type" feedthrough igniter.

(b) Picture of the fully packaged static structure with fluidic and igniter interconnects. (Note: This version had a resistive igniter.)

Figure 4-25: Pictures of the fully-packaged static structure with mechanical and electrical igniter interconnects. Devices with this packaging were used for most of the experimental testing presented in Section 4.6.

4.6 Experimental Testing

Following the satisfactory packaging of the static structure with fluidic and electrical igniter interconnects, detailed experimental testing was carried out to characterize the performance of the device for hydrogen and hydrocarbon fuels. This section first presents the overall objectives of the experimental tests, then describes the experimental setup and diagnostics, and finally presents the detailed test results.

4.6.1 Experimental Objectives

Although the overall goal of the static structure was to develop a fully-packaged hydrogen-microcombustion system for the microengine, the experiments were intended to achieve the following specific objectives:

1. Baseline characterization of the hydrogen-fueled device to:
    (a) Evaluate the combustor performance using the exit and wall temperatures, pressure loss and combustor efficiency as primary figures of merit.
    (b) Measure non-premixed performance to identify the better of the three fuel injection schemes.
    (c) Compare the performance of the static structure with that of the 3-stack microcombustor to evaluate the effectiveness of the recirculation jacket, and to quantify the resulting increase in efficiency.
    (d) Evaluate the mechanical and structural integrity of the device.
    (e) Evaluate the performance of two different combustor inlet configurations with respect to flame holding and stabilization.

(f) Identify the combustion stability boundary for hydrogen in order to define the feasible operating space in the current design of the microengine.

2. Experimentation to explore the combustion stability boundaries for hydrocarbon fuels.

3. Comparison of the experimental measurements with numerical models to validate and assess the effectiveness of the design methodology, and to present overall implications for the design and operation of the microcombustor.

4.6.2 Experimental Apparatus and Diagnostics

Pictures of the fully-packaged experimental rig are shown in Figures 4-24 (b) and 4-25 (b). The braze plate attached to the kovar tubes was fastened to a larger invar plate that housed macro-fluidic connections, and sealed via individual o-ring fittings. The rig was fed by a total of four fluidic connections - one for the main air, and three for each of the individual fuel plenums.

During testing, the rig was instrumented with:

1. Mass flow controllers to independently measure and control the fuel and air flow rates.

2. Two type K, 10 mil sheathed wall thermocouples to measure the temperature of the outer walls.

3. One type K, 10 mil sheathed thermocouple downstream of the NGV's to measure the temperature of the exhaust gas.

4. Digital pressure transducers to measure the static pressure downstream of the compressor vanes and inside the combustion chamber. Analog Bourdon tube gauges were also used to measure the line pressure of the fuel and air supply.

4.6.3 Cold-Flow Tests

Mass Flow vs. Pressure Curves: Prior to combustion tests, the device was cold-flow tested to see if it could be sealed under pressure. These tests were also intended to validate the cold-flow CFD solutions used during the initial design the static structure.

Figure 4-26 (a) plots the chamber total pressure as a function of mass flow and compares it with the intended design curve for the static structure. The analytical design curve is based on an idealized 1-D model that uses the design throat area of the NGV's to calculate the pressure-mass flow relation of the static structure under cold-flow conditions:

$$\begin{aligned} P_t &= P_{atm}(1 + \frac{\gamma - 1}{2} M^2)^{\gamma/(\gamma-1)} \quad \text{for the unchoked regime,} \\ \dot{m} &= \frac{A_{throat} P_t}{\sqrt{T_t}} \sqrt{\frac{\gamma}{R}} \frac{1}{(1 + \frac{(\gamma-1)}{2})^{\frac{\gamma+1}{2(\gamma-1)}}} \quad \text{for the choked regime.} \end{aligned} \tag{4.3}$$

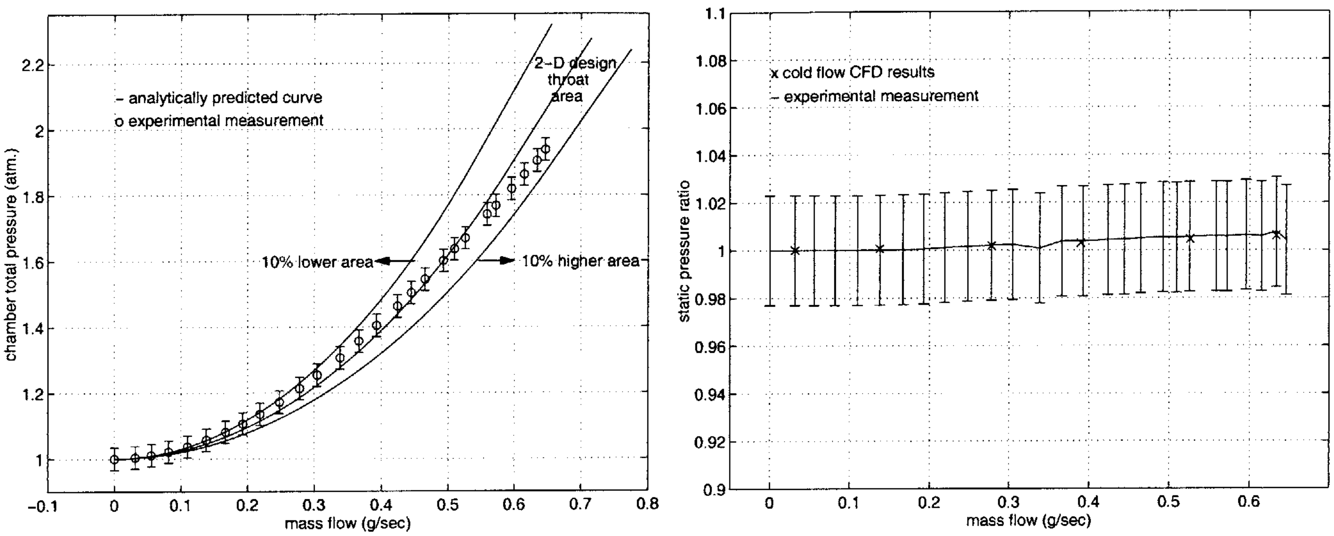

(a) Total pressure measurement.

(b) Static pressure ratio.

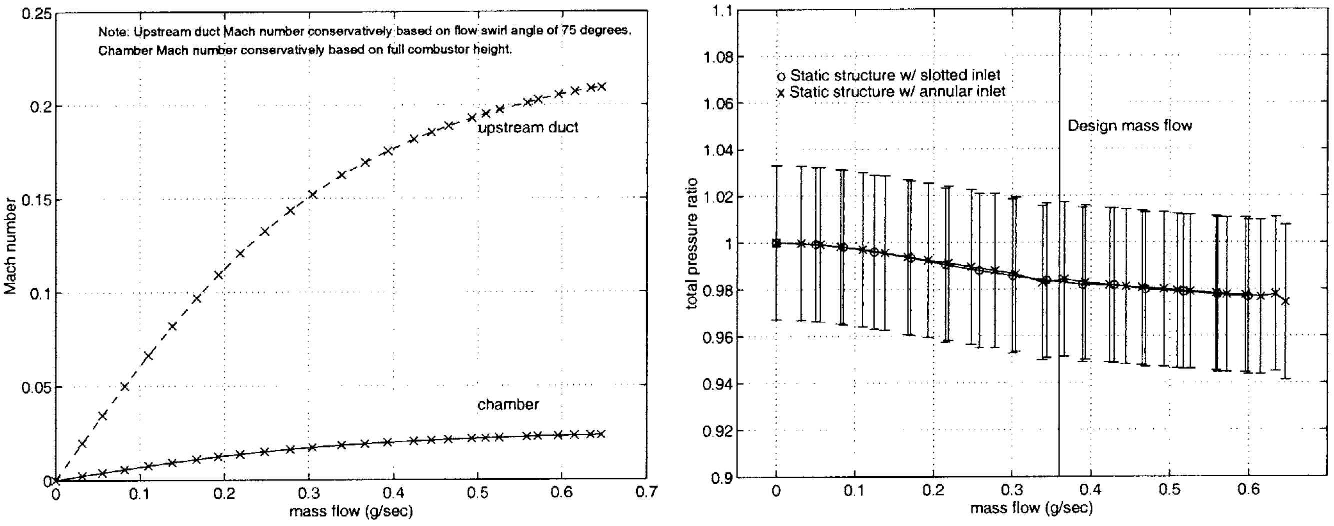

(c) Mach number at the pressure ports.

(d) Total pressure ratio across the chamber.

Figure 4-26: Cold-flow test results for the static structure.

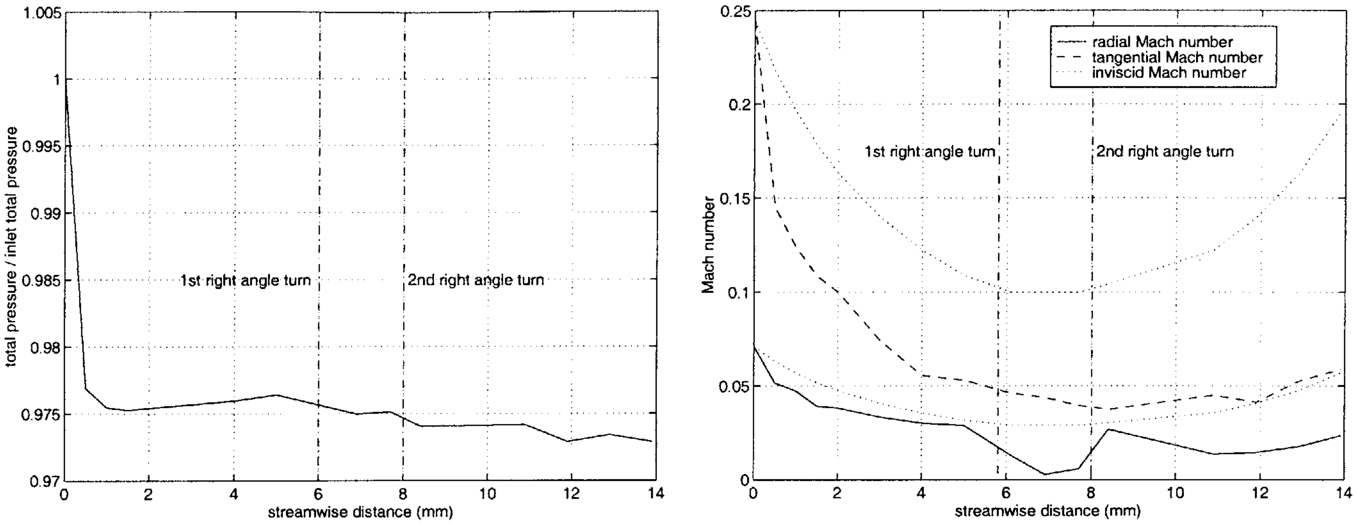

(a) Average total pressure ratio along the static structure flow path, showing an immediate drop downstream of the inlet.

(b) Radial and tangential Mach numbers along the static structure flow path, showing rapid dissipation of the inlet dynamic swirl. (Note: The dotted line shows the inviscid Mach numbers assuming continuity and conservation of angular momentum.)

Figure 4-27: 2-D axisymmetric cold-flow CFD results showing a rapid drop in the total pressure ratio due to dissipation of the inlet dynamic swirl.

The figure shows good agreement between the experimental and analytically predicted values suggesting that the NGV's are performing as designed. The static pressure ratio as plotted in Figure 4-26 (b) also compares well with CFD results, details of which are provided in Chapter six.

Cold-Flow Total Pressure Loss: Based on an estimate of the Mach numbers, the static pressure ratio plotted in Figure 4-26 (b) was subsequently used to estimate the total pressure loss across the chamber under cold-flow conditions.

Figure 4-26 (c) plots the estimated Mach number at the two pressure port locations. As designed, the cold-flow pressure loss at the design operating mass flow is less than 2% percent, and increases with increasing mass flow (and hence Mach number). These experimental measurements are compared with the predicted CFD results in Chapter six; the combustor pressure loss at high temperatures is presented in Section 4.6.4. (Note: The combustor inlet area for the slotted and annular inlets was within 10% of each other. The maximum Mach number through the inlet during the cold-flow tests was expected to be approximately 0.05. As shown in Figure 4-26 (d), the total pressure loss through the two devices can therefore be expected to be comparable.)

In order to identify the dominant sources of pressure loss, axisymmetric 2-D cold-flow CFD solutions were generated at the design mass flow rate of microengine. Figure 4-27 (a) plots the average total pressure ratio along the flow path of the static structure, and shows an immediate drop downstream of the inlet. A closer examination of the radial and tangential Mach numbers along the flow path shown in Figure 4-27 (b)

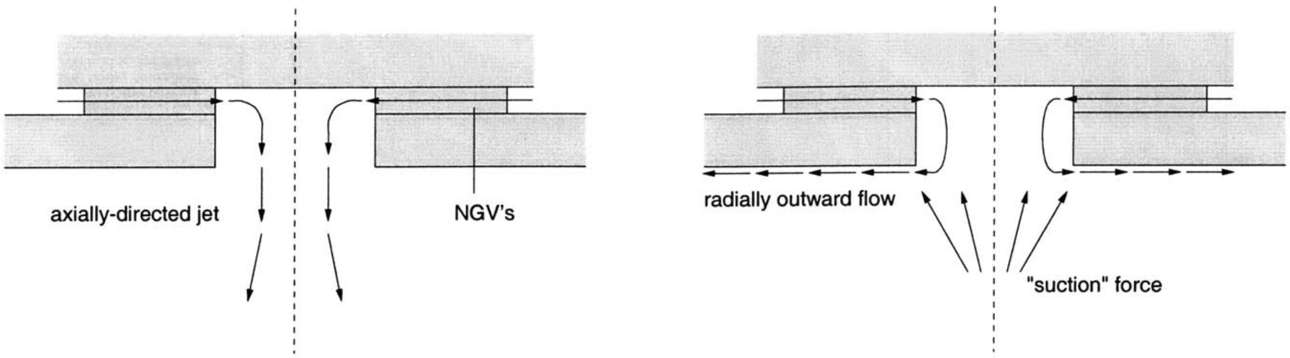

(a) The flow did not exit as an axially directed jet at the exit of the combustor.

(b) Instead, it attached itself to the outer wall of the device and flowed radially outwards creating a "suction" force at the exit of the device.

Figure 4-28: A schematic illustration of the wrap-around effect that occurred due to the high swirl at the exit of the combustor.

shows that this pressure drop results from a viscous dissipation of the inlet dynamic swirl. Most of the total pressure loss in the static structure is therefore attributed to the loss of the inlet tangential head; Table 4.4 tabulates the different sources of pressure loss as calculated from the cold-flow CFD solution. (The cold-flow pressure ratio of the device in the absence of inlet swirl is approximately 0.4%.)

Source	**% loss**
Inlet $q_{tangential}$	2.3%
Inlet q_{radial}	0.2%
Pressure drop	0.2%
TOTAL	2.7%

Table 4.4: Sources of cold-flow total pressure loss in the static structure. (Note: The total pressure ratio from the CFD was referenced from the inlet boundary to the computational domain; the experimental measurements were referenced from the pressure port located downstream of the inlet. The difference in the pressure loss from the two cases therefore results from the change in flow Mach number between the inlet and the pressure port location.)

Exhaust Flow Characteristics: Preliminary cold-flow testing of the rig also revealed additional flow phenomenon that mandated more investigation. Instead of coming out as an axially directed jet at the exit of the combustor, the flow wrapped around the exit and flowed radially outwards along the aft wall of the device. It also created a suction force axially downstream of exit; Figure 4-28 shows a schematic illustration of this effect.

The tendency of the flow to make a 180° turn and attach itself to the outer wall of the device can be explained by the high swirl velocity at the exit of the NGV's. The NGV's were designed with an exit flow angle of 81°, consequently, the flow had a high swirl component at the exit of the device. As illustrated in Figure 4-29, this caused the flow to be centrifuged outwards and flow radially along the back wall of the

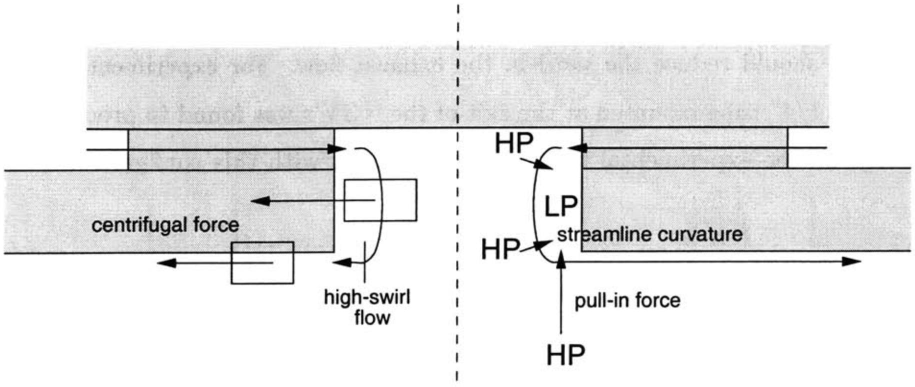

Figure 4-29: An illustrative explanation of the wrap-around effect that occurred due to the high swirl at the exit of the combustor.

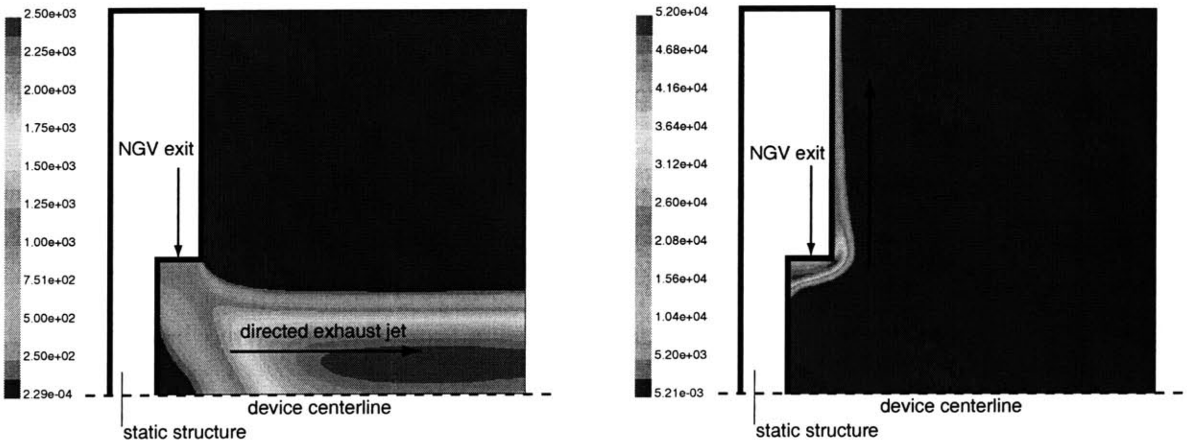

(a) Contours of dynamic pressure for the no-swirl case showing an axially directed jet at the exit of the static structure.

(b) Contours of dynamic pressure for the case with swirl at the exit of the NGV's, showing radially directed flow along the back wall of the static structure.

Figure 4-30: CFD solutions showing the change in the exit flow behavior of the static structure upon addition of swirl at the exit of the NGV's.

device. (Alternatively stated, the high swirl velocity at the exit of the NGV's created a low pressure region along the edge of the circular exhaust that made the streamlines curve 180°.) The low pressure region resulting from the high swirl velocity immediately downstream of the NGV's also explains the suction force experienced near the exhaust.

To confirm this effect, a CFD solution was generated for the exit configuration with and without swirl. Figure 4-30 (a) shows the contours of dynamic pressure for the no-swirl case, showing the axially directed jet that would normally be expected at the exit of the combustor. Figure 4-30 (b) shows the dynamic pressure contours for the same configuration with 80° of swirl, showing the flow making a 180° turn to attach to the outer wall of the device and flow radially outwards along the back wall.

The absence of an axially directed jet at the exit of the device could be a source of concern because of the potential loss of thrust. This is not expected to be a problem in the final engine configuration because the rotating turbine should reduce the swirl in the exhaust flow. For experimental testing of the static structure however, a 1/4" tube mounted at the exit of the NGV's was found to produce an axially directed jet. Consequently, all the experimental tests were carried out with this configuration, and are presented here on.

4.6.4 Baseline Device Characterization (Hydrogen Tests)

Evaluation of the Igniter Performance

Spark Igniters: The feedthrough igniters were found to be unsuitable for initiating combustion inside the static structure.

Preliminary experimental testing showed onset of a corona discharge at voltages much lower than the breakdown voltage for the design separation. This suggested that the feedthrough was sparking to the adjacent silicon, not between the two pins. Thus, even though the igniters generated a spark inside the chamber, it was too small to initiate combustion.

This behavior resulted from the difficulty in controlling the axial location of the pins inside the chamber. Since the glass preform tended to soften during the high temperature packaging step, the pins of the feedthrough shifted, making axial control of their location a difficult proposition.

The feedthrough spark igniters were therefore abandoned in favor of the resistively heated igniters.

The Resistive Igniters: were found to perform quite satisfactorily. They were able to initiate combustion reliably, and survived multiple ignition cycles. They also survived the hot combustion environment throughout the entire duration of testing, and were therefore deemed to be satisfactory for incorporation into future microengine packages.

Hydrogen Tests in the Annular Inlet Combustor Geometry

This section presents the baseline characterization of premixed hydrogen combustion in the annular-inlet combustor. Figure 4-31 plots the measured exit gas temperature, combustor efficiency, operating pressure and outer wall temperature as a function of the mass flow for different equivalence ratios. The following observations are noteworthy:

1. The break in the ϕ=0.5, 0.6 curves results from an inability to measure exit gas temperatures in excess of ~1600K. Experimental testing in this range was however continued.
2. The ϕ=0.7 curve stops at a mass flow of 0.015 gm/sec because of upstream burning in the recirculation jacket. This shall be examined in more detail in a later section.
3. The combustor produces an exit gas temperature of 1600K at a mass flow of 0.11 gm/sec, an operating pressure of 1.13 atm., and a combustor efficiency in excess of 80%. This demonstrates the satisfactory

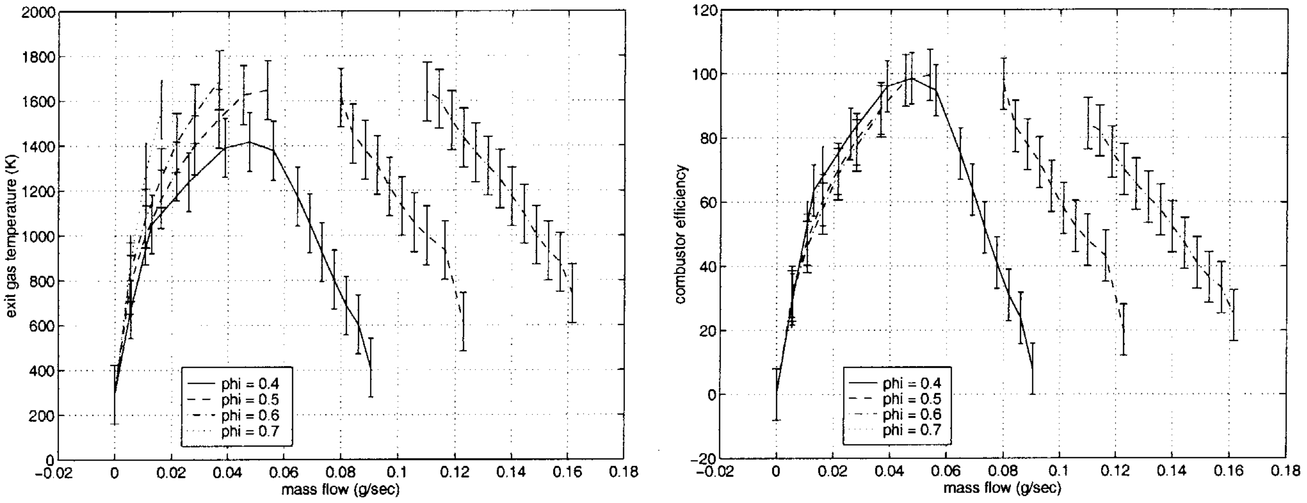

(a) Exit gas temperature measurements.

(b) Combustor efficiency.

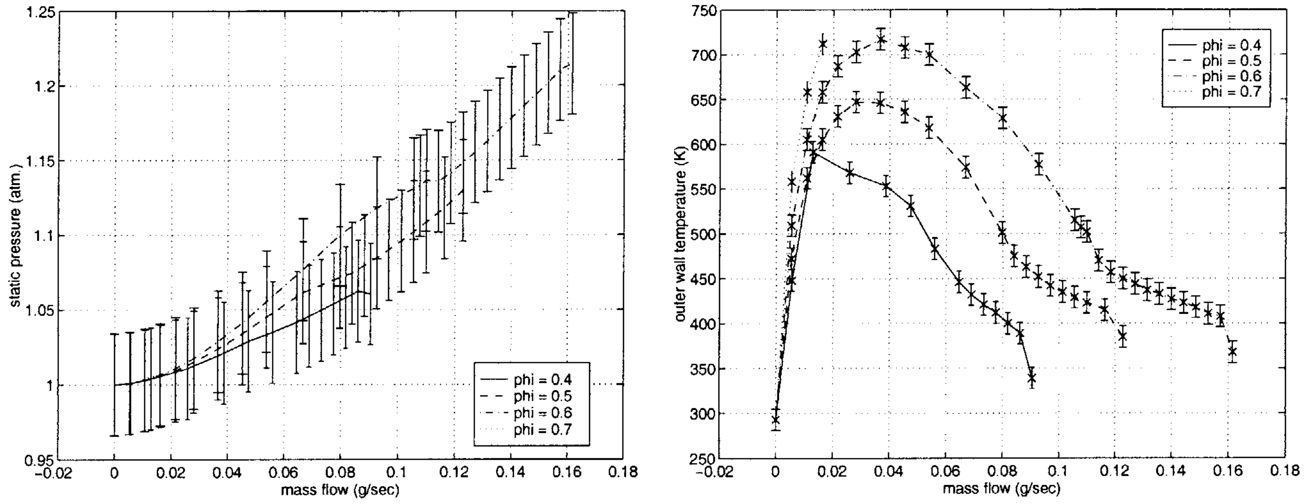

(c) Chamber operating pressure.

(d) Outer wall temperature measurements.

Figure 4-31: Baseline performance characterization of the annular-inlet combustor

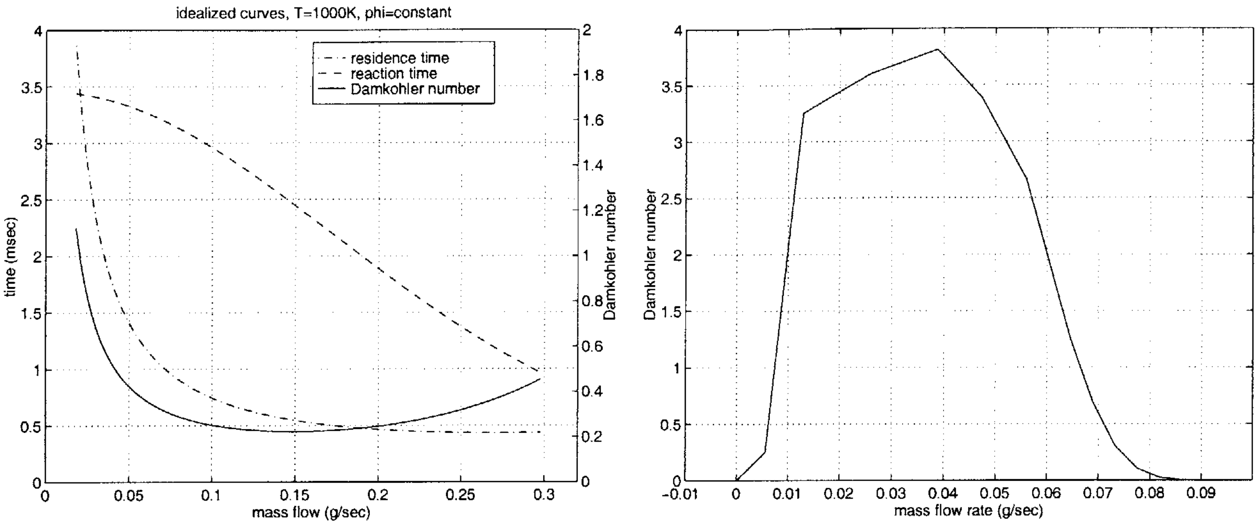

(a) Idealized τ_{res}, τ_{chem} and Da as a function of mass flow for T=1000K.

(b) Da along the experimentally measured ϕ=0.4 curve.

Figure 4-32: Estimates of τ_{res}, τ_{chem} and Da along a constant equivalence ratio curve.

operation of the static structure within microengine system constraints at 80% of the scaled design mass flow[5].

The inability of the device to reach design point operation at 0.36 gm/sec and 3 atm., and the general shape of the exit temperature and efficiency curves can be explained by an examination of the changes in residence and reaction times along a constant equivalence ratio curve.

Neglecting heat loss, and assuming constant gas temperature along a fixed equivalence ratio curve, the *average* flow residence time for different mass flows can be estimated using:

$$\tau_{res} = \frac{PV}{\dot{m}RT} \tag{4.4}$$

Using this equation with Eq. 4.3 for a mass flow-pressure relation, the residence time along a constant equivalence ratio curve is plotted in Figure 4-32 (a) for increasing mass flow. (Note: This model uses average values of temperature, pressure and volume to estimate the residence time in the chamber. The validity of these assumptions is discussed in Appendix E.)

Figure 4-32 (a) shows that as long as the NGV's are unchoked, mass flow increases faster than pressure, hence, residence time decreases monotonically. Once the device is choked, residence time remains constant because pressure and mass flow increase linearly from thereon.

---

[5] Since design mass flow rate of the static structure is 0.36 gm/sec at an operating pressure of 3 atm, the pressure-scaled design mass flow required to maintain the same flow residence time in the chamber at 1.13 atm. is 0.136 gm/sec. A mass flow rate of 0.11 gm/sec therefore represents operation at 80% of the *scaled* design mass flow rate.

The chemical reaction times along this curve may also be estimated by using a simple one-step mechanism for hydrogen [20] & [21]:

$$\tau_{chem} = \frac{[H_2]_{t=0}}{A\ exp(-E_a/RT)[H_2]^2[O_2]} \tag{4.5}$$

where A and E_a are empirically determined as 1.58×10^{17} $(\text{cm}^3/\text{mole})^2\cdot\text{sec}$ and 15.2 kcal/mole, respectively.

As plotted in Figure 4-32 (a), the resulting chemical reaction time along a constant temperature line shows a decrease due to increasing pressure, however the decrease in reaction time is not as fast as that in residence time.

Combining the two times to estimate the Damkohler number along a constant equivalence ratio curve therefore shows a decrease in the Damkohler number in the unchoked regime. Once the device is choked, the residence time remains constant, however the reaction time continues to decrease - this causes the Damkohler number to increase from thereon.

Using this simple analytical model, the general shape of the exit temperature curves in Figure 4-31 (a) may therefore be explained by the following hypothesis:

1. At very low mass flow rates, the device loses a large fraction of the heat being generated, hence, the exit temperature and efficiency is low. Figure 4-33 (a) plots the fuel power as a function of the mass flow rate for a constant equivalence ratio of 0.4. It also plots the enthalpy rise of the exit gas stream, along with estimates for the heat transfer from the device using a 1-D heat transfer model.

   The resulting chemical, thermal and overall combustor efficiency is plotted in Figure 4-33 (b) as a function of the mass flow rate along the ϕ=0.4 curve. The figure shows that for low mass flow rates, a relatively large fraction of the heat being generated is lost to the ambient, hence the thermal efficiency is low. *The efficiency along the left-hand side of the curves in Figure 4-31 is therefore limited by the thermal efficiency of the combustor.*

2. As the mass flow rate is increased, a greater fraction of the heat of combustion is transferred to the gas stream, hence, the exit temperature and combustor efficiency increase. This is corroborated by the fact that the thermal efficiency begins to asymptote towards unity at higher mass flows.

3. Continued increase in the mass flow however causes a decrease in the Damkohler number since the device is still unchoked. Because there is less time available for combustion, the exit temperature and efficiency therefore begin to go down until the reaction is ultimately blown out of the chamber. *The right hand side of the curve is therefore limited by the chemical efficiency of the combustor.*

Operating Line Considerations - Results for an Externally Throttled Combustor

Faced with the dilemma of not being able to reach design point operation at 0.36 gm/sec and 3 atm. because of a decrease in Damkohler number prior to choking, one has the following options:

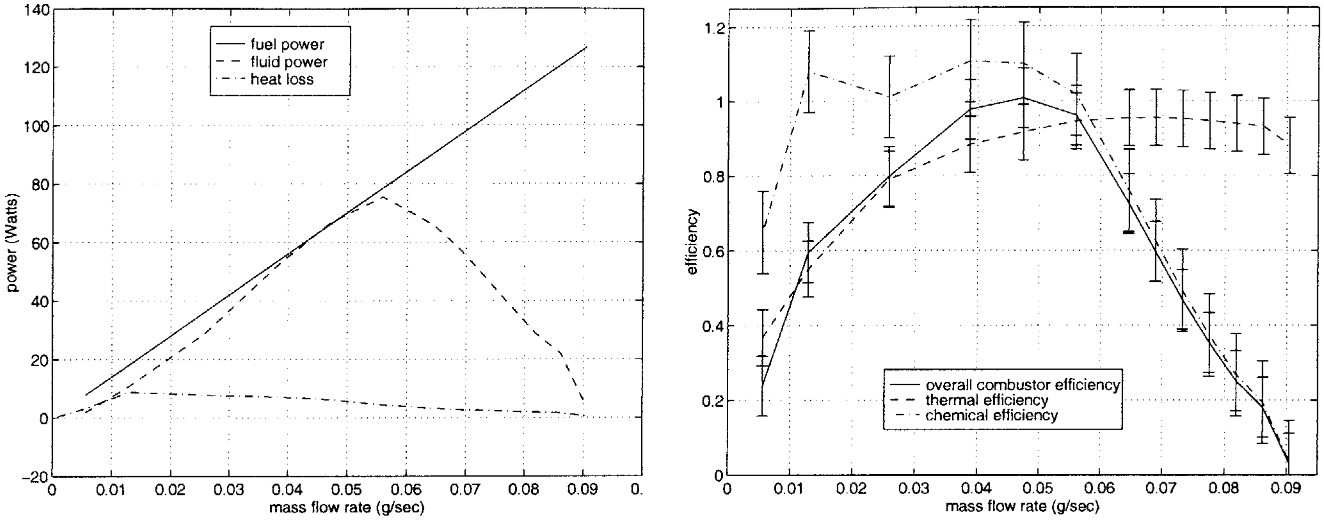

(a) Fuel power, fluid power, and heat loss along the ϕ=0.4 curve.

(b) Chemical efficiency, thermal efficiency, and overall combustor efficiency along the ϕ=0.4 curve.

Figure 4-33: Results of a 1-D heat transfer model showing the left hand side of the curve being limited by thermal efficiency, and the right hand side being limited by chemical efficiency.

1. Increase the size of the chamber so that it can sustain combustion at the minimum Da.
2. Increase equivalence ratio while increasing mass flow so that $\tau_{reaction}$ decreases faster than τ_{res}.
3. Independently increase the operating pressure of the chamber to augment the reaction rates.

The first of these options is infeasible because it would require a redesign and rebuild of the device. The second option runs into structural limitations that prevent operation at equivalence ratios above 0.7.

The third option was however practically realized by using an external throttle to increase the operating pressure in the chamber. Figure 4-34 shows cold-flow curves for a device that was fitted with an exhaust tube to reduce the effective throat area downstream of the NGV's. It also shows the estimated Damkohler number for the ϕ=0.5 curve as a function of mass flow, and compares it with the same for the original unthrottled die. As shown in the figure, increasing the operating pressure in the chamber increased the reaction rates and extended the operating range by ~25% at ϕ=0.5. The detailed combustion results for different equivalence ratios are shown in Figure 4-34 (c) & (d); the following considerations are noteworthy:

1. Even though the external throttle extended the stable operating range of the combustor, it was insufficient to reach design point.
2. Because the external throttle reduced the height of the exit passage to 4 mil., it was difficult to position an exit gas thermocouple immediately downstream of the NGV's. During tests, the exit gas temperature was measured by inserting an unsheathed thermocouple in the exhaust tube, and may therefore have been influenced by reactions inside the tube.

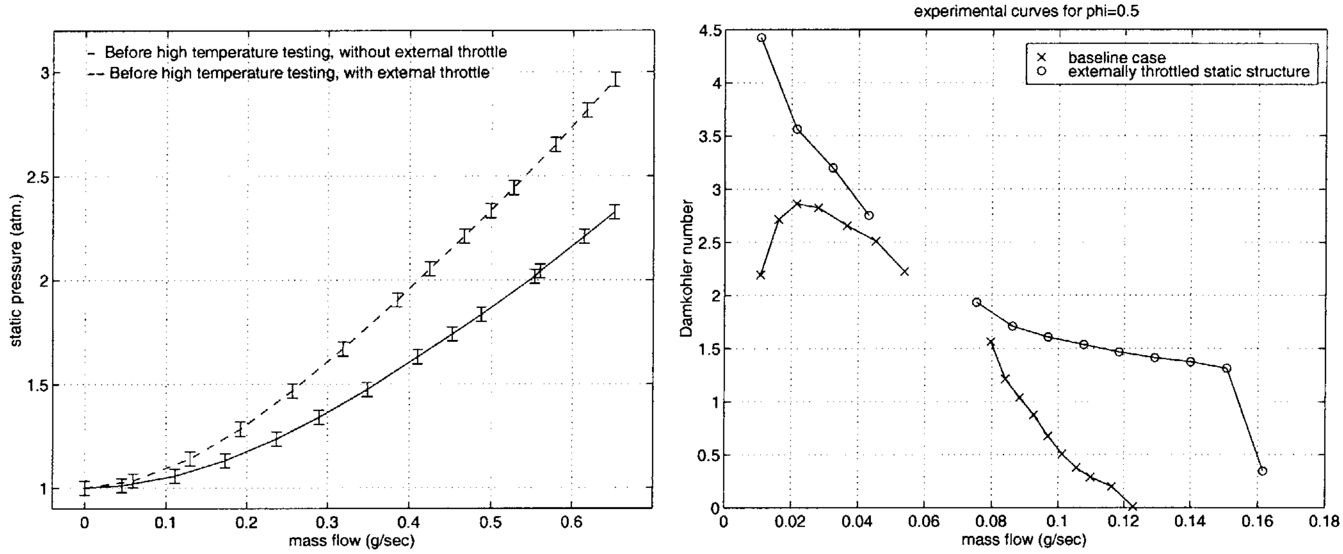

(a) Cold-flow curves.

(b) Damkohler number along the ϕ=0.5 curve.

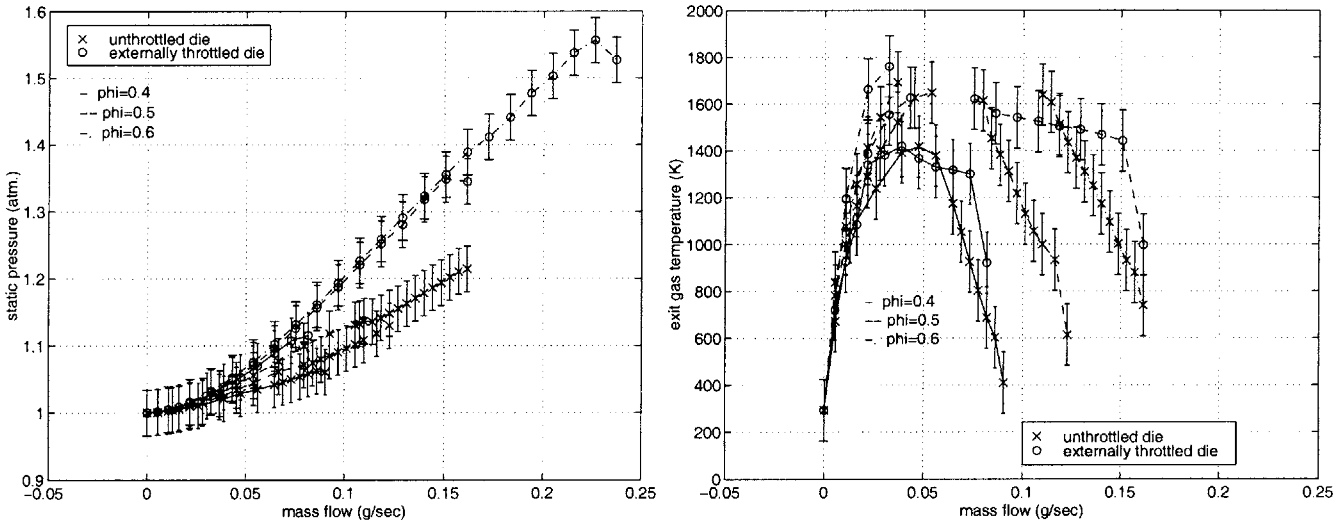

(c) Operating pressure.

(d) Exit gas temperature.

Figure 4-34: Results for the externally throttled combustor.

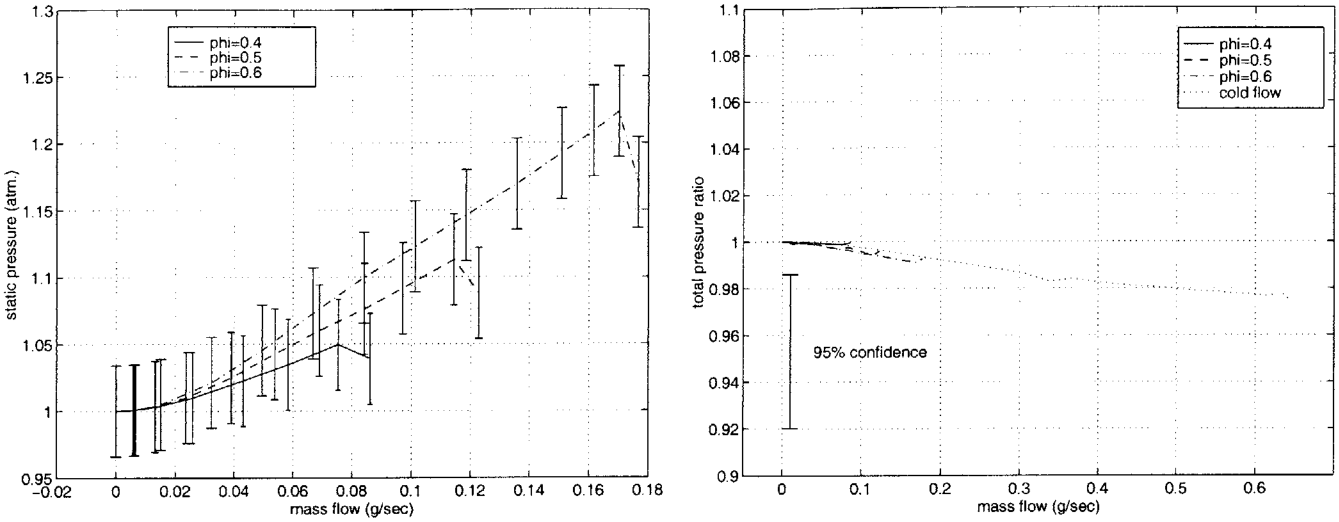

(a) Chamber operating pressure.

(b) Total pressure ratio.

Figure 4-35: Hot-flow total pressure measurements in the static structure.

As currently designed, the static structure was therefore successfully operated up to 64% of the design mass flow of 0.36 gm/sec, and at 52% of the design operating pressure of 3 atm. Operation at higher mass flows and pressure would either require a redesign of the rig, or better designs for a variable throttle to independently control the mass flow and pressure in the device. Recommendations for these changed are presented in Chapter six and seven.

Hot-Flow Total Pressure Loss

Since combustor pressure loss is an important consideration for closing the microengine thermodynamic cycle, the static structure was also intended to measure the "hot-flow" pressure ratio across the combustor.

Although the device could not be operated at design pressure, static pressure measurements were taken at low mass flow operating points. Figure 4-35 (a) plots the chamber operating pressure as a function of the mass flow for different equivalence ratios; the total pressure ratio as derived from estimates of the flow Mach number at the two pressure port locations is plotted in Figure 4-35 (b).

The results showed that the hot-flow total pressure loss was approximately 50% higher than the cold-flow pressure loss for the low mass flow operating points at which the measurements were taken. In the absence of measurements at higher mass flows, an extrapolation of the this trend suggests that the combustor pressure loss at design conditions can be expected to be approximately 3%.

This agrees with analytical predictions for the pressure loss due to heat addition. Applying:

$$\frac{dP_t}{P_t} = -\frac{\gamma M^2}{2}\frac{dT_t}{T_t}, \qquad (4.6)$$

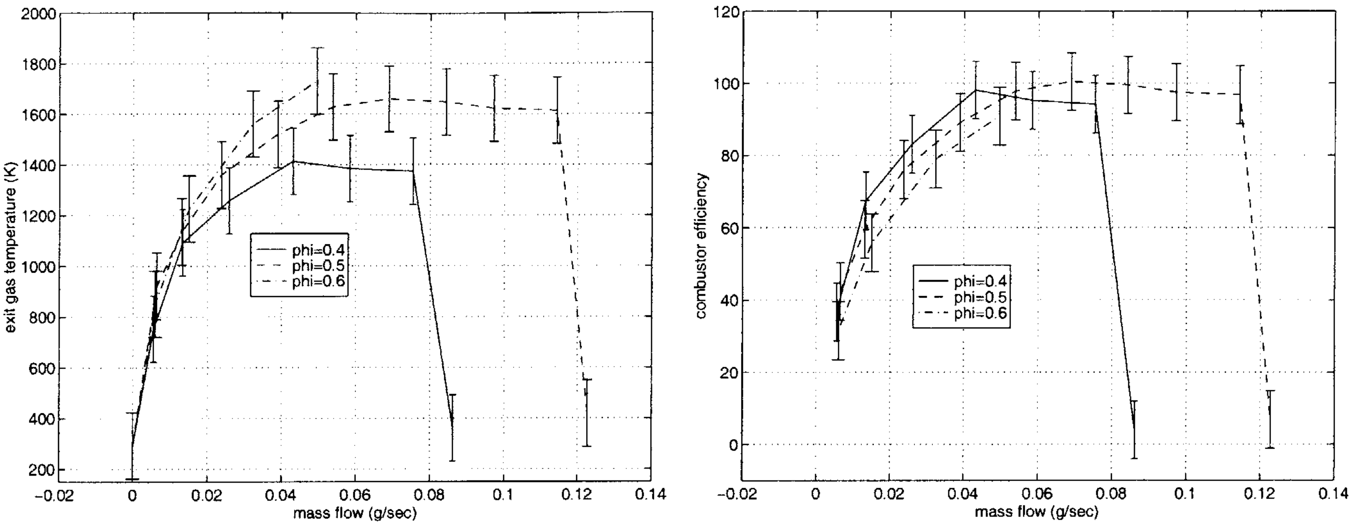

(a) Exit gas temperature measurements.

(b) Combustor efficiency.

Figure 4-36: Baseline performance characterization of the slotted-inlet combustor

and assuming an average Mach number of 0.1 in the chamber, and a temperature rise of 1000K over 500K, the predicted pressure drop due to heat addition is approximately 1.2% at design conditions. Combined with the 2% cold-flow pressure loss at design conditions, this results in an expected hot-flow total pressure ratio of approximately 0.97. (In the absence of inlet swirl, the hot-flow Π_b is expected to be approximately 0.99.)

Hydrogen Tests in the Slotted Inlet Combustor Geometry

Combustion test results for the slotted-inlet geometry are plotted in Figure 4-36. The results show similar performance as that for the annular-inlet combustor, however, the slotted-inlet combustor produces higher exit temperatures and efficiencies in the kinetically limited operating regime of the combustor. This is attributed to the presence of multiple recirculation zones at the inlet of the chamber that facilitate uniform and rapid ignition of the incoming reactants.

The implications of these results shall be discussed in greater detail in Chapter six.

Overall Device Improvement - Static Structure versus 3-Stack Microcombustor

In order to compare the performance of the static structure with that of the 3-stack microcombustor, premixed hydrogen-air combustion tests were carried out in the static structure at the atmospheric design mass flow rate of the 3-stack microcombustor ($\dot{m}_a$=0.045 gm/sec). Although it might be argued that such a test is not a fair comparison because the static structure is not being operated at its design mass flow rate, a comparison of the two devices under back-to-back test conditions would allow a quantification of the aggregate performance increase resulting from:

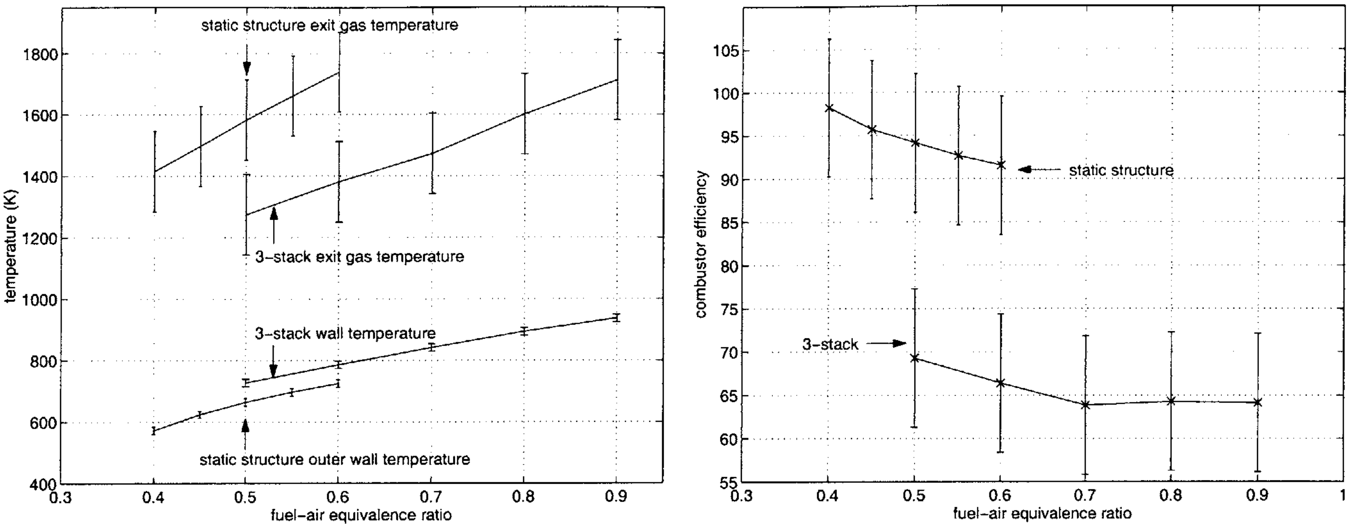

(a) Exit and wall temperature measurements.

(b) Efficiency calculations showing an improvement in the efficiency of the static structure.

Figure 4-37: Exit and wall temperature, and efficiency for the two devices, showing a ~20% increase in efficiency of the static structure.

1. The recirculation jacket in the static structure,
2. The larger combustion chamber, and
3. Improved packaging of the device.

Figure 4-37 (a) compares the experimentally measured exit and wall temperatures for the two devices under similar operating conditions, and shows an increase in static structure exit gas temperature for similar equivalence ratios. This suggests that the static structure is capable of attaining the desired 1600K turbine inlet temperature at a lower equivalence ratio - the resulting increase in efficiency is shown in Figure 4-37 (b).

Overall, improvements in the static structure increased the combustor efficiency by approximately 20%. The outer wall temperatures were also lower by approximately 100K, making packaging of the device somewhat easier than that of the 3-stack.

Evaluation of the Three Fuel Injection Schemes

The performance of the three fuel injectors was evaluated by comparing exit gas temperature and efficiency measurements to those from the premixed case. Figure 4-38 plots these measurements for different equivalence ratios at operating conditions corresponding to approximately 40% of the atmospherically scaled design mass flow (0.045 gm/sec).

The figures show a 5-point drop in efficiency for axial injection through the first set of injectors located at a radius of 4.8 mm. Injection through the second set located at a radius of 8 mm shows a further drop

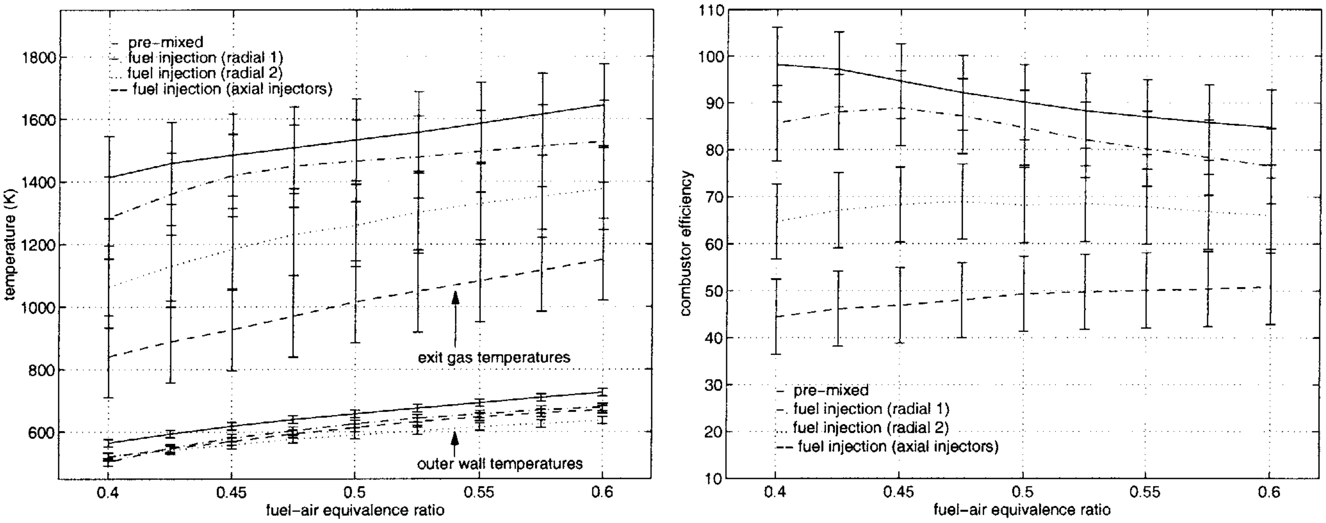

(a) Exit and wall temperature measurements.

(b) Combustor efficiency measurements.

Figure 4-38: A comparison of the fuel injector performance at low mass flows.

	As designed	As operated
$\rho_a U_a^2/\rho_f U_f^2$ (inj 1.)	4.55	21.2
Streamwise penetration length (inj 1.)	1.45 mm	6.7 mm
$\rho_a U_a^2/\rho_f U_f^2$ (inj 2.)	4.61	18.4
Streamwise penetration length (inj 2.)	1.67 mm	6.67 mm

Table 4.5: Expected performance of the fuel injectors as designed and as operated.

of 15-20 points. Finally, radial injection through the side injectors located at the base of the recirculation jacket results in efficiencies as low as 40-50%.

One possible explanation for the poor performance of the fuel injectors may lie in the off-design operation of the injectors[6]. Table 4.5 shows the ratio of the fuel and air momentum fluxes for the two radial injectors at design point, and compares it with those at the operating conditions shown in Figure 4-38. The table also lists the expected streamwise mixing length needed for complete penetration of the fuel jet into the recirculation jacket as calculated by the simple design model described in Section 4.3.2.

The results in Table 4.5 indicate a five-fold increase in the streamwise mixing length needed for axial injection through the first set of radial injectors. Since these injectors are located immediately downstream of the compressor stator blades, there is approximately 6 mm of streamwise length available for fuel-air mixing in the recirculation jacket - this is approximately 90% of the length needed for complete fuel-air mixing. As shown in Figure 4.5, the performance with injection through the first set of fuel injectors should

---

[6] The injectors were designed to operate at an equivalence ratio of 1.0, however, structural constraints and upstream ignition limited testing to equivalence ratios below 0.6.

therefore be quite similar to that of the premixed case.

For the second set of radial injectors however, the 3 mm of available mixing length is only 50% of the 6 mm needed for complete penetration; consequently, the impact can be expected to be more severe.

Overall, the trends observed in the measurements are explainable by the injection design model described in Section 4.3.2[7]. Injection through the first set of radial holes shows acceptable performance, furthermore, the performance is expected to improve as one is able to get closer to design conditions.

The placement of the first set of radial fuel injectors is therefore recommended as a suitable injection location for the microengine, however, the size and spacing of the injectors need to be re-designed for operation at lower equivalence ratios.

Investigation of Upstream Burning

The downside of fuel injection through the first set of radial injectors lies in the possibility of recirculation jacket combustion that might compromise the insulating properties of the jacket and possibly damage the device. Upstream combustion tests were therefore intended to identify the space in the operating map where this occurs so that subsequent operation in that part of the operating envelop may be avoided.

Recirculation jacket combustion in the static structure was generally observed at equivalence ratios above 0.7 and at mass flow rates in the 0.01-0.1 gm/sec range. Figure 4-39 (a) shows a picture of the static structure with upstream combustion in the recirculation jacket; Figure 4-39 (b) shows the dramatic increase in outer wall temperature that occurs upon initiation of recirculation jacket combustion.

It was hypothesized that outer wall temperature was the primary driver of whether or not combustion occurred in the recirculation jacket. The hypothesis was supported by the following observations:

1. Figure 4-39 (c) shows experimental measurements of the outer wall temperature as function of the mass flow for different equivalence ratios and for premixed and non-premixed operation with fuel injection through the first set of radial injectors. The plot shows the onset of recirculation jacket combustion for outer wall temperatures above ~800K. Furthermore, since outer wall temperature generally dropped back down with increasing mass flow, the experimental data showed a corresponding extinction of upstream combustion once the outer wall temperature dropped back below 800K (see Figure 4-39 (b)).

2. Figure 4-39 (c) shows no upstream burning for non-premixed injection. This is because the incomplete fuel-air mixing kept the outer wall temperature below 800K. Externally heating the outer wall with a flame did however ignite the mixture in the recirculation jacket for *all three* fuel injection schemes, causing it to burn immediately downstream of the injection location in each case.

3. The onset of upstream combustion was accompanied by a "pop" characteristic of hydrogen ignition, suggesting a secondary ignition of the mixture in the recirculation jacket instead of upstream flashback

---

[7] The design of the side injectors was primarily dictated by fabrication constraints, hence, their comparison is not modeled here.

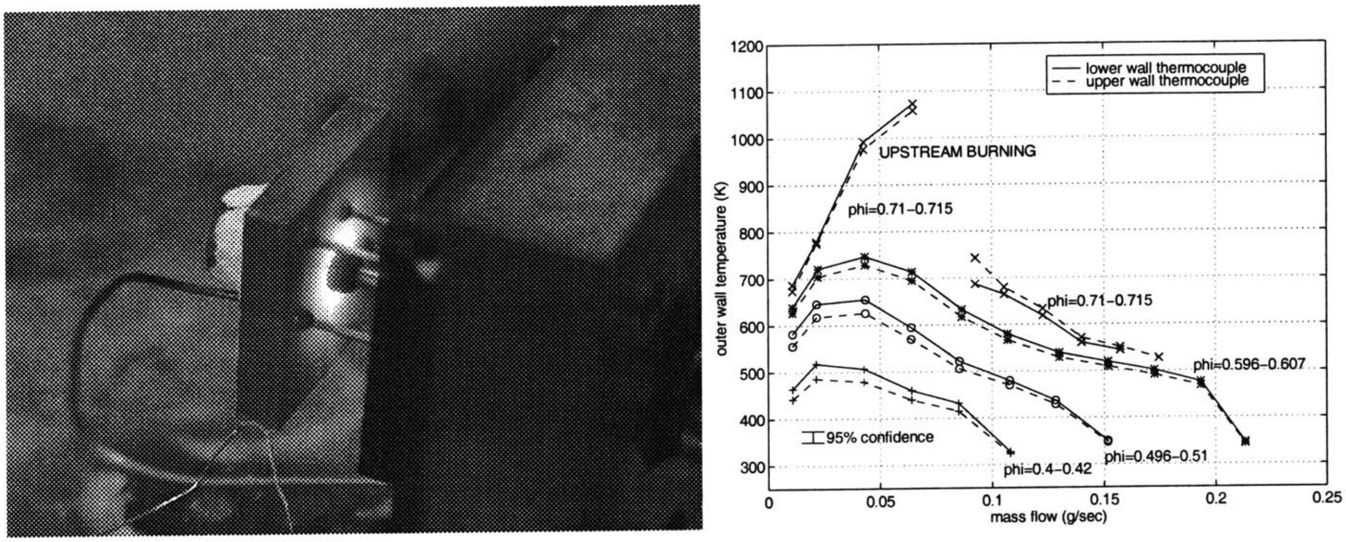

(a) Static structure w/ recirculation jacket burning.

(b) Temperature increase due to upstream burning.

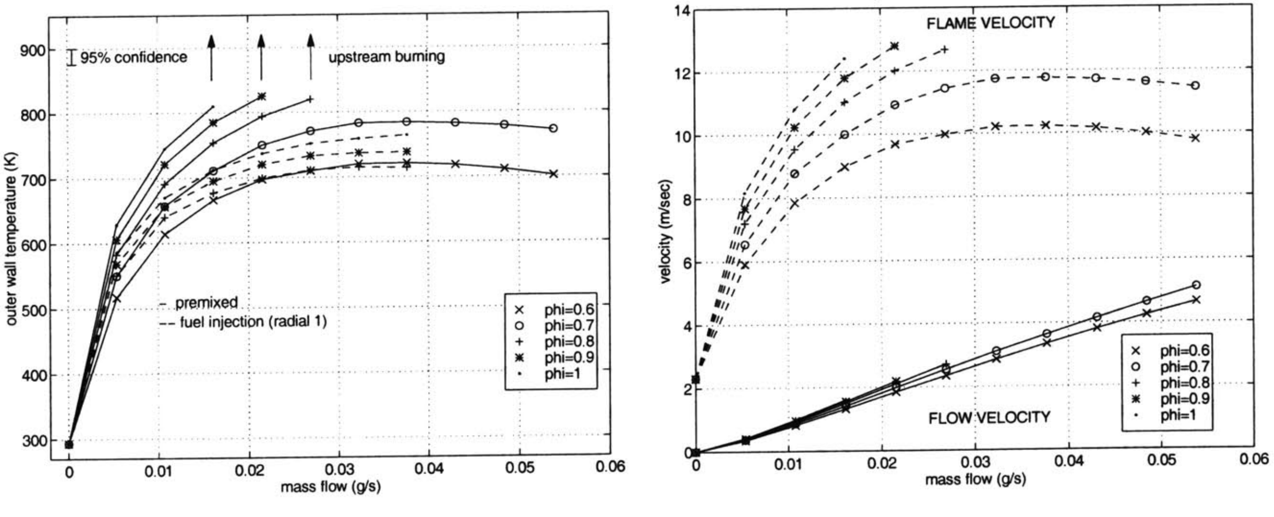

(c) Upstream burning for $T_{wall} > \sim 800K$.

(d) Flame speed versus flow speed.

Figure 4-39: Investigation of upstream combustion in the recirculation jacket.

of the flame. Furthermore, an estimation of the flame speed and flow speed along these operating points did not show a sudden change prior to the onset of upstream combustion. Figure 4-39 (d) plots these values using the following empirical co-relation for the flame speed [20] & [21][8]:

$$S_L = 0.442 + 0.0001906T^{1.655} \tag{4.7}$$

The figure shows that the flow speed is lower than the flame speed at all the operating points. This suggests that the flame is free to move up into the recirculation jacket at any of the operating points shown in Figure 4-39 (b), what prevents it from doing so however, is the quenching effect of a cold outer wall - once the wall temperature is sufficiently high, the flame does indeed stabilize all the way up to the very entrance of the device (see Figure 4-39 (a)).

Upstream combustion therefore has the following implications for the operation of the microengine:

1. Since it only occurs in the extreme upper-left hand corner of the operating space at very low mass flows and high equivalence ratios, it should not effect the operation of the device. The designer of the microengine does however need to be cognizant of this boundary in the operating space.

2. Since this phenomenon is empirically observed to occur at outer wall temperatures above 800K provided the flow speed is low enough to stabilize a flame, an *in situ* monitoring of the outer wall temperature is recommended to serve as a precursor to this phenomenon.

Mechanical Integrity

Mechanical integrity of the static structure following high temperature operation was evaluated by measuring the chamber pressure as a function of the mass flow under cold-flow conditions after each progressive run. Figure 4-40 plots these results for four different dies.

Figure 4-40 (a) & (b) show that the mass flow rate through the device is constant to within 7% after up to 38 hours of high temperature testing at pressures up to 1.3 atm. Ultimately, occurrence of upstream combustion in the recirculation jacket fractured the silicon in both the devices and compromised the structural capability of the rigs.

Figure 4-40 (c) plots the results for a third die that was damaged due to upstream combustion, and shows the subsequent deterioration that occurred due to the initial failure of the silicon. Preliminary examination of the NGV throat area under an infra-red microscope showed no visible change in the blade dimensions.

Figure 4-40 (d) shows results for the externally throttled combustor before and after 5.5 hours at pressures up to 1.55 atm. The plot shows up to a 12% change in mass flow; this is partly attributed to increased leakage through the ceramic adhesive used to attach the external throttle-tube.

---

[8] The flow speed is calculated at the smallest area location along the recirculation jacket length; the flow temperature is assumed to be equal to the outer wall temperature.

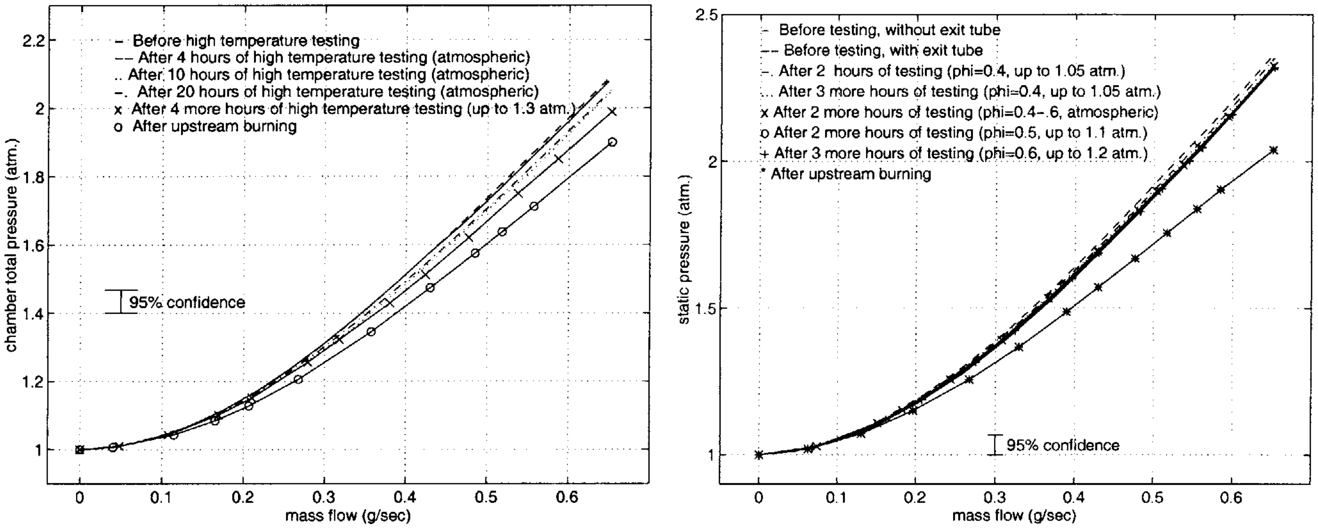

(a) Rig 1.

(b) Rig 2.

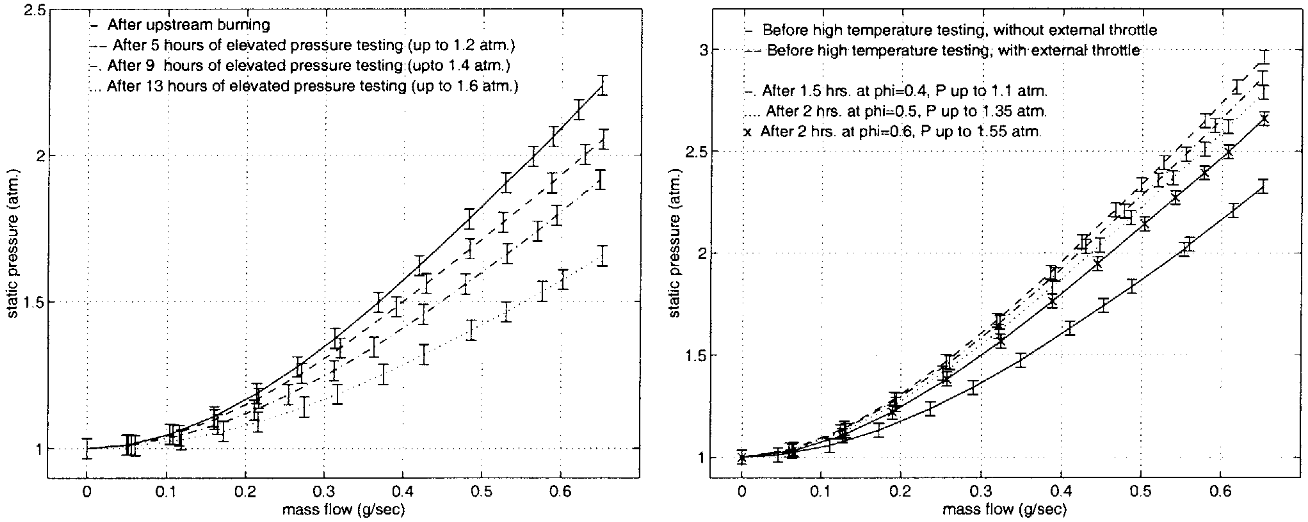

(c) Rig 3.

(d) Rig 4.

Figure 4-40: Cold-flow curves for four different samples after progressive high temperature exposure.

Overall, before and after cold-flow characterization of the devices demonstrated the structural integrity of the packaged static structure at outer wall temperatures up to 800K, and pressures up to 1.55 atm., so long as upstream combustion did not occur in the recirculation jacket. The static structure could not be tested at higher pressures because of the blow out phenomenon described earlier; recommendations for additional high temperature and pressure testing of the static structure shall be made in Chapter six.

4.6.5 Empirical Identification of the Microcombustor Operating Space

Synthesizing the results presented thus far, Figure 4-41 presents the experimentally determined operating space for the microcombustor. It plots:

1. The lean blow out boundary,
2. The boundary for combustion in the upstream recirculation jacket, and
3. Two structural limits - the limit at low mass flow rates and ϕ=1 was realized upon combustion in the upstream recirculation jacket, and melted the inner wall of the chamber; the limit at higher mass flow rates and ϕ=0.7 melted the exhaust gas tube at the exit of the chamber.

The figure also plots the 1600K T_{t4} constraint assuming 100% combustor efficiency, and the 0.36 gm/sec design operating mass flow rate of the static structure.

The figure shows a narrow operating corridor between the the lean blow out limit and the upstream combustion limit for the current static structure configuration, however, design point operation within the 1600K T_{t4} constraint will either require:

1. An extension of the lean blow out boundaries to allow stable operation at the design mass flow rate at equivalence ratios below 0.5, or
2. Operation at combustor efficiencies that are low enough to allow stable high-equivalence ratio combustion with exit gas temperatures below the 1600K T_{t4} limit.

The former option will require operation at higher chamber pressures or an increase in the chamber volume; the latter option will sacrifice combustor efficiency and increase the fuel consumption of the engine.

Recommendations for achieving design point operation in the current design of the static structure will be presented in Chapter six.

4.6.6 Hydrocarbon Tests

In addition to characterizing the base line performance for hydrogen-air combustion, the static structure was also intended to explore the possibility of hydrocarbon combustion at the micro-scale.

This section presents the test results for ethylene and propane combustion in the static structure.

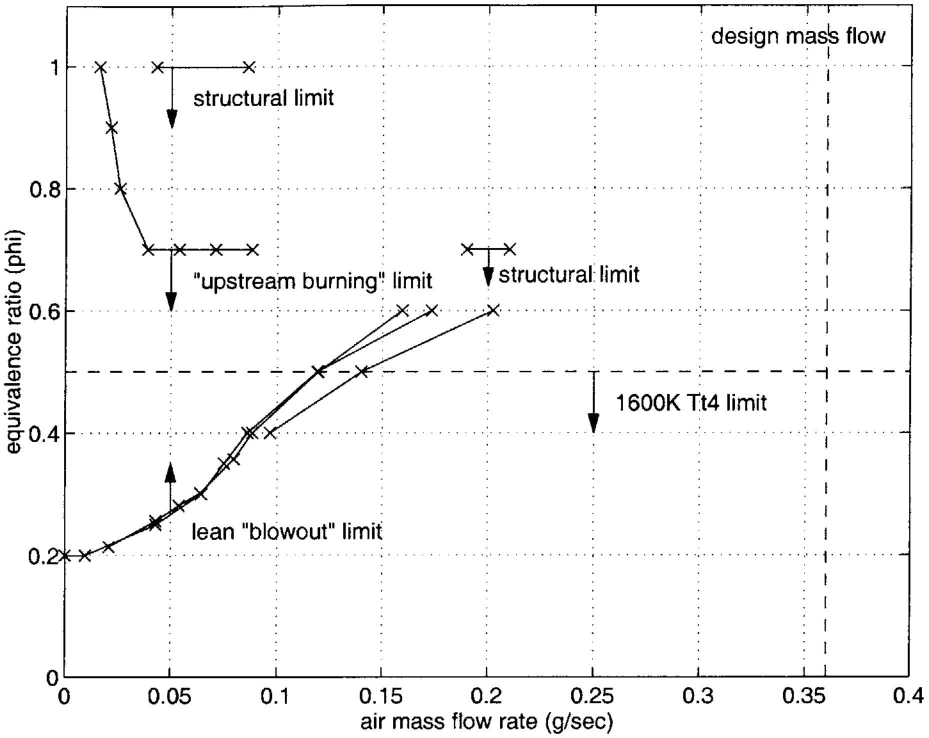

Figure 4-41: Experimentally measured operating space for the static structure, showing the lean blow out boundary, the upstream propagation boundary, the structural limits, and the 1600K T_{t4} constraint.

Ethylene Tests

Preliminary system analysis by Spadaccini [105], suggested that the fast chemical kinetic rates of ethylene make it a suitable fuel for a hydrocarbon-powered microengine so long as it is stored as a liquid above ~900 psi. Combustion tests were therefore conducted in order to map the feasible operating space for ethylene-air combustion in the static structure.

Figure 4-42 shows the experimentally measured exit gas temperatures and combustor efficiency under atmospheric test conditions for equivalence ratios ranging between 0.6 and 0.9.

The results show stable combustion at conditions corresponding to 60% of the atmospherically scaled design residence time of the microengine at an equivalence ratio of 0.9, an exit gas temperature of 1400K, and an overall combustor efficiency of 60%. *These results serve as the first demonstration of stable hydrocarbon combustion at the micro-scale; the resulting fluid power density is estimated to be ~500 MW/m^3.* Additional analyses from a systems perspective are recommended to evaluate the feasibility of an ethylene-powered microengine for propulsion applications.

Propane Tests

In addition to ethylene tests, propane-air combustion tests were also conducted to map the stable operating regime in the static structure. Since the chemical kinetic rates of propane are not as fast as those for ethylene, propane combustion could only be stabilized at equivalence ratios as high as 0.8. Even then, a

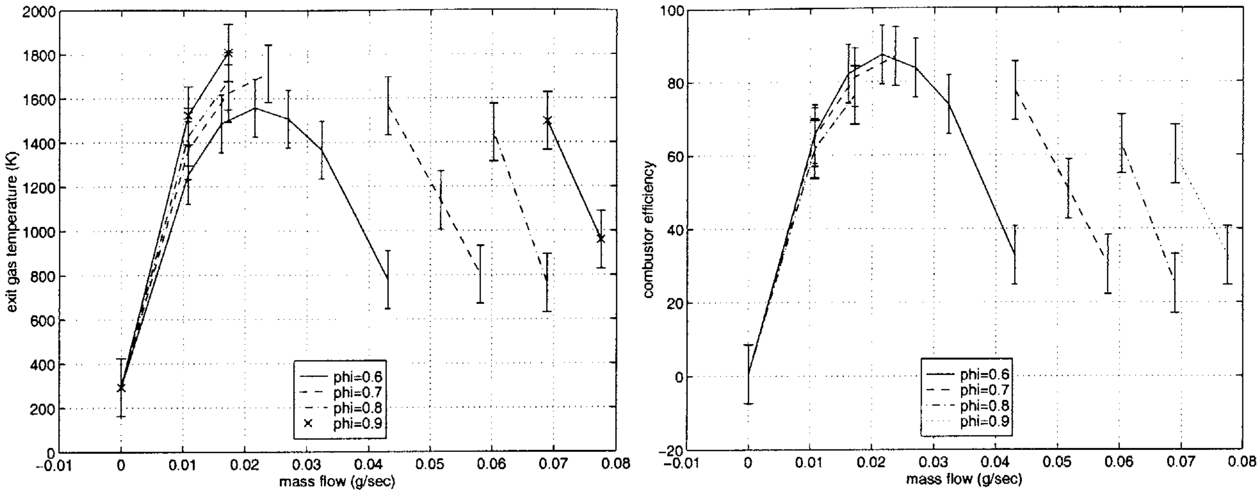

(a) Exit gas temperature.

(b) Combustor efficiency.

Figure 4-42: Experimental test results for ethylene-air combustion in the static structure.

large fraction of the reaction appeared to occur downstream of the NGV's, and was characterized by a visible blue flame in the exit tube. Figure 4-43 (a) & (b) plots the exit gas temperature and efficiency measurements from these tests.

Propane-air combustion was also stabilized in the recirculation jacket by heating the walls with hydrogen-air combustion first, and then gradually switching to propane fuel. The wall temperature measurements for the cases with and without recirculation jacket combustion are shown in Figure 4-43 (c) & (d). As expected, the outer wall temperatures with recirculation jacket combustion are considerably higher.

Overall, propane-air combustion was stabilized in the chamber at 17% of the atmospherically scaled residence time at an equivalence ratio of 0.8, an exit gas temperature of 1250K, and an efficiency of 55%. This corresponded to a power density of ~140 MW/m^3.

4.6.7 Repeatability of the Test Results

This last section presents the repeatability of the test results.

Repeatability of the Pressure Measurements: Figure 4-44 plots the repeatability of the cold-flow pressure measurements for three different runs, and for two different dies. The results are within the experimental uncertainty and establish the repeatability of the pressure measurements.

Repeatability of the Temperature Measurements and Efficiency Calculations: Figure 4-45 shows run-to-run and die-to-die repeatability of the temperature and efficiency measurements in the static structure for different fuel-air equivalence ratios. The results are repeatable within the experimental uncertainty in all cases, and establish the repeatability of the measurements.

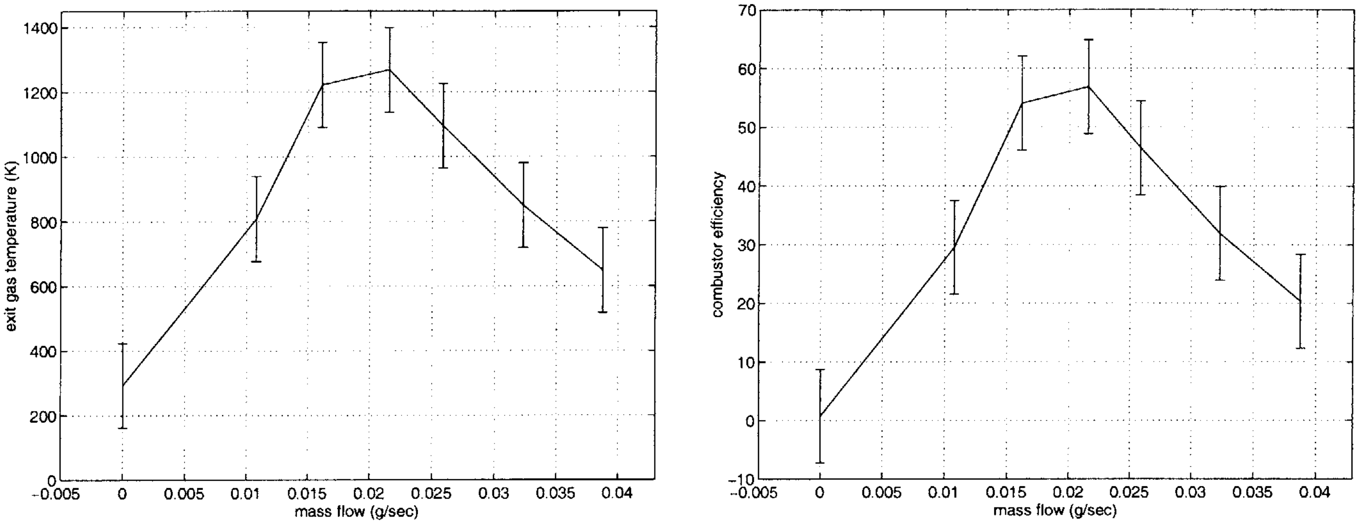

(a) Exit gas temperature.

(b) Combustor efficiency.

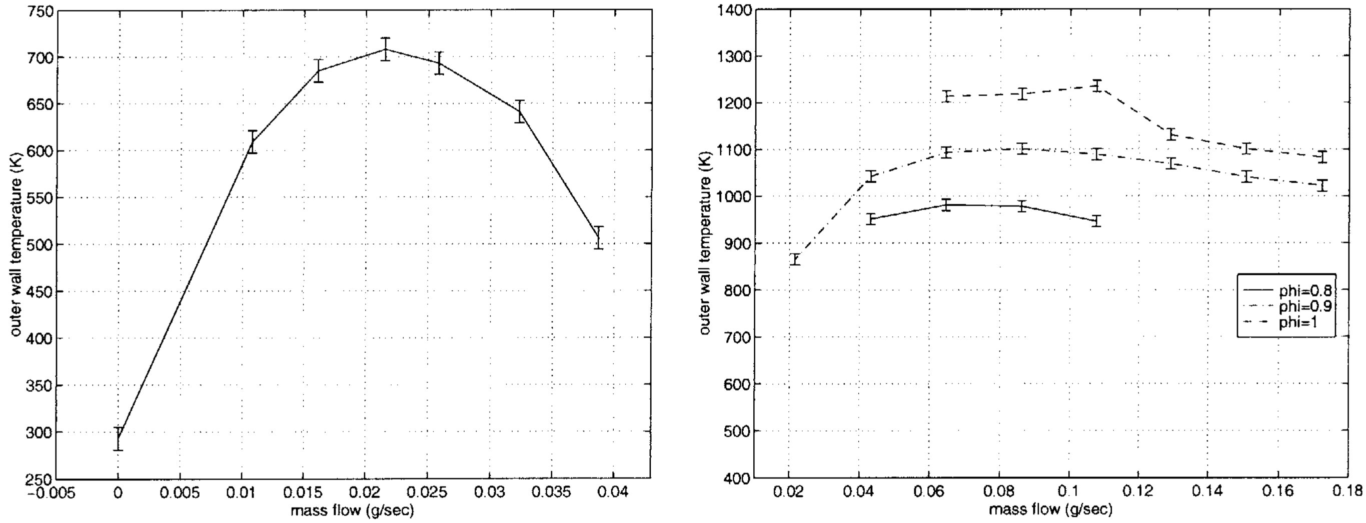

(c) Outer wall temperature (without upstream burning).

(d) Outer wall temperature (with upstream burning).

Figure 4-43: Experimental test results for propane-air combustion in the static structure.

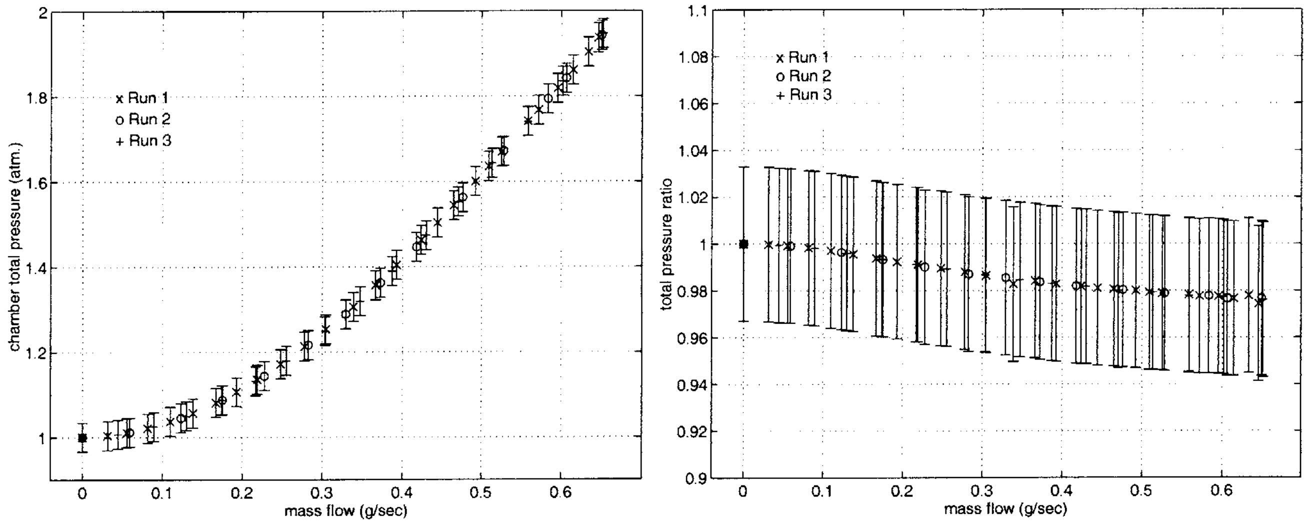

(a) Pressure measurements for different runs in the same die.

(b) Pressure ratio for different runs in the same die.

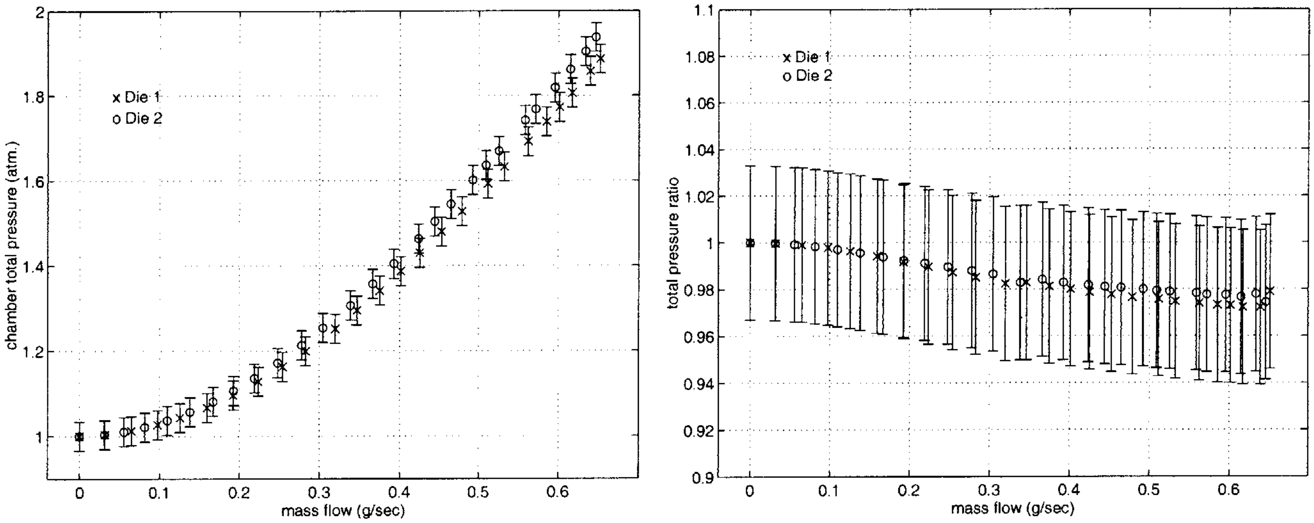

(c) Pressure measurement in different dies.

(d) Pressure ratio across different dies.

Figure 4-44: Repeatability of the cold-flow measurements.

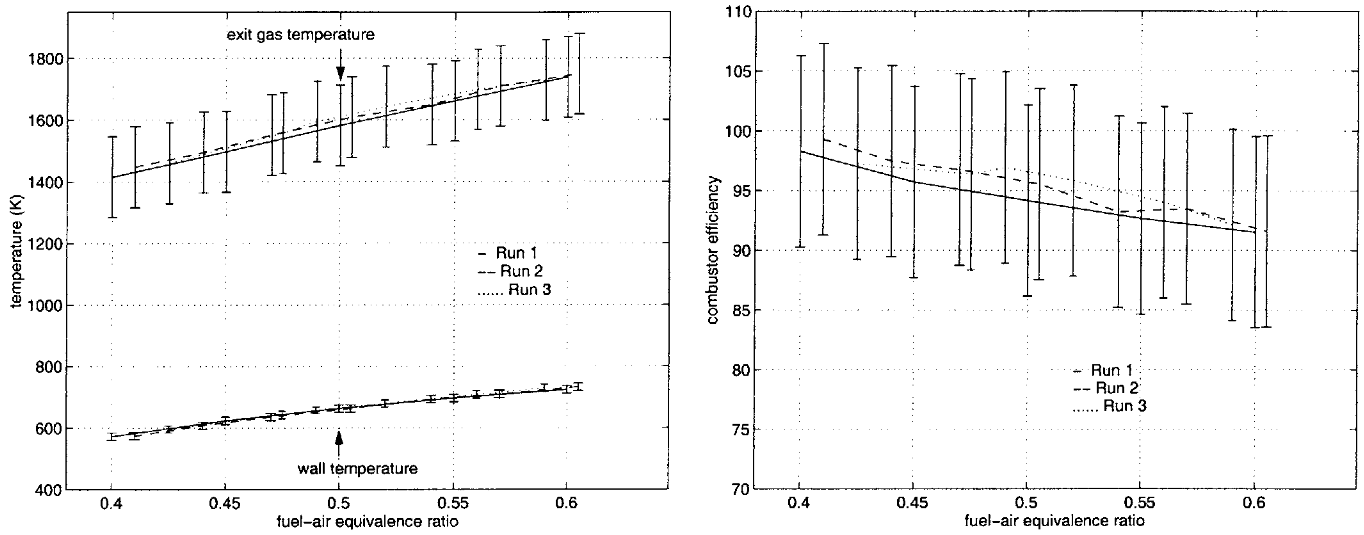

(a) Temperature measurements for different runs.

(b) Efficiency measurements for different runs.

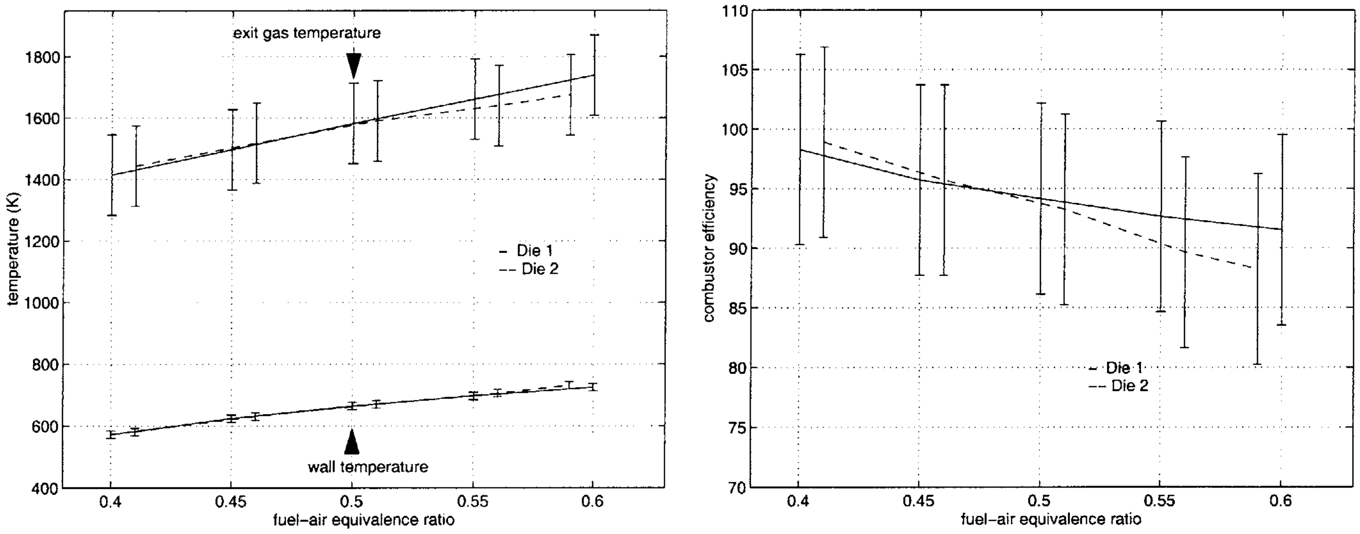

(c) Temperature measurements in two different dies.

(d) Efficiency measurements in two different dies.

Figure 4-45: Repeatability of the temperature measurements and efficiency calculations.

4.7 Chapter Summary

This chapter presented the design, fabrication, packaging and experimental testing of the first microcombustion system for a silicon gas turbine engine. The primary conclusions from the chapter can be summarized as follows:

1. It is possible to DRIE and align wafer bond six wafers in order to produce a 3.8 mm thick silicon structure that comprises all the non-rotating components of a microengine.
2. The device can be packaged and integrated with igniters and fluidic interconnects. The igniters are shown to reliably ignite the mixture and survive multiple ignition cycles; the fluidic interconnects have been successfully demonstrated to withstand wall temperatures up to 800K at pressures up to 1.55 atm.
3. Cold-flow tests show performance as expected; the total pressure loss at design conditions is less than 2%, and agrees with cold-flow CFD solutions used during the initial design of the flow path. The hot-flow total pressure loss is expected to be approximately 3% - this is sufficiently low to close the thermodynamic cycle for the microengine.
4. Premixed hydrogen-air combustion was stabilized at 64% of the design mass flow and at 52% of the design pressure of the microengine. The device could not be operated at design point because of a decreasing Damkohler number that results from increasing mass flow during the unchoked operating regime of the device. Implications for achieving design point operation in the static structure will be presented in Chapter six.
5. The performance of the combustor was found to be limited by poor thermal efficiency at low mass flow rates. At high mass flow rates, the device operated with thermal efficiencies close to unity, however, the chemical efficiency dropped off rapidly to a decreasing Damkohler number with increasing mass flow rate.
6. Compared to the previously demonstrated 3-stack, incorporation of a combustor recirculation jacket and improved thermal isolation of the device resulted in an "aggregate" 20-point increase in the overall efficiency of the combustor under back-to-back operating conditions.
7. Evaluation of the different fuel injection schemes suggested that axial injection through the first set of radial injectors would provide adequate fuel-air mixing. However, additional testing at design conditions is still required to demonstrate acceptable performance of the injectors at design conditions.
8. Increasing the outer wall temperature above 800K resulted in combustion in the upstream recirculation jacket. This phenomenon occurred at low mass flow rates and high equivalence ratios, and was found to catastrophically damage the device.

9. Structural integrity of the packaged device was demonstrated at pressures up to 1.55 atm., and at equivalence ratios up to 0.6. Once again, the nozzle guide vanes showed no visible damage.
10. Stable ethylene-air and propane-air microcombustion was demonstrated inside the static structure at power density levels of 500 $\mathrm{MW/m^3}$ and 140 $\mathrm{MW/m^3}$, respectively.
11. The pressure and temperature measurements, and efficiency calculations were shown to be repeatable within the experimental uncertainty.

The overall implications of these results for microcombustor design shall be presented in Chapter six.

Chapter 5

Development of Interconnects, Igniters and Temperature Sensors

5.1 Introduction

This chapter presents the results of a parallel effort that was undertaken to develop "on-chip" igniters and wall temperature sensors for the microengine.

The primary objective of this work was the identification of key issues that must be considered prior to incorporating thin film igniters and temperature sensors into the engine. It was specifically intended to:

1. Demonstrate a novel through-wafer interconnect scheme capable of making reliable electrical connections to the backside of a wafer,
2. Use these interconnects to make electrical contacts to a thin-film polysilicon resistor and evaluate its ignition capability,
3. Evaluate the durability of such a resistor in a high temperature environment, and
4. Evaluate its use as a wall temperature sensor for the microengine.

(Note: Since this chapter primarily deals with thin-film integration issues, all temperatures will be listed in degrees Celsius for consistency with fabrication conventions.)

5.2 Requirements for On-Chip Igniters and Temperature Sensors

The concept of an on-chip igniter is a simple one - a thin-film of a conductive material is laid down along the inner wall of the combustor and patterned in the shape of a resistor. Upon passage of current, this resistive element heats up and initiates combustion.

The requirements for such an element can be stated as follows:

1. It should be able to heat the mixture up to its point of ignition while consuming no more than a few Watts of power (~600°C for a hydrogen-air mixture and ~200°C for a hydrocarbon-air mixture [115]).
2. It must be placed within the combustor recirculation zone to facilitate ignition.
3. It must survive exposure to wall temperatures up to ~1000°C.
4. It must be compatible with electrical leads that connect to the outside of the device, and with the overall fabrication sequence of the engine.

The concept of using the same igniter as a wall temperature sensor is based on an *in situ* resistance measurement to back-out the operating temperature of the sensing element from its temperature coefficient of resistance (TCR).

The requirements for such a wall temperature sensor are:

1. It must be in good thermal contact with the wall.
2. The resistivity change with temperature should be measurable in the room temperature-1000°C range.
3. It must not degrade in the high temperature environment of the engine.
4. It must be compatible with electrical leads and with the overall fabrication sequence of the engine.

(Note: Although thin-film resistors are routinely used in the integrated circuit industry, the primary challenge herein lies in operating them at combustion temperatures in the 1300°C-2000°C range, and being able to make electrical contacts to them inside a multi-level MEMS device.)

5.3 Design of the Thin Film Resistors

Igniters and temperature sensors for the microengine comprise a thin layer of conductive material that is patterned in the shape of a resistor and isolated from the underlying substrate via an oxide layer.

While typical applications for resistors in the integrated circuit industry have utilized metals such as aluminum, gold and platinum, the high temperature environment of the combustion chamber precludes their use for igniters and temperature sensors in the microengine. (Gold and aluminum will melt at the operating temperatures of the combustor; platinum is know to agglomerate at temperatures above 700°C [39]. Other high temperature metals such as nickel and molybdenum were also considered, however, they are also known to degrade due to the formation of silicides at temperatures around 800°C [93].)

Similar to previously reported high temperature applications [22] & [116], polysilicon was therefore selected as a suitable material for the thin-film igniters because:

1. It is integrable with the fabrication sequence for a silicon engine,

2. CVD polysilicon has the desirable temperature and structural capabilities for the application,
3. Its resistivity can be tailored by controlling the dopant concentration, and
4. Thin film polysilicon resistors have previously been demonstrated to produce Joule heating up to 1200°C without exhibiting severe electromigration effects [22].

Having chosen polysilicon as the conductive material, a test device comprising eight different geometrical designs was subsequently fabricated. These designs were based on devices reported by Cole *et al.* [22], and were only intended for use in a short-loop experiment to identify suitable resistor geometries. Figure 5-1 shows two of these resistors along with an illustration of the fabrication process for this chip.

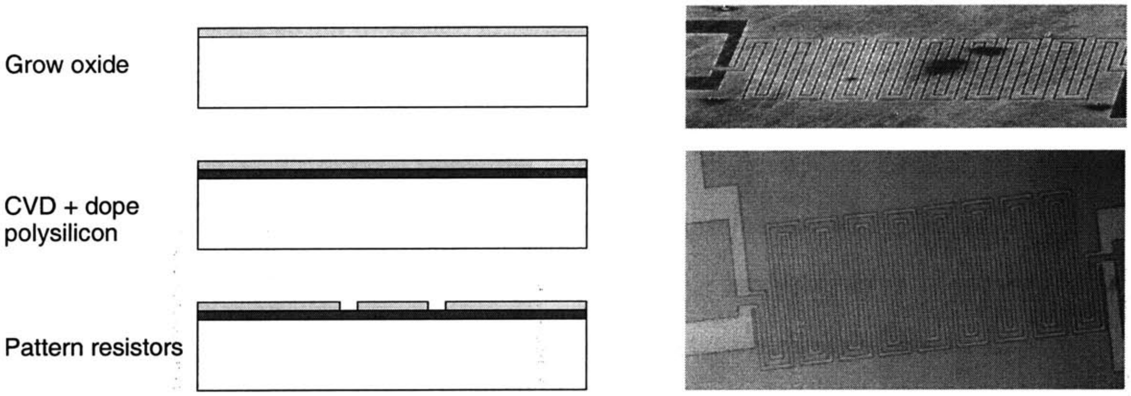

(a) Fabrication process for the igniters.

(b) SEM and optical image of two of the igniter configurations.

Figure 5-1: Fabrication process and images of the test igniters. (Note: The polysilicon linewidth is 20 μm.)

The resistors on this chip were designed to operate at a current density of $2\times10^5\,\mathrm{A/cm^2}$ based on previously reported observations of incandesence in doped polysilicon resistors at this current density level [22]. The resulting designs had linewidths between 10-25 μm, lengths of approximately 1 mm, and overall resistances between 1 kΩ and 14 kΩ. The polysilicon thickness was 0.25 μm, its sheet-resistivity was approximately 10 Ω/square, and the insulating oxide thickness was 0.5 μm.

Preliminary testing of the resistors showed that it was possible to raise the temperature of the chip to approximately 700°C by passing current through the 12 kΩ resistor. Prior to further integration with the rest of the device however, two additional issues needed to be resolved:

1. Infra-red camera (IR) images showed that the heating was not localized around the igniter. Instead, the resistor dissipated a significant amount of heat into the supporting substrate, raising the temperature of the entire chip to 700°C. While this was acceptable from a combustion ignition perspective, it utilized more power than was necessary to locally heat and ignite the mixture. Consequently, future designs were intended to incorporate 2 μm thick oxide layers to improve the thermal insulation between

the heating element and the substrate[1].

2. The igniters required sealed wafer-level leads along bondlines to make electrical contacts to an external power supply. While this scheme was acceptable for the 3-stack microcombustor, it would sacrifice the insulating properties of the recirculation jacket in the final engine configuration. Consequently, a new electrical interconnect scheme that obviated the need for taking lateral electrical leads through the recirculation jacket was developed.

5.4 Development of A Novel Interconnect Scheme

The difficulty in taking out sealed wafer-level leads through bondlines motivated the development of a through-wafer interconnect scheme to allow direct electrical contact to the backside of the wafer. Conceived by Schmidt [98], and illustrated in Figure 5-2, the use of this novel technique can be expected to facilitate electrical connections in other microfabricated devices as well.

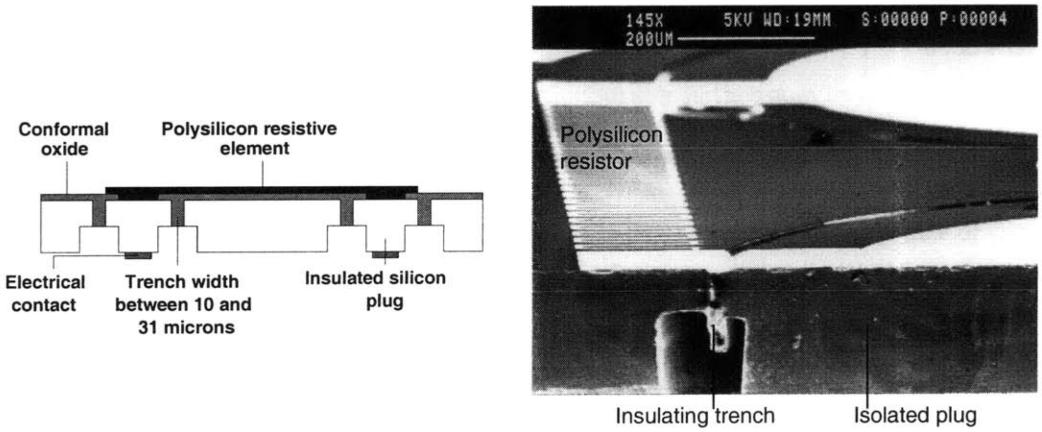

Figure 5-2: A schematic of a through-wafer interconnect alongside a cross-section of the isolated silicon plug.

The concept of this through-wafer interconnect exploits the ability to conformally coat a high-aspect ratio trench with a thick insulating layer so as to isolate a through-wafer via that can be used to provide electrical contact across two sides of a low-resistivity wafer.

A fabrication demonstration and application of these interconnects to make electrical contacts to a second build of igniters and temperature sensors for the microengine is described in the following sections.

5.5 Fabrication of the Thin Film Resistors and Interconnects

The fabrication process for the second igniter and interconnect test wafer is described in Figure 5-3, alongside a picture of a demonstration device.

---

[1] 2 μm oxide was found to be the thickest layer that could be deposited and densified without introducing excess wafer bow or stress-induced cracking.

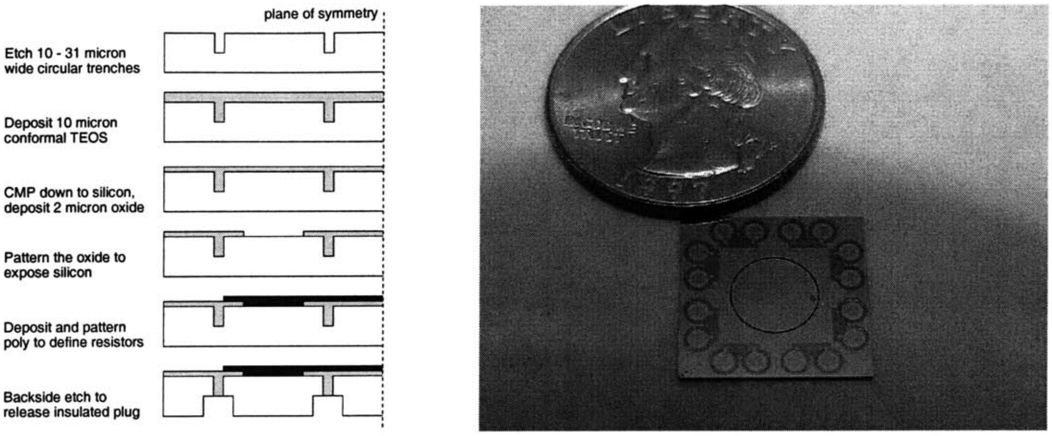

(a) Fabrication process for the igniters and interconnects.

(b) A picture of the characterization dies used to test the isolated igniters and temperature sensors.

Figure 5-3: Fabrication process for the test igniters and interconnects alongside a picture of the characterization device.

The process was completed by Zhang [122], and is explained as follows:

1. Using deep reactive ion etching (DRIE), 100 μm deep circular trenches were etched into the top surface of 300 μm n-type <100> silicon wafers that had a resistivity of 0.01-0.02 Ω cm.

2. A 10 μm coating of tetraethylorthosilicate (TEOS) was then deposited at 350°C in order to isolate the silicon plug from the rest of the substrate. The film was left undensified to avoid excessive residual stresses that could result in wafer fracture.

   Since the conformality of the TEOS in a high aspect-ratio trench was unknown, the dies contained eight different sets of interconnects with trench widths varying between 10 μm and 31 μm. As shown in Figure 5-4, "key-holing" of the TEOS was observed in trenches wider than 16 μm. Subsequent builds incorporated a 1 μm thick nitride coating prior to the TEOS deposition to relieve the residual stress in the film, and were observed to be more conformal.

3. Following the TEOS deposition, the oxide was chemically-mechanically polished down to the silicon surface to allow subsequent photolithography steps. 2 μm of TEOS was then additionally re-deposited and patterned to provide electrical access for the polysilicon.

4. 0.5 μm thick polysilicon was then deposited at 625°C, $POCl_3$ phosphorus-doped at 925°C, and patterned to define the resistors. The resistor linewidth was 20 μm; the length was 2 mm. The design sheet resistivity was 10 Ω/square; the overall design resistance was approximately 5 kΩ.

5. Finally, 100 μm wide circular trenches were dry-etched from the backside to release the isolated silicon plugs and provide electrical contact across the two sides of the wafer.

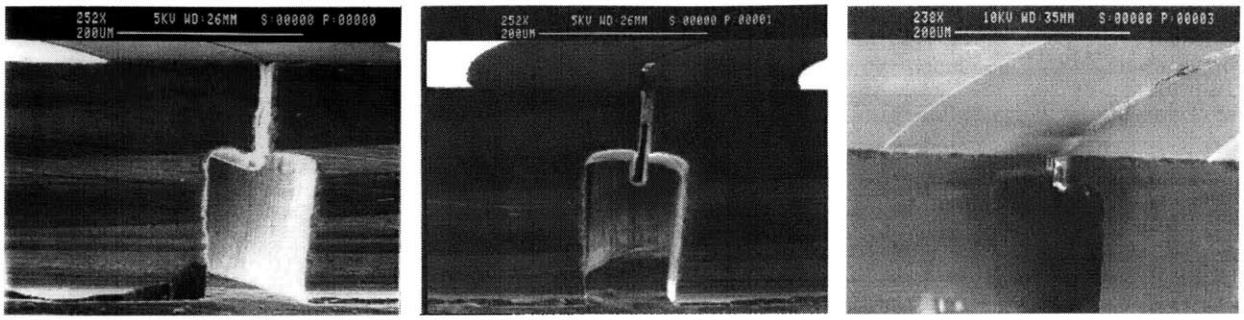

(a) Fully-conformal TEOS in a 16 μm trench.

(b) Key-holing of the TEOS in a 31 μm trench.

(c) Conformal TEOS+nitride deposition in a 31 μm trench.

Figure 5-4: SEM's showing the conformality of the TEOS and nitride layers in a 16 μm and 31 μm wide trench.

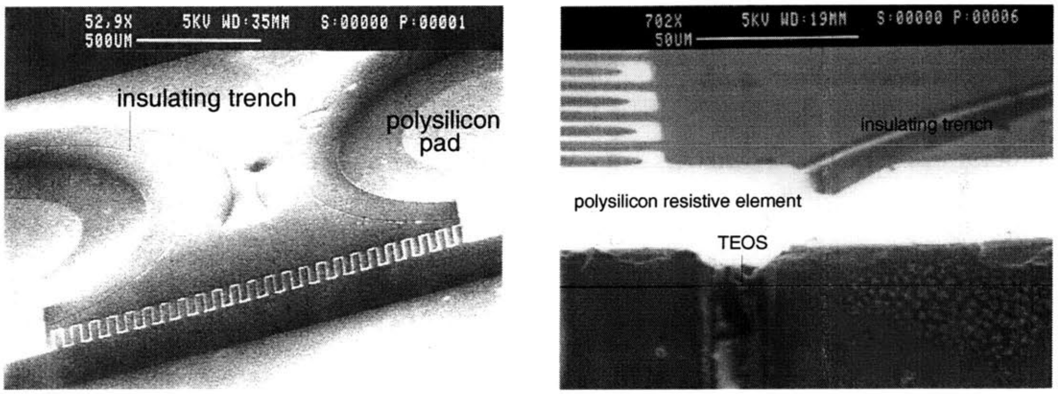

(a) An SEM of the entire igniter.

(b) A close-up view of the resistor.

Figure 5-5: SEM's of a representative igniter alongside a close-up of the polysilicon across the isolating trench.

Figure 5-5 shows an SEM of this fabricated igniter alongside a close-up view of the polysilicon resistor.

The resistance across the backside contacts was measured to be approximately 6 kΩ. This was within 20% of intended design value of 5 kΩ; the additional measured resistance was attributed to the polysilicon leads to the resistor, the through-wafer silicon plugs, and probe contacts.

Among the devices that were fabricated without the nitride layer, only three out of the eight igniters on a die were successfully isolated from the surrounding substrate (10 μm, 13 μm and 16 μm trench widths). The remaining five resistors were found to be open due to discontinuities in the polysilicon across the isolating trenches. Figure 5-6 shows SEM's of the polysilicon across the isolating TEOS trench for these two cases.

5.6 Experimental Test Results

Following fabrication, the igniters were first tested in a thermally isolated configuration, and then integrated with the 3-stack microcombustor.

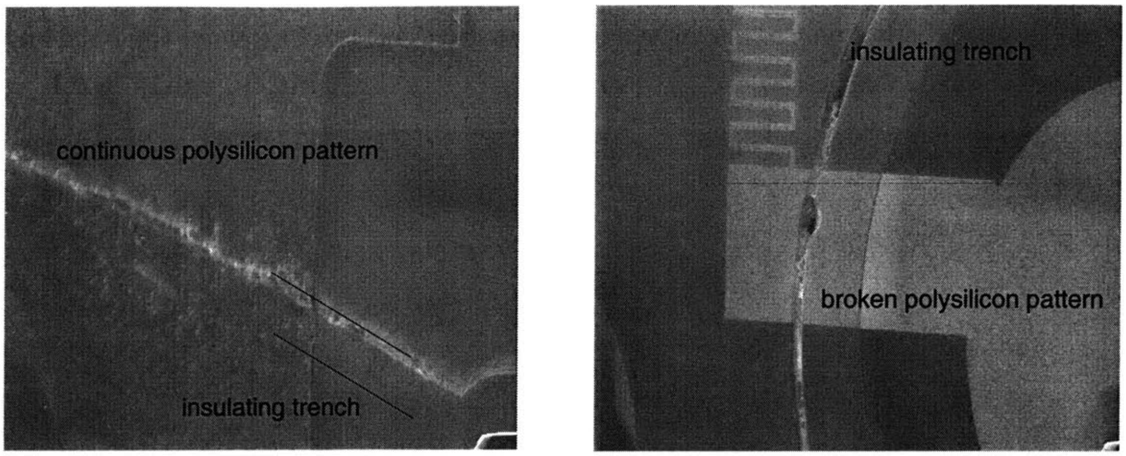

(a) An SEM of a continuous polysilicon pattern across a closed-up 13 μm TEOS trench.

(b) SEM of a resistor that was electrically open due to discontinuities in a 28 μm trench.

Figure 5-6: SEM's showing the polysilicon deposition across different sized trenches.

5.6.1 Isolated Igniter Test Results

Isolated igniter tests were conducted by using probe-tips to apply a voltage across the the backside of the interconnect-pairs. Figure 5-7 shows the current through the igniter as a function of the applied voltage, and also plots the resistance and applied power as a function of the igniter temperature. (The igniter temperature was measured with an IR camera calibrated to a polysilicon emissivity of 0.5.)

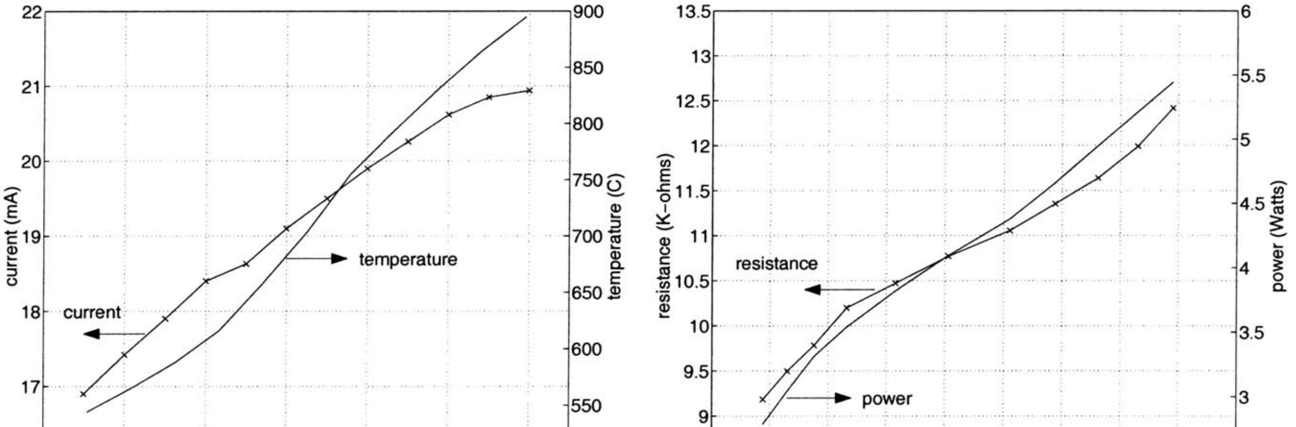

Figure 5-7: V-I and power-temperature curves for the igniters.

The figure shows increasing resistance and temperature with input power. The igniter current is of the order of tens of milliamperes, and corresponds to the intended current density of 10^5 A/cm^2. Since Cole *et al.* [22], did not observe electromigration in similarly doped polysilicon until current densities of 10^6 A/cm^2, the igniters were expected to be free of electromigration effects.

Figure 5-7 also shows that the power utilization of the igniters is between 3 and 6 Watts. The igniters exhibited localized heating upon passage of current; Figure 5-8 shows two IR and one optical image showing the localized nature of this heating.

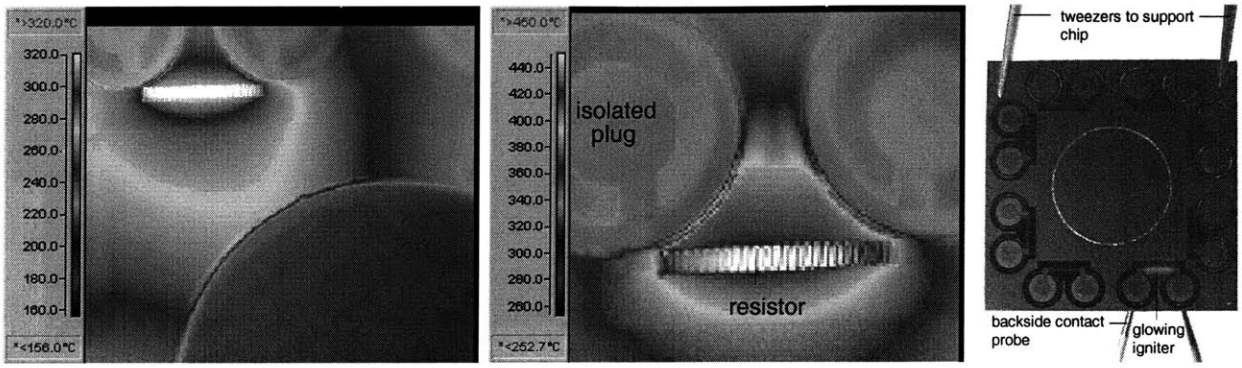

Figure 5-8: IR and optical images of an igniter showing localized heating. (Note: The IR images on the left were taken for an earlier version of the igniters that did not include the nitride coating.)

The experimental tests were repeated on multiple dies to gauge the repeatability of the results. Figure 5-9 shows these results for multiple runs, and for multiple dies, and indicates good repeatability of the results. It also establishes the reliability of the electrical contacts and demonstrates the viability of the novel through-wafer interconnect scheme.

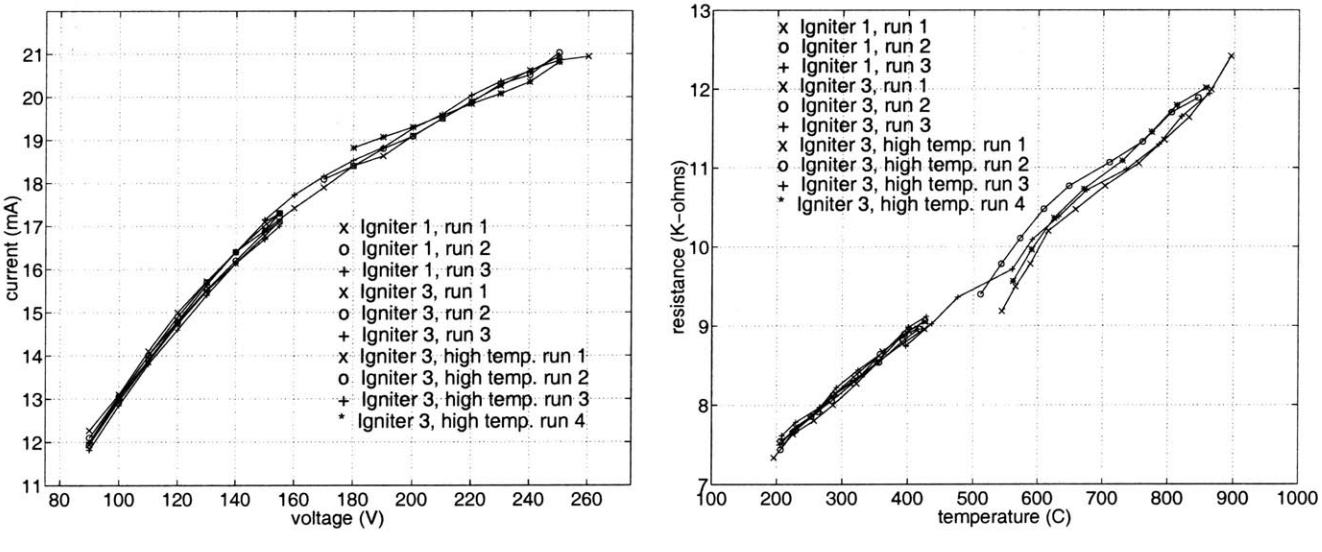

Figure 5-9: V-I and R versus T curves for multiple igniter runs showing good repeatability of the results.

Following tests in a thermally insulated configuration, combustion tests were subsequently conducted in order to accomplish the remaining objectives listed in Section 5.1, i.e. evaluate whether the igniters can:

1. Ignite a combustible mixture,

2. Be used as a temperature sensor, and

3. Survive in a hot temperature combustion environment.

5.6.2 Evaluation of the Ignition Capability

The ignition capability of a thermally isolated igniter chip was evaluated by passing a combustible hydrogen-air mixture over a single heater element (as shown in Figure 5-8). The igniter was able to reach a temperature of ~900°C and repeatedly ignite the mixture while consuming approximately 5 Watts of power.

Upon integration with the 3-stack microcombustor however, the igniter was unable to initiate combustion. This was attributed to a "heat-sinking" effect from the rest of the silicon structure which prevented the heater from reaching a temperature of 900°C empirically observed to be necessary for ignition.

To confirm this hypothesis, and to better understand the behavior of the integrated igniter, a finite-element heat transfer model was subsequently developed in conjunction with MIT Lincoln Laboratories by Huang [52]. This is presented in the following section.

5.6.3 Thermal Modeling of the Igniters

Goals of the Model: The goal of the FEM analysis used to model the igniter was two-fold:

1. To predict the surface temperature of the igniter in a thermally isolated configuration and compare it with experimentally measured values. Such a comparison would not only serve to validate the model, it would also indicate whether the surface temperatures measured by the IR camera were reasonable and numerically repeatable.

2. To subsequently model the integrated igniter and determine its surface temperature in a "heat-sunk" configuration. This would quantify the temperature drop resulting from integrating the igniter chip with the rest of the 3-stack microcombustor.

Description of the Model: The isolated igniter chip was modeled as a 1.5 cm × 1.5 cm plate covered by 2 μm of oxide and 0.5 μm of polysilicon. The resistor was modeled as a 1.9 mm × 0.2 mm strip of polysilicon; the interconnects were modeled as 30 μm wide trenches filled with oxide. Figure 5-10 (a) shows the grid used for this purpose.

In each case, the model was run to steady-state until the prescribed power input through the igniter equaled the heat dissipated to the ambient. (A convective heat transfer coefficient of 5 W/m^{2}K and a polysilicon emissivity of 0.5 was used for this purpose.) Figure 5-10 (b) shows a resulting sample surface temperature distribution as obtained from the model. This is similar to the IR temperature distribution shown in Figure 5-8; quantitative results from the analysis are presented in the following section.

Isolated Igniter Results: Figure 5-11 (a) plots the igniter surface temperature as a function of the input power and compares it with the experimental IR measurements. The numerical results agree with

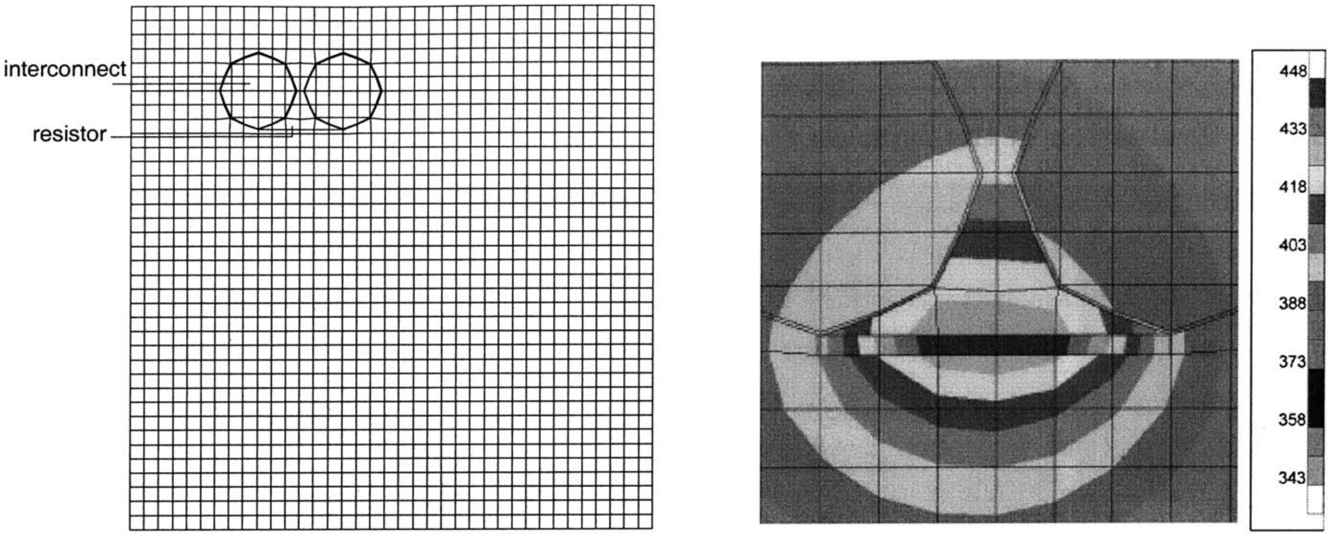

(a) FEM grid used to model the isolated igniters.

(b) Sample temperature distribution for the isolated igniter configuration.

Figure 5-10: FEM grid and sample surface temperature distribution from the igniter thermal model. (Picture courtesy: Dr. Eugene Huang, MIT Lincoln Laboratories)

the experimental measurements to within 55°C, and suggest that the simplified geometrical model of the resistor and interconnect is sufficient to capture the temperature behavior of the igniter.

Figure 5-11 (a) also plots the amount of heat being conducted into the substrate, and shows that most of the input power is being dissipated via the silicon. This implies a lack of thermal isolation between the resistor and the underlying silicon substrate; the implications of this design shall be discussed in Section 5.7.

Overall, the results of the analysis increase the confidence in the IR measurements and show that they are numerically repeatable via finite element modeling. They also confirm the ability to be able to heat the igniter up to 900°C, and re-affirm the ignition capability of an isolated igniter.

Integrated Igniter Results: Next, the integrated igniter geometry was modeled in order to quantify the "quenching" effect of the silicon combustor by specifying experimentally measured wall temperatures as a constant temperature thermal boundary condition along the edge of the igniter chip.

Figure 5-11 (b) plots the resulting igniter surface temperature in the integrated 3-stack configuration and compares it with the surface temperature predicted in the thermally isolated configuration. The results show a temperature drop of approximately 500°C due to the presence of the additional silicon structure - this explains why the igniter was unable to initiate combustion when integrated in the 3-stack configuration. Recommendations for improving its design will be presented in Section 5.7.

Conclusions

Combined with the experimental observations, the results of the numerical model may be used to make the following conclusions about the ignition capabilities of the igniters:

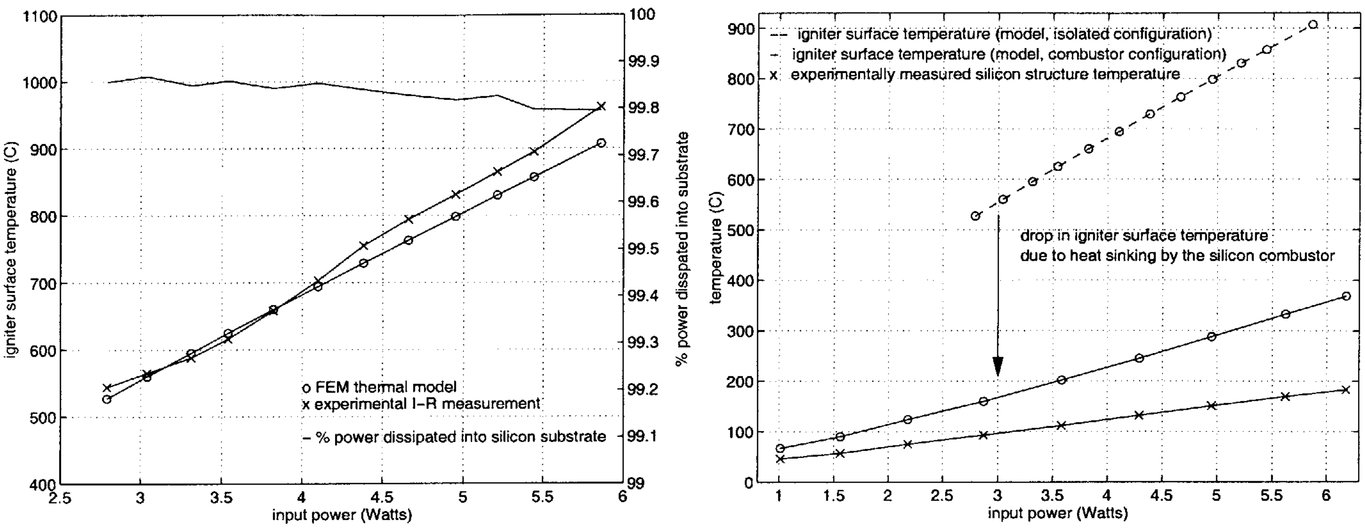

(a) Igniter temperature versus input power.

(b) Results for the 3-stack configuration.

Figure 5-11: Numerically predicted values of the igniter surface temperature, showing good comparison with the experimental data, and significant "heat-sinking" effect upon integration with the 3-stack.

1. The numerical and experimental results are in good agreement with each other, and suggest that it is possible to locally raise the temperature of the igniter to 900°C.
2. As long as the igniter reaches this temperature, it is able to reliably ignite a hydrogen-air mixture.
3. The igniter, as currently designed, is unable to initiate combustion in a silicon microcombustor because it is "quenched" by the rest of the silicon structure. This prevents it from reaching the high temperatures necessary for initiating combustion.

In theory, one could "inefficiently" ignite the mixture by adding enough power so that the entire structure heats up to the combustion temperature. The voltage required to achieve this however, was found to electrically break down the interconnects prior to the attainment of ignition temperature.

This electrical breakdown, along with overall material integrity issues, is described in the next section.

5.6.4 Material Integrity and Polysilicon Degradation

The igniters were found to exhibit two modes of failure:

Electrical Breakdown: At voltages above 300V, the polysilicon above the isolating trench was observed to electrically breakdown. As shown in Figure 5-12, this electrical breakdown resulted in loss of material above the insulating trench.

The power input to the igniters was therefore limited by this breakdown phenomenon.

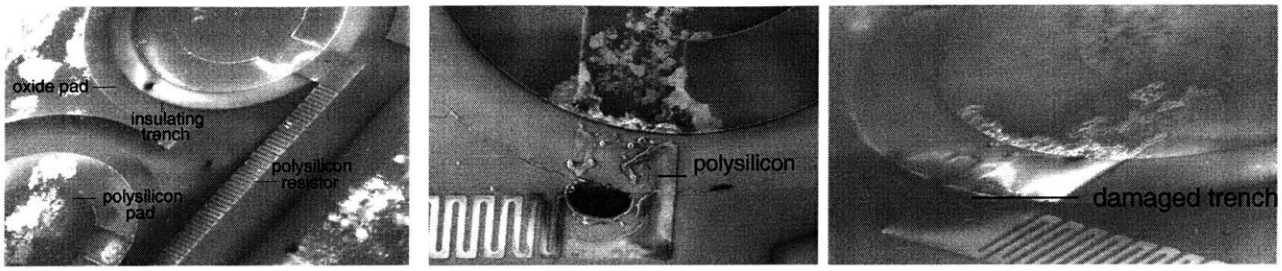

(a) SEM of an igniter prior to tests.

(b) SEM's showing the electrical breakdown of the igniter.

Figure 5-12: SEM's showing the igniters before and after electrical breakdown.

High Temperature Degradation: In addition to electrical breakdown, exposure to hot combustion gases was also found to thermally degrade the resistive elements.

Since evaluation of the structural survivability of the resistive elements was considered to be one of the primary objectives of the igniter study, considerable effort was spent in evaluating the mechanical integrity and high temperature degradation of the polysilicon. The experiments conducted for this purpose can be categorized as follows:

1. Combustion Tests: In order to evaluate the susceptibility of the polysilicon resistors to combustion gases, an igniter chip was attached to the 3-stack microcombustor and exposed to hydrogen-air combustion at equivalence ratios between 0.3 and 0.7. The corresponding combustion gas temperature was expected to be in the 1000°C - 1800°C range; the wall temperature ranged between 400°C and 700°C.

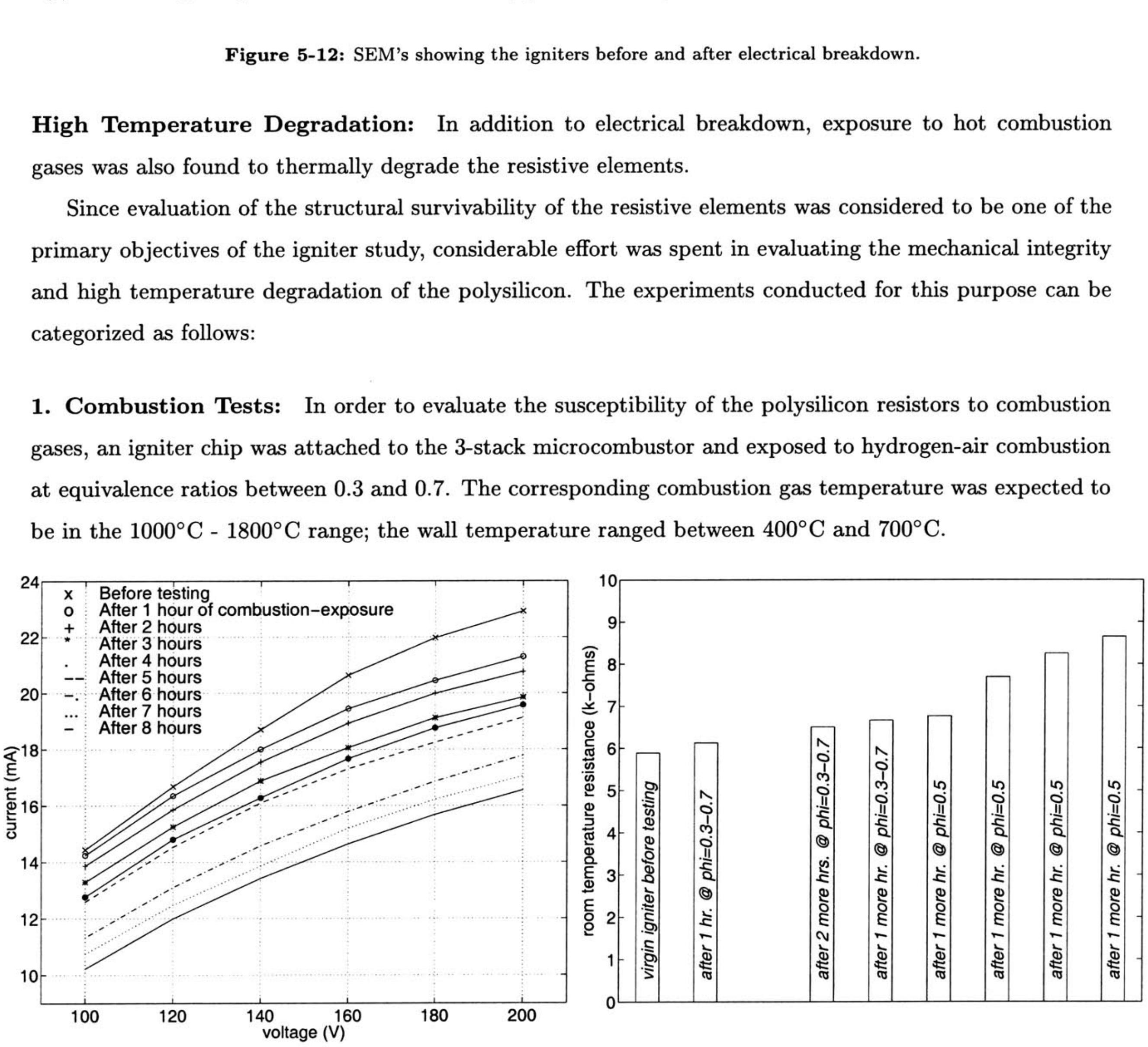

Figure 5-13: Igniter V-I curves before and after exposure to combustion gases, showing a minor increase in resistance. (During hours 1-4, the equivalence ratio of the mixture was varied between 0.3 and 0.7; during hours 5-8, the equivalence ratio was fixed at approximately 0.5.)

Figure 5-13 shows the room temperature V-I curves for one of the samples after progressive exposure to high temperature gases. The plots show a monotonic decrease in the current that suggests an increase in the element resistance with increasing exposure times. This increase is confirmed by a measurement of the room temperature resistance after each hour of high temperature exposure.

The increase can be explained by an examination of the igniters after these tests. As shown in Figure 5-14, although the resistor exhibited no visible degradation, the polysilicon above the oxide in the isolating trenches appeared to be severely damaged.

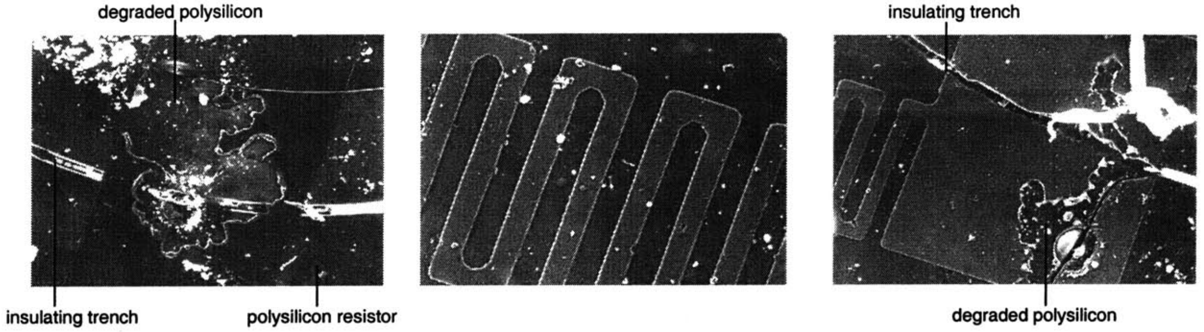

Figure 5-14: SEM's of the resistors after 8 hours of exposure to combustion gases, showing degradation of the polysilicon near the isolating trenches.

The exact cause of this degradation has not been determined, however, several contributing mechanisms can be identified:

1. *TEOS-polysilicon mismatch:* Since the polysilicon above the isolating trench rested on 100 μm deep TEOS, it is possible that plasticity in the TEOS at high temperatures caused the polysilicon to delaminate. Thermal expansion mismatch between the two materials, and release of trapped gases in the undensified TEOS [67] & [120], could also contribute to additional polysilicon degradation.

2. *Thermal oxidation:* Since the resistor was exposed to high temperature, lean-burning oxidizing environments, thermal oxidation could also be partly responsible for increasing its resistance.

3. *Chemical erosion:* The aforementioned contributors could also be chemically aggravated by the presence of combustion products.

It is also plausible that the polysilicon surface might be reaching its melting/evaporation temperature, however, this explanation was discounted because of the localized nature of the polysilicon failure. Since the resistor and interconnects were uniformly exposed to high temperature gases, pure thermal degradation of the polysilicon should have manifested itself uniformly across the element; the fact that the polysilicon preferentially degraded near the isolating trenches suggests that the presence of thick underlying TEOS in the isolating trench aggravates the degradation process observed in Figure 5-14.

In order to confirm this effect, and to evaluate the survival of the interconnects in the absence of oxidation or chemical effects, isothermal furnace tests were subsequently carried out in an inert ambient.

2. Isothermal Tests: were conducted by progressively exposing an igniter sample to a 200°C, 400°C, 600°C, 800°C, 900°C, 1000°C, 1100°C, 1150°C and 1200°C ambient for four hours each. SEM images of the each of the eight resistors were taken at each stage in order to document the onset of visible degradation.

Figure 5-15 shows one such igniter sample with visible degradation of the underlying TEOS after a 1200°C exposure. It also shows localized failure of the polysilicon near the isolating trench in a manner that is similar to the degradation observed during the combustion tests, and confirms that the presence of the underlying TEOS aggravates the degradation of the polysilicon.

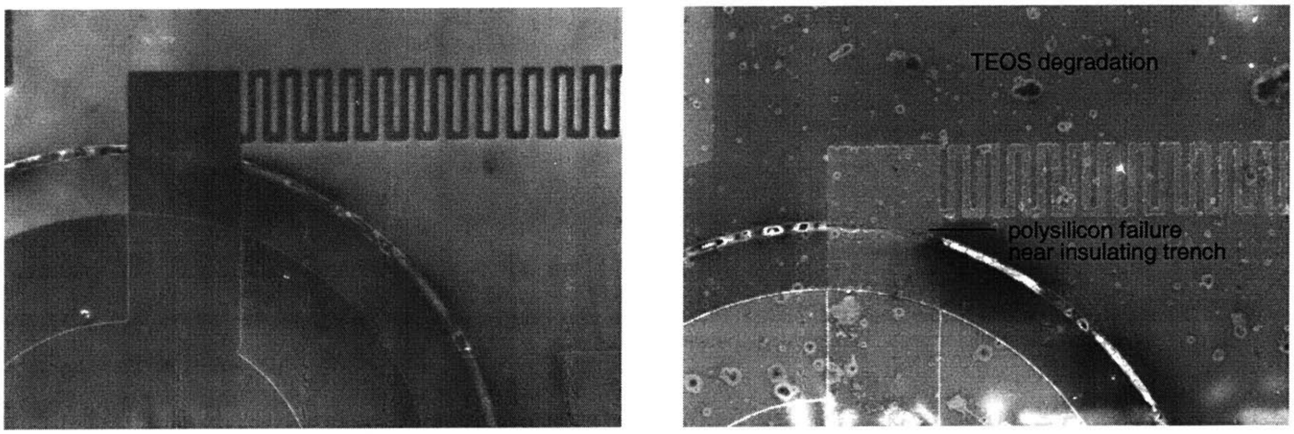

(a) Before exposure.

(b) After high temperature exposure.

Figure 5-15: SEM sample of an igniter before and after high temperature exposure in a furnace, showing localized polysilicon failure near the isolation trench, and visible degradation of the underlying TEOS.

3. TEOS versus Thermal Oxide: The influence of the underlying TEOS was further corroborated by high temperature tests on polysilicon samples with thermal oxide.

Figure 5-16 compares the surface roughness of polysilicon on TEOS with that of polysilicon on thermal oxide, and shows that polysilicon on TEOS exhibits approximately 50% more surface roughness after six hours of high temperature exposure under similar conditions.

The figure also shows that the surface roughness of a virgin sample prior to high temperature exposure is in the range of 3-5 nm. As shown in Figure 5-17, although signs of surface roughness and granularity first become visible at temperatures around 1000°C, severe degradation occurs at temperatures approaching 1200°C. This suggest that as currently designed, applications of the interconnects in inert high temperature ambients are therefore limited to temperatures up to 1200°C[2].

4. Oxidation Tests: were conducted by exposing a polysilicon igniter sample to an 1100°C ambient for six hours; the 0.5 μm thick polysilicon was found to grow 0.09 μm of oxide after the exposure. The test

---

[2] The maximum temperature seen by the samples during the fabrication process is 925°C, and is encountered during polysilicon doping.

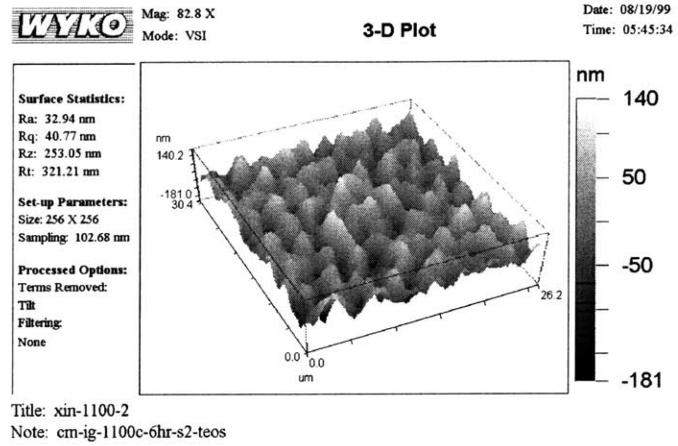

	R$_{average}$	R$_{RMS}$
Virgin poly before	3.6 nm	4.5 nm
Poly+thermal, after	19.6 nm	29.0 nm
Poly+TEOS, after	32.9 nm	40.8 nm

Figure 5-16: Polysilicon roughness before and after 6 hours at 1100°C for poly+TEOS and poly+thermal oxide samples. (Picture courtesy: Dr. Xin Zhang)

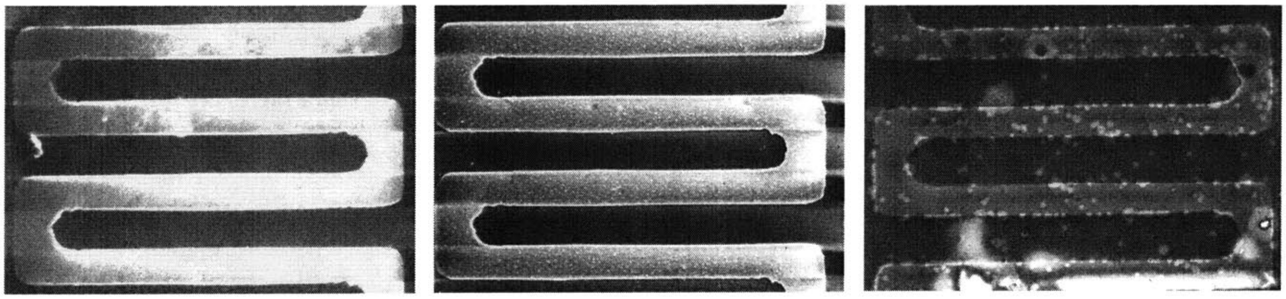

(a) Virgin igniter prior to testing.

(b) After 4 hours at 200°C, 400°C, 600°C, 800°C, 900°C and 1000°C, showing visible surface grains.

(c) After 4 more hours at 1100°C, 1150°C and 1200°C.

Figure 5-17: SEM's of the igniters after progressive high temperature exposure in a furnace, showing visible surface granularity at 1000°C, and severe surface degradation at 1200°C.

showed that oxidation can play a significant role in increasing the resistance of the igniters. Extended operation in the high temperature environment of a microengine combustor will therefore mandate a protective coating to retard the oxidation of the polysilicon resistors.

Conclusions

The results of the materials integrity study can be summarized as follows:

1. Although thin-film polysilicon can survive in a high temperature combustor environment, polysilicon on thick TEOS shows severe degradation. As currently designed, the polysilicon-TEOS interconnect is therefore considered unsuitable for direct exposure to combustion gases.

2. Exposure to inert high temperature environments also showed localized failure of the polysilicon above thick TEOS. Since the onset of severe degradation was first observed at temperatures nearing 1200°C, the maximum operating range of the through-wafer interconnects appears to be limited to 1200°C.

3. Oxidation of the thin-film polysilicon in high temperature environments can significantly alter the resistance of the elements. Long-term operation in combustion environments will therefore require a protective coating to retard the oxidation process.

5.6.5 Temperature Sensor Test Results

This section discusses the use of the polysilicon resistors as temperature sensors for the engine.

Use of the resistor as a temperature sensor is based on the ability to calibrate the TCR of the material, and then use an *in situ* measurement of the resistance to back-out its operating temperature. Figure 5-18 shows a calibration curve obtained from the resistance versus temperature data for various igniter runs.

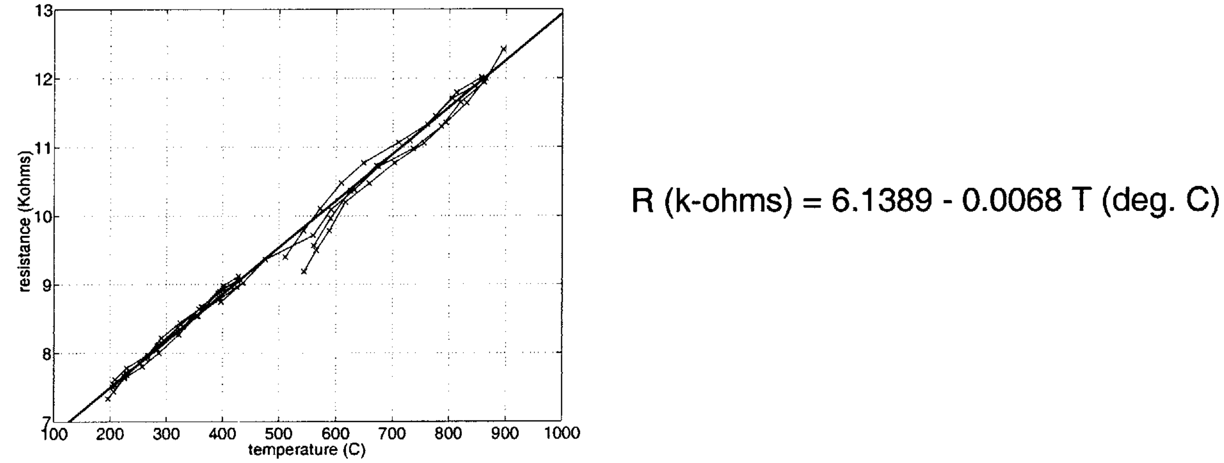

Figure 5-18: Linear fit to the resistance versus temperature data for the temperature sensor. (Note: Each curve represents a different run.)

The temperature sensing capability of the resistors was evaluated by exposing them to a combustion environment with equivalence ratios between 0.3 and 0.7. As shown in Figure 5-19, the resistance-based sensor measurements were then compared with independent measurements from an adjacent thermocouple. The figure shows that the resistance-based measurements from the sensor differ by as much as 150°C from the thermocouple results[3], however, more interestingly, it also shows a consistent increase in the sensor measurements with increasing exposure to hot combustion gases.

The increase in the resistance-based temperature measurement with increasing high temperature exposure can be explained by a change in the morphology of the polysilicon. As shown in Figure 5-13, prolonged exposure to high temperature combustion gases produces a bias increase in the polysilicon resistance which dynamically shifts the sensor calibration curve upwards. Consequently, the longer the sensor is exposed to high temperature gases, the higher is its temperature reading.

The change in the calibration curve also suggests that the sensor, as currently designed, is unusable in the high temperature environment of a microcombustor.

---

[3] The difference in the two temperature measurements may be attributed to inaccuracies in the sensor calibration curve.

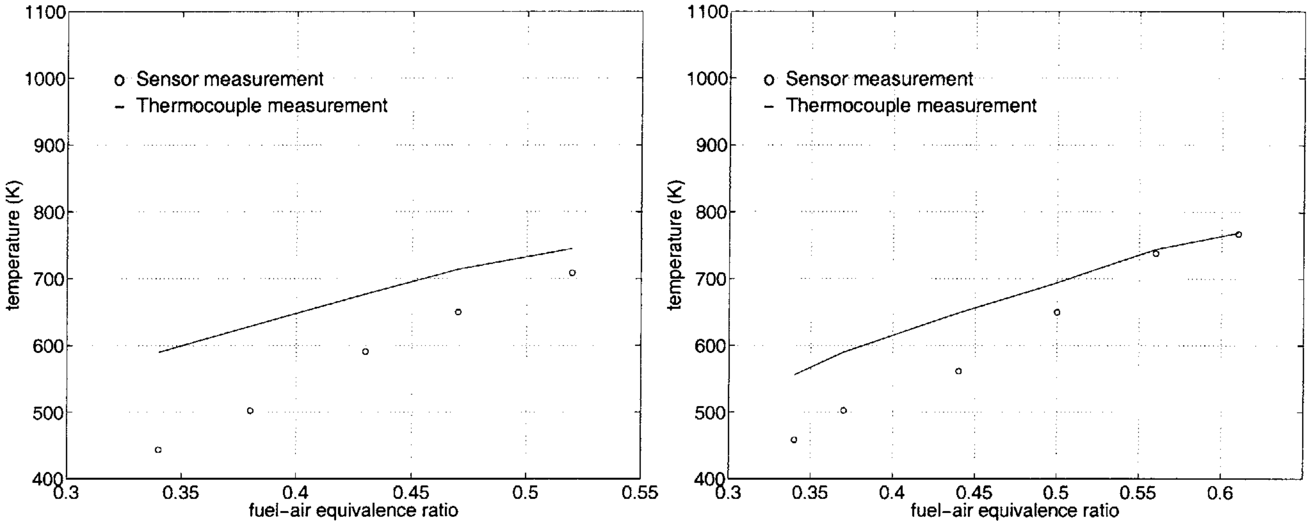

(a) Run 1.

(b) Run 2, after 1 hour of exposure.

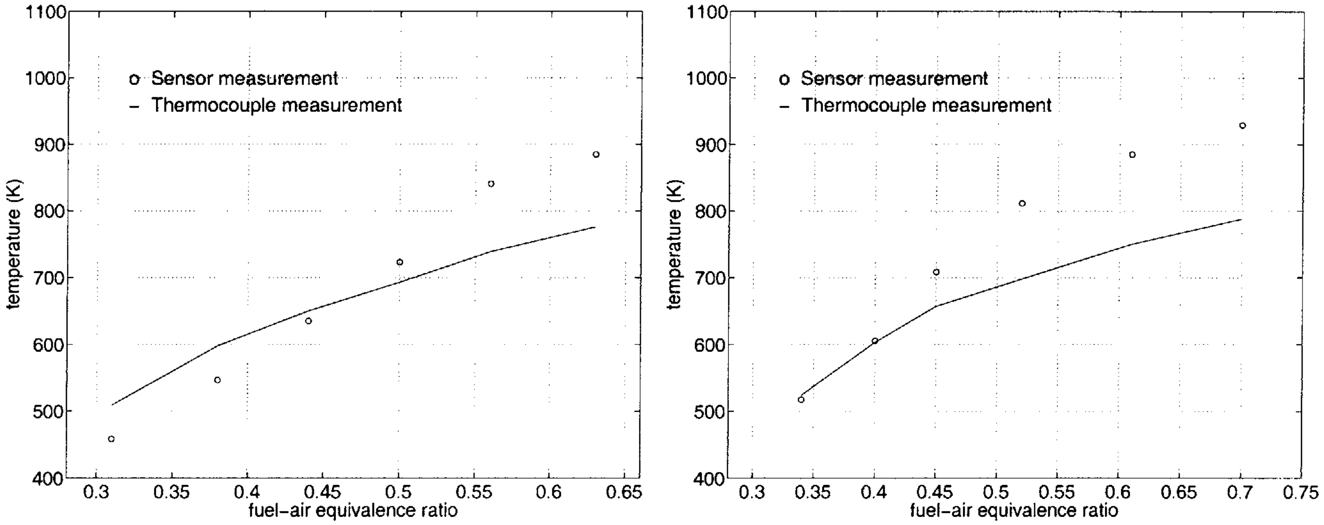

(c) Run 3, after 2 hours of exposure.

(d) Run 4, after 3 hours of exposure

Figure 5-19: Comparison of the sensor measurements with those from a conventional thermocouple. (Note: The plots represent four different runs after progressive exposure to combustion gases, and show a monotonic increase in the resistance-based measurement with increasing high temperature exposure.)

Consequently, in order to understand the increase in film resistance, and to identify a stable operating range for the sensor, patterned polysilicon films on thermal oxide were subjected to three different annealing experiments. These experiments were not intended to develop detailed mechanisms for high temperature polysilicon degradation; instead, they were only intended to see whether the behavior of the sensor was consistent with previously reported observations in the literature.

5.6.6 Determination of a Stable Temperature Regime for Polysilicon

Experiment one: Herein, samples were progressively exposed to temperatures between 200°C and 1000°C for four hours. The room temperature resistance of the igniter was measured after each run, and as shown in Figure 5-20, remained stable until 400°C and then became non-linear after a 600°C thermal anneal.

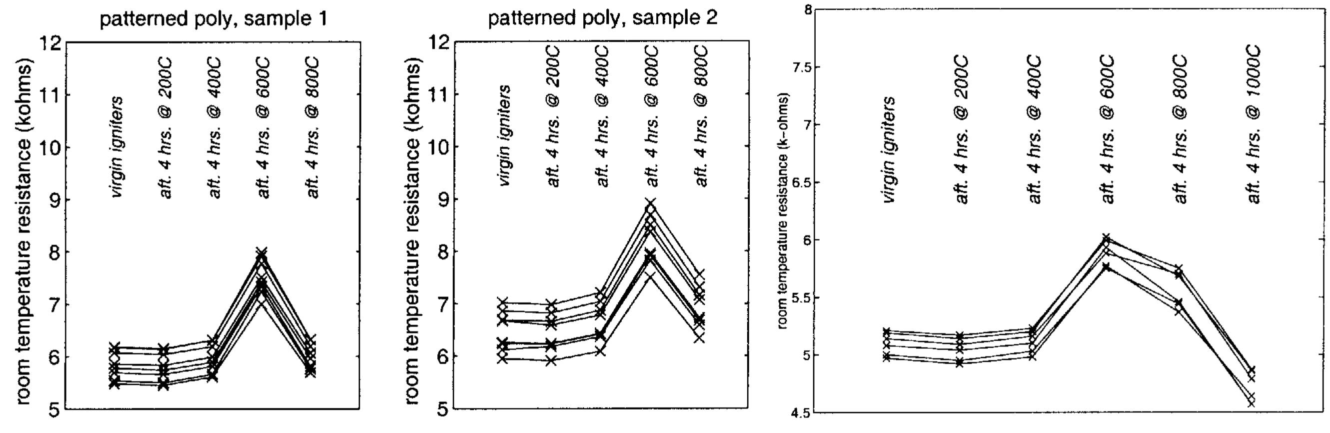

(a) Air-ambient.

(b) Nitrogen-ambient.

Figure 5-20: Measurement of the room temperature resistance of the polysilicon igniters after progressive high temperature exposure, showing a rapid drop in the resistance after a 800°C run. (Note: The different curves represent eight different igniters on a single chip.)

The behavior shown in Figure 5-20 has also been observed by other groups. Based on the results reported in references [9], [23], [70], [72], [74], [75], [86] & [103], the following mechanisms are proposed to explain the changes shown in Figure 5-20:

1. The initial increase in resistance may be explained by *changes in the concentration of electrically active dopant atoms*. Phosphorus atoms are known to diffuse towards the grain boundaries and become electrically inactive [23], [70], [75] & [86]. This phenomenon is known as dopant atom segregation, and can increase polysilicon resistance due to a reduction in the concentration of active carriers.

   Since the dopant level of the polysilicon films considered herein (10^{20} /cm^3) exceeds the theoretical saturation values for temperatures up to 1100°C [74] & [103], the films are in a super-saturated state after dopant diffusion. Therefore upon annealing, dopant atom segregation drives them towards equilibrium by reducing the concentration of active carriers, thereby causing the resistance to increase initially[4].

2. At higher temperatures, the increase in resistance due to dopant atom segregation is countered by the combined and dominating influence of two additional phenomenon:

   (a) *Secondary grain growth* with increasing temperatures [23], [74] & [75], increases carrier mobility due to a decrease in grain boundary scattering [103]. This may be predominantly responsible for the decrease in resistance that is observed in Figure 5-20 at temperatures beyond 800°C.

   (b) *Crystallographic relaxation* proposed by Colinge *et al.* partly removes grain boundary defects and increases the free carrier concentration at high temperatures [23]. This may also be partially responsible for the decrease in resistance observed at temperatures above 800°C.

Experiment two: was intended to see whether the sensor could be operated stably after an initial high temperature exposure of the type shown in Figure 5-20, and to evaluate the effects of multiple annealing cycles. The results are plotted in Figure 5-21, and show that the room temperature resistance of polysilicon following isochronal anneals settles into a cyclic pattern. Consistent with the observations of Makino *et al.* [74], this suggests that the resistance is predominantly determined by a combination of the solid solubility limit and the carrier mobility at each annealing temperature, and is therefore uniquely and reversibly determined by the last annealing temperature.

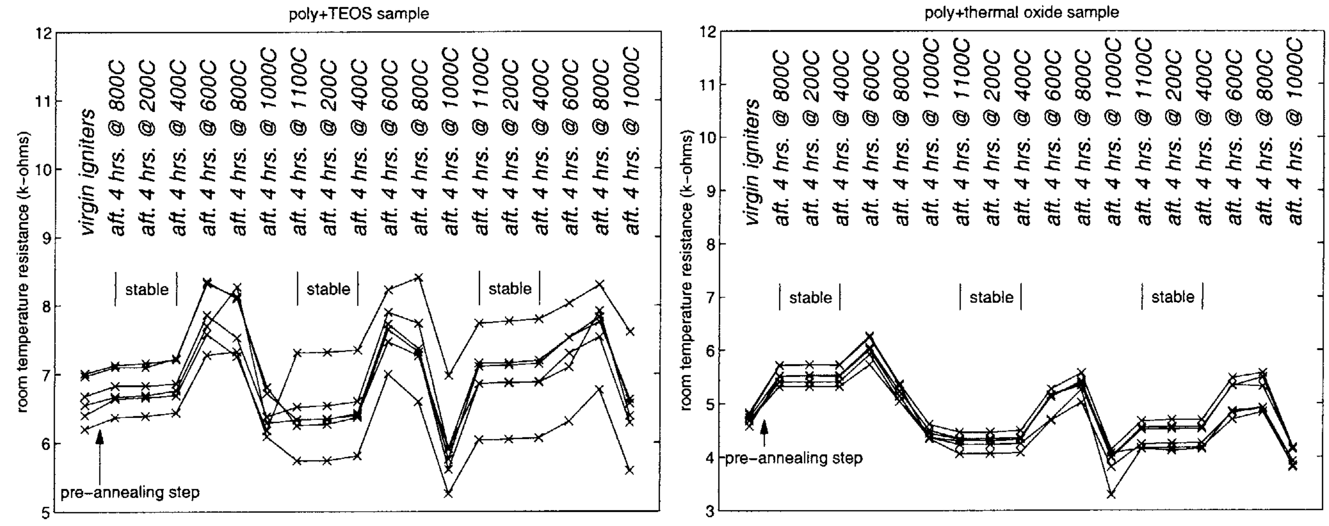

Figure 5-21: Room temperature resistance measurements of a pre-annealed polysilicon resistor after progressive exposures to an inert high temperature environment.

---

[4] Charge trapping effects are also known to cause an increase in resistance due to a reduction in the charge carrier concentration. However, since the 10^{12} /cm^3 sites available for charge trapping saturate at a negligible fraction of the total carrier concentration for heavily doped films [9], this effect is expected to be minimal for the films considered herein.

Experiment three: was intended to determine a stable operating regime for the sensor.

The results plotted in Figures 5-20 & 5-21 suggest that the resistance of the polysilicon is stable as long as it is annealed below 600°C. (Additional tests actually showed that the resistance was barely stable up to 450°C (Figure 5-22 (a)). With hopes to try and extend the operating range of the sensor, an attempt was made to stabilize carrier concentration at the highest annealing temperature at which resistance-reducing effects due to secondary grain growth and crystallographic relaxation have not yet set in. This temperature was empirically determined to be approximately 650°C for these particular samples.

In order to stabilize the carrier concentration, the samples were sequentially annealed in an inert ambient at 650°C until the resistance was observed to reach the equilibrium value; the results are plotted in Figure 5-22 (b). A similar stabilization of the resistivity due to attainment of equilibrium carrier solubility has also been reported by Makino *et al.* [74].

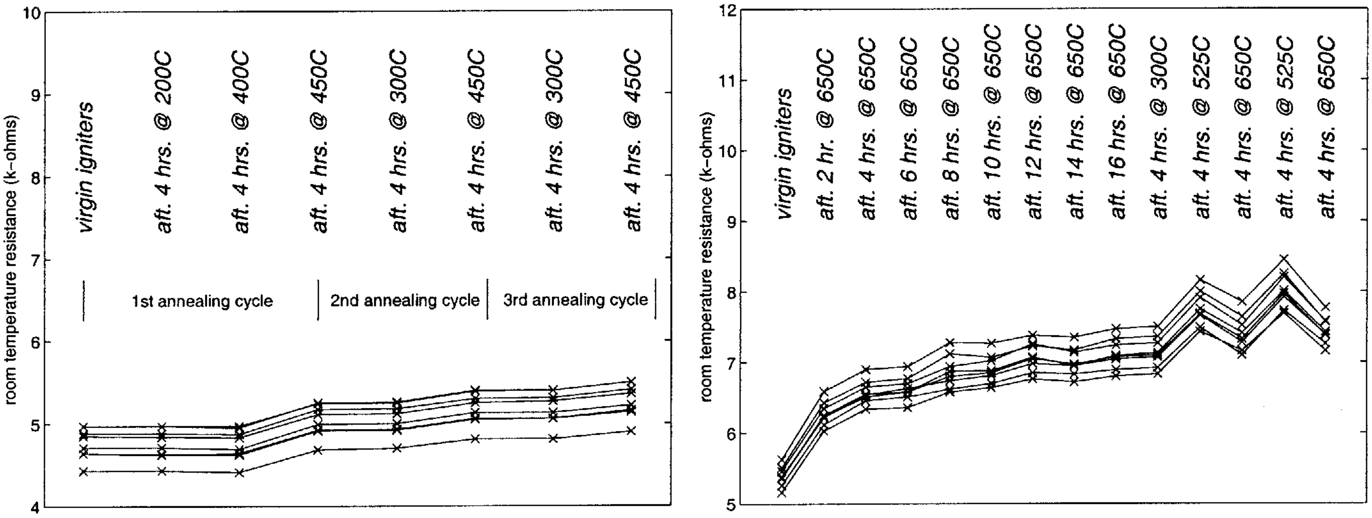

(a) Repeated anneals to 450°C show that the resistance of the sensor is barely stable beyond 450°C.

(b) Resistance of the sensor continues to change after an initial annealing-to-equilibrium step at 650°C.

Figure 5-22: Stability of the polysilicon resistance during repeated anneals up to 450°C and 650°C.

The samples were then isochronally re-annealed at temperatures between 300°C and 650°C to see whether the resistance remained stable thereafter. The results are plotted in Figure 5-22 (b), and show that even after the sensor has been pre-annealed to equilibrium at 650°C, its resistance continues to reversibly change between equilibrium values at 525°C and 650°C, and is uniquely determined by the last annealing temperature in the 400°C-650°C range. This suggests that as currently designed, the thin-film polysilicon sensors can only be used up to 400°C.

Conclusions

Results about the use of the polysilicon resistor as a high temperature sensor may be summarized as follows:

1. Prolonged exposure of the polysilicon to temperatures above 400°C dynamically changes the sensor calibration due to complex effects that result from dopant atom segregation, increased carrier mobility due to secondary grain growth, and crystallographic relaxation. As currently designed, the sensors are therefore unsuitable for use in the combustion environment of a microengine.
2. Since the sensor appears to be stable below 400°C for several hours, it may be suitable for use in some of the cooler sections of the microengine.

5.7 Recommendations for Design Improvements

5.7.1 Igniters

Even though the igniters could be heated up locally to 900°C, they were plagued by excessive heat loss to the supporting silicon substrate. This rendered them incapable of initiating combustion when integrated with the 3-stack microcombustor.

To improve the ignition capability of the igniters, partial under-cutting of the oxide below the resistor is recommended in order to reduce the heat loss to the silicon. As shown in Figure 5-23, results from the FEM model show that for operating conditions similar to the current 3-stack configuration described in Section 5.6.2, suspending the polysilicon igniter above a 2 μm air-gap can increase its surface temperature by up to 1400°C for the same power input.

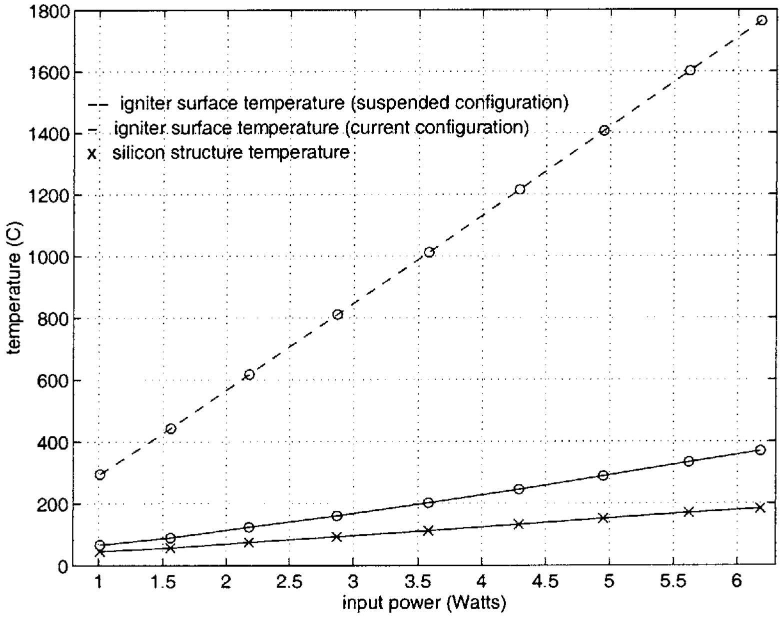

Figure 5-23: Results of the FEM model, showing a dramatic increase in the surface temperature of a suspended polysilicon igniter.

Isolation of the igniters in such a manner however, raises two additional issues:

1. Since polysilicon films are known to be in compressive residual stress, a long beam of thin-film polysilicon is likely to sag and contact the underlying silicon [98]. The resistor will therefore have to be shortened and redesigned to avoid this possibility.

   Alternatively, the underlying oxide could be patterned such that the resistor is supported by oxide posts along its length.

2. Isolating the thin-film polysilicon increases its susceptibility to high temperature degradation inside the combustion chamber. The functional design of the igniters may therefore have to be traded-off against their durability in a high temperature microengine environment.

5.7.2 Temperature Sensors

The evaluation of the temperature sensing capabilities of heavily doped thin-film polysilicon resistors showed that dynamic changes in the calibration curve due to charge segregation, secondary grain growth and crystallographic relaxation renders them unstable beyond 400°C.

Although there is no way to change the intrinsic behavior of polysilicon at high temperatures, the performance of the sensors may be improved by examining the following possibilities:

1. Since charge segregation effects are a strong function of dopant type and concentration, the doping process may be altered to delay the onset of these effects. This may extend the stable operating range of the sensors beyond 400°C[5].

2. The change in resistivity due to oxidation of the polysilicon may be retarded by incorporation of a protective oxide or nitride coating.

3. The inaccuracies in the calibration of the sensor may be reduced by using a more rigorous procedure to measure the temperature coefficient of resistance in an isothermal furnace environment.

4. The operating range of a thin-film temperature sensor may be also extended by re-examining the use of alternative metallic thin-films.

Experimentation on the temperature sensors also raises a more fundamental question - are the requirements for an igniter and a wall temperature sensor similar enough so that the same resistive element can perform as both ?

It is hypothesized that the results presented thus far suggest the contrary.

Since a good igniter is one that is able to initiate combustion with minimal power consumption, it must be isolated from the supporting substrate to avoid heat loss to the underlying silicon. A good temperature

---

[5] In addition, analysis using transmission electron microscopy is also suggested to correlate resistivity changes with increased grain size, and further substantiate the degradation mechanisms described in Section 5.6.6.

sensor on the other hand, is one that operates stably, and therefore needs to be shielded from the hot combustion gases via a thermal short to the substrate.

The requirements for a good igniter therefore mandate its direct and isolated exposure to combustion gases, and hence, its consequent degradation; the stability requirements for a good temperature sensor demand that it is heat sunk to the rest of the structure so that it does not degrade because of exposure to hot combustion gases.

These arguments suggest that the design requirements for a good igniter and temperature sensor are intrinsically divergent. The capabilities of both of these elements may be improved if they are individually re-designed for their specific functions; it is therefore recommended that:

1. The igniter be redesigned for lower power consumption and improved ignition capability through partial suspension above the silicon substrate. It should also be implicitly accepted that it will suffer some degradation, and have limited durability.
2. The temperature sensors be moved to cooler regions of the engine, or be heat sunk to the underlying silicon so that they can operate stably below 400°C.

5.7.3 Through-Wafer Interconnects

The through-wafer interconnects were found to suffer from the following shortcomings:

1. The silicon plugs were unable to sustain mechanical loading in excess of 0.2-0.4 lbf across the two sides of the wafer because they were only weakly supported by the TEOS in the isolating trench (40-80 psi. for a 2 mm diameter plug).

   The structural capability of the interconnects may be extended by examining the following possibilities:

   (a) Using directional DRIE to angle the sidewall profile of the through-wafer vias [8],

   (b) Corrugating the sidewalls of the plug to increase the contact surface area, or

   (c) Depositing an additional oxide coat on the backside of the trench.

2. Polysilicon on thick undensified TEOS was also found to degrade in high temperature environments. This may be remedied by:

   (a) Densifying the thick TEOS using techniques suggested in Ref. [43], or

   (b) Replacing the TEOS with higher temperature thermal oxide.

5.8 Chapter Summary

This chapter described the development of microfabricated "on-chip" igniters and temperature sensors for the combustion system of the engine.

It first presented the design and fabrication results of a novel through-wafer interconnect scheme that could greatly facilitate electrical contacts in multi-level MEMS devices by allowing direct electrical access to the backside of a wafer. The interconnects were shown to reliably contact to a polysilicon resistive element, however, material degradation of polysilicon on thick TEOS limited their operation to temperatures up to 1200°C.

The application of thin-film polysilicon resistive elements as igniters for the microengine combustor showed that it was possible to locally heat an isolated element up to 900°C and ignite a combustible hydrogen-air mixture. Prior to their integration into the microcombustor however, additional design changes are still needed to better insulate them from the supporting silicon substrate.

The use of doped polysilicon resistors as temperature sensors for the engine was also evaluated. The results suggested that a suitably calibrated sensor may be used in some of the cooler sections of the microengine up to temperatures of 400°C. This range is primarily limited by complex resistivity changes due to charge segregation, secondary grain growth and crystallographic relaxation effects that rendered the sensor difficult to calibrate.

Chapter 6

Implications for the Design of a Microcombustor

This chapter synthesizes the experimental results described in Chapters three and four to present overall implications for the design of a microcombustion system.

It begins by evaluating the effectiveness of the numerical tools used for the design of the static structure by comparing their predictions with experimental measurements. It then describes a simple design methodology that can be used as a first-order design tool for microcombustors, and finally presents recommendations for future builds for the MIT microengine. It also re-examines the primary drivers that differentiate microcombustors from their large-scale counterparts.

6.1 Assessment of the Design Methodology

6.1.1 Validation of the CFD Tools

This section compares the experimental results with predictions from CFD codes in an attempt to evaluate their effectiveness as a design tool.

The use of CFD during the initial design of the static structure was limited to cold-flow solutions, hence, this section shall only present comparisons with cold-flow experimental measurements discussed in Section 4.6.3.

Figure 6-1 shows the grid used for this purpose, along with a sample total pressure distribution from the CFD. It also plots the experimental and computational results for the static and total pressure ratios across the chamber. (Note: The results presented herein are for for the annular-inlet geometry.)

The figure shows that the computationally predicted values are within the experimental uncertainty of the measurements. However, although the static pressure ratios are in excellent agreement with each other, the experimentally measured total pressure loss is seen to be up to 50% higher than the computationally

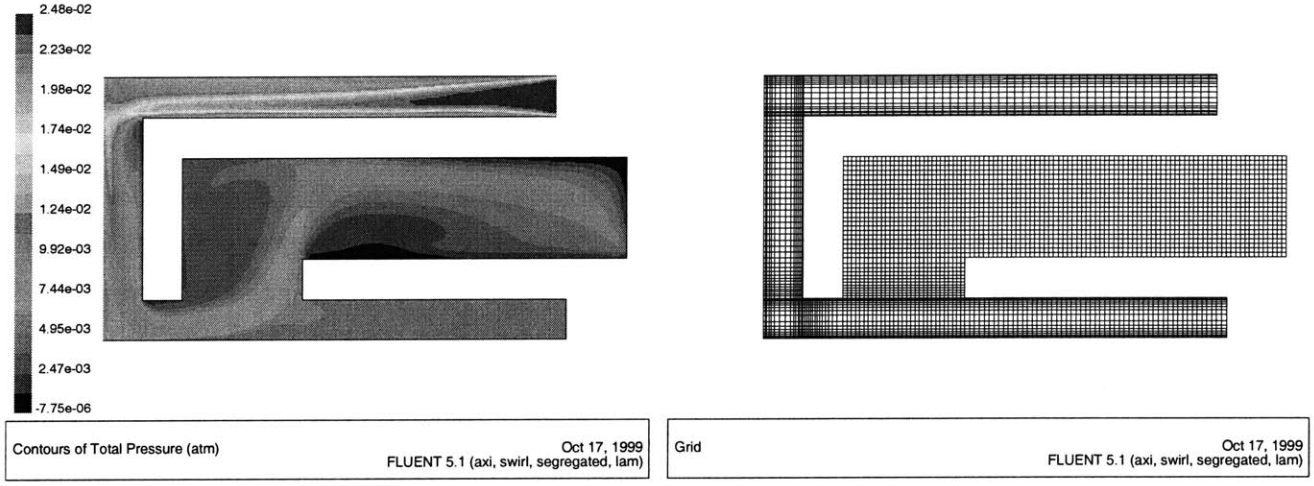

(a) Sample total pressure plot (gauge pressure).

(b) An illustration of the grid.

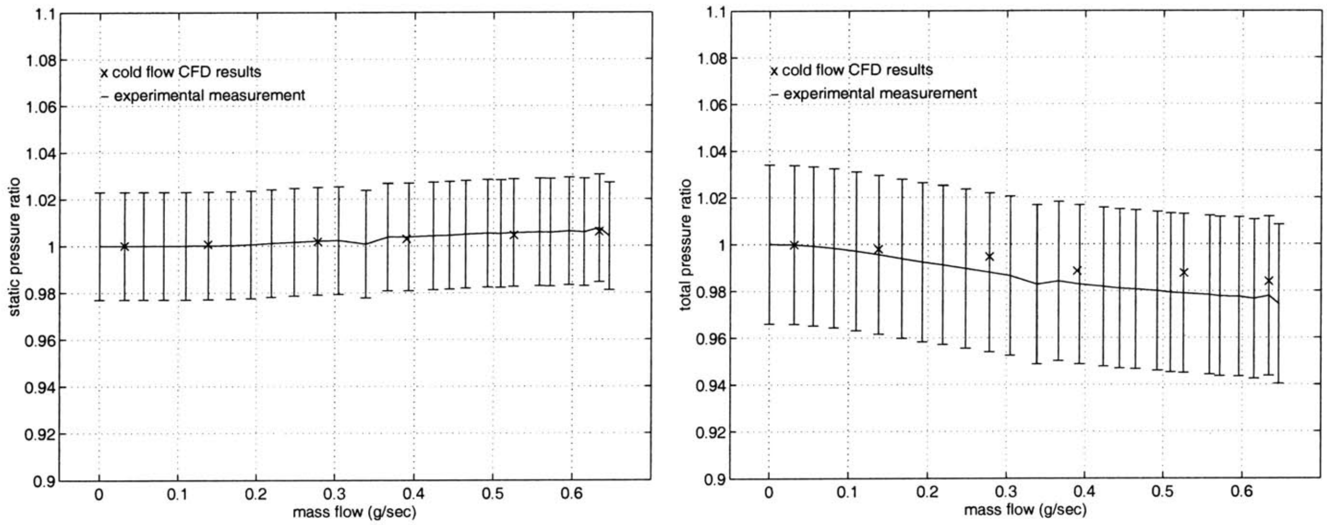

(c) Static pressure ratio versus mass flow.

(d) Total pressure ratio versus mass flow.

Figure 6-1: Comparison of the experimental cold-flow measurements with CFD solutions.

predicted value. This discrepancy is directly attributed to the uncertainty in the Mach number at the upstream pressure port location. Whereas the CFD solution showed that the compressor exit swirl had partly dissipated by the time the flow reached the pressure port location, the experimental derivation of the total pressure measurement assumed a flow angle of 75°. The upstream total pressure from the experimental measurement was therefore higher - this resulted in a lower total pressure ratio for similar downstream pressures.

Overall, 2-D axisymmetric cold-flow CFD models show good comparison with the experimental measurements for the annular inlet geometry. This suggests that they are suitable for estimating the cold-flow behavior of the static structure, and could serve as a useful design tool to predict the cold-flow performance of future designs[1].

6.1.2 Validation of the Heat Transfer/Structural Model

This section compares the predictions of the structural model developed by Huang [52] & [51] with experimental results in order to evaluate its effectiveness as a predictive tool. Details of this FEM structural model are presented in Appendix D.

Figure 6-2 (a) shows the experimental measurements of exit gas temperature, outer wall temperature and exit tube temperature as a function of equivalence ratio for one of the low mass flow runs described in Chapter four. It also plots the numerical predictions for the same conditions.

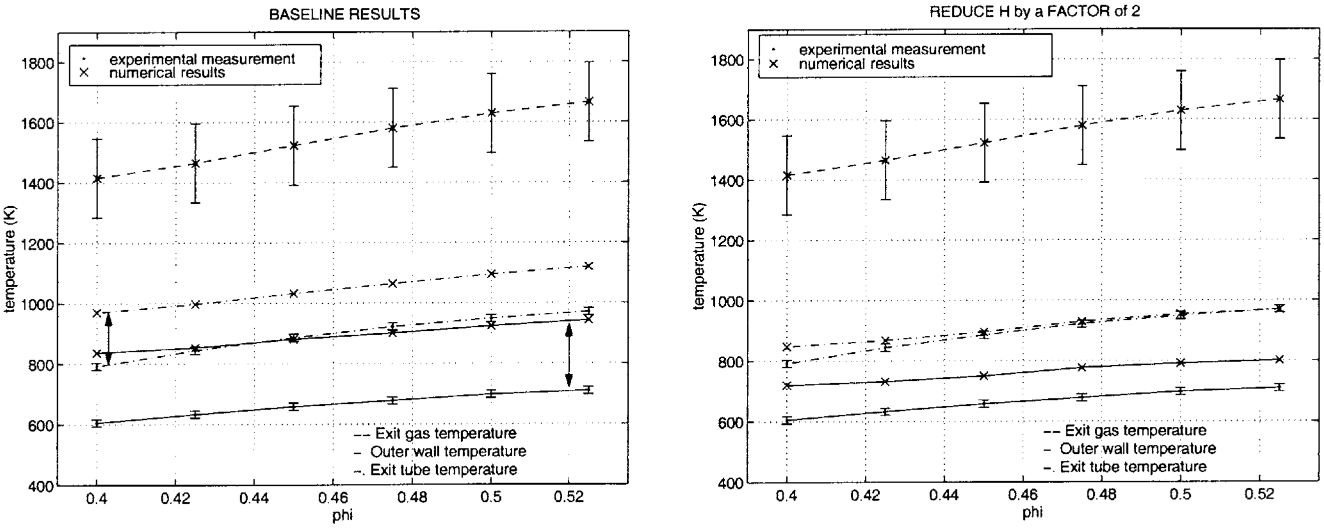

(a) Baseline comparison of the results from the heat transfer model with experimental measurements.

(b) Comparison with heat transfer coefficients reduced by a factor of two.

Figure 6-2: Comparison of results from the heat transfer model with experimental temperature measurements.

---

[1] The comparisons for the slotted inlet configuration were not carried out as part of this exercise - presumably, modeling the slotted inlet would require 3-D CFD.

The results show agreement within approximately 200K for outer wall and exit tube temperatures for matched exit gas temperatures and mass flow conditions. The discrepancy between the experimental measurements and FEM predictions is attributed to the following uncertainties:

1. The heat transfer coefficients in the FEM model were derived by Jacobson [55], from simple boundary layer correlations for the Stanton number. Since in fact, the flow in the combustor forms large recirculation zones, the heat transfer coefficients might deviate significantly from the values obtained by simple models for attached laminar boundary layers.

   The sensitivity of the FEM results to heat transfer coefficients was evaluated by uniformly reducing the value of h by a factor of two inside the computational domain. The results are shown in Figure 6-2 (b), and now show improved agreement within 40K for the exit tube temperature, and 120K for the outer wall temperature.

2. The FEM model uses species independent C_p to spatially update the fluid temperatures in the computational domain. Since the presence of combustion products in the NGV flow can change the C_p by up to 20%, inclusion of this effect will reduce the outer wall temperatures, and further improve the match between the experimental and numerical results.

3. The large uncertainty in the exit gas temperature measurement also contributes to the disagreement between the two results. If in fact, the exit gas temperatures in the FEM model were lowered, the resulting outer wall and exit tube temperatures would also be lower, once again, improving the agreement between the two results.

Overall, the discrepancy between the experimental and FEM results stems from the uncertainty in the inputs to the numerical model. This limits its capabilities as a predictive design tool. To improve this capability, it is therefore recommended that:

1. Efforts be undertaken to improve estimates of the heat transfer coefficients inside the static structure. These may include iterative collaboration between the FEM model, and turbomachinery and reacting flow CFD.

2. The FEM model be refined to include accurate representations of the fluid thermal properties.

6.1.3 Role of Conjugate Reacting-Flow, Heat Transfer CFD

In addition to the cold-flow CFD and FEM heat transfer models used during the design of the static structure, conjugate heat transfer-reacting flow CFD capabilities were also simultaneously developed by Lee in order to model the performance of the static structure [62]. Although the results from these computations are limited, this thesis will briefly introduce this model as a possible design tool for microcombustors. Inclusion of this "hot flow" CFD is not intended for detailed comparison of the experimental and numerical results, instead, it is only intended to present the full gamut of the numerical tools available to the designer of a microcombustion system.

Figure 6-3 plots a sample temperature distribution of the fluid and structural domains for one of the experimentally determined operating points for hydrogen-air combustion. It also compares the numerically predicted values of exit gas temperature and outer wall temperature with the experimental measurements for two different inlet temperatures into the device[2].

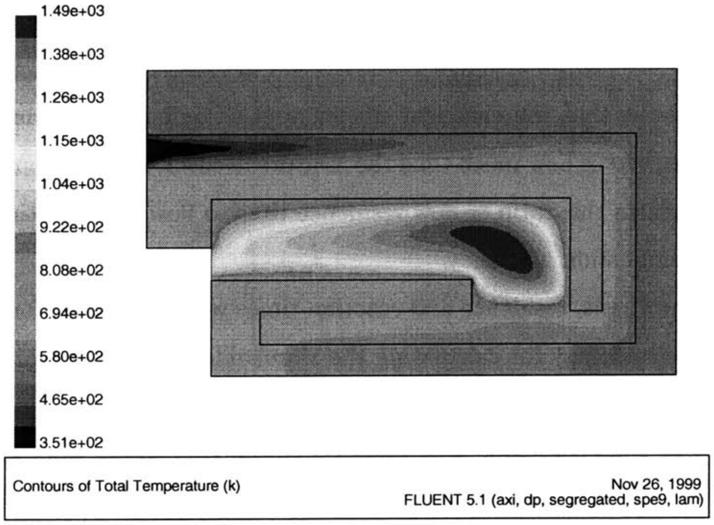

	CFD	Expt.
T_{in}=350K		
Exit temp. (K)	~800 (953)	750
Wall temp. (K)	500	415
T_{in}=500K		
Exit temp. (K)	~965 (1115)	750
Wall temp. (K)	800	415

Figure 6-3: Results from the conjugate reacting flow CFD showing good agreement with the experimental measurements, however, high sensitivity to inlet temperature boundary conditions. (Note: The exit gas temperature listed in parenthesis is the number at the inlet of the NGV's. Since the heat transfer analysis predicted a temperature drop of approximately 150K through the NGV's, 150K was subtracted from the computational results prior to comparison with experimental measurements downstream of the NGV's.)

The figure shows good agreement between the experimental and numerical results, however, it shows a high sensitivity to inlet gas temperature. Without detailed modeling of the compressor stator blades and turbine NGV's, the predictive capability of this axisymmetric 2-D computational model is therefore limited by the uncertainty in the inlet boundary condition.

Nonetheless, the results from the hot flow CFD show that it can serve as a powerful numerical tool for the design and analysis of such microcombustion devices. Additional efforts to refine and develop this model, especially in conjunction with the FEM heat transfer model, are therefore recommended for the continued development of microcombustion devices.

6.1.4 A Simple Damkohler Number Based Design Methodology

Although conjugate reacting flow CFD can serve as a useful tool for the design and analysis of microcombustion systems, it is cumbersome and time consuming. Faced with the inability to model all the experimental

---

[2] In this simplified 2-D axisymmetric model, the entrance to the computational domain was located at the exit of the compressor stator blades. The fluid temperature at this location was therefore unknown, and constituted a significant source of uncertainty.

operating points with detailed reacting flow CFD, this section presents a simple Damkohler number based model to:

1. Capture and explain the trends observed in the experimental data.
2. Identify the governing physics.
3. Serve as a first-cut design tool to evaluate different design options and concepts.

This model is similar to the one used in Chapter four to explain the shape of the exit gas temperature and efficiency curves for the static structure.

The model is based on the simple hypothesis that the chemical efficiency of a combustor is primarily determined by how much time the mixture has, versus how much time the mixture needs in order to complete combustion. Since the Damkohler number reflects this ratio of flow residence time to flow reaction time, it should be the fundamental determinant of combustion efficiency.

In order to evaluate the validity of the hypothesis, residence and reaction times were calculated for each of the experimental operating points. The methodology for calculating the Damkohler number is evaluated and presented in Appendix E.

Figure 6-4 plots the chemical efficiency of the combustor as a function of the Damkohler number for different operating points in the microcombustor. The figure shows 3-stack and 6-stack data for hydrogen-air combustion, and shows a gradual increase in combustion efficiency with increasing Damkohler number. It also shows a flattening of the combustion efficiencies for larger values of the Damkohler number.

As discussed in Appendix E, given the simplicity of using a single step reaction rate to approximate a complex chemical reaction, the uncertainty in the calculation of the reaction time can be large (up to a factor of two). Nonetheless, overall, the plot shows an initial increase in combustion efficiency with increasing Damkohler number, following which, the combustion efficiency asymptotes to unity for sufficiently large values of Da. The simple Damkohler number analysis is able to capture this trend successfully, and therefore corroborates the hypothesis that high power density microcombustors are primarily limited by residence time versus reaction time constraints.

6.1.5 Design Guidelines, Methodology for Microcombustion Systems

The results from the simple Damkohler number model suggest that it might be useful as a first cut design tool for microcombustion systems. As shown in Figure 6-5, the following design methodology is therefore proposed for this purpose:

1. Given basic system requirements for a microcombustor, the Damkohler number analysis may be used to calculate a first-order estimate of the minimum chamber volume necessary for complete combustion.
2. The estimate may be updated for any reduction in temperature that might result from heat transfer out of the chamber.

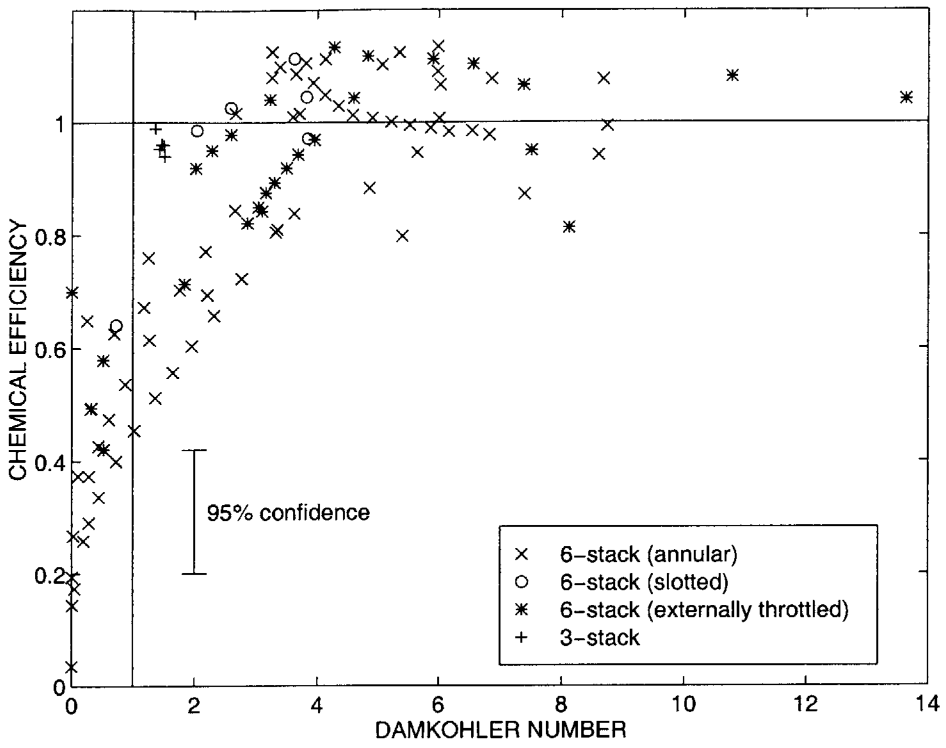

Figure 6-4: Combustion efficiency versus Damkohler number for various operating points.

3. The suitable geometry may be then be analyzed using reacting flow CFD and FEM structural models for more accurate estimates of its performance.
4. Finally, experimental data may be used to validate and empirically fine-tune the model for future design iterations.

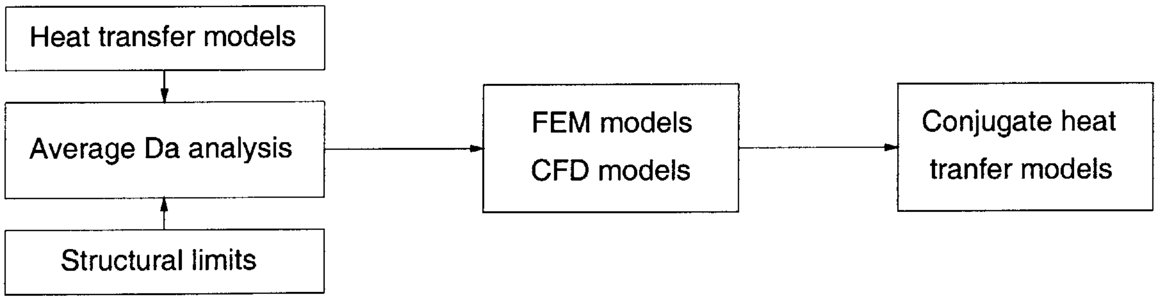

Figure 6-5: Design methodology for microcombustors.

It should be noted that this design model is not intended to be a predictive tool that replaces other computational tools. Instead given its simplicity, its utility is maximized if it is empirically tuned through CFD, and subsequently used for:

1. Comparing and evaluating trade-offs between different design concepts.

2. Estimating the limits of the design space - i.e., what is the smallest volume capable of sustaining combustion under certain operating conditions ?
3. Estimating trends, i.e., the relative leverage that may be obtained by increasing pressure versus temperature, etc.

6.1.6 Utility of the Model - Thought Experiments

The Damkohler model may also be used to make limited predictions for future microcombustor designs. Although the model cannot be used to estimate the exit gas temperature from the chamber, it may be used to estimate the residence and reaction times in the chamber for given operating pressures and temperatures. These estimates may then be used to answer questions like:

1. Assuming the exit gas temperature from the combustor is 1600K, how high does the operating pressure have to be in order to allow complete combustion at the design mass flow rate of the microengine ?
2. Given certain temperature and pressure, what is the maximum possible reduction in reaction rates the combustor can sustain, etc. ?

In order to answer these questions, the Damkohler number model was run at the design mass flow rate of the microengine. Figure 6-6 (a) plots the residence time and reaction time in the chamber as a function of the exit gas temperature for different operating pressures; Figure 6-6 (b) plots the Damkohler number under these conditions. The figures show the large benefit obtained by being able to operate at higher pressure, and suggest that as long as one is able to obtain an exit gas temperature of 1600K at 3 atm., the Damkohler number in the chamber should be high enough to allow complete hydrogen-air combustion at ϕ=0.5 - whether or not the combustor will actually produce 1600K exit gas temperature at 3 atm., ϕ=0.5, and $\dot{m}$=0.36 gm/sec, only experimental testing or conjugate heat transfer, reacting flow CFD can determine.

Figure 6-6 (b) may also be used to assess the viability of hydrocarbon combustion at the design mass flow rates of the microengine in the current design of the static structure. Since hydrocarbon reaction rates can be slower than hydrogen reaction rates by a factor of 10-60, reducing the rates by this amount will result in a Damkohler between 0.3-2 for an exit gas temperature of 1600K at 3 atm. Based on results shown in Figure 6-4, this is insufficient for design point hydrocarbon operation in the current design of the static structure.

Splitting the combustor into a dual zone geometry with a stoichiometric primary zone however, shows promise. Figure 6-7 plots the residence time, reaction time and Damkohler number for the primary zone of a dual zone geometry, assuming stoichiometric operation with half the air mass flow rate. The plot shows that as long as one is able to realize an exit gas temperature of 2400K at a pressure of 3 atm., the Damkohler number in the primary zone can be as high as 80. Reducing the chemical reaction rates by a factor of 10-60

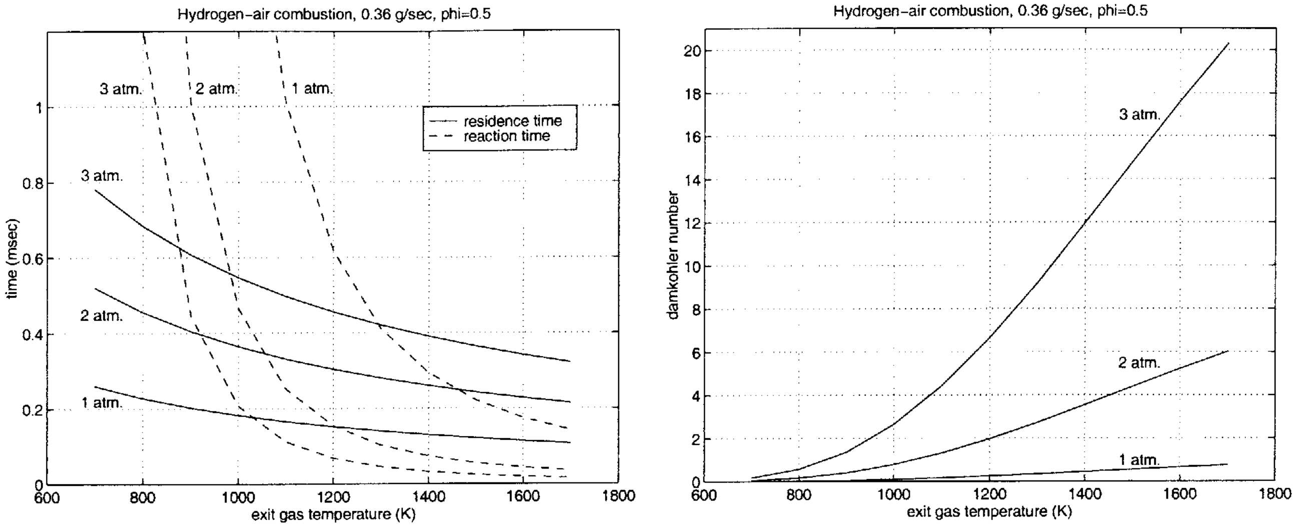

(a) Residence and reaction times for different operating pressures.

(b) Damkohler number for different operating pressures.

Figure 6-6: Predictions of the residence time, reaction time and Damkohler number in the chamber as a function of exit temperatures and operating pressure.

now only reduces the Damkohler number to 1.3-8. The possibility of hydrocarbon combustion is much more likely under this scenario. (Once again, whether the temperature at the exit of the primary zone will actually be as high as 2400K, only detailed reacting flow modeling or experimental testing can determine.)

6.2 Implications, Design Recommendations for the MIT Microcombustor

Based on the experimental and numerical results presented thus far, this thesis makes the following specific recommendations for future testing of the current configuration of the static structure:

1. Since experimental testing of the static structure showed acceptable operation up to 80% of the scaled design mass flow of the microengine, increasing reaction rates with increasing pressure suggest that it should be possible to operate at design mass flow and pressure without increasing the volume of the chamber. Efforts should therefore be directed at addressing operating line issues to get to design point by:
    - Either redesigning the NGV's to allow operation at higher pressures, or
    - Designing an external throttle that allows independent control of the pressure in the chamber.
2. The inability to get to design point due to operability issues also implies that it is not only sufficient to design a microcombustor for design point operation - operating line issues to get there also need to

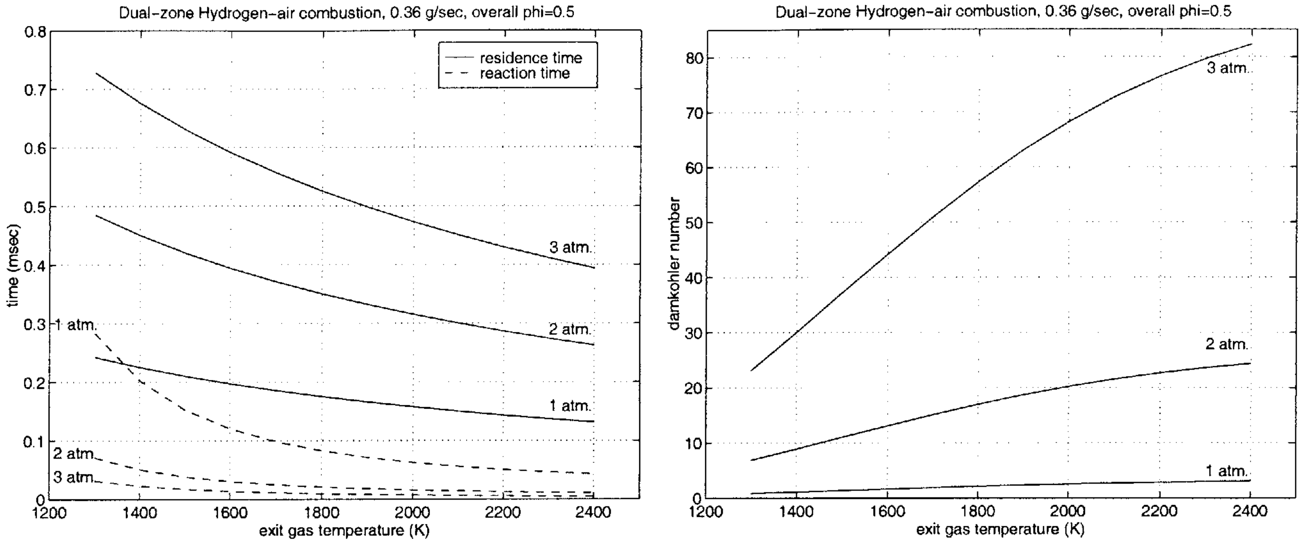

(a) Residence and reaction times for a dual zone combustor geometry.

(b) Damkohler number for different operating pressures.

Figure 6-7: Predictions of the residence time, reaction time and Damkohler number for a dual zone geometry.

be considered.

3. It should also be noted that the operating line issues described in Chapter four are only a concern for an unchoked-NGV combustor that is fed by externally pressurized air. Since the mass flow versus pressure curve for a combustor fed by a compressor will be different from that for a NGV-throttled combustor, these concerns will be alleviated once the combustor is integrated with the engine. Nonetheless, testing the static structure along the real operating line of the engine is critical for evaluating the start-up and off-design performance of the combustor.

4. Since the heat transfer coefficient in the FEM model have large uncertainty, efforts should be made to refine these values, thereby increasing the predictive capabilities of the analysis.

5. Based on packaging related difficulties, it is recommended that the backside pressure port be eliminated and replaced with internal plumbing to the front side of the chip.

6. The exhaust pipe used to axially direct the exhaust jet should also be permanently packaged into the static structure using the glass bead interconnect scheme.

Development of the next generation of microcombustor devices: Effective completion of the combustion process in the microcombustor requires three things:

1. Recirculation zones to rapidly initiate combustion,

2. Adequate residence time to complete combustion,

3. Mitigation of the effects of heat loss from the chamber.

Given these three requirements, and based on an examination of the computational and experimental results, this thesis makes the following general recommendations for the development of the next generation of microcombustion systems:

1. The geometry of the chamber should be tailored to allow maximum encapsulation of the incoming flow with multiple recirculation zones in order to facilitate rapid and uniform ignition of the reactants. This recommendation is based on the following two observations:
   (a) As shown in Figure 6-8, the incoming flow in the 3-stack is uniformly surrounded by hot recirculation zones on both sides - this causes all the streamlines to ignite simultaneously. In the 6-stack however, the ignition source is a single recirculation zone in the upper right-hand corner of the combustor. This is only able to ignite the streamline that is immediately next to it - the remaining streamlines are ignited by propagation through neighboring streamlines. It therefore takes longer for the bulk of the flow to ignite, hence up to 40% of the residence time in the chamber is not being utilized for combustion.
   (b) As stated in Chapter four, and shown in Figure 6-9, the slotted inlet configuration of the 6-stack showed higher efficiencies in the kinetically limited regime of the device. This corroborates the benefits of encapsulating the incoming flow with multiple recirculation zones that facilitate rapid ignition of the cold reactants.

2. The quenching effects of a cold combustor wall may be minimized by tailoring the geometry to insulate the chamber walls from the core flow with a region of stagnant air.

   This recommendation is based on an examination of streamline patterns for non-adiabatic solutions of the 3-stack and 6-stack configurations. As shown in Figure 6-8 (a), because the core flow is insulated from the chamber wall by two large recirculation zones on either side, the bulk of the flow does not lose heat as it passes through the 3-stack geometry (see Figure 6-10 (a)). In the case of the 6-stack however, the core flow is in direct contact with the top and bottom walls of the chamber (see Figure 6-8 (b)). As shown in Figure 6-10 (b), all the streamlines in the 6-stack non-adiabatic configuration therefore lose heat to the chamber walls as the flow passes through the combustor.

6.3 Re-Examining the Primary Drivers for Microcombustion Systems

This section utilizes the knowledge gained from the experimental and computational results to re-examine the key differentiators and drivers for microcombustor design and operation.

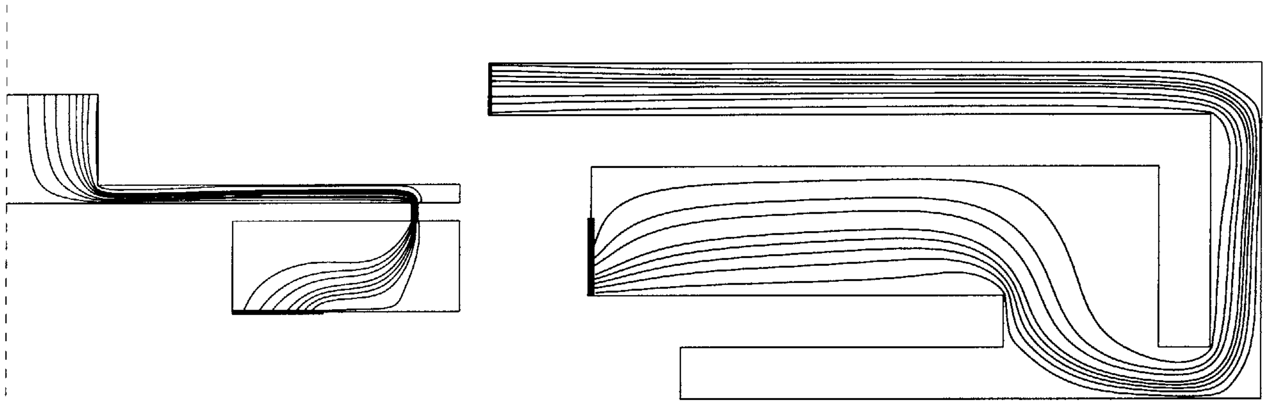

(a) Streamline pattern in the 3-stack.

(b) Streamline pattern in the 6-stack.

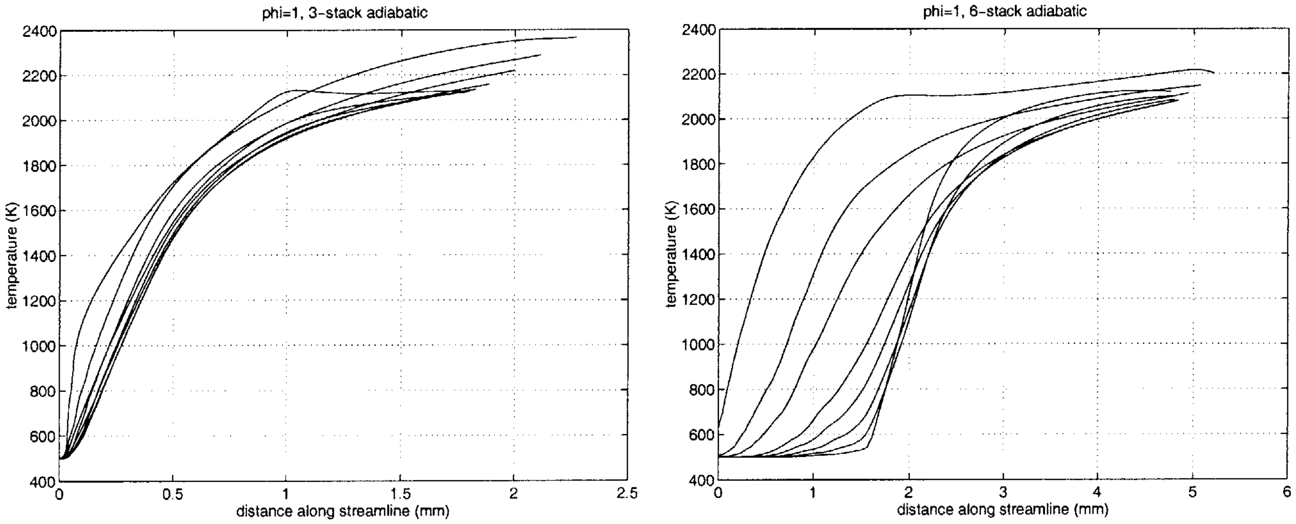

(c) Temperature along the streamlines in the 3-stack.

(d) Temperature along the streamlines in the 6-stack.

Figure 6-8: Recirculation zone and streamline patterns in the 3-stack and 6-stack, showing more effective ignition of the streamlines in the 3-stack configuration.

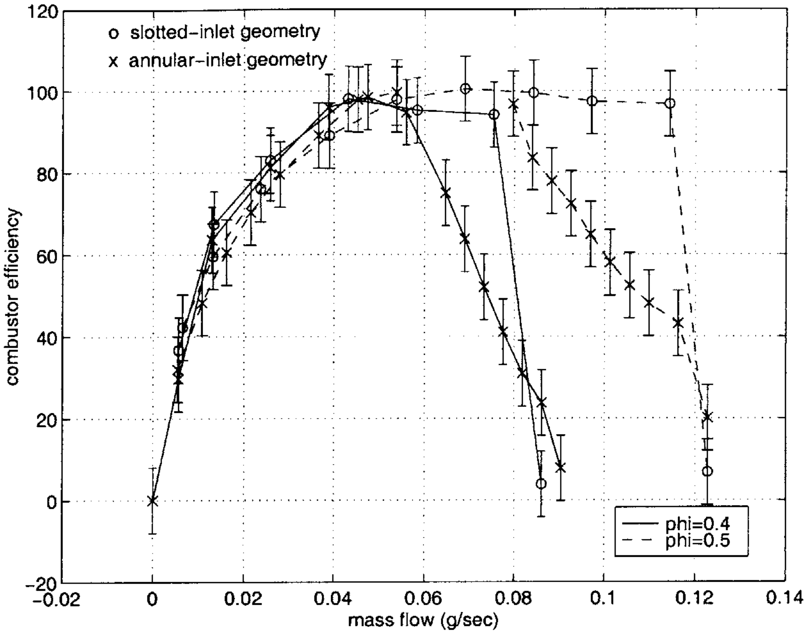

Figure 6-9: Comparison of the performance of the annular and slotted inlet geometries, showing higher efficiencies in the kinetically limited regime of the slotted inlet configuration due to more effective ignition of the incoming reactant stream.

Damkohler number constraints: The high power density requirement for microcombustor mandates high mass flow rates per unit volume. As shown in Figure 6-4, the design and operation of a high power density microcombustor is therefore limited by the Damkohler number in the chamber. Unlike large-scale combustors that operate at Damkohler numbers of 50-100, microcombustors operate at Damkohler numbers in the 1-10 range. This is graphically depicted in Figure 6-11.

Unlike large-scale combustors that are limited by fuel-air mixing rates, atomization and vaporization of the fuel, and emissions, stability, durability and pattern factor considerations, the design and operation of microcombustor is therefore fundamentally limited by the chemical reaction rates of the fuel.

Heat transfer effects: The large-surface area-to-volume ratio of microcombustor devices makes non-adiabatic operation intrinsic to their design. The coupling between the heat transfer and chemical kinetics is therefore a critical element of the design process.

The effects of heat transfer are illustrated in Figure 6-12 (a), which plots the thermal efficiency of the 3-stack as a function of equivalence ratio. Although design and packaging refinements can increase the thermal efficiency of the device close to unity (as in the case of the 6-stack shown in Figure 6-12 (b)), the presence of a cold chamber wall can have a severely detrimental effect on the reaction rates in the combustor. Figure 6-10 (b) shows the temperature drop due to heat transfer from the streamlines in the 6-stack, and serves as compelling evidence of the strong influence of heat transfer on chamber temperature, and hence, performance.

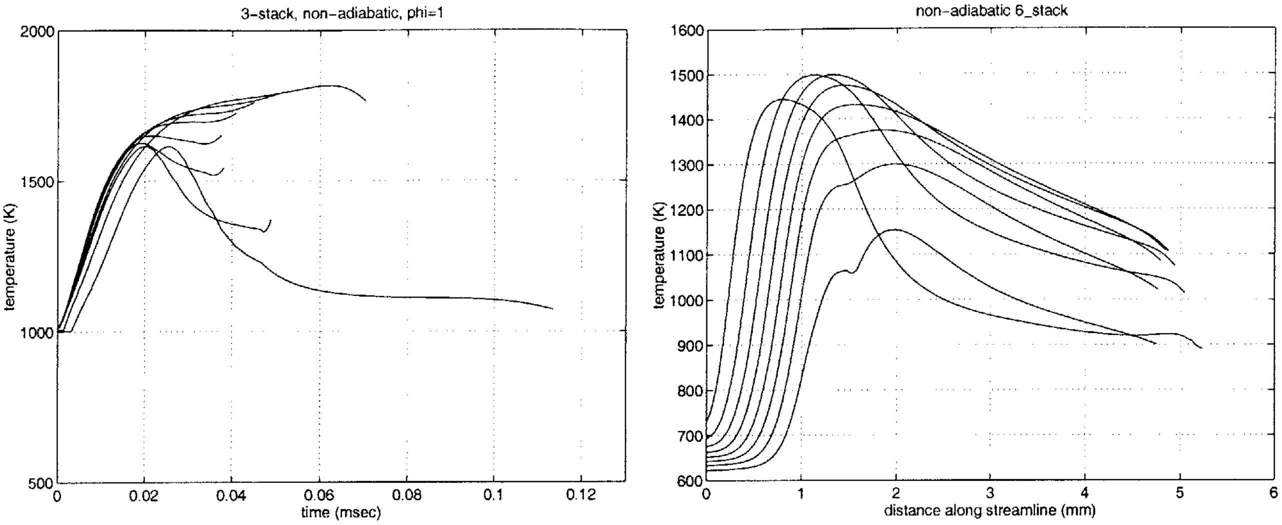

(a) Non-adiabatic streamline pattern in the 3-stack.

(b) Non-adiabatic streamline pattern in the 6-stack, showing a large temperature drop due to heat transfer to the chamber walls.

Figure 6-10: Streamline patterns from non-adiabatic solutions of the 3-stack and 6-stack geometries.

Limitations of the silicon microfabrication paradigm: Finally, use of silicon microfabrication techniques limits the geometrical flexibility availability to the designer of a microcombustor. The creep constraints of silicon also pose severe limitations on the maximum gas temperatures inside the chamber.

Use of these fabrication techniques therefore limits the design of the microcombustor to planar, stacked-wafer configurations out of silicon.

Since this thesis has examined microcombustion phenomenon in this type of configuration only, future designers are recommended to examine the possibility of working outside the paradigm chosen for the design and fabrication of the devices presented herein. Recommendations for dual-zone combustor geometries, improved cooling schemes and catalytic hydrocarbon combustion are presented in Chapter seven of this thesis.

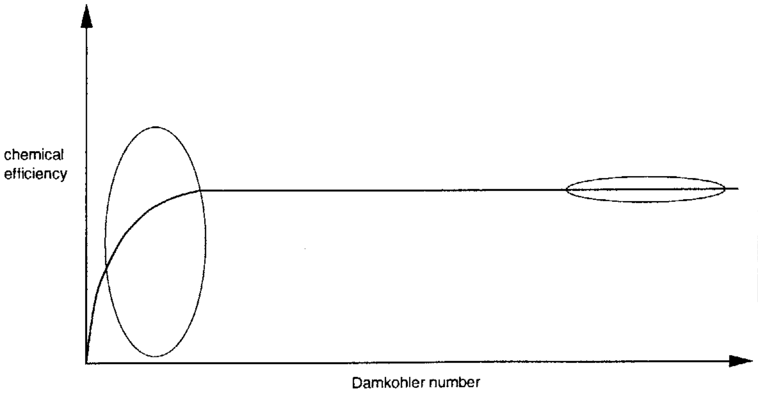

	μ-engine	JT-9D	μ/macro
P (atm.)	4	21	
$\dot{m}$ (kg/s)	1.8×10^{-4}	110	1.6×10^{-6}
V (m^3)	6.6×10^{-8}	.1	$.66\times10^{-6}$
τ_{res}	~.5 msec	~7 msec	.07
T$_{max}$ (K)	~1800	~2500	

Figure 6-11: Comparison of the operating regimes for microcombustors and large-scale combustion devices.

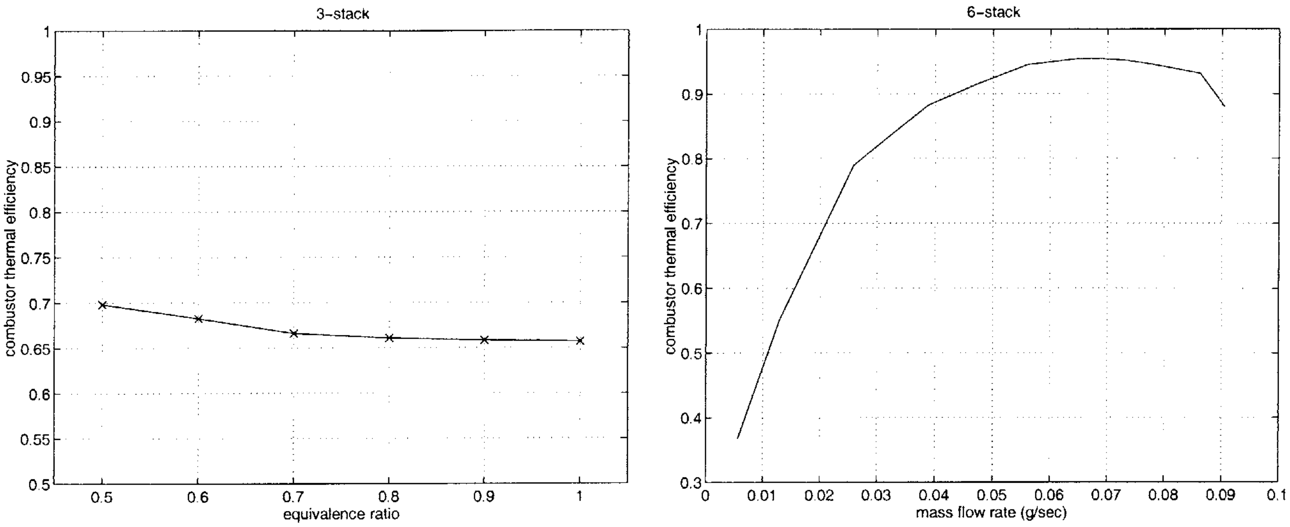

(a) Thermal efficiency of the 3-stack configuration.

(b) Thermal efficiency of the 6-stack configuration.

Figure 6-12: Thermal efficiency of the 3-stack and 6-stack configurations.

6.4 Chapter Summary

This chapter presented key implications for the design of microcombustion systems by first evaluating the effectiveness of the numerical tools used for the design of the static structure. It then presented a simple model that correlated an estimate of the Damkohler number with the combustion efficiency in the device, and proposed a general design methodology for microcombustor design.

Finally, it concluded with recommendations for future builds of the MIT microcombustor, and re-examined the primary drivers of combustion phenomena at the micro-scale.

Chapter 7

Conclusions

This chapter summarizes the research described in this thesis and presents conclusions and recommendations for future work.

7.1 Summary of the Research

As part of an effort to develop a new generation of micro gas turbine engines, a high power density hydrogen microcombustion system was designed, fabricated, packaged and tested. The experimental performance of the device was characterized in order to map its operating space, and to provide data for validation of the numerical models and design tools. The device was also used to explore the use of hydrocarbon fuels, and to present design guidelines for the future development of microcombustion systems.

The first step of the development process involved the identification of a lean burn hydrogen combustion strategy capable of satisfying all the system requirements and constraints of a micro gas turbine engine. Since the design of a high power density microcombustor is primarily dictated by residence time constraints and temperature limitations of silicon, the wider flammability limits and higher chemical reaction rates of hydrogen allowed timely completion of the chemical reactions within the fabrication and structural constraints of a small silicon chamber.

Using this scheme, the viability of non-premixed hydrogen microcombustion was demonstrated within the structural and volume constraints of a 0.066 cm^3 micromachined 3-stack silicon combustor with space heating rates at least an order of magnitude higher than that of any other power-MEMS device (2000 MW/m^3). Combined with results from a materials and oxidation study that showed acceptable oxidation and erosion rates in the high temperature and high Mach number environment of turbine nozzle guide vanes, the 3-stack microcombustor laid the foundation for an all-silicon micro heat engine.

The microcombustor was subsequently integrated with the remaining non-rotating components of the microengine in an effort to develop the engine "static structure". Intended to be the first demonstration of the completed hot flow path of multi-level microengine, the device was fully packaged and complete with fuel plenums, pressure ports, fuel injectors, compressor and turbine static airfoils, igniters and electrical and mechanical interconnects. The primary goal of the static structure was to serve as an experimental test bed for the identification of the stability boundaries for hydrogen and hydrocarbon combustion in the current design of the microengine.

The development process for the static structure comprised the following steps:

1. *Design:* Based on the results from the 3-stack microcombustor, and by using a combination of chemical kinetic, computational fluid dynamic and structural/heat transfer analyses, a design that satisfied the functional requirements and constraints of the MIT microengine was completed.

2. *Fabrication:* The 6-wafer, 3.8 mm thick-static structure was then fabricated using a combination of deep reactive ion etching and aligned fusion bonding.

3. *Packaging and integration:* The dies were packaged using glass bead pre-forms to make five frontside and one backside fluid connection. They were also integrated with sealed, resistively heated igniters.

   A parallel effort to use a novel through-wafer interconnect scheme to make direct electrical contacts to thin film polysilicon igniters and temperature sensors for the engine was also undertaken. The durability of the interconnects and resistive elements in a high temperature combustion environment was also extensively evaluated.

4. *Experimental testing:* The static structure was experimentally tested to:

   (a) Characterize its baseline performance for hydrogen and hydrocarbon fuels, i.e., measure the exit gas temperature, wall temperature, combustor efficiency and pressure loss for different equivalence ratios and operating pressures and mass flows.

   (b) Identify the combustion stability boundaries for hydrogen and hydrocarbon fuels, and map the feasible operating space for the device.

   (c) Evaluate the performance of different fuel injection schemes in order to identify the best location for fuel injection.

   (d) Evaluate the structural stability of the silicon in an engine-like configuration.

   (e) Provide data to validate the design analyses and tools.

The results from the experimental tests and numerical analyses were finally synthesized to propose design improvements and methodologies for future versions of microcombustors, and to make recommendations for future work.

7.2 Contributions of the Work

The most significant contributions of this thesis can be summarized as follows:

1. Design, fabrication, packaging and testing of the first high power density, hydrogen-fueled, micro-combustion system for a silicon micro gas turbine engine (power density=2000 MW/m^3). Specific contributions include:
    (a) First fabrication demonstration of the ability to deep reactive ion etch and align fusion bond six wafers with a total thickness of 3,800 μm in order to obtain a multi-level microengine structure.
    (b) Development of a methodology for packaging and integrating the device with fluidic interconnects and electrical contacts for resistively heated igniters.
    (c) Demonstration of premixed hydrogen-air combustion with 1600K exit gas temperature at 80% of the scaled design mass flow, and 84% combustor efficiency.
    (d) Identification of critical operating issues such as:
        - Empirical determination of the upstream burning and blow out boundaries in the device,
        - Evaluation of the effectiveness of the recirculation jacket, fuel injection schemes, etc., and
        - Identification of operating-line considerations to reach design point.
2. First demonstration of homogeneous hydrocarbon combustion in a micro-scale combustor:
    (a) Stabilization of ethylene-air combustion at 60% of the atmospherically scaled design mass flow of the microengine (T_{exit}=1400K, $\eta_{combustor}$=60%, power density=500 MW/m^3).
    (b) Stabilization of propane-air combustion at 17% of the atmospherically scaled design mass flow of the microengine (T_{exit}=1250K, $\eta_{combustor}$=55%, power density=140 MW/m^3).
3. Synthesis of the experimental results to present a simple Damkohler number based design methodology that:
    - Serves as a useful first-cut design tool to predict trends and evaluate different design concepts.
    - Captures important physical phenomenon.
    - Identifies Damkohler number versus power density as the primary trade-off for the design and operation of reaction time-limited microcombustors.

Additional contributions include:

1. Identification of the primary design challenges:
    - The power density of a microcombustion system is limited by the mixing and chemical reaction rates of the fuel. These in turn, are limited by the structural and fabrication constraints of the material. The key challenge facing the design of a high power density silicon microcombustor therefore lies in being able to complete the chemical reactions for higher and higher volumetric flow rates, and within the structural constraints of a microfabricated combustor.

- The coupling between fluid dynamics, heat transfer and chemical kinetics is much more pronounced for small-scale microcombustion systems, and is therefore a critical element of the design process.

2. Comparison of micro and macrocombustion systems:
   - Unlike the design of large-scale combustion systems that is typically driven by emissions, stability, pattern factor requirements, etc., the design of microcombustors is more fundamentally limited by the inability to complete combustion within the specified volume, and by material and fabrication constraints, low inlet pressures, and the inherently non-adiabatic nature of the operating space.

3. Thermal oxidation, materials and creep failure testing of silicon:
   - High temperature oxidation tests in a combustion environment produced oxidation rates between 0.1-0.9 μm/hr depending on the local temperature. These rates were found to be in good agreement with conventional thermal oxidation models for silicon, and suggested that the walls were not being subjected to "active-oxidation".
   - High temperature flow tests in the high Mach number and heat transfer environment of choked nozzle guide vanes showed minimal degradation and no more than 2% change in throat area after five hours at a gas temperature of 1800K, a pressure of 2.5 atm., and at a mass flow rate of 0.1 gm/sec. These results demonstrated the survivability of a static vane structure in a high pressure, temperature, and high Mach number flow environment.
   - Silicon was shown to exhibit creep failure following a brittle-to-plastic transition at approximately 900K, confirming structural predictions that the highly stressed components of the engine need to be operate below this temperature.

4. Interconnect, igniter and temperature sensor development:
   - A novel through-wafer interconnect scheme that provided electrical contact across two sides of a wafer was developed and applied to the fabrication and testing of thin-film polysilicon resistors. The scheme allows direct electrical access to components inside the engine, and can be expected to facilitate electrical connections in other multi-level MEMS devices as well.
   - An application of the through-wafer interconnects to a concept demonstration of thin-film polysilicon resistive igniters for the microengine showed that it was possible to initiate combustion and locally raise the temperature of the igniter to 900°C so long as the chip is thermally isolated. Prior to their integration with the microengine however, the results of the experiments and finite element modeling suggested that thermal insulation between the polysilicon and the underlying silicon substrate needed further improvement.

- The evaluation of the use of doped polysilicon resistors as temperature sensors for the microengine showed that non-linear resistivity changes of the polysilicon due to complex effects resulting from dopant atom segregation, secondary grain growth and crystallographic relaxation reduced the operating range of the sensors to 700K. A properly calibrated polysilicon resistor may therefore only be used as a temperature sensor in some of the cooler portions of the engine.

7.3 Recommendations for Future Work

Based on conclusions from this work, additional research is suggested in the following areas:

1. Design point operation of the static structure in order to evaluate combustor performance and silicon structural integrity may be obtained through a:
   (a) Redesign of the external throttling scheme to allow independent control of the pressure, or
   (b) Redesign of the nozzle guide vanes to allow higher operating pressures with in the chamber.

   Evaluation of the combustor performance along the true operating line of the engine is also recommended prior to its integration with the rotating components of the engine.
2. The performance of the hydrogen combustor may be further improved via redesigns that:
   (a) Encapsulate the combustor inlet flow with multiple recirculation zones in order to facilitate rapid and uniform ignition of the reactants.
   (b) Insulate the core flow from the cold walls with a layer of stagnant air in order to minimize the effect of heat loss.
3. The uncertainty in the measurement of exit gas temperatures may be reduced through the use of alternative infra-red or optical pyrometric measurement techniques [17] & [47]. Additional diagnostic techniques such as infra-red examination of thin-film polysilicon patterns inside the chamber would also provide valuable design information.
4. Uncertainty in the calculation of the combustion efficiency may be reduced through an independent measurement of the exhaust gas products using a gas sampling system.
5. Hydrocarbon combustion in the microengine may be explored via the following efforts:
   (a) Conducting system-level analysis to evaluate the acceptability of "fast-reacting" hydrocarbon fuels such as ethylene and acetylene.
   (b) Evaluating the effectiveness of seeding the fuel with hydrogen to spike the reaction rates.
   (c) Conducting materials tests to evaluate the durability of thin film platinum and palladium to catalyze the reaction.

    (d) Re-examining the design space of the microengine to evaluate the possibility of increasing the volume of the chamber.
    (e) Examining other combustion concepts such as a conventional dual-zone combustor, an externally-mounted chamber, etc.

6. The performance of the electrical interconnects, igniters and sensors may be improved by:
    (a) Increasing the structural and high temperature capability of the through-wafer interconnects using techniques recommended in Chapter five.
    (b) Redesigning the igniters for reduced power consumption by undercutting the underlying oxide.
    (c) Examining alternative metals or doping schemes for thin-film sensors inside the engine.

Appendix A

Uncertainty Analysis

This appendix quantifies the uncertainty in the measurements presented in this thesis. It first presents the uncertainty associated with the independent measurements, and then presents the predicted uncertainty in the derived quantities.

The uncertainty in the independent measurements will be based on the accuracy of the instruments. The random/precision uncertainty in the derived quantities will be propagated using:

$$p_y = \sqrt{\sum_{i=1}^{n} (\frac{\partial y}{\partial x_i} p_i)^2} \tag{A.1}$$

The bias/systematic uncertainty in the derived quantities will be propagated using:

$$b_y = \sum_{i=1}^{n} \frac{\partial y}{\partial x_i} b_i \tag{A.2}$$

where y is a function of n independent variables $x_1, x_2, .., x_n$, p_i is the random/precision uncertainty in each of the variables x_i, and b_i is the bias/systematic uncertainty in each of the variables [13].

The overall uncertainty u_y will be calculated by combining p_y and b_y using:

$$u_y = \sqrt{(p_y^2 + b_y^2)} \tag{A.3}$$

A.1 Uncertainty in the Independent Measurements

A.1.1 Mass Flow Measurements

The air mass flow was measured by an *MKS* 0358C meter (range: 20,000 sccm air). The meter was rated at 0.5% full scale accuracy. The manufacturer provided a 4-point calibration with a -0.273%, -0.235%, -0.448% and -0.050% deviation from full scale. The 95%-coverage bias uncertainty can be calculated by using a

Student-t distribution [5],

$$b_{\dot{m}_a} = \sqrt{B^2 + (t\sigma_x)^2} \tag{A.4}$$

where B is the mean bias, t is the t-value for a two-tailed Student-t table based on the number of sample points, and σ_x is the standard deviation of the sample.

Based on Eq. A.4, the 95%-confidence uncertainty in the air mass flow rate is ±0.68% F.S. or ±136 sccm.

The hydrogen mass flow was measured using an *MKS* 1359C meter (range: 10,000 sccm hydrogen). The accuracy of the meter was rated at 0.5% full scale. The 4-point calibration provided by the manufacturer showed a -0.28%, -0.19%, -0.19% and -0.58% deviation from full scale. Based on Eq. A.4, this corresponds to a 95%-confidence uncertainty of ±0.64% F.S. or ±64 sccm in the hydrogen mass flow measurement.

A.1.2 Pressure Measurements

The upstream and combustor chamber pressures were measured using *Sensotec* pressure gauges in the 100 psi range (Model LV/8183-15). The gauges were rated at 0.5% F.S. accuracy, hence, uncertainty in the measurement of the static pressure is ±0.5 psi.

A.1.3 Temperature Measurements

Wall temperatures were measured using *Omega* 10 mil type K sheath thermocouples (chromel-alumel). Exit gas temperatures were measured using *Omega* 10 mil type K unsheathed thermocouples (chromel-alumel). The manufacturer specified 2-σ error limits were 0.75% in a 273K-1523K range. This corresponds to an uncertainty of ±12K in the uncorrected temperature measurements presented in this thesis.

A.2 Uncertainty in the Derived Quantities

A.2.1 Equivalence Ratio

The equivalence ratio of the fuel-air mixture is defined as:

$$\phi = \frac{\dot{m}_f/\dot{m}_a}{\dot{m}_f/\dot{m}_a|_{stoichiometric}} \tag{A.5}$$

The uncertainty in the equivalence ratio is introduced by a bias uncertainty in the measurement of the hydrogen and air mass flow rates. Assuming a maximum air mass flow rate of 20000 sccm and a corresponding stoichiometric hydrogen mass flow rate of 8392 sccm, the maximum uncertainty in the equivalence ratio is given by:

$$b_\phi = \frac{\partial \phi}{\partial \dot{m}_f} b_{\dot{m}_f} + \frac{\partial \phi}{\partial \dot{m}_a} b_{\dot{m}_a} \tag{A.6}$$

Using this equation, the 95%-confidence uncertainty in the calculation of the equivalence ratio is ±0.014.

A.2.2 Combustor Static Pressure Ratio

The combustor and recirculation jacket pressure loss was calculated by measuring the static pressure at two locations - in the compressor exit duct upstream of the recirculation jacket, and inside the chamber. The static-to-static pressure ratio across the combustor is defined as:

$$\pi_c = \frac{P_2}{P_1} \tag{A.7}$$

where station (2) refers to a location inside the combustor, and station (1) refers to a location downstream of the compressor. (Note: This assumes that the two right-angle turns in the recirculation jacket downstream of the compressor are part of the combustor. Also, since no pressure measurements were made in the 3-stack combustor, the pressure uncertainty analysis is only valid for the static structure.)

Using Eq. A.2, the bias uncertainty in the combustor static pressure ratio is given by:

$$b_\pi = \frac{\partial \pi}{\partial P_1} b_{P_1} + \frac{\partial \pi}{\partial P_2} b_{P_2} \tag{A.8}$$

By assuming no pressure drop through the device, and an operating pressure of 3 atm., the 95%-confidence uncertainty in the combustor static pressure ratio is ±0.023.

A.2.3 Combustor Total Pressure Ratio

Since the combustor total-to-total pressure ratio needs to be calculated to determine the overall performance of the engine, it must also be derived from the two static pressure measurements in the static structure. The combustor total-to-total pressure pressure ratio is defined as:

$$\Pi_c = \frac{P_{2t}}{P_{1t}} = \frac{P_2(1 + \frac{\gamma_2 - 1}{2} M_2^2)^{\frac{\gamma_2}{(\gamma_2 - 1)}}}{P_1(1 + \frac{\gamma_1 - 1}{2} M_1^2)^{\frac{\gamma_1}{(\gamma_1 - 1)}}} \tag{A.9}$$

where station (2) refers to a location inside the combustor, and station (1) refers to a location downstream of the compressor.

In practice, the Mach number inside the compressor exit duct is expected to be 0.15 at design conditions[1]. The Mach number in the chamber is also expected to be as low as 0.1.[2] This makes the static pressure lie within 1.6% of the total pressure at these locations (i.e. the precision uncertainty in the total pressure

---

[1] The pressure port in the static structure is located at a radius of 6 mm. Assuming an operating pressure of 3 atm., a design mass flow of 0.36 g/sec, a compressor exit flow angle of 80°, and a temperature of 500K, the velocity at this location is expected to be 65 m/sec.

[2] Assuming a radius of 5.5 mm, an operating pressure of 3 atm., a temperature of 1600K, and radial flow in a 400 μm high streamtube, the velocity in the combustor is approximately 40 m/sec.

measurement is ±1.6%). Using Eq. A.1, the precision uncertainty in the total pressure ratio is:

$$p_{\Pi} = \sqrt{(\frac{\partial \Pi}{\partial P_{1t}} p_{P_{1t}})^2 + (\frac{\partial \Pi}{\partial P_{2t}} p_{P_{2t}})^2} \tag{A.10}$$

By assuming no pressure drop through the combustor, and a design point operating pressure of 3 atm., this is calculated to be ±0.023.

Using Eq. A.3 to combine the precision uncertainty with the bias uncertainty,

$$u_{\Pi} = \sqrt{(b_{\pi})^2 + (p_{\Pi})^2} \tag{A.11}$$

the 95%-confidence uncertainty for the combustor total pressure ratio is ±0.033.

A.2.4 Corrected Wall Temperature

The wall temperature thermocouples were inserted through microfabricated channels in the die that were approximately 400 μm high and 7000 μm long. The high aspect ratio of the channel was intended to eliminate radiative heat transfer between the wire and the wall. It was also intended to eliminate conduction corrections by providing a large surface area for contact [4].

A simple 1-D model showed that for these dimensions and operating conditions, the difference between the wall temperature and the thermocouple bead temperature would be less than 2K. Consequently, no additional conductive or radiative corrections were included in the wall temperature measurements, the uncertainty being limited to the manufacturer specified 95%-accuracy of ±12K.

A.2.5 Corrected Exit Gas Static Temperature

Unlike the wall temperature thermocouples, the gas temperature thermocouples were employed in a small and unshielded operating environment. Consequently, large temperature gradients are expected in both the flow field, and along the thermocouple wire. This results in a large difference between the flow temperature and the thermocouple bead temperature and thus, corrections must be made for the conductive, convective and radiative heat transfer along the thermocouple wire.

A thermocouple data reduction methodology to correct for the heat transfer losses has been described by Tzeng [114]. The energy balance across the thermocouple wire is provided in Ref. [15]:

$$\frac{d}{dl}(k\frac{dT}{dl}) + \frac{4h}{d}(T_{flow} - T) - \frac{4\sigma\epsilon}{d}(T^4 - T_w^4) = 0 \tag{A.12}$$

Tzeng [114] used a Gauss-Seidel numerical iterative scheme to solve for the flow temperature by imposing a known temperature boundary condition at some location along the wire, and by prescribing an initial guess for the flow temperature profile along the wire. For a converged solution, the corrected static temperature of the flow can then be expressed as a sum of the measured thermocouple temperature, a conductive correction, and a radiation correction:

$$T_{flow} = T_{measured} + \delta T_{conduction} + \delta T_{radiation} \tag{A.13}$$

The corrective terms in the numerical solution are:

$$\delta T_{conduction} = \frac{k_{tip} d(\Delta T)}{h_{tip} \Delta l (\Delta l \sqrt{26} + 3d)} \tag{A.14}$$

$$\delta T_{radiation} = \frac{\sigma \epsilon (T_{tip}^4 - T_{wall}^4)}{h_{tip}} \tag{A.15}$$

where Δl is the distance between the nodes on the spatially discretized thermocouple wire, and ΔT is the temperature difference between the tip and the adjacent node.

Using Eqs. A.1-A.3, the uncertainty in the measurement of the static temperature of the flow is:

$$u_{T_{flow}} = \sqrt{(b_{T_{flow}})^2 + (p_{T_{flow}})^2} \tag{A.16}$$

$$b_{T_{flow}} = b_{T_{measured}} + b_{\delta T_{conduction}} + b_{\delta T_{radiation}} \tag{A.17}$$

$$p_{T_{flow}} = \sqrt{(p_{T_{measured}})^2 + (p_{\delta T_{conduction}})^2 + (p_{\delta T_{radiation}})^2} \tag{A.18}$$

Each of these uncertainties can be quantified as follows:

Uncertainty in $T_{measured}$

There are two sources of bias uncertainty in the uncorrected temperature measurement:

1. Based on the manufacturing specifications, the Type K, 10 mil thermocouples are 2-σ accurate to within ±12K in a 273K-1523K range.

2. Tzeng [114] observed a drift of up to -20K after prolonged exposure in an oxidizing environment.

The overall bias uncertainty in the uncorrected measurement ($b_{T_{measured}}$) is therefore ±32K.

A precision uncertainty is also introduced into the static temperature measurement due to the stagnation of the flow at the tip of the thermocouple. The static temperature at the tip is given by:

$$T_{static} = \frac{T_{measured}}{1 + r[(\gamma - 1)/2]M^2} \tag{A.19}$$

where r is the recovery factor of the thermocouple, and usually varies between 0.6 and 0.9 for a bare thermocouple sensor [28]. A precision uncertainty is therefore introduced in the uncorrected static temperature measurement due to the variation of γ, M and r. Assuming:

1. The mean γ is 1.28, and varies between 1.31 and 1.26[3],
2. The mean Mach number at the exit is 0.05[4], with a variation of ±0.05, and
3. The average recovery factor is 0.75, with a variation of ±0.15,

the precision uncertainty in the measurement of the uncorrected static temperature is given by:

$$p_{T_{measured}} = \sqrt{(\frac{\partial T_{measured}}{\partial \gamma} p_{\gamma})^2 + (\frac{\partial T_{measured}}{\partial M} p_M)^2 + (\frac{\partial T_{measured}}{\partial r} p_r)^2} \quad (A.20)$$

This is calculated to be ±0.85K.

Uncertainty in $\delta T_{conduction}$

As stated earlier, the conduction correction is given by:

$$\delta T_{conduction} = \frac{k_{tip} d(\Delta T)}{h_{tip} \Delta l (\Delta l \sqrt{26} + 3d)}$$

There are three sources of precision uncertainty in the conduction correction:

1. A ±1 mm uncertainty in the measurement of the thermocouple length results in a precision uncertainty $p_{\Delta l}$=±0.05 mm in Δl (assuming 20 discretized nodes).
2. An uncertainty in the correlations used to calculate the convective heat transfer coefficient results in a precision uncertainty in the value of h_{tip}. To calculate this, Tzeng [114] used the following equations:

$$h_{tip} = \frac{Nu_d k_{flow}}{d} \quad (A.21)$$

$$Nu_d = sin^2\theta Nu_{d,parallel} + cos^2\theta Nu_{d,cross} \quad (A.22)$$

$$Nu_{d,parallel} = 0.085 Re_d^{0.674} \text{ and } Nu_{d,cross} = 0.44\sqrt{Re_d} \quad (A.23)$$

$$Re_d = \frac{Ud}{\nu} \quad (A.24)$$

where θ is the angle between the flow direction and the thermocouple wire, and $Nu_{d,parallel}$ and $Nu_{d,cross}$ are the Nusselt numbers for parallel and cross-flow over fine wires.

Tzeng [114] predicted an uncertainty of ±7.4% and ±13.7% in $Nu_{d,parallel}$ and $Nu_{d,cross}$, respectively. For a baseline Re_d=34, and $Nu_{d,parallel}$=0.9 and $Nu_{d,cross}$=2.53, the precision uncertainties

---

[3] The mean value is for the product-mixture resulting from hydrogen-air combustion at 1600K. The extrema are calculated for a fully-reacted mixture with ϕ varying between 0.3 and 0.7.

[4] Based on an exit temperature of 1600K, a mass flow rate of 0.36 g/sec, and an exhaust radius of 3.7 mm, the velocity at the exit of the static structure is expected to be approximately 40 m/sec. The variation is calculated assuming the device is operated at twice the mass flow.

in $Nu_{d,parallel}$ and $Nu_{d,cross}$ are ±0.07 and ±0.35, respectively. Assuming the thermocouple wire is transverse to the flow within 20°, the overall precision uncertainty in Nu_d is given by:

$$p_{Nu_d} = \sqrt{(\frac{\partial Nu_d}{\partial Nu_{d,parallel}} p_{Nu_{d,parallel}})^2 + (\frac{\partial Nu_d}{\partial Nu_{d,cross}} p_{Nu_{d,cross}})^2 + (\frac{\partial Nu_d}{\partial \theta} p_\theta)^2} = \pm 0.85 \tag{A.25}$$

The precision uncertainty in the calculation of the thermal conductivity of the mixture also needs to be calculated. Using Ref [58], the mixture-averaged thermal conductivity is given by:

$$k_{flow} = \frac{1}{2}(\sum_{i=1}^{n} X_i k_i + \frac{1}{\sum_{i=1}^{n} X_i/k_i}) \tag{A.26}$$

Since the exact composition or temperature of the mixture is an unknown, the average conductivity value shall be calculated for the products resulting from the complete combustion of a ϕ=0.5, hydrogen-air mixture at 1648K. The extrema shall be calculated for the complete reaction of a mixture with ϕ varying between 0.3 and 0.7. This places the average k_{flow} at 0.122 W/mK, and the uncertainty at ±0.035 W/mK.

Using the uncertainties in Nu_d and k_{flow}, the overall precision uncertainty in the calculation of the heat transfer coefficient is:

$$p_{h_{tip}} = \sqrt{(\frac{\partial h_{tip}}{\partial Nu_d} p_{Nu_d})^2 + (\frac{\partial h_{tip}}{\partial k_{flow}} p_{k_{flow}})^2} = \pm 545\ W/m^2K \tag{A.27}$$

This corresponds to uncertainty that is approximately 44% of the average h_{tip} (1235 W/m^{2}K).

3. An uncertainty in the thermal conductivity of the thermocouple wire also introduces an uncertainty in the conductive correction term. Tzeng [114] estimated this to be ±6.4% for a Type K, chromel and alumel lead. However, the data set used only extended to 773.2K.

   Consequently, the values at higher temperature were evaluated for pure Nickel. These were found to deviate as much as 60% from the extrapolated values for chromel and alumel. For a mean value of 80 W/mK, a conservative uncertainty of ±48 W/mK was therefore placed on this estimate.

Combining all of the uncertainties in Δl, h_{tip} and k_{tip}, the overall precision uncertainty in the conduction correction term is given by:

$$p_{\delta T_{conduction}} = \sqrt{(\frac{\partial \delta T_{conduction}}{\partial \Delta l} p_{\Delta l})^2 + (\frac{\partial \delta T_{conduction}}{\partial h_{tip}} p_{h_{tip}})^2 + (\frac{\partial \delta T_{conduction}}{\partial k_{tip}} p_{k_{tip}})^2} \tag{A.28}$$

This precision uncertainty ($p_{\delta T_{conduction}}$) is calculated to be ±75K.

Uncertainty in $\delta T_{radiation}$

The radiation correction is given by:

$$\delta T_{radiation} = \frac{\sigma\epsilon(T_{tip}^4 - T_{wall}^4)}{h_{tip}}$$

There are three sources of precision uncertainty in the radiation correction term:

1. At the peak of its operating range, the precision uncertainty in the emissivity of the thermocouple wire was estimated to be as high as 27% [114]. For a mean value of 0.78, this corresponds to a precision uncertainty of ±0.21.
2. There is a precision uncertainty of ±12K in the measurement of the wall temperature.
3. As calculated before, there is a precision uncertainty of ±545 W/m^2K in the measurement of heat transfer coefficient at the tip of the thermocouple.

Combining these uncertainties using

$$p_{\delta T_{ratiation}} = \sqrt{(\frac{\partial \delta T_{radiation}}{\partial \epsilon} p_\epsilon)^2 + (\frac{\partial \delta T_{radiation}}{\partial T_{wall}} p_{T_{wall}})^2 + (\frac{\partial \delta T_{radiation}}{\partial h_{tip}} p_{h_{tip}})^2} \tag{A.29}$$

the overall precision uncertainty in the radiation correction ($p_{\delta T_{radiation}}$) is ±103K.

Calculation of the overall uncertainty in the static temperature measurement

Using Eqs. A.16-A.18, the bias uncertainty in the measurement of the flow temperature is ±32, the precision uncertainty is ±127K, and the overall 95%-confidence uncertainty in the measurement of the static temperature at the exit of the combustor is ±131K.

A.2.6 Corrected Exit Gas Total Temperature

The total temperature at the exit of the combustor is given by:

$$T_t = T_{static}(1 + \frac{\gamma - 1}{2} M^2) \tag{A.30}$$

As before, assuming:

1. The average γ is 1.28, and varies between 1.31 and 1.26, and
2. The average Mach number at the exit is 0.05, with a variation of ±0.05,

the uncertainty in the total temperature measurement is given by:

$$p_{T_t} = \sqrt{(\frac{\partial T_t}{\partial T_{static}} p_{T_{static}})^2 + (\frac{\partial T_t}{\partial M} p_M)^2 + (\frac{\partial T_t}{\partial \gamma} p_\gamma)^2} \tag{A.31}$$

The 95%-confidence uncertainty in the measurement of the total temperature of the exit flow is therefore ±131.1K.

A.2.7 Combustor Efficiency

The combustor efficiency is defined as:

$$\eta_c = \frac{(\dot{m}_a + \dot{m}_f)h_{exit} - \dot{m}_a h_{inlet}}{\dot{m}_f h_f} \tag{A.32}$$

where station (1) refers to the state of the inlet air, and station (2) refers to the exit of the combustor (downstream of the NGV's in the case of the static structure). The large uncertainty in the exit temperature measurement directly translates to an uncertainty in the enthalpy content of the exit gas, and can therefore result in large uncertainty bounds on the efficiency calculation.

To calculate the uncertainty in combustor efficiency, the following assumptions will be made:

1. The incoming gas is assumed to be at 300K. Since any pre-heating of the gas results from the heat loss from the combustion chamber, it is reasonable to include this loss in the calculation of the combustor efficiency.
2. The uncertainty in the calculation of h_{exit} shall be based on a ±131K deviation from the exit temperature measurement. The mixture composition shall be based on a fully-reacted mixture at the prescribed equivalence ratio.

Based on a 131K deviation about the design exit temperature of 1600K, the precision uncertainty in the efficiency calculation is ±0.074.

Using Eq. A.2, the bias uncertainty in the calculation of combustor efficiency is:

$$b_\eta = \frac{\partial \eta}{\partial \dot{m}_f} b_{\dot{m}_f} + \frac{\partial \eta}{\partial \dot{m}_a} b_{\dot{m}_a} = \pm 0.03 \tag{A.33}$$

Using Eq. A.3 to combine the two, the 95%-confidence uncertainty in the calculation of the combustor efficiency is ±0.08.

A.2.8 Thermal Efficiency

The combustor thermal efficiency is defined as:

$$\eta_{thermal} = \frac{(\dot{m}_a + \dot{m}_f)h_2 - \dot{m}_a h_1}{[(\dot{m}_a + \dot{m}_f)h_2 - \dot{m}_a h_1] + \dot{Q}_{loss}} \tag{A.34}$$

The uncertainty in the calculation of the heat loss in the 3-stack can be estimated as follows:

1. *Conductive losses:* in the 3-stack were calculated using:

$$q_{cond} = \frac{\Delta T}{R_{thermal}}; \qquad R_{thermal} = \frac{L_{SS}}{k_{SS}A_{SS}} + \frac{L_{Cu}}{k_{Cu}A_{Cu}} \tag{A.35}$$

   Since the thermal resistance of the connecting tubes can be estimated with relative accuracy, uncertainty in the temperature drop across the tubes constitutes the dominant source of uncertainty. Furthermore, since the 1-D conduction model does not account for convective heat transfer along the tubes, the uncertainty in the estimation of the temperature drop can be up to 100K.

   Using these values, the uncertainty in the conductive loss is 2 Watts. (This is approximately 30% of the total conductive loss at stoichiometric operating conditions.)

2. *Convective losses:* in the 3-stack were calculated using:

$$\dot{q}_{conv} = hA(T_{wall} - T_{ambient}) \tag{A.36}$$

   Assuming that the uncertainty in the heat transfer coefficients constitutes the dominant source of uncertainty, and that p_h is ±10 W/m^{2}K, the uncertainty in the estimation of the convective heat transfer from the 3-stack is 14 Watts. (This is approximately 70% of the total convective loss at stoichiometric conditions.)

3. *Radiative losses:* in the 3-stack were calculated using:

$$q_{rad} = \epsilon\sigma A(T^4_{wall} - T^4_{ambient}) \tag{A.37}$$

   Assuming an uncertainty of 0.1 in the value of ϵ, and an uncertainty of ±12K in the measurement of the wall temperature, the uncertainty in the estimation of the radiative heat transfer from the 3-stack is 12 Watts. (This is approximately 50% of the total radiative loss at stoichiometric operating conditions.)

Using Eq. A.34 to propagate these values, the uncertainty in the estimation of the thermal efficiency of the 3-stack is ±0.11.

The uncertainty in the calculation of the thermal efficiency of the 6-stack can be estimated in a similar manner:

1. *Conductive losses:* Assuming an outer wall temperature of 800K, the conductive losses through the five kovar tubes in the static structure is less than a Watt. Its contribution to the overall uncertainty can therefore be assumed to be negligible.

2. *Convective losses:* Assuming an outer wall temperature of 800K and a baseline heat transfer coefficient of 20 W/m^{2}K, the convective loss from the static structure is approximately 12 Watts. Assuming an

uncertainty of ±10 W/m^{2}K in the heat transfer coefficient, the uncertainty in the estimation of the convective heat transfer losses from the static structure is 6 Watts.

3. *Radiative losses:* Assuming an outer wall temperature of 800K, and an emissivity of 0.3, the radiative loss from the static structure is approximately 8 Watts. Assuming that the uncertainty in the emissivity is ±0.1, and that the uncertainty in the wall temperature measurement is 12K, the overall uncertainty in the radiative losses through the static structure is ±3 Watts.

Propagating these values through, the uncertainty in the estimation of the thermal efficiency at the low equivalence ratios and mass flow rates of the static structure is ±0.075.

A.2.9 Chemical Efficiency

The chemical efficiency of the combustor is estimated using:

$$\eta_{chem} = \frac{\eta_{combustor}}{\eta_{thermal}} \tag{A.38}$$

The uncertainty in the estimation of the chemical efficiency is given by:

$$p_{\eta_{chem}} = \sqrt{(\frac{\delta\eta_{chem}}{\delta\eta_{combustor}} p_{\eta_{combustor}})^2 + (\frac{\delta\eta_{chem}}{\delta\eta_{thermal}} p_{\eta_{thermal}})^2} \tag{A.39}$$

For the 3-stack, $p_{\eta_{chemical}}$ is ±0.14; for the 6-stack, $p_{\eta_{chemical}}$ is ±0.11.

A.3 Summary

This appendix presents an uncertainty analysis for the experimental measurements in this thesis. These are summarized in Tables A.1 and A.2 for each of the independent and derived quantities.

Quantity	**2-σ**	**% design**
Air mass flow	±136 sccm	±0.81
Hydrogen mass flow	±64 sccm	±1.82
Pressure	±0.5 psi	±1.1
Temperature	±12K	N/A

Table A.1: The uncertainty in the measurement of the independent quantities. (Note: The percent error is calculated as a fraction of design conditions, i.e., $\dot{m}_a$=16720 sccm (0.36 g/sec), $\dot{m}_f$=3508 sccm and P=3 atm.)

Quantity	**2-σ**	**% design**
Equivalence ratio	±0.014	±2.8
Combustor static pressure ratio	±0.023	±2.4
Combustor total pressure ratio	±0.033	±3.5
Corrected wall temperature	±12K	±1.2
Corrected exit gas static temperature	±131K	±8.2
Corrected exit gas total temperature	$\pm131.1K$	±8.2
Combustor efficiency (%)	±0.08	±8.9
Thermal efficiency (3-stack) (%)	±0.11	±11
Thermal efficiency (6-stack) (%)	±0.075	±7.5
Chemical efficiency (3-stack) (%)	±0.14	±14
Chemical efficiency (6-stack) (%)	±0.11	±11

Table A.2: The uncertainty associated with the calculation of the derived quantities. (Note: The percent error is calculated as a fraction of design conditions, i.e., ϕ=0.5, π=0.95, T_{wall}=1000K, T_{exit}=1600K and η=0.90.)

Appendix B

Numerical Models for the Silicon Oxidation Study

This appendix describes the numerical analysis that was used to model the materials and oxidation study described in Chapter three. The first section of the appendix uses a thermal oxidation model to predict the silicon oxidation thickness as a function of temperature, and compares it with the experimental results for the fingered-combustor described in Section 3.6.1. The second section describes a 1-D heat transfer model used to predict the creep behavior of the fingered-combustor under high temperature conditions (Section 3.6.2).

The primary goal of this appendix is:

1. To show that the experimental oxidation results agree with the predictions of a numerical model for the thermal oxidation of silicon, and
2. To show that a 1-D heat transfer model can be used to explain the trends observed in the creep failure tests described in Chapter three.

B.1 Oxidation Model

Since post-combustion examination of the 3-stack microcombustor revealed oxidation patterns (Figure 3-10), a fingered silicon plate was exposed to hot combustion gases to quantify the oxidation rates in the microcombustor (Figure 3-15). The plate, that comprised finger-like structures with sizes ranging between 20 μm × 500 μm × 450 μm and 1600 μm × 2000 μm × 450 μm, was exposed to a stoichiometric hydrogen-air mixture for eight hours. The fingers were observed to grow between 1 μm and 7 μm of oxide. Depending on the size of the fingers, the temperature along the length of the fingers ranged between 1000-2400K.

In order to assess the agreement of these results with conventional thermal oxidation models for silicon, the Deal-Grove model was run at the same conditions to calculate the expected oxide thickness [26]. Using this to model the diffusion through the oxide and reaction at the silicon-silicon dioxide interface, the oxide thickness can be expressed as:

$$X_{ox} = 0.5A(\sqrt{1 + \frac{4B}{A^2}(t + \tau)} - 1) \tag{B.1}$$

where B/A is called the linear rate constant, B is called the parabolic rate constant, and $\tau = X_i^2/B + X_i/(B/A)$ (X_i is the native oxide thickness).

The rate constants are a function of oxidation ambient and substrate orientation, and have a strong dependence on temperature. They can be represented using an Arrhenius relationship as:

$$B = D_0 e^{(-E_a/kT)}; \qquad B/A = D_0 e^{(-E_a/kT)} \tag{B.2}$$

The values for D_o and E_a for wet and dry oxidation are given in Table B.1 [99]. Using these constants, the oxide thickness after eight hours of exposure is plotted as a function of temperature in Figure B-1.

	Wet O_2 (X_i=0 nm)		Dry O_2 (X_i=25 nm)	
	D_o	E_a	D_o	E_a
<100> Linear (B/A)	9.7×10^7 μm/hr	2.05 eV	3.71×10^6 μm/hr	2.00 eV
<100> Parabolic (B)	386 μm^2/hr	0.78 eV	772 μm^2/hr	1.23 eV
<111> Linear (B/A)	1.63×10^8 μm/hr	2.05 eV	6.23×10^6 μm/hr	2.00 eV
<111> Parabolic (B)	386 μm^2/hr	0.78 eV	772 μm^2/hr	1.23 eV

Table B.1: Rate constants for the oxidation of silicon [99].

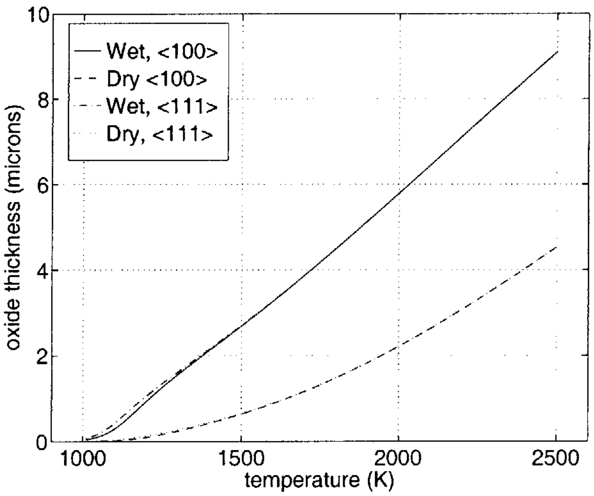

Figure B-1: Oxide thickness as predicted by the Deal-Grove oxidation model, showing thicknesses between 0.5 μm and 9 μm after 8 hours of exposure.

Since the combustion products contain water vapor, the wet oxidation results can be considered to be more representative of the fingered-combustor oxidation experiments described in Section 3.6.1. The results in Figure B-1 show that the oxide thicknesses predicted by the Deal-Grover thermal oxidation model agree well with the experimentally observed oxide thickness of 1-7 μm for the 1000-2400K temperature range, and after eight hours of exposure. This suggests that the oxide growth observed in the silicon microcombustor can be explained by conventional thermal oxidation models for silicon. It also suggests that the silicon is not being subject to "active-oxidation", and that conventional thermal oxidation models may used to approximate the oxide growth inside the silicon microcombustor.

B.2 Heat Transfer Model

In addition to atmospheric testing of the fingered-combustor, elevated pressure testing was also conducted to understand the failure mechanisms of silicon at high temperatures and pressures (Section 3.6.2). These tests resulted in the plastic deformation of the fingers at different locations along their length. Since the fingers were of different sizes, and hence, had different temperature profiles along their length, it was hypothesized that creep failure occurred at the brittle-to-plastic transition temperature of approximately 900K [19]. To support this hypothesis, a 1-D heat transfer model was constructed to see if the experimental trends could be explained physically. This analysis was not meant to replicate the experimental results in detail; instead, given its simplicity, it was only intended to support the experimental observations qualitatively.

B.2.1 Description of the Model

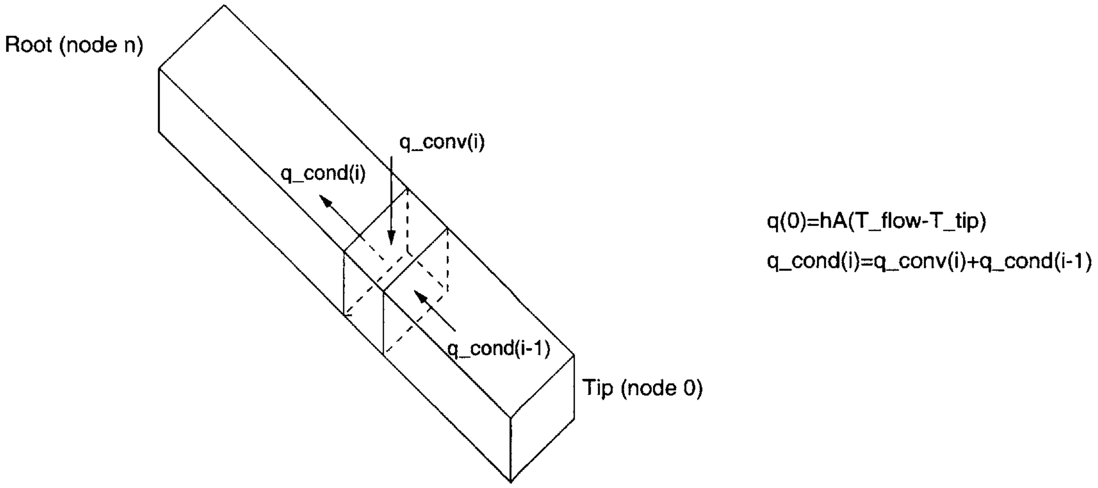

Figure B-2: An illustrative description of the model used to study the creep behavior of the fingered-combustor.

Figure B-2 shows an illustration of the 1-D model used to study the heat transfer along the fingers of the combustor plate described in Section 3.6.1. Each finger was discretized into approximately 20 spatial nodes, the energy balance across each cell being given by:

$$q_{cond}(i) = q_{conv}(i) + q_{cond}(i-1) \tag{B.3}$$

$$q_{cond}(0) = hA(T_{flow} - T_{tip}) \tag{B.4}$$

$$q_{cond}(i) = kA\frac{T(i) - T(i-1)}{\Delta l} \qquad q_{conv}(i) = hA[T_{flow} - T(i)] \tag{B.5}$$

For the purpose of this model, the flow temperature was assumed to be 2400K, and the wall temperature at the root of the fingers was assumed to be 800K. Using these values, an initial guess for the tip temperature was iterated upon until the root temperature agreed with the prescribed value. The thermal conductivity and heat transfer coefficients were assumed to be 150 W/mK and 5000 W/m^{2}K, respectively[1].

B.2.2 Comparison with Experimental Results

Figure B-3 shows the results of the model for fingers of different lengths and widths. Given a common flow temperature at the tip and a wall temperature at the root, the results show that longer, thinner fingers are not only expected to have higher tip temperatures, they also equilibrate to flatter temperature profiles along a greater portion of their lengths.

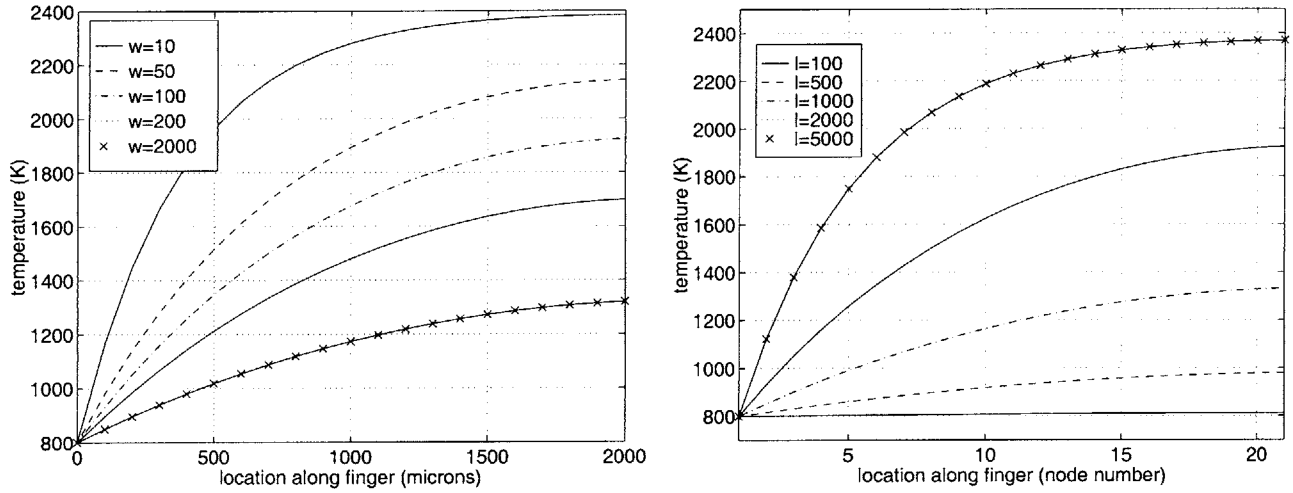

(a) Temperature profiles along a 2000 μm long finger with widths varying between 10 μm and 2000 μm.

(b) Temperature profiles along a 100 μm wide finger with length varying between 100 μm and 5000 μm.

Figure B-3: Temperature profiles along fingers of different lengths and widths, showing that long thin fingers have higher temperatures at the tip and along the length.

Figure B-3 (a) shows that for a fixed length, as the width of a finger is reduced, not only does the tip

---

[1] The results of a sensitivity study showed that the trends predicted by the model were largely independent of the assumed values of h and k. Since the model was only intended to compare trends, baseline values of h and k were considered sufficient for this purpose

temperature increase, but the "knee" in the temperature profile also moves closer to the root. Consequently, thinner fingers with the same length should experience more damage, and should fail closer to their root.

These results compare well with the following experimental observations:

1. Among the 2000 μm long fingers, the 100 μm wide finger melted, the 200 μm wide finger bent near the root, and the 400 μm wide finger remained intact.
2. Among the 1000 μm long fingers, the 50 μm wide finger bent closer to its root than the 100 μm wide finger; the 250 μm wide finger showed no damage.

Figure B-3 (b) shows the temperature profiles for a constant width finger with varying length. Again, long fingers are expected to be more susceptible to damage. These results also agree with the experimental observation wherein, the 2000 μm long, 100 μm wide finger melted, while the 1000 μm long, 100 μm wide finger showed relatively less damage.

Overall, the results of this simple 1-D heat transfer model bear the trends observed during the experimental testing of the fingered-combustor. While this model is not intended to completely replicate the experimental observations, it predicts the long and thin fingers to creep closer to their roots, and supports the hypothesis that the creep failure of the different fingers occurred at the location where each individual finger reached its brittle-to-plastic transition temperature.

B.3 Summary

This appendix described the models that were used to support the experimental observations during the testing of the fingered-combustor. The two models used for this purpose were as follows:

1. The Deal-Grove thermal oxidation model was used to predict the oxidation thickness that would be expected under the experimental conditions described in Section 3.6.1. The results compared well with the experimental observations, suggesting that conventional thermal oxidation models could be used to predict oxidation growth in the microcombustor.
2. The results of a simple 1-D heat transfer model for the temperature profiles along the lengths of the fingers showed that long, thin fingers were more susceptible to damage. This trend agreed with the experimental observations, and supported the hypothesis that the fingers failed when they reached the brittle-to-plastic transition temperature for silicon.

Appendix C

Combustor-Inlet Design Models

C.1 Introduction

This appendix describes the models that were used to design the two inlet geometries for the combustor.

The first section of the appendix describes the 2-D shear layer analysis that was used to size the inlet slots to the combustor; the second section presents the PSR model developed by Lukachko to evaluate the stability of the recirculation zones in the annular-inlet combustor [73].

C.2 Design of the Combustor Inlet Slots

As shown in Figure C-1 (a), the inlet slots to the combustor were intended to generate multiple recirculation zones behind the inter-slot wall. Initially, two inlet locations were considered for this purpose:

1. A "picket-fence" like side wall for radial injection into the combustor, and
2. A disk with radial slots for axial injection from the bottom of the combustor.

Figure C-1 (b) shows schematics of both these configurations.

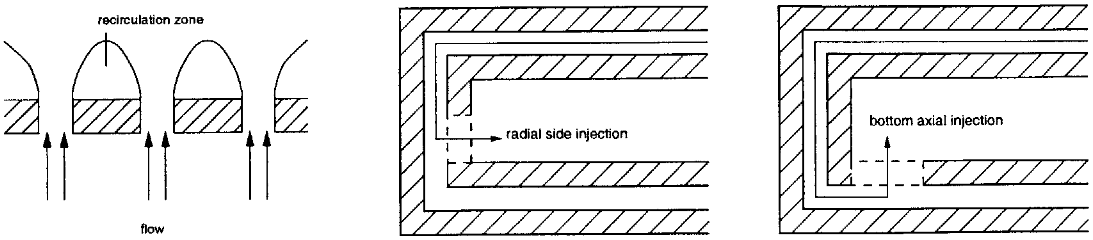

(a) Recirculation zones in a slotted inlet.

(b) Schematic illustrations of the two slotted-inlet configurations for the static structure.

Figure C-1: Schematic illustrations of the slotted-inlet configurations for the static structure.

Preliminary analysis showed that the bottom injection scheme was preferable because:

1. The height of the side slots would have to be 400 μm, 600 μm or 1000 μm to be in etch-line with other features in the chamber. This would limit the flexibility available for tailoring the inlet flow.
2. Cold-flow CFD showed that side injection caused the flow to propagate through the chamber as a 400 μm high jet. As shown in Figure C-2, since this did not utilize a large volume of the chamber, it was considered undesirable.

Consequently, axial injection through the bottom was chosen as a suitable configuration for the slotted inlet.

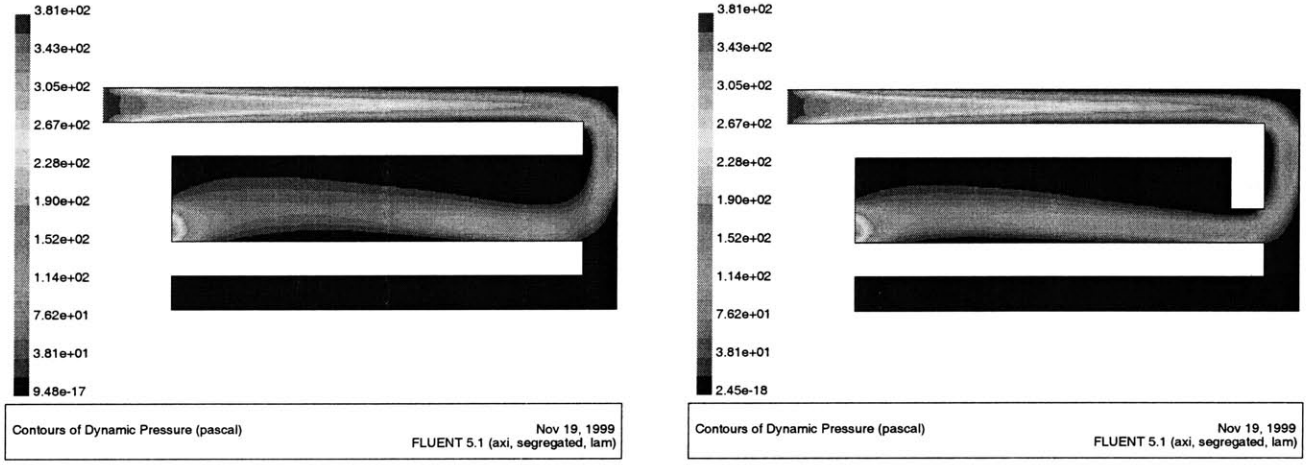

(a) CFD solution for a 1000 μm high slot.

(b) CFD solution for a 400 μm high slot.

Figure C-2: Cold-flow CFD solutions showing the flow propagating across the chamber as a 400 μm high jet.

The radial extent of the inlet slots was set at 2.2 mm based on cold-flow CFD solutions that showed reasonable spreading of the jet inside the chamber for a 2.2 mm long slot.

The circumferential size and spacing of the slots was subsequently optimized so that the axial height of the recirculation zones was equal to the height of the chamber. This was done by using the following equations for a plane laminar jet to ensure that the circumferential spreading of the jet equaled half the inter-slot spacing by the time it reached the opposite wall (see Figure C-3 (a)) [118]:

$$y \approx 21.8\left(\frac{x^2\mu^2}{J\rho}\right)^{1/3}, \qquad J = \rho\int_{-\infty}^{+\infty} u^2 dy \tag{C.1}$$

The results from the simple analytical model were also compared with cold-flow CFD solutions. Figure C-3 (b) plots the non-dimensionalized recirculation zone length from the two calculations as a function of the duty-cycle of the slots, and shows good agreement for small duty cycles. At higher values however, the

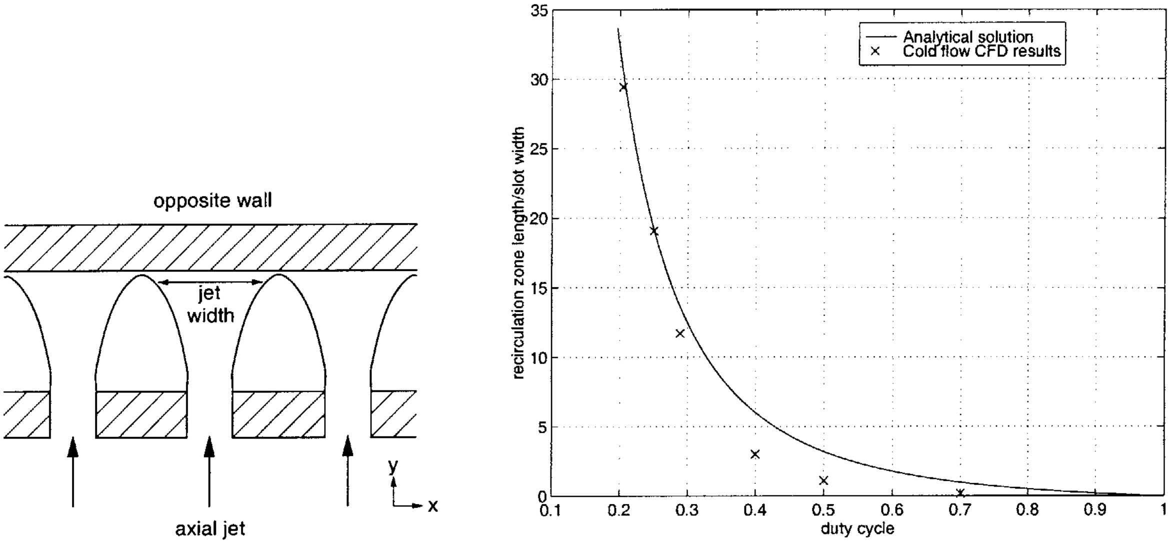

(a) Schematic illustration of jet spreading through a combustor inlet slot.

(b) Comparison of the analytical results with cold-flow CFD solutions.

Figure C-3: Jet spreading analysis used to size the combustor inlet slots.

analytical model for an isolated jet breaks down because of the close proximity of the neighboring jets. (Note: The duty cycle of the slot is defined as: $\frac{\text{slot width}}{\text{slot width + inter-slot spacing}}$. As duty cycle increases, the inter slot spacing therefore becomes smaller.)

Overall, the analytical model was considered suitable for calculating the length of the recirculation zones; the final design comprised 60 slots that were 2.2 mm long and 0.62 mm wide at an outer radius of 9.2 mm.

C.3 Sizing of the Annular Inlet

The annular inlet was sized using a PSR model developed by Lukachko to evaluate the stability of the combustor recirculation zones under different heat loss conditions [73]. The analysis assumed that the fuel-air mixture entering the combustor is ignited through recirculation of hot combustion products towards the inlet, and was specifically intended to answer the following questions:

1. Does the recirculation zone provide a stable heat source for ignition of the incoming reactants ?
2. Is it hot enough to ignite the mixture ?
3. How much heat loss can it sustain before it is rendered incapable of igniting the incoming mixture ?

The recirculation zones were modeled as a PSR using a H_2-O_2-N_2 mechanism [30]. Although recirculation zones were formed at several locations inside the combustor, cold-flow CFD showed that the recirculation zone in the upper corner near the inlet had the largest volume. This was therefore considered to be the controlling recirculation zone; the analysis was carried out with this assumption, and is described next.

C.3.1 Description of the PSR Model

A perfectly stirred reactor is an idealized system in which the reacting mixture flows into a chamber and mixes with combustion products perfectly [45]. As it mixes with the products, it releases energy and then flows out at the same conditions as those prevailing inside the chamber (see Figure C-4 (a)).

The energy added to the flow is given by:

$$\dot{Q}_{flow} = \dot{m}C_p(T_{reactor} - T_{inlet}), \tag{C.2}$$

and must be equal to the difference between the heat release and the heat loss:

$$\dot{Q}_{reaction} - \dot{Q}_{loss} = V\Delta h_r w_f - \dot{Q}_{loss} \tag{C.3}$$

where V is the volume of the reactor, Δh_r is the specific enthalpy of reaction, and w_f is the mass-rate of fuel consumption per unit volume.

The steady state solution for the PSR can be obtained by solving Eqns. C.3 & C.2 simultaneously for $\mathrm{T}_{reactor}$; a typical solution is shown in Figure C-4 (b) for different mass flow rates. For $\dot{m}$ greater than the blow-out mass flow, the only solution obtained is a cold solution near T_o. As the mass flow rate is reduced, two stable solutions exist - a cold solution with $\mathrm{T}_{exit} < \mathrm{T}_{ignition}$, and a hot solution with $\mathrm{T}_{exit}=\mathrm{T}_{reactor}$.

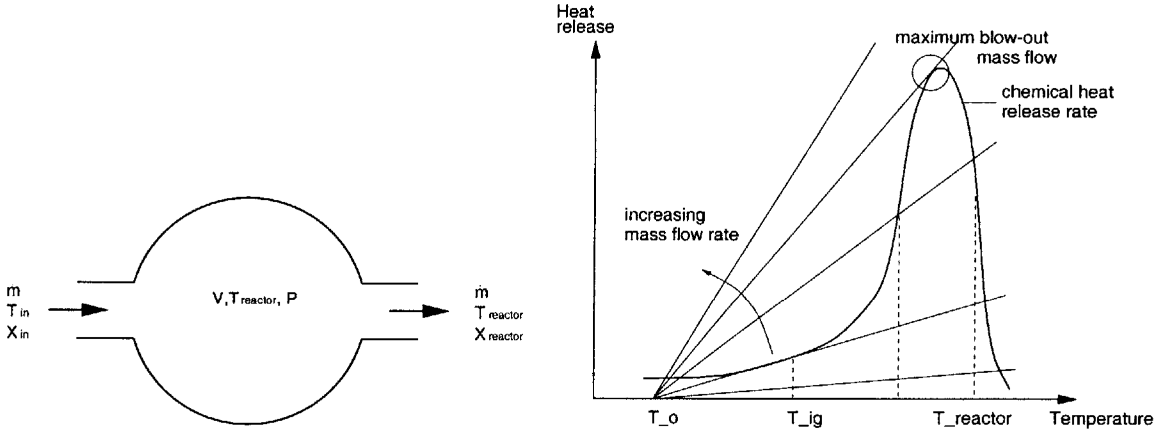

(a) Schematic representation of a PSR.

(b) Solution of a PSR on a Q-T diagram [45].

Figure C-4: Schematic illustrations of a perfectly stirred reactor.

Additional details about the behavior of a PSR can be found in Ref. [102].

C.3.2 Results for the Static Structure Combustor

The stability analysis for the PSR required estimates for the volume of the recirculation zone, the mass flow entering this volume, the range of heat loss through adjacent walls, and operational parameters for the properties and composition of the incoming gas. For all of the analysis:

- The recirculation zone volume was estimated from cold-flow CFD computations [89].
- The mass flow entering the recirculation zone was estimated using correlations for laminar layers.
- The heat loss out of the recirculation zone was varied between 0-600 Watts.

The ignition analysis required estimates for the time of contact between the incoming reactants and the recirculation zone, the temperature of the mixing layer, and the composition of the mixture. The time of contact was estimated from cold-flow CFD; the mixing layer temperature was averaged from the inlet and recirculation zone temperature.

Ignition capability was subsequently evaluated by setting the shear layer contact time as the minimum ignition time available for achieving 5% of the total heat release. This defined a minimum mixing layer temperature, which in turn defined the minimum temperature, and hence, the maximum heat loss from the recirculation zone. The relationship between the maximum heat loss and the equivalence ratio for different inlet temperatures then defined the stability boundary for the combustor.

Figure C-5 shows sample stability boundaries for hydrogen and hydrocarbon fuels at P=2.7 atm. and T_{inlet}=700K for the controlling recirculation zone resulting from a 1.2 mm wide annular inlet.

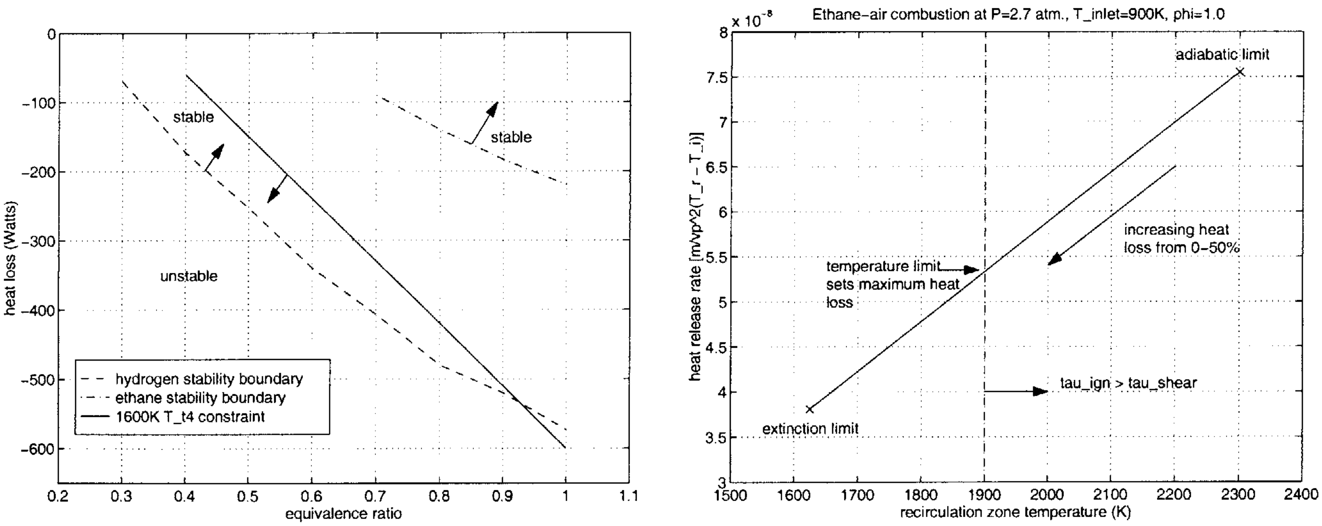

(a) Design space for hydrogen and ethane combustion at P=2.7 atm. and T_{inlet}=700K.

(b) Stability plot for ethane-air combustion.

Figure C-5: Results from the recirculation zone stability model. (Model courtesy: S. Lukachko [73])

The results show that as designed, there is a stable operating regime for hydrogen combustion within the 1600K T_{t4} constraint, however, ethane-air combustion mandates higher operating temperatures. In fact, in order to ignite the incoming products within the residence time of the shear layer, the recirculation zone must operate above 1900K.

The recirculation zones were therefore only sized for hydrogen combustion.

C.4 Summary

This appendix presented the models that were used to design the slotted and annular inlets for the combustion chamber in the static structure.

It begins with the thought process used for the design and placement of the slotted inlet followed by a description of the PSR model developed by Lukachko to analyze the stability of the controlling recirculation zone in the combustion chamber [73].

Appendix D

Structural / Heat Transfer Analysis for the Static Structure

This appendix describes the heat transfer/structural analysis that was conducted in conjunction with MIT Lincoln Laboratory by Huang to design and analyze the engine [52]. It begins with a description of the model followed by a presentation of the baseline results for the static structure described in Chapter four.

D.1 Description of the Model

The heat transfer analysis used two models to determine the temperature distribution in the static structure:

1. NASTRAN Model: The solid structure was modeled via an axisymmetric finite element NASTRAN model that used 1-D conductive and convective heat transfer equations to calculate the heat flux through the structure, and at the solid-fluid interfaces.

Non-axisymmetric features were "smeared-out" circumferentially to obtain equivalent values for the heat transfer coefficient and thermal conductivity. The thermal conductivity was assumed to be temperature dependent; heat transfer coefficients were individually prescribed along the fluid path at 154 surface elements [55].

The model was initialized with fluid temperature boundary conditions which were subsequently iterated upon using a fluid temperature model to account for the heat transfer between the structure and the fluid.

2. Fluid Temperature Model: The fluid temperature boundary conditions for the solid structure were iterated upon to account for the heat flux from the NASTRAN model using:

$$T(n+1) = T(n) + \frac{\dot{Q}}{\dot{m}C_p}, \text{ where } T(n) \text{ is the fluid temperature at station } n. \tag{D.1}$$

Generally, a converged solution required 2-3 iterations between the fluid and structural models.

Figure D-1 shows the FEM grid developed for this purpose along with sample values for the heat transfer coefficients and temperature distribution in the structure.

D.2 Results

The heat transfer analysis was intended for two purposes:

1. Sizing the wafer thicknesses in the static structure to ensure that the operating stress in the structure did not exceed the material strength at that temperature, and
2. Estimating the structural temperature and heat transfer across various surfaces in the baseline device.

D.2.1 Wafer Sizing

Since the allowable structural temperature depends on the material yield strength and localized stress at that location, the model utilized experimentally measured yield strength data to determine the minimum thicknesses of the wafers in the static structure [19].

The yield strength for silicon was expected to be approximately 1000 MPa for temperatures between 673K and 1273K, however, since the strength decreases sharply to 20 MPa at 1273K, the device was designed for a maximum structural temperature of 1200K. Using this criteria, wafer thicknesses were subsequently chosen such that the structure operated below the maximum permissible thermal stresses. A sample distribution of the thermal stress in the static structure is shown in Figure D-2; the wafer thicknesses have already been listed in Chapter four.

D.2.2 Evaluation of the Baseline Performance

In addition to predicting the structural temperature distribution, the model was also used to quantify the heat transfer through the device. The results are shown in Table D.1 for design point operation, and predict a total heat loss of approximately 6 Watts from the static structure.

The heat loss from the combustion chamber was expected to be 70 Watts at design conditions.

	Attributes	Heat loss (Watts)
Radiation	e=0.8	2.4
Natural convection	h=5 W/m^2K	3.2
Forced convection	h=100 W/m^2K	64.1
Conduction	Kovar tubes (0.8 mm o.d., 0.56 mm i.d.)	0.7

Table D.1: Heat loss predictions for the static structure at design conditions. (Source: Ref. [51])

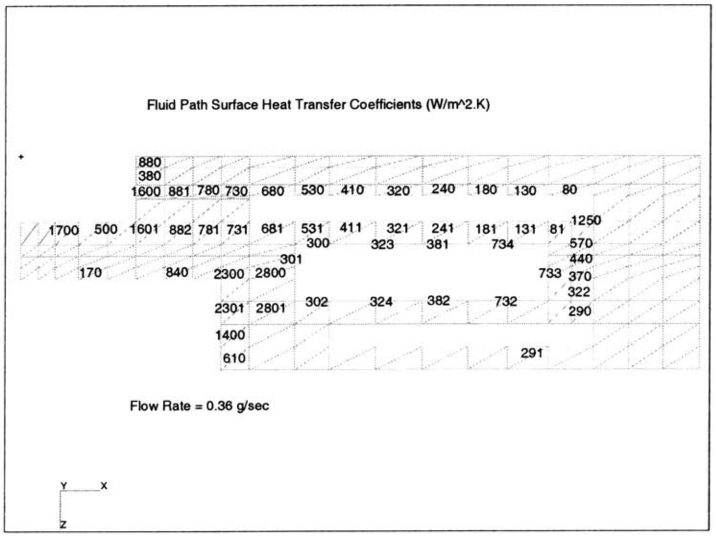

(a) FEM grid showing typical heat transfer coefficients along the surface elements.

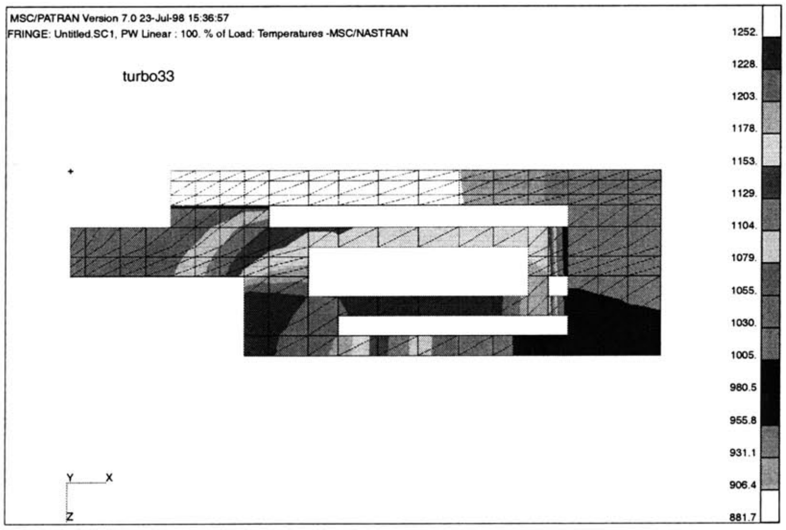

(b) Temperature distribution in the static structure at design conditions (scale in Kelvin).

Figure D-1: FEM grid, heat transfer coefficients, and sample temperature distribution in the static structure.

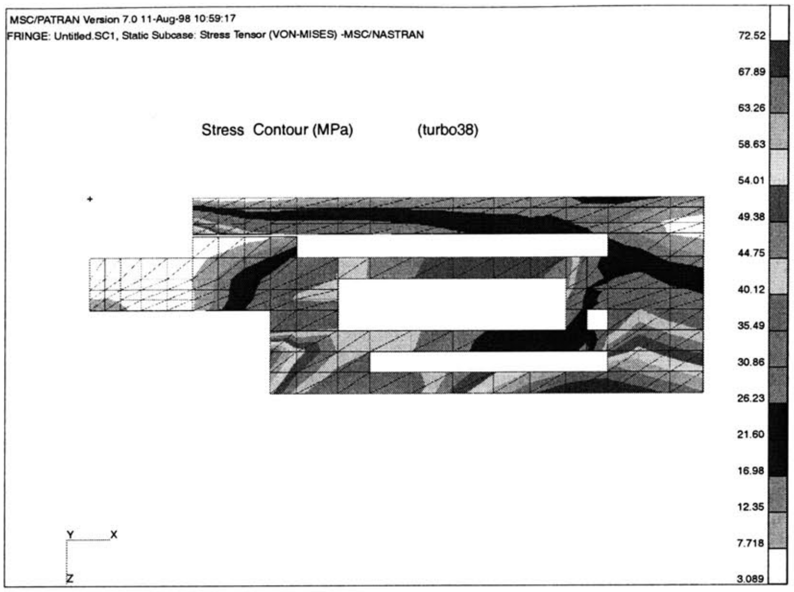

Figure D-2: Results of the FEM model showing sample stress distribution in the static structure.

D.3 Summary

This appendix described the heat transfer/structural analysis that was conducted by Huang for the design of the static structure [51]. It presented a brief description of the the structural and fluid models, followed by baseline results for the device.

Comparisons of these numerical results with experimental data from the static structure have already been presented in Chapter six.

Appendix E

Development of the Damkohler Number Model

This appendix presents the development of the Damkohler number model used to explain the results presented in Chapter four. It evaluates the assumptions used to calculate residence and chemical reaction times, and then compares the results from the model with estimates from reacting flow CFD solutions.

The primary goal of this appendix is to justify the assumptions used for calculating the Damkohler number for the experimentally measured operating points.

E.1 Approach

Chapter four presented a methodology for estimating the Damkohler number in the combustor:

$$Da = \frac{\tau_{res}}{\tau_{reaction}} \tag{E.1}$$

$$\tau_{res} = \frac{PV}{\dot{m}RT}; \qquad \tau_{reaction} = \frac{[H_2]_{initial}}{Aexp(-E_a/RT)[H_2]^2[O_2]} \tag{E.2}$$

Given the simplicity of using a single step reaction mechanism to capture the chemical kinetic time in a complex reacting flow, the uncertainty in the estimation of the Damkohler number can be large. Furthermore, it is unclear whether the inlet, exit or some form of average temperature be used to estimate the residence and reaction times.

In order to evaluate these assumptions, the results from the model were bench-marked against reacting flow CFD solutions obtained by Lee [62]. These solutions utilized a 9-species, 30-step reaction mechanism for hydrogen-air combustion. Since reacting flow solutions were not available for every operating point, the results from the model were compared with select solutions only - the same assumptions were then carried over to the remaining experimental data.

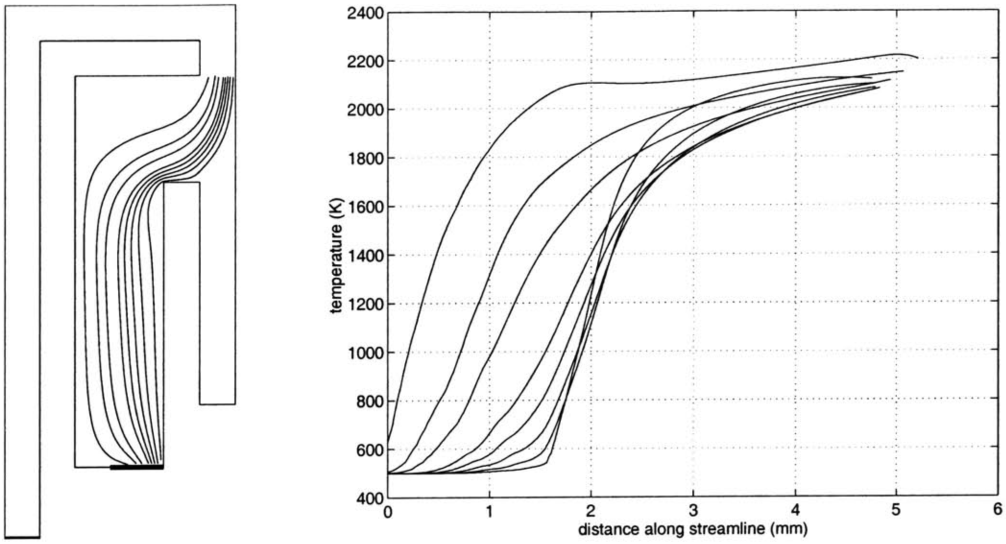

(a) Sample streamlines in the 6-stack.

(b) Temperature along the streamlines.

Figure E-1: Sample CFD solution, showing the temperature along different streamlines in the 6-stack.

Figure E-1 (a) shows the streamlines from a sample reacting flow solution for the 6-stack; the temperature along the streamlines is plotted in Figure E-1 (b). For all comparisons, eight streamlines were chosen; typically 90-95% of the mass flow was contained within the two bounding streamlines.

E.2 Estimation of the Residence Time

In order to determine the residence time in the combustion chamber, the streamline velocity and co-ordinates were used to calculate an integrated flow residence time in the chamber for each streamline. Figure E-2 (a) plots this residence time for adiabatic 3-stack solutions at ϕ=0.6, 0.8 and 1.0. It also calculates the mass-weighted average of the residence time for the different streamlines in order estimate an average flow residence time in the chamber.

The value of the mass-averaged residence time from the CFD solution was then compared with four different methods of evaluating the residence time from the simple Damkohler number model:

1. *Exit temperature based:* Using Eq. E.2, this method used T_{exit}, and the entire volume of the combustion chamber to estimate the residence time.
2. *Average temperature based:* This used the average of the inlet and exit temperature to calculate τ_{res}.
3. *Exit temperature, reduced volume based:* Herein, T_{exit} was still used, however, the effective volume of the chamber was reduced to account for the presence of the recirculation zones.

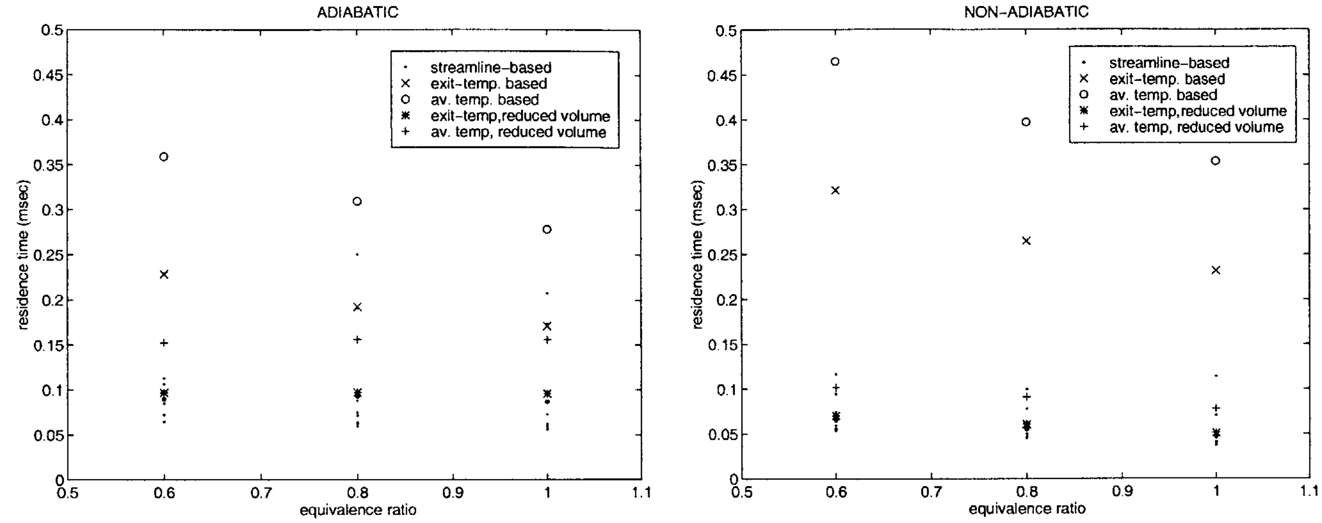

(a) Adiabatic 3-stack.

(b) Non-adiabatic 3-stack.

Figure E-2: Residence time estimates for the 3-stack geometry, showing good agreement between the mass averaged value from the CFD and the exit-temperature, reduced volume based estimate from the simple Damkohler number model. (Note: The small dots represent the residence time for each of the eight streamlines, the big dot shows the mass-average value.)

4. *Average temperature, reduced volume based:* This used the average temperature and reduced volume to calculate τ_{res}.

Figure E-2 shows that the exit temperature, reduced volume based residence time estimates from the simple model are in good agreement with the mass averaged values from the code. The result carries over to non-adiabatic solutions for the 3-stack, and to adiabatic and non-adiabatic solutions of the 6-stack as well (see Figure E-3). In the case of the 6-stack however, the disagreement is observed to be up to 25%; this is attributed to the more convoluted flow path in the 6-stack.

E.3 Validity of a 1-Step Reaction Model

In addition to bench-marking the residence time calculations, the CFD solutions were also intended to evaluate the assumptions used to estimate the chemical reaction time of the fuel. Specifically, the following two questions were of interest:

1. Can a one-step reaction mechanism be used to calculate the reaction time ?
2. If so, what is the appropriate temperature and concentrations ?

In order to answer the first question, hydrogen mass fraction along the center streamline was extracted from the ϕ=1.0, adiabatic 3-stack solution. Using the initial temperature and H_2 and O_2 concentrations, the following single-step reaction rate expression proposed by Coffee *et al.* [20], was then used to calculate

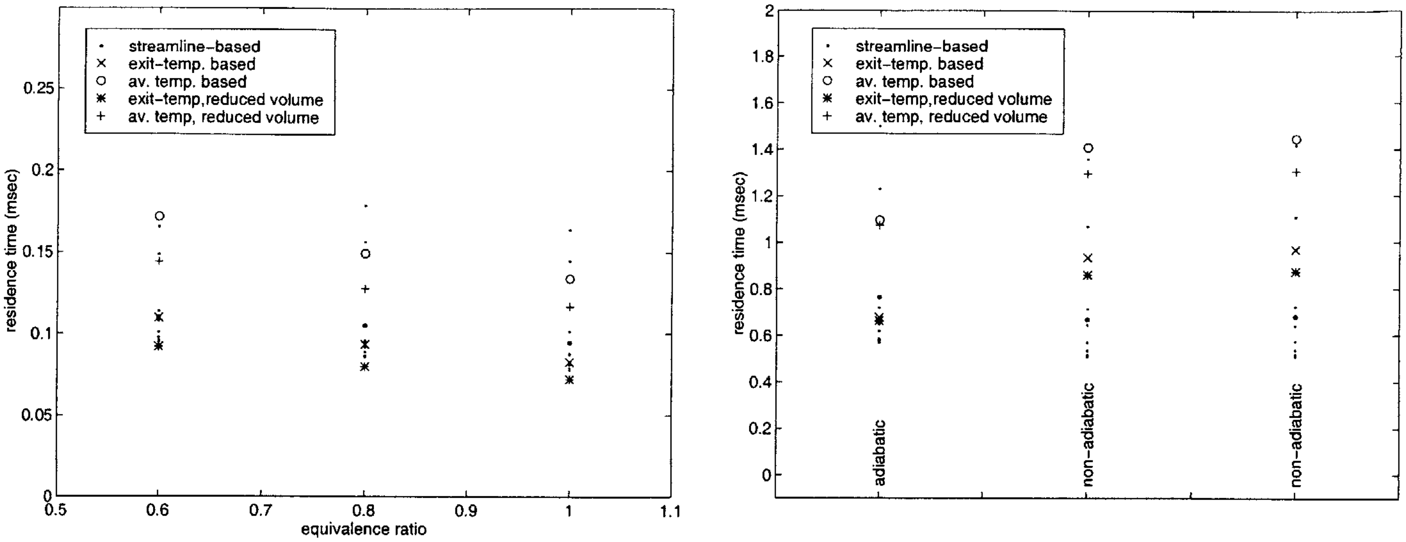

(a) Adiabatic 6-stack.

(b) Non-adiabatic 6-stack.

Figure E-3: Residence time estimates for the 6-stack geometry.

the initial rate of H_2 consumption:

$$\frac{d[H_2]}{dt} = 1.58 \times 10^{17} exp(-15200/1.9782 \times T)[H_2]^2[O_2] \tag{E.3}$$

The procedure was repeated for each incremental time step in order to calculate the equivalent H_2 mass fraction along the streamline. Figure E-4 (a) compares the H_2 mass fraction as obtained from the reaction rate proposed in the literature with that from the detailed reaction mechanism in the streamline, and shows poor comparison between the two[1].

Consequently, a least-squares fit was used to estimate new reaction rate constants for the single step mechanism - the resulting H_2 mass fraction using the following refined rate expression is also plotted in Figure E-4 (a), and shows good comparison with results from the detailed mechanism:

$$\frac{d[H_2]}{dt} = 1.82 \times 10^{17} exp(-4640/1.9782 \times T)[H_2]^2[O_2] \tag{E.4}$$

Since the rate expression was derived from a least squares fit to a single streamline in the adiabatic 3-stack solution, its applicability across different cases was evaluated by using the same procedure to compare the H_2 mass fractions across different streamlines, and for adiabatic and non-adiabatic 3-stack solutions with different equivalence ratios. These results are also plotted in Figures E-4 & E-5, and show reasonable

---

[1] Since single-step reaction mechanisms are derived for specific conditions, they cannot generally be applied across all reactions. The poor comparison between the CFD results and the *Coffee* mechanism [20], is therefore attributed to the difference in operating conditions.

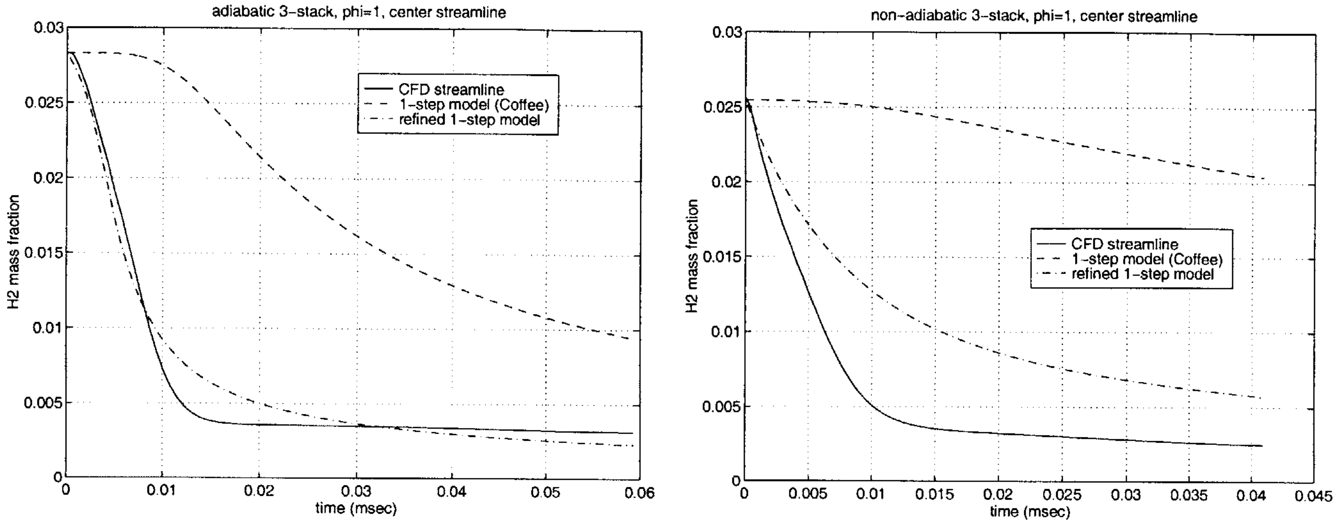

(a) Adiabatic 3-stack, ϕ=1, center streamline.

(b) Non-adiabatic 3-stack, ϕ=1, center streamline.

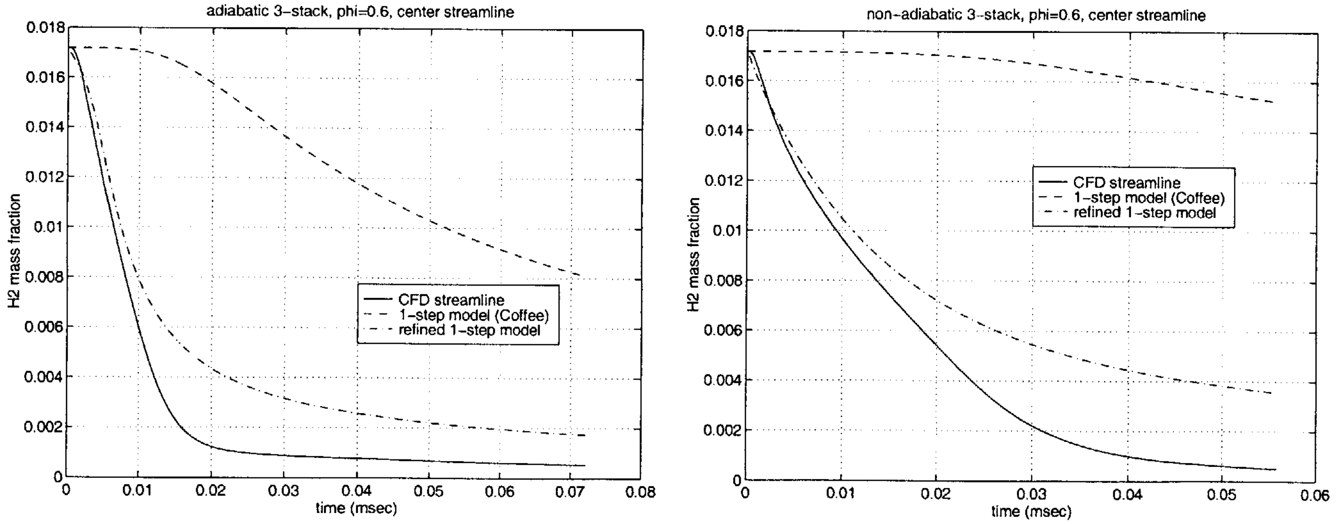

(c) Adiabatic 3-stack, ϕ=0.6, center streamline.

(d) Non-adiabatic 3-stack, ϕ=0.6, center streamline.

Figure E-4: Hydrogen mass fraction along the center streamline in the 3-stack, showing good comparison between the refined 1-step model, and the detailed CFD solutions.

comparison. The differences are once again attributed to the simplicity of trying to model a complex multi-step reaction with a single rate expression across different equivalence ratios and heat loss conditions.

The same procedure was also repeated for the 6-stack; the results are plotted in Figures E-6 & E-7. The figures show that the rate expression derived in Eq. E.4 for the 3-stack is unable to capture the mass fraction dependence along the streamline. Particularly, the initial slope of the mass fraction as derived from the 3-stack rate expression shows poor comparison with the CFD results. This is attributed to the difference in the behavior of the streamlines in the two configurations. As discussed in Chapter six, since the annular geometry of the 6-stack does not have recirculation zones on both sides of the incoming jet, unlike the 3-stack, the streamlines in the 6-stack do not ignite immediately. The ignition behavior of the two geometries is therefore quite different, hence, the 3-stack rate expression is unable to model the initial ignition process for the 6-stack.

A different single-step rate expression was therefore derived for the 6-stack geometry:

$$\frac{d[H_2]}{dt} = 1.62 \times 10^{18} exp(-10950/1.9782 \times T)[H_2]^2[O_2] \tag{E.5}$$

The mass fraction dependence as derived from this reaction rate is plotted in Figures E-6 & E-7, and shows good comparison with the results from the detailed mechanism.

Overall, the results suggest that although single-step rate expressions are unable to capture the physical rate controlling steps in the reaction, they can be empirically tuned through CFD for the 3-stack and 6-stack configurations to provide reasonable agreement with detailed reaction mechanisms. The expressions derived in Eqs. E.4 & E.5 were therefore considered as a suitable first-step approximation for estimating the chemical reaction times for the experimental operating points.

E.4 Calculation of the Reaction Times

Having evaluated the effectiveness of using a single-step reaction mechanism to model the chemical process, the next step involved comparison of model-based reaction time estimates with those from detailed CFD solutions.

Figure E-8 plots hydrogen concentration along the streamlines for sample 3-stack and 6-stack solutions. The effective reaction time along each streamline was defined as the time for the hydrogen concentration to change from 95% to 5% of the initial concentration. This is plotted in Figure E-9 for the different streamlines, along with the mass averaged value of the reaction time for each of the four cases considered herein[2].

The mass-averaged values of the reaction time from the CFD were then compared with estimates from

---

[2] Since many of the streamlines did not reach 95% completion, only four solutions were used for this comparison.

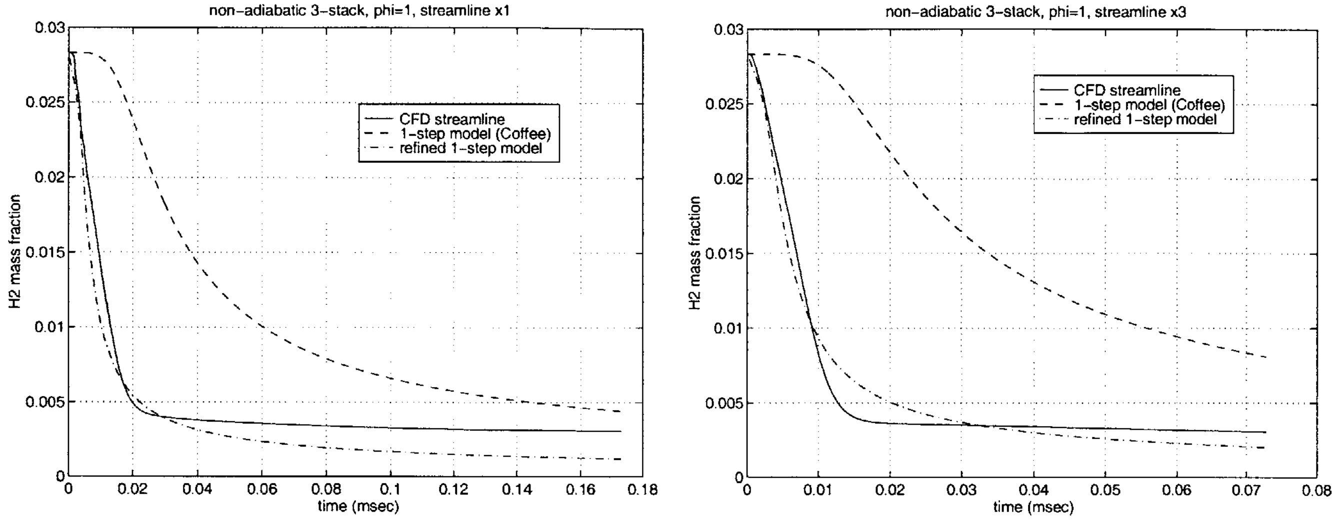

(a) Non-adiabatic 3-stack, ϕ=1, streamline 1.

(b) Non-adiabatic 3-stack, ϕ=1, streamline 3.

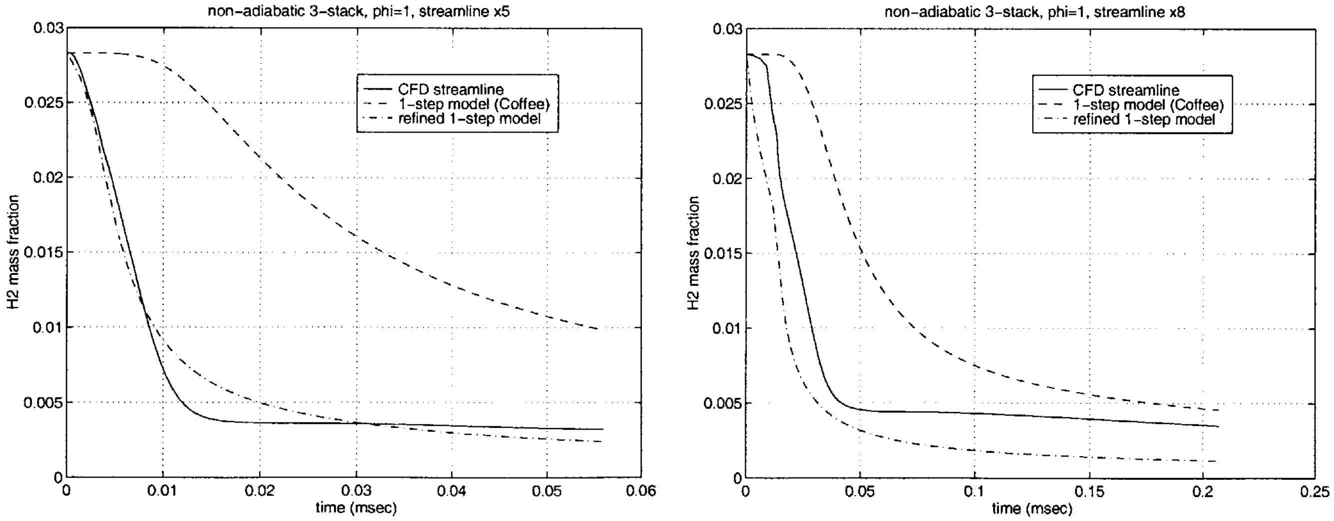

(c) Non-adiabatic 3-stack, ϕ=1, streamline 5.

(d) Non-adiabatic 3-stack, ϕ=1, streamline 8.

Figure E-5: Hydrogen mass fraction along different streamlines in the 3-stack.

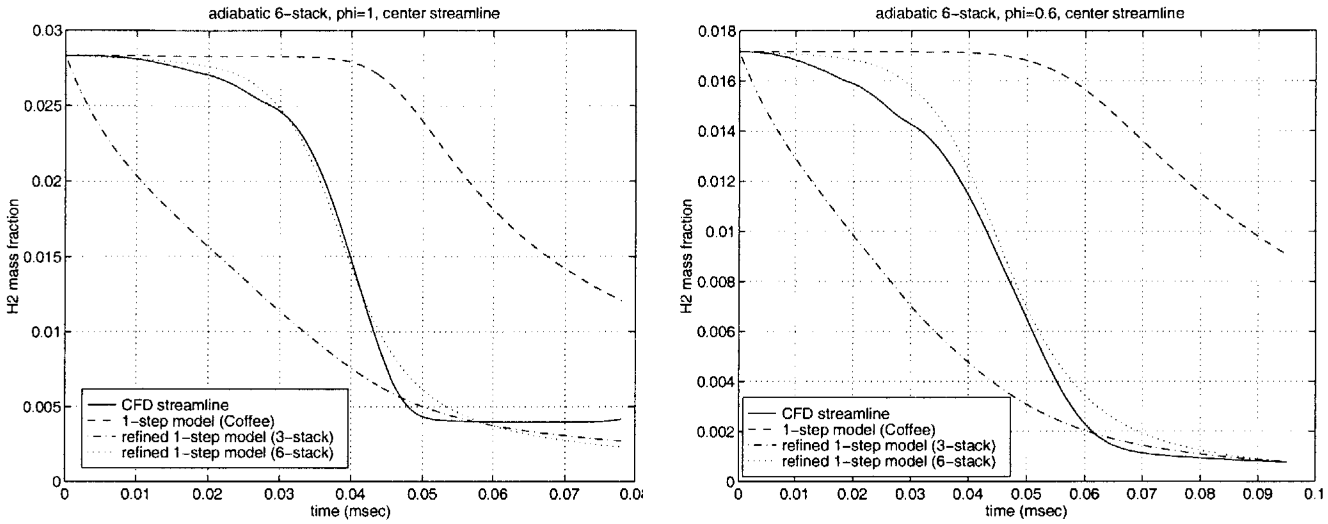

(a) Adiabatic 6-stack, ϕ=1, center streamline.

(b) Adiabatic 6-stack, ϕ=0.6, center streamline.

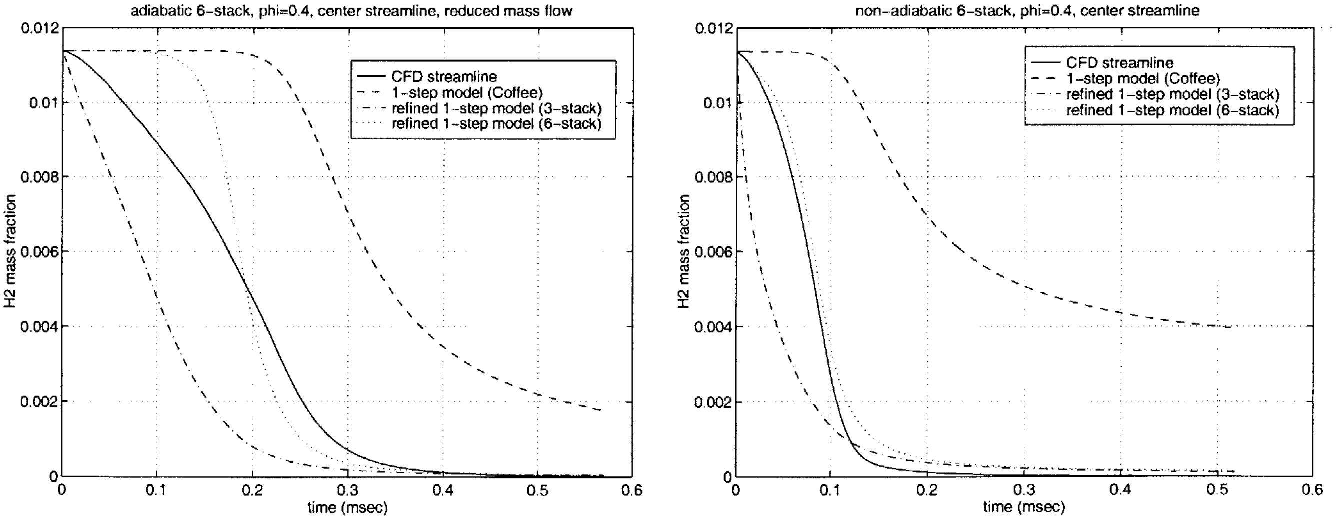

(c) Adiabatic 6-stack, ϕ=0.4, center streamline.

(d) Non-adiabatic 6-stack, ϕ=0.4, center streamline.

Figure E-6: Hydrogen mass fraction along the center streamline in the 6-stack.

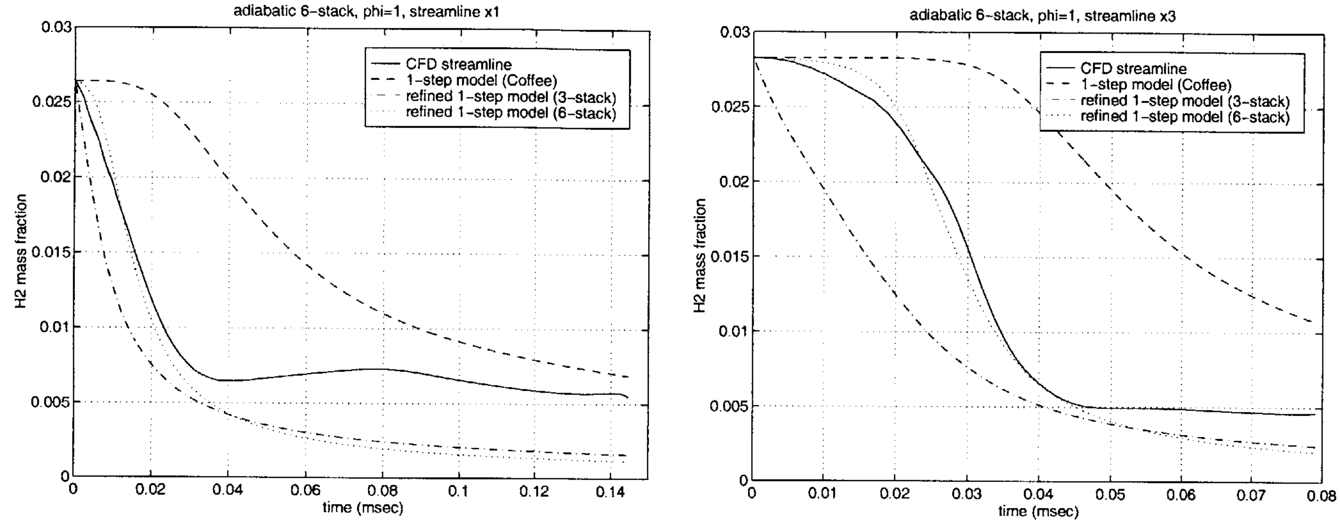

(a) Adiabatic 6-stack, ϕ=1, streamline 1.

(b) Adiabatic 6-stack, ϕ=1, streamline 3.

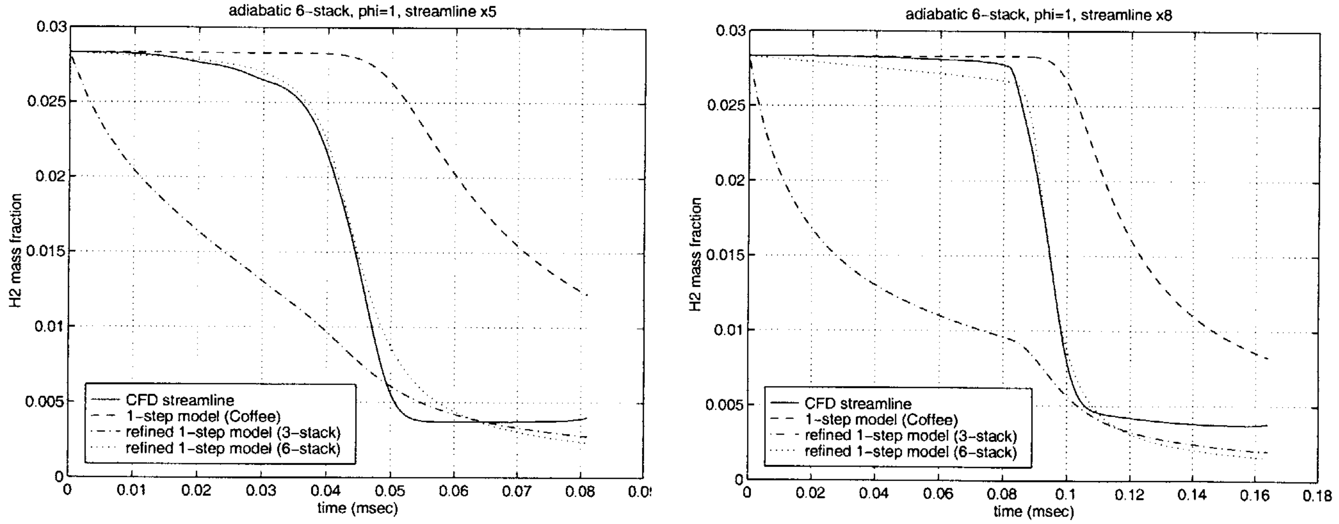

(c) Adiabatic 6-stack, ϕ=1, streamline 5.

(d) Adiabatic 6-stack, ϕ=1, streamline 8.

Figure E-7: Hydrogen mass fraction along different streamlines in the 6-stack.

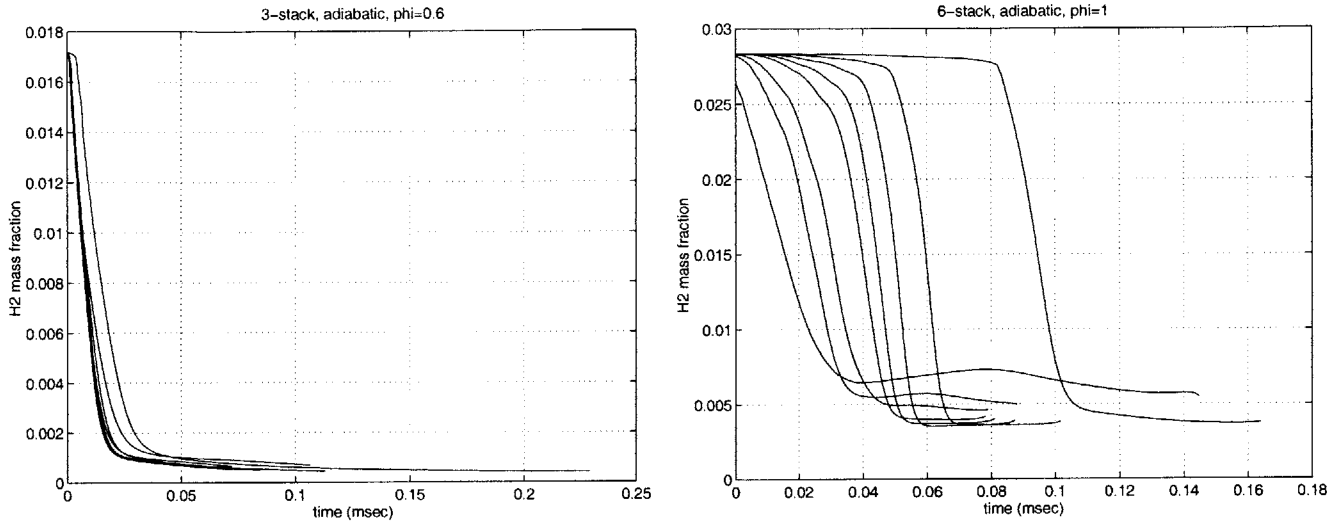

(a) 3-stack configuration.

(b) 6-stack configuration.

Figure E-8: Hydrogen mass fraction along streamlines in the 3-stack and 6-stack.

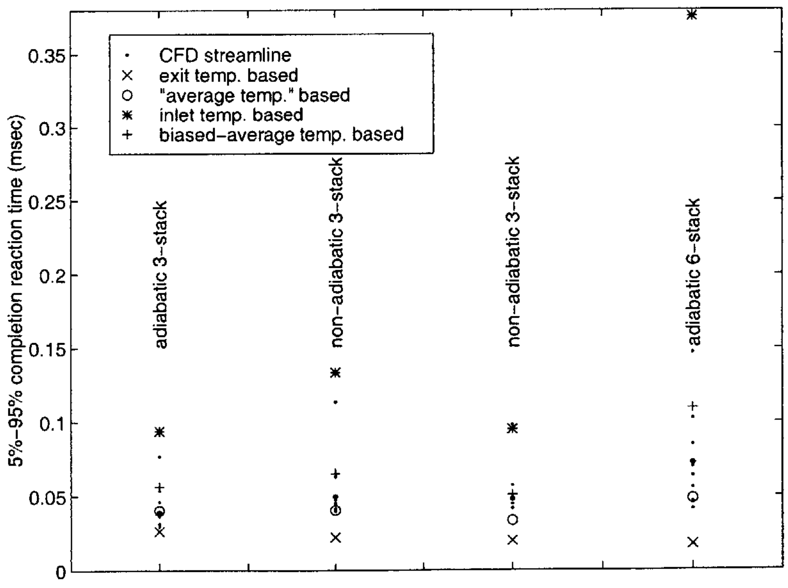

Figure E-9: Reaction time comparison for the 3-stack and 6-stack, showing good agreement between the CFD-based mass averaged reaction time and the "biased-average" temperature model-based reaction time.

the single-step rate expressions derived in Eqs. E.4 & E.5 using the following methodology:

$$\tau_{react} = \frac{[H_2]_{initial}}{Aexp(-E/RT)[H_2]^2_{average}[O_2]_{average}} \quad \text{(E.6)}$$

$$[H_2]_{initial} = \frac{X_{H_2}P}{RT_{inlet}} \qquad [O_2]_{initial} = \frac{X_{O_2}P}{RT_{inlet}} \quad \text{(E.7)}$$

$$[H_2]_{average} = \frac{[H_2]_{initial}}{2} \qquad [O_2]_{average} = \frac{[O_2]_{initial}}{2} \quad \text{(E.8)}$$

Since the temperature of the outer walls of the combustor was empirically observed to be approximately half the exit gas temperature, the combustor inlet temperature was assumed to be half the exit temperature. Figure E-9 plots the reaction time as estimated from the model using four different assumptions for the representative temperature in the reaction:

1. $T=T_{exit}$,
2. $T=T_{inlet}$,
3. $T=T_{average}=\frac{T_{inlet}+T_{exit}}{2}$, and
4. $T=T_{biased-average}=\frac{T_{inlet}+T_{average}}{2}$.

The figure shows that the mass averaged reaction times from the CFD are bounded by average-temperature and inlet-temperature based estimates from the model. The "biased-average" temperature as defined before was therefore considered to be a representative temperature for calculating the reaction time from the single step reaction rates in Eqs. E.4 & E.5. This may physically be explained by the fact that since reaction rates have a Arrhenius dependence on temperature, most of the chemical reaction time "accrues" due to reactions at low temperatures. A temperature that is biased towards the inlet temperature may therefore serve as representative temperature for calculating the overall reaction time from a single-step mechanism.

E.5 Implications for the Damkohler Number Model

The implications of the comparisons presented thus far are as follows:

Calculation of the Residence Time: Figures E-2 & E-3 show that there can be considerable uncertainty in the estimation of the residence time using Eq. E.2. In fact, assuming that the effective volume of the combustor could be estimated to within 20%, and that the exit temperature was within 500K of the representative value, the uncertainty in the estimation of the residence time could be up to 40%.

This uncertainty could be reduced by using the CFD solutions to refine these estimates. For the purpose of calculating the residence time for the experimental operating points, the following empirically-based rules were therefore used as heuristics:

1. T_{exit} was used as the representative temperature in the chamber,

2. $V_{effective}$=0.3 × $V_{chamber}$ for the 3-stack geometry, and
3. $V_{effective}$=0.9 × $V_{chamber}$ for the 6-stack geometry.

Calculation of the Reaction Time: Figures E-4 through E-7 show that a single step reaction mechanism as presented in the literature compares poorly with the CFD results form a detailed reaction mechanism. The single-step rate expressions therefore have to be empirically tuned against detailed reaction mechanisms from the CFD.

Although this greatly limits the predictive capability of the Damkohler number model, it provides a simple methodology for evaluating the reaction times for different experimental runs. With the concession that the uncertainty in the estimation of the reaction time can still be large (up to a factor of two), Eqs. E.6 - E.8 are therefore considered to provide a suitable approximation to the chemical reaction times inside the chamber.

E.6 Summary

This appendix presented a methodology for calculating the Damkohler number for the combustor. It evaluated various methods that could be used to estimate the residence and reaction times inside the chamber, and compared the results from simple first order models with those from reacting flow CFD solutions.

The overall goal of this appendix was to justify the assumptions used to calculate the Damkohler number for different experimental runs, and to anchor the Damkohler number model with detailed results from reacting flow CFD solutions.

Bibliography

[1] Advisory Group for Aerospace Research and Development (AGARD), *"Materials Properties Handbook"*, North Atlantic Treaty Organization, Volume IV - Heat Resistant Alloys, 1966.

[2] Ahn, C. H., Allen, M. G., *"A Fully Integrated Micromagnetic Actuator with a Multilevel Core"*, Digest, IEEE Solid-State Sensor and Actuator Workshop, pp. 14-18, Hilton Head, 1992.

[3] Ahn *et al.*, *"A Planar Variable Reluctance Micromotor with Fully Integrated Stator and Wrapped Coils"*, Proc. Micro Electro Mechanical Systems, IEEE Robotics and Automation Society, pp. 1-6, 1993.

[4] American Society for Testing and Materials, *"Manual on the Use of Thermocouples in Temperature Measurement"*, ASTM Special Technical Publication 470, 1970.

[5] ASME American National Standard, *"Measurement Uncertainty: Part 1, Instruments and Apparatus"*, ANSI/ASME Supplement to Performance Test Codes, PTC 19.1-1985, 1986.

[6] Ayón *et al.*, *"Etching Characteristics and Profile Control in a Time Multiplexed Inductively Coupled Plasma Etcher"*, presented at the Solid-State Sensor and Actuator Workshop at Hilton Head, June 1998.

[7] Ayón *et al.*, *"Characterization of a Time Multiplexed Inductively Coupled Plasma Etcher"*, Journal of the Electrochemical Society, Vol. 146, No. 1, January 1999.

[8] Ayón *et al.*, *"Tailoring Etch Directionality in a Deep Reactive Ion Etching Tool"*, presented at Transducers '99, International Conference on Solid-State Sensors and Actuators, Sendai, Japan, June 1999.

[9] Baccarani *et al.*, Journal of Applied Physics, 49, 5565, 1978.

[10] Ballal, D. R. and Lefebvre, A. H., *"Flame Quenching in Turbulent Flowing Gaseous Mixtures"*, Sixteenth Symposium (International) on Combustion, pp. 1689-1698, The Combustion Institute, Pittsburgh, 1977.

[11] Bart, S. F., *"Modeling and Design of Electroquasistatic Microactuators"*, Ph.D. Thesis, Massachusetts Institute of Technology, 1990.

[12] Bates *et al.*, *"Rechargeable Solid State Lithium Microbatteries"*, Proc. Micro Electro Mechanical Systems, IEEE Robotics and Automation Society, pp. 1-6, 1993.

[13] Beckwith, T. G., Marangoni, R. D., Lienhard, J. H., *"Mechanical Measurements"*, Fifth Edition, Addison-Wesley Publishing Company, June 1995.

[14] Benson, R. S., Ponton, J. W., *"Process Miniaturization - A Route to Total Environmental Acceptability"*, Trans IChemE 71 A, pp. 160-168, 1993.

[15] Bradley, D., Matthews, K. J., *"Measurement of High Gas Temperatures with Fine Wire Thermocouples"*, Journal of Mechanical Engineering Science, Vol. 10, No. 4, 1968.

[16] Brooks *et al.*, *"Integrated Microchannel Combustor/Evaporator Development"*, Process Miniaturization: 2nd International Conference on Microreaction Technology, Topical Conference Reprints, 1998.

[17] Buttner *et al.*, *"A Study of Flame Temperatures as Determined by the Sodium Line Reversal Method in Totally and Partially Colored Flames"*, Project SQUID TM PUR-27-M, September 1949.

[18] Chen *et al.*, *"ALLSPD-3D, Version 1.0"*, Internal Fluid Mechanics Division, NASA Lewis Research Center, November 1995.

[19] Chen, K-S., *"Materials Characterization and Structural Design of Ceramic Microturbomachinery"*, Ph.D. Thesis, Massachusetts Institute of Technology, 1999.

[20] Coffee *et al.*, *"The Overall Reaction Concept in Premixed, Laminar, Steady-State Flames. I. Stoichiometries."*, Combustion and Flame 54, 155-169, 1983.

[21] Coffee *et al.*, *"The Overall Reaction Concept in Premixed, Laminar, Steady-State Flames. II. Initial Temperatures and Pressures"*, Combustion and Flame 58, 59-67, 1984.

[22] Cole *et al.*, *"OBIC Analysis of Stressed, Thermally-Isolated Polysilicon Resistors"*, presented at the International Reliability Physics Symposium, Las Vegas, 3-6 April 1995.

[23] Colinge *et al.*, *"Grain Size and Resistivity of LPCVD Polycrystalline Silicon Films"*, J. Electrochem. Soc., Solid-State Science and Technology, pp. 2009-2014, September 1981.

[24] Damkohler, G., Z. Electrochem., Vol. 46, p. 601, 1940.

[25] Damkohler, G., NACA Tech Memo. No. 1112, 1947.

[26] Deal, B. E., Grove, A. S., *"General Relationship for the Thermal Oxidation of Silicon"*, Journal of Applied Physics, Vol. 36, p. 3770, 1965.

[27] Dhuler *et al.*, *"A Comparative Study of Bearing Designs and Operational Environments for Harmonic Side-Drive Micromotors"*, Proc. IEEE Workshop on Micro Electro Mechanical Systems, Travemunde, Germany, February 1992.

[28] Doebelin, E. O., *"Measurement Systems - Applications and Design"*, Fourth Edition, McGraw-Hill, 1990.

[29] Drela, M., Youngren, H., *"A User's Guide to MISES 2.1"*.

[30] Egolfopoulos, F. N., Law, C. K., *"An Experimental and Computational Study of the Burning Rates of Ultra-Lean to Moderately-Rich $H_2/O_2/N_2$ Laminar Flames with Pressure Variations"*, Twenty-Third Symposium (International) on Combustion, The Combustion Institute, 1990, pp. 333-340.

[31] Epstein *et al.*, *"Micro Turbine Generators"*, Final Technical Report prepared for MIT Lincoln Laboratory, 1995.

[32] Epstein *et al.*, *"MIT-ARO Micro-Gas Turbine Generator Review"*, MIT-Army Research Office, Multidisciplinary University Research Initiative First Annual Program Review, May 1996.

[33] Epstein *et al.*, *"Micro Gas Turbine Generators"*, First Semi-Annual Interim Technical Progress Report on Grant #DAAH04-95-1-0093, January 1996.

[34] Epstein *et al.*, *"Micro Gas Turbine Generators"*, Third Semi-Annual Interim Technical Progress Report on Grant #DAAH04-95-1-0093, January 1997.

[35] Epstein *et al.*, *"The MIT Microengine Project"*, Annual Technical Report, January 1999.

[36] Epstein, A. H., Senturia, S. D., *"Macro Power from Micro Machinery"*, Science, Volume 276, p. 1211, May 23 1997.

[37] Epstein *et al.*, *"Power MEMS and Microengines"*, presented at IEEE conference on Solid State Sensors and Actuators, Chicago, June 1997.

[38] Epstein *et al.*, *"Micro-Heat Engines, Gas Turbines, and Rocket Engines"*, presented at the 28th AIAA Fluid Dynamics Conference and the 4th AIAA Shear Flow Control Conference, Snowmass Village, June 1997.

[39] Firebaugh, S. L., Jensen, K. F., Schmidt, M. A., *"Investigation of High Temperature Degradation of Platinum Thin Films with an In-situ Resistance Measurement Apparatus"*, Journal of Microelectromechanical Systems, Vol. 7, No. 1, pp. 128-35, March 1998.

[40] Friend, W. Z., *"Corrosion of Nickel and Nickel-Base Alloys"*, John Wiley & Sons, Inc., 1980.

[41] Gauba, G., personal communication, unpublished work.

[42] Galasso, F. S., *"Chemical Vapor Deposited Materials"*, UTRC, E. Hartford, Con., CRC Press, Boston, 1991.

[43] Ghodssi *et al.*, *"Thick Buried Oxide in Silicon (TBOS): An Integrated Fabrication Technology for Multi-Stack Wafer-Bonded MEMS Processes"*, poster, Transducers '99, International Conference on Solid-State Sensors and Actuators, Sendai, Japan, June 1999.

[44] Groshenry, C., *"Preliminary Study of a Micro-Gas Turbine Engine"*, S.M. Thesis, Massachusetts Institute of Technology, 1995.

[45] Ghoniem, A. F., *"Combustion in Homogeneous Gaseous Mixtures"*, Chapter IV, 2.280 class notes, Fundamentals, Modeling and Computations in Combustion, Massachusetts Institute of Technology, 1998.

[46] Hagendorf *et al.*, *"A* Pt/Al_2O_3 *Coated Microstructured Reactor/Heat Exchanger for the Controlled* H_2/O_2*-Reaction in the Explosion Regime"*, Process Miniaturization: 2nd International Conference on Microreaction Technology, Topical Conference Reprints, 1998.

[47] Heidmann, M. F. and Priem, R. J., *"A Modified Sodium-Line Reversal Technique for the Measurement of Combustion Temperatures in Rocket Engines"*, J. Am. Rocket Soc. 23, 248, 1953.

[48] Hill, P. G., Peterson, C. R., *"Mechanics and Thermodynamics of Propulsion"*, Second Edition, Addison-Wesley Publishing Company, 1992.

[49] Holman, J. P., *"Heat Transfer"*, Seventh Edition, McGraw Hill Book Company, 1992.

[50] Hsu, C. H., Schmidt, M. A., *"Micromachined Structures Fabricated Using a Wafer Bonded Sealed Cavity Process"*, Technical Digest, IEEE Sensors Workshop, Hilton Head, SC, pp. 151-155, 1994.

[51] Huang, E., *"Thermal Design Trade Studies for a Silicon Turbojet Engine"*, Initial Report, Massachusetts Institute of Technology, Lincoln Laboratory, October 1998.

[52] Huang, E., personal communication, unpublished work, Massachusetts Institute of Technology, Lincoln Laboratory, July 1999.

[53] Huff *et al.*, *"Design of Sealed Cavity Microstructures Formed by Silicon Wafer Bonding"*, Journal of Microelectromechanical Systems, Vol. 2, No. 2, pp. 74-81, 1993.

[54] Jacobson, S. A., *"Aerothermal Challenges in the Design of a Microfabricated Gas Turbine Engine"*, presented at the 29th AIAA Fluid Dynamics Conference, Albuquerque, June 1998.

[55] Jacobson, S. A., personal communication, unpublished work.

[56] Jensen *et al.*, *"Reaction Engineering for Microreactor Systems"*, Microreaction Technology, Proceedings of the First International Conference on Microreaction Technology, 1997.

[57] Juan, W-H., Pang, S. W., *"Released Si Microstructures Fabricated by Deep Etching and Shallow Diffusion"*, Journal of Microelectromechanical Systems, Vol. 5, No. 1, March 1996.

[58] Kee *et al.*, *"The Chemkin Collection III Transport User's Manual"*, Reaction Design, 1998.

[59] Kern, W., Puotinen, D. A., *"Cleaning Solutions Based on Hydrogen Peroxide for Use in Silicon Semiconductor Technology"*, RCA Review, Vol. 31, pp. 187-206, 1970.

[60] Kerrebrock, J. L., *"Aircraft Engines and Gas Turbines"*, 2nd ed., MIT Press, 1992.

[61] Klaassen *et al.*, *"Silicon Fusion Bonding and Deep Reactive Ion Etching: A New Technology for Microstructures"*, The 8th International Conference on Solid-State Sensors and Actuators, and Eurosensors IX, Stockholm, 1995.

[62] Lee, J. W., "Computational Modeling of a Silicon Microcombustor", S.M. Thesis, Massachusetts Institute of Technology, expected June 2000.

[63] Lee *et al.*, *"A Miniaturized High-Voltage Solar Cell Array as an Electrostatic MEMS Power Supply"*, Journal of Microelectromechanical Systems, Vol. 4, No. 3, September 1995.

[64] Lerou *et al.*, *"Microfabricated Minichemical Systems: Technical Feasibility"*, Microsystem Technology for Chemical and Biological Microreactors, DECHEMA Monographs, 132, Frankfurt am Main, p. 51, 1996.

[65] Lerou, J. J., Ng, K. M., *"Chemical Reaction Engineering: A multiscale approach to a multiobjective task"*, Chemical Engineering Science 51, pp. 1595-1614, 1996.

[66] Lewis *et al.*, *"Digital MicroPropulsion"*, 12th IEEE International Micro Electro Mechanical Systems Conference (MEMS '99), January 1999.

[67] Li, S. C., *"OBIC Hydrogen-Related Electrical Instabilities in MOS capacitors of LPCVD Silicon Oxides"*, Ph.D. Thesis, Rensselaer Polytechnic Institute, Troy, NY, pp. 69-122, 1991.

[68] Lin *et al.*, *"Fabrication of a Micro Turbine/Bearing Rig"*, Late News Poster, Solid-State Sensor and Actuator Workshop at Hilton Head, 1998.

[69] Lin *et al.*, *"Fabrication and Characterization of a Micro Turbine/Bearing Rig"*, presented at MEMS '99, Orlando, 1999.

[70] Loh, E., Journal of Applied Physics, 54, 4463, 1983.

[71] London, A., Harrison, T., Spearing, M., personal communication.

[72] Lu *et al.*, IEEE Trans. on Electron Devices, ED-30, 137, 1983.

[73] Lukachko, S., personal communication, unpublished work, Massachusetts Institute of Technology, 1999.

[74] Makino, T., and Nakamura, H., *"Resistivity Changes of Heavily-Boron-Doped CVD-Prepared Polycrystalline Silicon Caused by Thermal Annealing"*, Solid-State Electronics, Vol. 24, pp. 49-55, 1981.

[75] Mandurah *et al.*, *"Phosphorus Doping of Low Pressure Chemically Vapor-Deposited Silicon Films"*, J. Electrochem. Soc., Solid-State Science and Technology, pp. 1019-1023, June 1979.

[76] Matgason, R. J., *"The Path of a Jet Directed at Large Angles to a Subsonic Free Stream"*, National Aeronautics and Space Administration, NASA TN D-4919.

[77] Mattingly, J. D., Heiser, W. H., Daley, D. H., *"Aircraft Engine Design"*, AIAA Education Series, New York, 1987.

[78] Measley, M. L., Smyth, J. R., *"Ceramic Gas Turbine Technology Development"*, ASME paper 96-GT-367, 1996.

[79] Mehra *et al.*, *"Aerodynamic Design Considerations for the Turbomachinery of a Micro Gas Turbine Engine"*, presented at the 25th National and 1st International Conference on Fluid Mechanics and Fluid Power, India, December 1998.

[80] Mehra, A., *"Computational Investigation and Design of Low Reynolds Number Micro-Turbomachinery"*, S.M. Thesis, Massachusetts Institute of Technology, 1997.

[81] Mehra, A., Waitz, I. A., *"Development of a Hydrogen Combustor for a Microfabricated Gas Turbine Engine"*, presented at the Solid-State Sensor and Actuator Workshop at Hilton Head, June 1998.

[82] Mehregany *et al.*, *"Operation of Microfabricated Harmonic and Ordinary Side-Drive Motors"*, Proceedings: IEEE Workshop of Micro Electro Mechanical Systems, pp. 1-8, 1990.

[83] Mehregany, M., *"Microfabricated Silicon Electric Mechanisms"*, Ph.D. Thesis, Massachusetts Institute of Technology, 1990.

[84] Mellor, A. M., *"Design of Modern Turbine Combustors"*, Academic Press, 1990.

[85] Miyajima, H., Mehregany, M., *"High-Aspect Ratio Photolithography for MEMS Applications"*, Journal of Microelectromechanical Systems, Vol. 4, No. 4, pp. 220-229, December 1995.

[86] Murota, J., and Sawai, T., *"Electrical Characteristics of Heavily Arsenic and Phosphorus Doped Polycrystalline Silicon"*, Journal of Applied Physics, Vol. 53, No. 5, May 1982.

[87] Nagle, S. F., and Lang, J. H., *"A Micro-Scale Electric-Induction Machine for a Micro Gas Turbine Generator"*, presented at the 27th Annual Meeting of the Electrostatics Society of America, June 1999.

[88] Nakazawa *et al.*, *"Radial Turbine Development for the 100 kW Automotive Ceramic Gas Turbine"*, ASME paper 96-GT-366, 1996.

[89] Pennathur, S., personal communication, unpublished work.

[90] Peters, N., and Rogg, B., (Eds.), *"Reduced Kinetic Mechanisms in Combustion Systems. Lecture Notes in Physics"*, Chapter 2, "A Compilation of Experimental Data on Laminar Burning Velocities", Law, C. K., Springer, 1992.

[91] Piekos *et al.*, *"Design and Analysis of Microfabricated High Speed Gas Journal Bearings"*, AIAA paper 97-1966, presented at the 28th AIAA Fluid Dynamics Conference, Snowmass Village, June 1997.

[92] Piekos, E. S., Breuer, K. S., *"Pseudospectral Orbit Simulation of Non-Ideal Gas-Lubricated Journal Bearings for Microfabricated Turbomachines"*, Paper no. 98-Trib-48, presented at the Tribology Division of The American Society of Mechanical Engineers Joint ASME/STLE Triboloy Conference, Canada, October 1998.

[93] Poate, J. M., Tu, K. N., Mayer, J. W., (editors), *"This Films - Interdiffusion and Reactions"*, The Electrochemical Society, Inc., Chapter 10, Silicide Formation, p. 378, 1978.

[94] Purdue University Thermophysical Properties Research Center, *"Thermophysical Properties of Matter"*, Edited by Touloukian, Y. S., IFI/Plenum, New York, NY, 1970.

[95] Ramberg *et al.*, *"Oxidation Behavior of CVD and Single Crystal SiC at 1100° C"*, J. Electrochem. Soc., Vol. 142, No. 11, November 1995.

[96] Reynolds, W. C., STANJAN - Chemical Equilibrium Code, Department of Mechanical Engineering, Stanford University, 1987.

[97] Robert Bosch Gmbh, Patents 4855017 and 4784720 (USA), and 4241045C1 (Germany).

[98] Schmidt, M. A., personal communication.

[99] Schmidt, M. A., Senturia, S. D., Harrison, D. J., *"Microelectronic Fabrication"*, Chapter 3, 6.971 class notes, 1998.

[100] Schmidt, M. A., *"Silicon Wafer Bonding for Micromechanical Devices"*, presented at the Solid-State Sensor and Actuator Workshop at Hilton-Head, 1994.

[101] Schetz, J. A., *"Injection and Mixing in Turbulent Flow"*, AIAA Prog. in Aeronautics and Astronautics, Vol. 68, 1980.

[102] Smith, J. M., *"Chemical Engineering Kinetics"*, Third Edition, McGraw-Hill Book Company, 1981.

[103] Solmi *et al.*, *"Electrical Properties of Thermally and Laser-Annealed Polycrystalline Silicon Films Heavily Doped with Arsenic and Phosphorus."*, J. Electrochem. Soc., Solid-State Science and Technology, pp. 1811-1818, August 1982.

[104] Somiya, S., Inomata, Y., *"Silicon Carbide Ceramics - 1, Fundamentals and Solid Reaction"*, Ceramic Research and Development in Japan Series, Elsevier Applied Science, 1991.

[105] Spadaccini, C. M., personal communication.

[106] Srinivasan *et al.*, *"Chemical Performance and High Temperature Characterization of Micromachined Chemical Reactors"*, International Conference on Solid-State Sensors and Actuators , Digest of Technical Papers, Volume 1, 1 C3.01, 1997.

[107] Srinivasan *et al.*, *"Micromachined Reactors for Catalytic Partial Oxidation Reactions"*, Reactors, Kinetics, and Catalysis, AIChE Journal, Vol. 43, No. 11, pp. 3059-3069, November 1997.

[108] Sutton, G. P., *"Rocket Propulsion Elements"*, Sixth Edition, John Wiley and Sons, Inc., 1992.

[109] Tai, Y-C., *"IC-Processed Polysilicon Micromechanics: Technology, Material, and Devices"*, Ph.D. Thesis, University of California, Berkeley, 1989.

[110] Tai *et al.*, *"IC-processed micromotors: design, technology and testing"*, Proc. Micro Electro Mechanical Systems, IEEE Robotics and Automation Council, pp. 1-6, 1989.

[111] Tanaka *et al.*, *"Development and Fabrication of Ceramic Gas Turbine Components"*, ASME paper 96-GT-446, 1996.

[112] The Carborundum Company, *"Physical Properties of Hexeloy SA Silicon Carbide - Technical Data"*, The Carborundum Company, November 1989.

[113] Tonkovich *et al.*, *"Microchannel Chemical Reactors for Fuel Processing"*, Process Miniaturization: 2nd International Conference on Microreaction Technology, Topical Conference Reprints, 1998.

[114] Tzeng, Y-S., *"An Investigation of Microcombustion Thermal Phenomena"*, S.M. Thesis, Massachusetts Institute of Technology, 1997.

[115] Waitz *et al.*, *"Combustors for Micro-Gas Turbine Engines"*, ASME Journal of Fluids Engineering, Vol. 20, pp. 109-117, March 1998.

[116] Wessel *et al.*, *"A CMOS Thermally-Isolated Heated Structure as a Substrate for Semiconductor Gas Sensors"*, Electronics Journal, 23, pp. 451-456, 1992.

[117] Westbrook, C. K., and Dryer, F. L., *"Chemical Kinetic Modeling of Hydrocarbon Combustion"*, Prog. Energy Combustion Science, Vol. 10, pp. 1-57, 1984.

[118] White, F. M., *"Viscous Fluid Flow"*, Second Edition, McGraw-Hill, Inc., 1991.

[119] Wu, C. K., Law, C. K., *"On the Determination of Laminar Flame Speeds from Stretched Flames"*, Twentieth Symposium (International) on Combustion, The Combustion Institute, pp. 1941-1949, 1984.

[120] Xiw, J. Z., *"Electrical Properties of Deposited Silicon Dioxide Films and Effects of Rapid Thermal Annealing on Such Properties"*, Ph.D. Thesis, Rensselaer Polytechnic Institute, Troy, NY, pp. 69-122, 1991.

[121] Youngren, H., *"Analysis and Design of Transonic Cascades with Splitter Vanes"*, S.M. Thesis, Massachusetts Institute of Technology, 1991.

[122] Zhang, X., personal communication, unpublished work.